

KU Leuven
Biomedical Sciences Group
Faculty of Medicine
Department of Imaging & Pathology



MULTI-MODAL SMALL ANIMAL IMAGING FOR BRAIN TUMOR THERAPY ASSESSMENT

Cindy LETEN

Dissertation presented in partial fulfilment of
the requirements for the degree of Doctor in
Biomedical Sciences

Supervisor: Prof. Uwe Himmelreich
Co-Supervisor: Prof. Annemie Van Der Linden
Chair: Prof. Philippe Demaerel
Secretary: Prof. Dr. Christophe Deroose
Jury members: Prof. Dr. Christophe Deroose
Prof. Dr. Stefaan Van Gool
Prof. Dr. Hrvoje Miletic
Prof. Dr. Mathias Hoehn
Prof. Bernard Gallez

July 2014

When you come to the end of your rope, tie a knot and hang on

Franklin D. Roosevelt (1882 - 1945)

Acknowledgments

“We must find time to stop and thank the people who make a difference in our lives”

John F. Kennedy (1917 - 1963)

Alright, so I finally made it. The expense: buckets of blood, sweat, tears and one car (for which I am still sorry Mom...). Off course I owe many people thanks for their help, support and never-ending patience. Without it, I would definitely not be here!

First of all I would like to thank my promoter, Prof. Uwe Himmelreich for his never-ending patience and support. Without you this thesis would definitely not have been possible. Thank you also for creating the amazing working environment which made me come to work with a smile on my face even when the science was not co-operating!

I would also like to express my gratitude towards my co-promoter, Prof. Annemie Van Der Linden for her support and encouragements. Your enthusiasm and working attitude were a true inspiration! I also enjoyed my stay in your lab in Antwerp very much!

Furthermore, I would like to thank Prof. Catherine Verfaillie for her support and enthusiasm with regard to all my stem cell related work. Even with your immense work-load, you always found the time and will to be actively involved in my work! You never hesitated to let me use the lab or the equipment for which I am truly grateful as it made my life a lot easier.

Next, I would like to thank all my jury members. Thank you, Prof. Dr. Christophe Deroose and Prof. Dr. Stefaan Van Gool for the many animated discussions and positive criticism, which guided me through my PhD. The love for research that you both possess is incredible. Furthermore, I would also like to thank Prof. Ghislain Opendakker, Prof. Hrvoje Miletic, Prof. Matthias Hoehn and Prof. Bernard Gallez for their willingness to act as my PhD jury members. Special thanks to Prof. Philippe Demaerel for chairing the PhD jury.

Furthermore, I would also like to thank Prof. Ivo Lambrichts from the University of Hasselt for allowing me to use your equipment when necessary. Special thanks also to Dr. Tom Struys and Ms Jeanine Santermans for their guidance and expertise in histology!

Due to the unique situation of performing a joint PhD with the University of Antwerp I had the opportunity to work in several different labs. I have to say all of them were amazing places to work and I owe an incredible thank you to everyone working there.

I would like to start with thanking all the people from Bil in Antwerp. Thank you for making my stay in Antwerp enjoyable. So thanks to Ilse, Pieter-Jan, Kasper, Geert, Jelle, Maarten, Ines, Dimitri, Christian, Lisbeth, Caroline, Disha and Julie for helping me and making me feel welcome! Special thanks to Johan for all the help with the MRI and to Elisabeth for helping me figure out the logistics with regard to my animals! Thank you as well to Prof. Peter Ponsaerts for allowing me to use your cell culture facilities during my stay in Antwerp.

Another lab where I spend quite some time is off course SCIL. I would really like to thank all the SCIL members for their hospitality and kindness! Special thanks are in order though for Kristel, Manja and Valerie. Thank you for your patience and incredible willingness to help me! Furthermore, I would also like to thank Rob, Pieter and Thomas for defrosting cells for me and helping me with experiments that I was less familiar with! Furthermore, I want to thank Sylvia for replenishing the stocks and her friendly nature!

Also special thanks to Antonio for helping me with the FACS! Finally, I would like to thank Veerle, Vicky and Christina for their help in keeping everything run smoothly!

Special thanks are also in order for the girls from Pediatric immunology. Tina, Lien and Carolien, thank you for the talks and help with my tumor cells!

And then off course, my lab buddies from MoSAIC. I intentionally say MoSAIC and not Biomedical MRI as there really is no difference in daily practice. All of you have my deepest sympathy and I can truly say there are no words to describe the gratitude I feel towards all of you! Let me start with my cell culture buddies Esther and Ashwini. I will never forget the “Wakka Wakka” times we shared in the cell culture room. Besides highly appreciated colleagues I also consider you friends and hope we keep in touch! Next off course Ann, thank you for arranging, well about everything in the lab... I really enjoyed your humor and wish you all the best. Also thanks to Peter for taking care of all the ordering and paper work! Jennifer, thank you for your kindness and optimism, it was a pleasure sitting next to you and your company definitely made the Zumba classes less exhausting! Greetje, thank you for your enthusiasm, love for science and off course for teaching me BLI! Jesse thank you for producing particles and performing ICP measurements! Special thanks also to Jennifer, Bryan, Marlein, Shweta, Akilla, Kristof, Bart and Sayuan for creating such a nice atmosphere in the office! You make every day a bit nicer! Cindy C., thank you for helping me with the PET images. Finally, a huge thank you for Tom D. Without you the MRI would fail and none of us would be able to finish anything! Thank you for your patience and again sorry to your wife for having to rescue me when I left my keys in the MRI on a Friday evening! Finally, also a very big thank you to Sofie. Although you spend most of your time in the clinic, I could always depend on you to read my articles or help me with clinical information. I really appreciated our talks! I will truly miss all of you very much!

Next I would like to thank Prof. Dirk De Ridder and Dr. Rudi Ory. Without your expertise and help I would not have been able to lead the life I have today.

When I try to express my gratitude towards my family and friends that have supported me for all these years, it gets even more difficult to put into words how much I owe every single one of you. First of all, thank you Sofie, Iris and Gijs. You have never given up on me when I did not reply e-mails or text messages. You guys mean the world to me! Next, I would like to thank Béné, Jean, Stijn, Nathalie, Rieko and Sofie for their unconditional friendship and fun weekends! Thanks also to Elke for the talks whenever I needed them and help with the paraffine embedding! I hope everything works out for you!! Finally I would also like to thank my friends from horse-back riding: Lise, Dagmar, Jolien, Jacqueline, Reine, Anke, Christophe, Lindsey,... You guys made it possible for me to relax and leave all the stress behind for a few hours, not an easy thing to do!

En dan, mama en papa... Het is onmogelijk om uit te drukken hoeveel liefde en steun ik van jullie heb ontvangen in de afgelopen jaren. Het leven is niet altijd gemakkelijk geweest voor ons maar weten dat er twee mensen zijn die onvoorwaardelijk achter je blijven staan ongeacht wat er gebeurd of wat je ook doet is van onschatbare waarde. Of ik nu kortaf, verdrietig of boos was, of je auto kapot reed..., jullie zijn mij altijd blijven steunen waarvoor dank uit de grond van mijn hart!

Ten slotte zou ik graag mijn vriend, Koen bedanken. Al die tijd heb je zonder klagen mijn driftbuiën ondergaan en mij moed gegeven om vol te houden. Vijf jaar, waarin ik je auto mocht lenen als ik 's nachts moest scannen en mijn eten op mij stond te wachten als ik weer eens belachelijk laat thuis kwam. Zelfs mijn diepvriezertje werd iedere week trouw bijgevuld tijdens mijn verblijf in Antwerpen. Woorden schieten zwaar tekort om uit te drukken hoe hard ik het op prijs stel wat je al die jaren voor mij gedaan hebt. Ik kan alleen maar proberen even begripvol te zijn tijdens het voltooien van jouw doctoraat!

Summary

Despite encouraging preclinical advances, patients diagnosed with glioblastoma still face a dismal prognosis. Suicide gene therapy has shown remarkable results in preclinical research but has generated rather disappointing results in patients. This is believed to be at least partly contributable to suboptimal distribution of the suicide gene throughout the tumor area. Therefore, attention turned to therapeutic stem cells that can track infiltrating tumor cells to deliver the therapeutic gene more efficiently. However promising some stem cells might be for this purpose, a safety issue remains when using stem cells. Stem cells have a tremendous potential as they are capable of differentiating into several types of tissue, which is also a reason for concern as this might result in mass growth or other unwanted side-effects.

Multi-modal imaging has been an increasingly important tool both clinically and preclinically to monitor tumor progression and therapeutic response to novel therapeutic approaches. In a clinical setting, magnetic resonance imaging (MRI) is mostly used for glioblastoma diagnosis and follow-up, although positron emission tomography (PET) can also be used for grading of tumors and assessment of tumor therapy. In our pre-clinical study, we aimed to follow-up not only treatment response but also guide treatment and gain further information on stem cell distribution prior to pro-drug initiation for the duration of treatment. Therefore, we used lentiviral vectors to express both a therapeutic gene, Herpes simplex virus – thymidine kinase (HSV-tk) and imaging reporter genes, enhanced green fluorescent protein (eGFP) and firefly luciferase (fLuc). Furthermore, stem cells were labeled using in house fabricated superparamagnetic iron oxide particles (SPIO's) for *in vivo* stem cell tracking by using MRI.

Already one day post intratumoral stem cell injection, stem cells were observed both inside and at the tumor border on 3D T2*-weighted MR images. Therefore, initiation of the pro-drug, ganciclovir (GCV) was commenced at that time. During therapy, stem cell viability was monitored by BLI using fLuc as a reporter gene.

Results showed that several stem cell lines (mouse mesenchymal stem cells (mMSC), mouse Oct4 positive bone marrow derived hypoblastlike stem cells (mOct4⁺ BM-HypoSCs), mouse Oct4 negative bone marrow multipotent adult progenitor cells (mOct4⁻ BM-MAPCs) and human Multistem's (hMultistem's) could be followed non-invasively for their therapeutic potential *in vivo* in three different malignant glioma models including a syngeneic mouse model (mMSC's, mOct4⁺ BM-HypoSCs and mOct4⁻ BM-MAPCs in a GL261 model) and two human glioma xenograft models (hMultistem's in the U87-MG and Hs683 models).

This strategy can now be used to further optimize and characterize the underlying mechanisms of stem cell based suicide gene therapy for glioblastoma by also directly and non-invasively comparing different cell lines in order to ameliorate treatment for not only this devastating disease but also for tracking of stem cells used for stem cell based therapies in other fields, such as for neurological diseases.

Samenvatting

Glioblastoma patiënten worden ondanks de vele bemoedigende preklinische resultaten nog steeds met een zeer lage levensverwachting geconfronteerd. Experimentele therapiën zoals o.a. behandelingen die gebruik maken van een zelfmoordgen hebben reeds opmerkelijke resultaten gegenereerd in de preklinische setting. In een klinische omgeving konden deze resultaten echter zelden bevestigd worden. Bij zelfmoordgentherapie wordt het zelfmoordgen in kwestie, in deze studie Herpes Simplex Virus-thymidine kinase (HSV-tk), tot expressie gebracht in de tumorregio. Wanneer vervolgens een voor de mens onschadelijke prodrug, in deze studie ganciclovir, wordt toegediend zal deze vervolgens in de gemanipuleerde cellen worden omgezet tot een toxisch product, wat de DNA-replicatie tijdens de celdeling verstoort en zo aanleiding geeft celdood van delende cellen. Dit effect wordt vervolgens nog versterkt door het bestaan van communicatiekanalen tussen naburige cellen waardoor het toxisch product zich verder kan verspreiden in de tumor massa. Er werd echter vastgesteld dat er een verminderde communicatie is tussen cellen van kwaadaardige tumoren wat aanleiding geeft tot een suboptimale verdeling van het gen en/of toxisch product in de tumor, wat de vaak teleurstellende resultaten bij patiënten verklaard. Vervolgens werd dan ook gezocht naar een andere manier om het zelfmoordgen meer gelijkmatig te kunnen verdelen over de gehele tumormassa. Hiervoor werd beroep gedaan op therapeutische stamcellen die in staat zijn infiltrerende tumorcellen op te sporen en zo het zelfmoordgen te verspreiden. Hoewel deze stamcellen over veelbelovende eigenschappen beschikken voor de behandeling van glioblastoma, zijn er ook mogelijke veiligheidsrisico's verbonden aan het gebruik van deze cellen. Zo zijn ze onder meer in staat te differentiëren naar verschillende weefseltypes, wat natuurlijk ook een risico inhoudt i.v.m. mogelijke tumorvorming of aanleiding kan geven tot het ontstaan van ongewenste neveneffecten.

Multimodale beeldvorming wint in toenemende mate aan belangrijkheid in zowel de klinische als de preklinische omgeving voor de opvolging van tumorprogressie en therapeutische respons na behandeling. In de klinische setting wordt vooral magnetische resonantie beeldvorming (MRI) toegepast voor zowel diagnostische doeleinden als voor de opvolging van patiënten tijdens en na behandeling.

Verder wordt ook positron emissie tomografie (PET) op regelmatige basis toegepast om het stadium te bepalen waarin de kanker zich bevindt.

In deze studie werd het effect van zelfmoordgentherapie, gebruik makend van stamcellen om het gen optimaal te verspreiden in de tumor, bestudeerd met verschillende beeldvormingstechnieken. Om dit mogelijk te maken werden lentivirale vectoren aangewend om zowel het therapeutische gen, Herpes simplex virus-thymidine kinase (HSV-TK) en de reporter genen, groen fluorescent proteïne (eGFP) en een luciferase afkomstig van de vuurvlieg (fLuc) tot expressie te brengen. Bovendien werden de stamcellen met superparamagnetische ijzeroxide partikels (SPIO's) opgeladen om ze te kunnen volgen m.b.v. MRI.

Alvorens de prodrug toe te dienen werd de verdeling van de stamcellen in en rond de tumor bepaald m.b.v. MRI. Reeds één dag na stamcelinfectie in de tumor werden de stamcellen zowel in de tumor als in de tumor rand gelokaliseerd m.b.v. 3 dimensionale T2* MR beelden. Vervolgens werd dan ook besloten met de prodrug, ganciclovir, te starten. Bovendien werd gebruik gemaakt van bioluminescente beeldvorming (BLI) met fLuc als reporter gen, om de overleving van de stamcellen op te volgen gedurende de behandeling.

De resultaten bekomen in deze studie toonden aan dat verschillende stamcellijnen, waaronder muis mesenchymale stamcellen (mMSC), muis Oct4 positieve van het beenmerg geïsoleerde hypblastachtige stamcellen (mOct4⁺ BM-HypoSCs), muis Oct4 negatieve van het beenmerg geïsoleerde multipotente adulte progenitorcellen (mOct4⁻ BM-MAPCs) en humane Multistem's (hMultistem's), niet-invasief konden worden opgevolgd *in vivo* met betrekking tot hun therapeutisch potentieel in drie verschillende hooggradige glioma modellen waaronder een syngeneisch muismodel (mMSC's, mOct4⁺ BM-HypoSCs en mOct4⁻ BM-MAPCs in het GL261 model) en twee humane gliomamodellen (hMultistem's in het U87-MG en het Hs683 model).

Deze werkwijze kan nu toegepast worden om zelfmoordgentherapie voor de behandeling van glioblastoma verder te optimaliseren en de onderliggende mechanismen te achterhalen om zo de behandeling voor niet uitsluitend deze ziekte met desastreuze gevolgen maar ook voor andere ziekten, zoals bijvoorbeeld beroertes, waarin stamcel gebaseerde behandelingen kunnen worden toegepast, te verbeteren.

List of Abbreviations

ADC	Apparent diffusion coefficient
a.u.	Arbitrary units
BBB	Blood-brain barrier
BLI	Bioluminescence imaging
CE-MRI	Contrast enhanced MRI
[¹¹ C]-MET	methyl-L-[¹¹ C]-Methionine
CMV promoter	cytomegalovirus promoter
CT	Computed tomography
DAPI	4'-6-DiAmidino-2-PhenylIndole
DC's	Dendritic cells
DMEM	Dulbecco's Modified Eagle's medium
DWI	Diffusion weighted MRI
EF-1 α	human elongation factor 1 α
EGF	Epidermal growth factor
eGFP	Enhanced green fluorescent protein
FBS	Fetal bovine serum
[¹⁸ F]-FCH	[¹⁸ F] fluorocholine
[¹⁸ F]-FDG	[¹⁸ F] fluoro-2-deoxyglucose
[¹⁸ F]-FET	[¹⁸ F] O-2-fluoroethyl-L-tyrosine
[¹⁸ F]-FHBG	[¹⁸ F] hydroxymethyl-butyl-guanine
fLuc	Firefly luciferase
GBM	Glioblastoma multiforme
GCV	Ganciclovir
Gy	Grey
hMultistem	Human Multistem
HSV-TK	Herpes simplex virus-thymidine kinase gene
ICP-OES	Inductively coupled plasma optical emission spectrometry
IMDM:	Iscove's modified dulbecco's medium
<i>i.p.</i>	Intraperitoneal
<i>i.v.</i>	intravenous

LA-BSA:	Linoleic acid bovine serum albumin
LIF	Leukemia inhibiting factor
mMSC	Mouse mesenchymal stem cells
mOct4 ⁺ BM-HypoSC	Mouse Oct4 positive bone marrow derived hypoblastlike stem cells
mOct4 ⁻ BM-MAPC	Mouse Oct4 negative bone marrow derived multipotent adult progenitor cells
mPEGSi	Methoxy-polyethyleneoxide-glycolated-silane
MRI	Magnetic resonance imaging
MRS	Magnetic resonance spectroscopy
NIR imaging	Near infrared imaging
PBS	Phosphate buffered saline
PDGF	Platelet-derived growth factor
PET	Positron emission tomography
PFA	Paraformaldehyde
PLL	Poly-L-Lysin
rLuc	Renilla reniformis luciferase
rOct4 ⁺ BM-HypoSC	Rat Oct4 positive bone marrow derived hypoblastlike stem cells
rOct4 ⁻ BM-MAPC	Rat Oct4 negative bone marrow derived multipotent adult progenitor cells
ROI	Region of interest
SEM	Standard error of mean
SMG ² –mPEGSi	Second seed mediated growth – magnetic nanoparticle cores coated with mPEGSi
SPIO	Superparamagnetic iron oxide particle
T	Tesla
TE	Echo time
T1	Longitudinal relaxation time
TR	Repetition time
T2	Transverse relaxation time
WT	Wild type

Table of Contents

Acknowledgements	V
Summary	VI
Samenvatting	IX
Abbreviations	X
Table of Contents	XII
Acknowledgments.....	3
Summary.....	7
Samenvatting	9
List of Abbreviations	11
Chapter 1: General Introduction	3
1.1 Gliomas in a clinical setting	3
1.2 Non-invasive imaging	5
1.2.1. Ultrasound.....	5
1.2.2 Photoacoustic imaging	5
1.2.3 Optical imaging.....	6
1.2.4. Computed tomography (CT).....	7
1.2.5. Radionuclide imaging: PET/SPECT	7
1.2.6 MRI/MRS	9
1.3 Glioma imaging in a clinical setting	12
1.4 Preclinical brain tumor rodent models.....	13
1.4 Innovative experimental tumor therapies	15
1.4.1 Anti-angiogenic treatment approaches.....	15
1.4.2 Immunotherapy.....	16
1.4.3 Gene therapy.....	16
1.4.4 Stem cell based suicide gene therapy for glioblastoma	17
1.5 Imaging in experimental glioma therapies	22
1.6 Conclusion	29

Chapter 2: Objectives and outline of this work.....	33
2.1 Outline of this work.....	33
2.2 Objectives.....	34
Chapter 3: Generation and validation of cell lines for non-invasive imaging of suicide gene therapy	39
Chapter 3: Generation and validation of cell lines for non-invasive imaging of suicide gene therapy	39
3.1 Introduction	39
3.2 Materials & methods.....	40
3.3 Results	43
3.3.1 Evaluation of transduction efficiency using a CMV promoter driven lentiviral vector	43
3.3.2 Evaluation of transduction efficiency using an EF1 α promoter driven lentiviral vector.....	45
3.3.3 Evaluation of the transduction using lentiviral vectors encoding for eGFP, fLuc and HSV-TK.....	47
3.3.4 Stem cell characterization and transduction related effects.....	50
3.3.5 Labeling stem cells with SPIO's.....	53
3.3.6 Transduction of glioma cells using a CMV promoter driven lentiviral vector encoding for mCherry and rLuc	55
3.4 Discussion.....	56
Chapter 4: <i>In vivo</i> validation of cell lines for non-invasive imaging of suicide gene therapy	61
4.1 Introduction	61
4.2 Materials & methods.....	64
4.3 Results	67
4.3.1 Safety studies m and rOct4 ⁺ BM-HypoSCs, m and rOct4 ⁻ BM-HypoSCs, mMSC's and hMultistem's.....	67
4.3.2 <i>In vivo</i> validation of fLuc and HSV-TK expression in eGFP-fLuc-HSVTK transduced stem cells	73
4.3.3 <i>In vivo</i> assessment of stem cells labeled with SPIO's using MRI.....	81
4.3.4 <i>In vivo</i> assessment of mCherry-rLuc transduction of malignant glioma cells using MRI and BLI.....	82
4.4 Discussion.....	85
Chapter 5: Malignant glioma model development	93
5.1 Introduction	93
5.2 Materials and methods	95
5.3 Results	97
5.3.1 Mouse glioblastoma model (GL261).....	97
5.3.2 Human malignant glioma xenograft models	99

5.4 Discussion	105
Chapter 6: Multi-modal imaging of the bystander killing effect in malignant brain tumors	111
6.1 Introduction	111
6.2 Materials and Methods	113
6.3 Results	115
6.3.1 Bystander killing effect assessment in a mouse glioblastoma (GL261) model 6.3.1.1 mMSC's	115
6.3.1 Bystander killing effect assessment in a human malignant glioma xenograft models (Hs683/U87-MG)	126
6.4 Discussion	132
Chapter 7: General conclusions & future perspectives	139
7.1 General conclusions	139
7.2 Future perspectives	150
7.3 List of publications	162
7.4 Conference abstracts	163

CHAPTER 1:

General Introduction

Chapter 1: General Introduction

Although numerous efforts have been made to develop new treatment modalities for gliomas in order to improve the prognosis for these patients, results have been limited so far [1]. This underlines the importance of well characterized preclinical glioma animal models that represent the situation in humans as close as possible. Animal models have the advantage that a thorough follow-up of experimental treatment modalities is possible. However, one always has to keep in mind that animal models in rodents do not reflect all aspects of the tumors in humans. Moreover, non-invasive diagnostic tests can be challenging in rodents and might require dedicated imaging hardware. On the other hand, imaging techniques not available or not feasible in humans, like some optical imaging approaches, can generate additional crucial information in particular when applied in a multi-modal imaging approach [2].

1.1 Gliomas in a clinical setting

Gliomas arise from the glial cell population (astrocytes, oligodendroglial and ependymal cells) and are the most common brain tumors in humans [1]. They comprise a broad range of lesions with distinct differences in malignancy, which is assessed according to the World Health Organization classification. Glioblastoma multiforme (GBM) is the most malignant tumor type (WHO grade IV) [1]. The prognosis of patients diagnosed with GBM is extremely poor with a five-year survival of less than 3% despite a combined treatment approach consisting of surgery and concomitant radio- and chemotherapy [3]. Currently, the golden standard for high-grade glioma treatment, such as for glioblastoma, is a combination of maximal safe resection, radio- (60 Gy in 30 daily fractions of 2.0 Gy fractions given 5 days a week for 6 weeks) and chemotherapy (Temozolomide) [4]. During surgery, 5-aminolevulinic acid [4] can be used to identify remaining tumor tissue thus enhancing chances of full resection. After resection, chemotherapy, usually temozolomide, which alkylates/methylates DNA preferably on a guanine residue and thus damages the DNA, triggering tumor cell death, is combined with radiotherapy. When temozolomide is administered, additional information on the methylation status of the promotor of MGMT, a DNA repair enzyme, which removes alkyl groups from guanine residues, is however required. When the promoter region is demethylated, the DNA

repair enzyme is active and alkylating chemotherapeutics, such as temozolomide will be ineffective. When methylated, the enzyme will be inactivated and the cells will therefore be unable to repair alkylated guanine residues. The Cancer Genome Atlas (TCGA) research network concluded that patients lacking this enzyme and treated with temozolomide develop mutations in the mismatch repair (MMR) genes, which results in a hypermutated phenotype [4].

The high mortality rate associated with GBM in adults is due to the several reasons. First, these tumors are usually diagnosed in advanced stages of the disease. At this time, tumors are generally quite large and well vascularized as they are capable of inducing neovascularisation when they become too large to receive sufficient nutrients from normal blood vessels [5]. Furthermore, their immunosuppressive properties [6] and their aggressive and invasive growth pattern makes them difficult to treat with standard therapy. Finally, in the last years, the glioma stem cell hypothesis has gained interest as these stem cells are believed to be capable of escaping treatment and drive tumor recurrence and progression [7].

Very few causal relationships have been shown for the development of brain tumors, such as therapeutic X-ray irradiation as found in children who received prophylactic CNS irradiation for acute lymphoblastic leukemia (ALL) and specific hereditary symptoms such as neurofibromatosis 1 and 2 and tuberous sclerosis complex [8]. Furthermore, certain genetic polymorphisms increase the risk for developing certain brain tumors. Both important genetic (inactivation of the p53 and retinoblastoma tumor suppressor (RB) pathways, dysregulation of growth factor and activation of the phosphatidyl inositol 3-kinase (PI3K) pathway) and epigenetic (promotor methylation status of the O6-methylguanine-DNA-methyltransferase (MGMT)) changes have been identified. Bleeker *et al.* provided an extensive overview of molecular alterations in glioblastoma [9].

1.2 Non-invasive imaging

A multitude of non-invasive imaging techniques is available both in a preclinical and clinical setting. Some techniques, such as some optical imaging, are however restricted to preclinical use only. Each of these techniques has its own specific advantages and limitations and therefore, multi-modal imaging is often of advantage to elucidate specific questions, for instance: Is there a reduction in tumor volume? Are cells still metabolically active?,... Contrast generation in these techniques can be based on native/intrinsic contrast or the use of contrast agents or reporter genes to generate contrast.

1.2.1. Ultrasound

During an ultrasound examination, high-frequency sound (1-20 MHz) waves emitted by an ultrasound transducer interact with the exposed tissue. The reflected waves are subsequently received and processed into an image by a computer. This imaging technique has been widely used as it is readily available both in the preclinical and clinical setting at relatively low cost. Furthermore, ultrasound has a favorable safety profile and a good temporal resolution [10]. Contrast generation on the images depends on several factors including the applied imaging algorithm, the backscatter, the attenuation of the sound caused by reflection, absorption or scattering and the speed of the sound waves. Additional contrast can be generated in, for instance, applications such as follow-up of therapeutic cells by labeling the cells with microbubbles or gas-filled microbubbles coated with lipids or polymers. One of the major limitations of ultrasound is however the severe attenuation by bone and air which makes it impossible to image the lungs or the brain [11].

1.2.2 Photoacoustic imaging

Photoacoustic imaging employs the same principles as ultrasound to reconstruct an image based on sound waves. Photoacoustic imaging however does not use high-frequency sound, like ultrasound for transmission but uses a nanosecond pulsed laser to irradiate a certain tissue. The resultant small and localized heating of the tissue subsequently generates ultrasound waves through thermo-elastic expansion. Imaging applications using native contrast is mainly limited to blood vessel imaging. Additional contrast can also be generated here for cell and specific tissue tracking purposes using for instance gold nanoparticles [10]. Due to the

similarities between ultrasound and photoacoustic imaging, they also share some advantages and limitations. As such, photoacoustic imaging also has a favorable safety profile but is more challenging for visualizing the lungs and the brain. Furthermore, photoacoustic imaging suffers less from artifacts compared to ultrasound imaging as photoacoustic imaging uses a laser light for transmission, which minimizes artifacts due to scattering [10].

1.2.3 Optical imaging

Optical imaging includes both fluorescence and bioluminescence imaging. In both cases, photons are captured by a charge coupled device (CCD) camera [12] and reconstructed into an image. The photon generation in fluorescence and bioluminescence imaging is however quite different.

In fluorescent imaging, a fluorescent reporter gene or a contrast agent such as quantum dots are used to tag for instance therapeutic cells. A light source is often required to excite the fluorescent reporter. When these compounds absorb light, photons are emitted back which are usually characterized by longer wavelengths compared to the absorbed light. When placed in tissues however attenuation occurs due to scattering and absorption of the emitted light by hemoglobin and water, thus generating an optical imaging window from 600-1000nm. Therefore, near infra red (NIR) fluorochromes were developed for *in vivo* applications due to its better tissue penetration. Some of these NIR fluorochromes have already been approved for clinical applications by the FDA [13].

In bioluminescent imaging the expression of a reporter gene is also required. Here however, a luciferase gene is used to generate light when a substrate is provided. Several luciferase genes have been isolated from living organisms such as firefly, click beetle, sea pansy (*Renilla reniformis*, *Gaussia princeps*, etc.), which resulted in several different luciferases such as firefly luciferase (fLuc), Renilla luciferase (rluc) and Gaussia luciferase (gLuc) with slightly different characteristics. Firefly luciferase for instance requires ATP, O₂ and Mg²⁺ to oxidize its substrate D-luciferin and generate light with a maximum wavelength at 560nm. As this reaction requires ATP, this technique is often used to assess viability of implanted cells or therapeutic response of fLuc expressing (tumor) cells [14, 15]. Some luciferases, such as rLuc and gLuc however require a

different substrate such as coelenterazin and emit light at a different maximum wavelength (rLuc: 482nm, gLuc: 475 nm, respectively). Thus, different cell lines can be distinguished based on the applied substrate. Although many improvements have been made regarding 3D reconstructions of this imaging technique, BLI remains however a 2D imaging modality and displays a low spatial resolution. Therefore, it is often combined with other imaging modalities such as MRI or CT [16]. As photons are generated exclusively by cells expressing the luciferase gene, background signals are low which renders BLI very sensitive as well as safe, easy and quick. Due to the absorption and scattering of the photons in living tissues however, its use is limited to preclinical imaging or superficial detection of up to 2-3 cm in depth [17].

1.2.4. Computed tomography (CT)

X-ray based computed tomography (CT) uses differences in X-ray attenuation by different tissues to generate an image. This implies a safety risk as radiation exposure is inevitable [10]. CT has an excellent resolution (1-10 μ m) with a high signal to noise ratio but unfortunately displays poor soft tissue contrast, which is why in a clinical setting, MRI has largely replaced CT for brain imaging.

1.2.5. Radionuclide imaging: PET/SPECT

Prior to positron emission tomography (PET) and single photon emission computed tomography (SPECT), a radioactive isotope or radionuclide is administered to the patient. During SPECT, the tracer emits gamma radiation that is measured directly by the camera. In contrast, the radionuclides used for PET decay are usually β -emitters, which results in the production of a neutrino and a positron of which the latter will annihilate when it encounters an electron. The energy released by this annihilation is transformed into two gammaphotons, each 511 keV, which are emitted in opposite directions. These gammaphotons can be detected by a camera, comprised of a ring of hundreds of detectors. A positive signal (event) is generated when two photons are detected simultaneously by two detectors, placed 180° opposite to each other. This process is also known as coincidence detection. The point of origin is located exactly on the line between the two detection points. Numerous dual hits are necessary to establish the area of emission and create an accurate image.

One of the main advantages of PET imaging is that it enables the *in vivo* three dimensional measurements of metabolic and molecular processes with very high sensitivity. Several tracers have been developed specifically for tumor imaging. The most commonly used tracers in the diagnosis of brain tumors are 2- ^{18}F fluoro-2-deoxy-D-glucose (^{18}F FDG), methyl- ^{11}C -L-methionine (^{11}C MET) and ^{18}F FET (O-(2- ^{18}F -fluoroethyl)-L-tyrosine). The accumulation of each tracer reflects the activity of its transporter via the blood brain barrier (BBB), as well as the activity of specific enzymes by which they are metabolized and trapped.

Due to their excessive growth, tumors require substantial higher amounts of glucose, amino-acids and DNA precursors. As ^{18}F FDG is phosphorylated by cellular hexokinase, it represents a specific tracer for glucose consumption. The insulin-dependent glucose GLUT transporters, located on capillary endothelial cells, transport ^{18}F FDG over the cell membrane. The transport rate of this process depends on the glucose level in the blood in accordance with the Michaelis-Menten kinetics for facilitated transport. After transport into the cell, ^{18}F FDG is phosphorylated by the cellular hexokinase into ^{18}F FDG-monophosphate, which accumulates in the cell. This accumulation represents both high expression of the GLUT transporters and hexokinase activity within the tumor [18]. ^{18}F FDG-PET reveals information on intratumoral glucose consumption and correlates with tumor grade [19], biological aggressiveness and prognosis of patients with both primary and recurrent gliomas [20]. Unfortunately, ^{18}F FDG is also metabolized in inflammatory brain lesions, focal epilepsy and recent ischemic infarcts which make it unspecific for tumor growth. An additional drawback is the high background activity of ^{18}F FDG in normal cortex. These disadvantages can sometimes complicate a diagnosis and therefore more specific radiotracers have been developed for the diagnosis of brain tumors.

^{11}C MET, an amino acid radionuclide is such a molecule. Due to increased transport rates mediated by type L amino acid carriers, amino acids accumulate in brain tumors and this seems to be directly mediated by tumor growth factors [21, 22]. ^{11}C MET PET detects brain tumors as well as infiltrating areas with both high sensitivity and specificity [23].

[¹⁸F] FET, another tumor specific radiotracer, which also represents a marker for amino-acid metabolism has furthermore been proven to be of help in distinguishing tumor recurrence from therapy related changes. The longer half-life of [¹⁸F] labelled radioisotopes means that a cyclotron is not required in close proximity to the PET imaging facility which is a major advantage compared to [¹¹C] labelled radioisotopes [24, 25].

As such, PET imaging supplies valuable information on, for instance, the tumor's extent, proliferative activity, metabolism and its relation to functionally relevant parts of the brain in patients diagnosed with brain tumors [26-28]. For tracking of cells, therapeutic cells can be labelled directly *in vitro* prior to injection and subsequently imaged. This method is however determined by the half-life of the radioisotope therefore limited in duration of the follow-up. An alternative method is to indirectly label therapeutic cells which express a reporter gene that allows radionuclide imaging such as Herpes simplex virus thymidin kinase (HSV-tk) or the sodium iodide symporter system (NIS) [29, 30].

In most applications of radionuclide imaging however close proximity to a cyclotron is required due to the short half-lives of many tracers. Furthermore, PET images are generally co-registered with MRI or CT to identify the anatomical localization of the tracers. For rodents, an atlas can be used to eliminate the need for additional imaging to some extent [31].

1.2.6 MRI/MRS

1.2.6.1 Magnetic resonance imaging

For magnetic resonance, a homogeneous magnetic field and a radio-frequency transmitter and detector are required. During ¹H magnetic resonance imaging (MRI), the proton nucleus of the hydrogen atom (= proton), aligns itself parallel or anti-parallel to the strong magnetic field and reaches a thermal equilibrium. The proton nuclei precess about the applied field at a characteristic frequency, but with a random phase with respect to one another. Application of a (90°) radio frequency (RF) electromagnetic pulse flips the equilibrium into the transverse plane and introduces a transient phase coherence that can be detected as a radio signal and turned into an image. Subsequently, relaxation occurs, involving an exponential decay of the signal intensity and ultimately a return of the magnetization to the equilibrium. One distinguishes between

two different types of relaxation, T1 and T2. The transverse relaxation time T2* is a resultant of both T2 decay (spin-spin relaxation) and inhomogeneities in the external magnetic field and local field variation due to particles or tissues with different magnetic susceptibilities. Due to both effects, dephasing will occur. The T2* signal generally fades away in a few milliseconds to tens of milliseconds. T1 relaxation also referred to as spin-lattice relaxation, describes the return of the magnetization to the thermal equilibrium. The observed radio signals from an object exposed to additional magnetic field gradients can be reconstructed into an image after multiple RF excitations [32]. Native contrast is generated due to differences in proton density and varying interactions of the protons with their environment in distinct tissues that result in T1 and T2(*) differences. Both the resonance frequency and the signal intensity depend on the external magnetic field strength. Using more specialized MRI protocols allows the generation of contrast based on properties like diffusion, flow, metabolism, blood oxygenation and others [33, 34].

Due to the required higher resolution when imaging animals, higher field strengths (>7 T) on dedicated animal scanners and smaller RF coils are required compared to clinical imaging. Furthermore, due to the higher field strengths, additional safety measures, such as better shielding to reduce the stray field, are taken to minimize the risk of accidents. Thus, it is possible to generate high resolution anatomical 2D or 3D images to determine tumor location and size, vasculature, growth pattern and the presence of necrosis and/or bleedings which correlates with histopathology. MRI displays however a low specificity and limitations concerning the generation of cell function or viability information. Furthermore, distinction between necrosis and bleedings is impossible based solely on MR images as they both generate hypointense contrast on T2 weighted images [35, 36].

When using therapeutic cells inside the brain, native contrast is generally not sufficient to distinguish engrafted from host cells. Therefore, additional contrast can be generated by pre-labeling the cells with MR contrast agents [37]. These modify the T1, T2 and/or T2* relaxation rates. Depending on which parameter contrast agents exert the strongest effect, contrast agents can be distinguished in paramagnetic compounds which contain lanthanide chelates (Gadolinium (Gd^{3+})) or manganese (Mn^{+}) and that have a stronger effect

on T1 than on T2 relaxation time and thus generating hyperintense contrast on T1-weighted images. Superparamagnetic agents like nanoparticles that are based on iron oxide mainly alter the T2/T2* relaxation time, thus generating hypointense contrast on T2/T2* weighted images. In addition, agents that are based on other MRI-active nuclei than ^1H (namely ^{19}F) and their altered spin-density have also been used for cell imaging [38].

1.2.6.2 Magnetic resonance spectroscopy (MRS)

Magnetic resonance spectroscopy (MRS) is based on the same physical principle as MRI, but here radio-frequency differences are mainly used for 'metabolic encoding' rather than spatial encoding. This technique enables detection of RF differences based on chemical composition [39]. The most extensively used nuclei in biological systems include ^1H , ^{31}P , ^{13}C , ^{23}Na . To assess tumor growth and malignancy, metabolites such as lactate, N-acetylaspartate, creatine and choline are monitored [40-42]. Information is usually acquired on relative large volumes. Additional anatomical MRI scans are required to gain anatomical information on the location of those voxels.

Due to the advantages and drawbacks of each individual imaging technique, multi-modal imaging is often applied to address certain questions in both a clinical and preclinical setting.

1.3 Glioma imaging in a clinical setting

Initial diagnosis and radiologic follow-up is routinely performed with serial magnetic resonance imaging scans (MRI) and radionuclide imaging in GBM patients [43-45]. However, routinely used MRI techniques still present some difficulties in clinical practice. For instance the radiological characteristics of tumor relapse and therapy related changes such as radiation necrosis are similar [45]. In recent years, advanced MR imaging techniques assessing vascularity, cell organisation and metabolism have become of increasing interest in therapy response assessment in neuro-oncology as they potentially provide more insights in tumoral pathophysiology, allowing a better distinction between progressive tumor and therapy induced reactions in the brain [46-48]. Positron emission tomography (PET) with radiolabeled amino acids such as [¹⁸F] FET (O-(2-18F-fluoroethyl)-L-tyrosine) has furthermore proven to be of help in distinguishing tumor recurrence from therapy related changes [25].

Combining non-invasive imaging techniques enables clinicians to diagnose and grade tumors with increasing accuracy. However, for ultimate confirmation stereotactically guided biopsies and resections are needed in order to accurately determine the lesion grade [26].

As the prognosis of these patients remains extremely poor with standard treatment consisting of surgery and combined radio- and chemotherapy, new treatment approaches are being developed. In recent years, clinical studies using gene therapy [49], immunotherapy [50] or anti-angiogenic approaches [51] have been performed with often limited results, thus underlining the importance of monitoring therapy in those patients closely with advanced imaging techniques but also for using well characterized preclinical animal models for the validation of new diagnostic techniques and thorough follow-up of experimental treatment modalities. Adequate and profound multi-modal imaging in those models is of vital importance before translating results to clinical practice.

1.4 Preclinical brain tumor rodent models

Several animal models have been developed to investigate new treatment modalities. However, no preclinical model currently available reflects all aspects of human high-grade gliomas. Tumor models vary in their immunogenicity, growth patterns and invasiveness.

An array of human glioma xenograft models exist for glioma. In these models, freshly isolated primary tumors, tumor stem cells [52], biopsy spheroids [53] or human brain tumor cell lines, such as Hs683 (oligodendroglioma) or U87-MG (glioblastoma), are transplanted into immune-deficient mice. Most of these tumor cells can be implanted both intracranially or subcutaneously. Several rodent models have also been developed using orthotopic injection of rat or mouse glioma cell lines, including the C6, 9L, T9, F98, RG2, RT2, avian sarcoma virus induced and CNS-1 rat models[54].

Some of these orthotopic models like the C6 rat glioma and the Avian sarcoma virus (ASV) induced gliomas do not have a syngeneic host or were proven immunogenic, resulting in clearance of the tumor due to an immune response [54]. Their usefulness as a preclinical model is therefore restricted.

The 9L and T9 rat gliosarcoma models were also proven to be highly immunogenic but cancer stem-like cells (CSLCs), which grow as neurospheres, have been demonstrated in the 9L cell line [54].

The CNS-1 rat astrocytoma model, derived from an inbred Lewis rat, proved an excellent model for investigation of immunological therapies and resembles human glioma cells quite well [55].

The F98 glioma model was generated in a CD Fisher rat and classified as an anaplastic or undifferentiated glioma [54]. Like human GBM, these cells overexpress *PDGF β* , and *Ras* along with an increase in *EGFR*, *cyclin D1* and *cyclin D2* expression. The tumor closely resembles human gliomas as it is only weakly immunogenic, infiltrates normal brain parenchyma and is very aggressive [54]. Histology shows GFAP and vimentin expression with negligible staining for CD3 + T cells [56].

The RG2 glioma model, also known as the D74 glioma model, displays an invasive growth pattern and is refractory to all therapeutic modalities. They show enhanced expression of *PDGF β* , *IGF-1*, *Ras*, *Erb3/HER3* precursor mRNA and *cyclin D2* [57]. It was also demonstrated that these tumors were non – immunogenic despite intensive immunization of syngeneic Fisher rats [58].

The BT4C glioma model shows high cellularity and has pleomorphic nuclei, numerous mitotic figures and abnormal blood vessels. BT4C cells express VEGF, tPA, uPA and MVD in the periphery of the growing tumor and are S100 positive by immunohistochemistry [54].

Murine models of malignant brain tumors were also developed [59]. The GL261 model, one of the most frequently used models was originally induced by intracranial injection of 3-methylcholantrene pellets into C57BL/6 mice and maintained by serial intracranial and subcutaneous transplantations of small tumor pieces on the syngeneic mouse strain [60, 61]. *In vitro* cell cultures were established with a population doubling time of 20h in log phase. GL261 cells do not express the most important glial differentiation markers but do display genetic anomalies such as p53 and K-ras mutations and elevated c-myc and p53 expression. Furthermore, these cells display an elevated MHC1 expression and low levels of B7-1 and B7-2 RNA, thus possibly explaining the low immunogenicity of the cells *in vivo* [62]. When transplanted in their syngeneic host, the cells display a high incidence of tumor formation, where survival time is dependent on the tumor cell number transplanted. These tumors are invasive but do not metastatize. For an overview of frequently used experimental glioma rodent models we refer to table 1.

Finally, also a number of transgenic models have been developed by introducing modifications in oncogenes with tissue-specific expression or deletion of tumor suppressor genes. These mice spontaneously develop cancer and mimic primary glioma in patients much more closely compared to tumor models that use engrafted tumor cells. Genetically engineered mice however also possess some disadvantages among which poor reproducibility, low tumor penetration, prolonged latency for tumor formation, increased heterogeneity and the need for advanced *in vivo* imaging techniques [59].

In contrast, models using engraftment of patient biopsies or tumor stem cells recapitulate the pheno- and genotype of patient GBM much better compared to cell-line based models and do show single cell invasion into the brain [52, 53]. These models however require access to patient material and the use of immunodeficient animals to establish tumor growth *in vivo*. Therefore, the assessment of immune system involvement in investigational therapeutic approaches is not possible.

Cell-line based models lack the stepwise genetic changes occurring during tumor progression. Therefore, many of them remain well circumscribed in the brain architecture, lack characteristic histological vascularization and rarely recapitulate the phenotype of the tumor of origin. Nevertheless, based on their fairly good reproducibility, tumor cell engraftment models have been mostly used for evaluating new therapeutic concepts [63].

Table 1: Overview of frequently used experimental glioma rodent models.

Model	Strain/species	Method	Typing	Syngeneic host	Immunogenicity	Invasiveness
C6	Outbred wister rat	MNU	Glial tumor	No	+++	
9L-9T	CD Fisher rat	i.v. MNU	Gliosarcoma	Yes	+++	
RT-2	Neonatal CD Fisher rat	i.c. ASV suspensions	Mostly anaplastic astrocytoma		++	
CNS-1	Inbred Lewis rat	i.v. MNU		Yes		
F98	Pregnant CD Fisher rat	i.v. ENU	Anaplastic glioma	Yes	+	Yes
RG2 (=D74)	Progeny of ENU injected Fisher rat			Yes	0	Yes
BT4C	Pregnant BDIX rat	Transplacental ENU				
GL261	C57BL6 mice	Intracranial 3-methylcholantrene pellets	Glioblastoma	Yes	0	Limited

1.4 Innovative experimental tumor therapies

Experimental treatment modalities under investigation include anti-angiogenic approaches, dendritic cell (DC) vaccination, virotherapy, gene therapy and usage of stem cells expressing a suicide gene.

1.4.1 Anti-angiogenic treatment approaches

In particular solid tumors depend on angiogenesis for their survival and growth, therefore anti-angiogenic approaches are under development for the treatment of brain tumors. Several molecules, such as Bevacizumab, Aflibercept, receptor tyrosine kinase inhibitors and Cediranib have already been developed which target vascular endothelial growth factor (VEGF) or its receptors VEGFR1, VEGFR2 and/or VEGFR3, the most important mediators of neovascularisation in gliomas. Despite encouraging preliminary results however, current anti-angiogenic therapies eventually resulted in tumor resistance and progression [51]. Both animal and human studies indicated that use of anti-angiogenic therapy might also result in an augmented infiltrative growth pattern [64, 65].

1.4.2 Immunotherapy

Dendritic cell (DC) vaccination is a promising new treatment modality. Here, autologous DC's, exposed to whole tumor cell lysates are administered. Presentation of tumor antigens in MHC I and II context results in activation of both CD4+ and CD8+ cells, which induce a specific anti-tumor immune response. Furthermore, this kind of active specific immunotherapy is also capable of inducing immunological memory [66]. Following promising results in preclinical studies [66], clinical studies are now conducted in patients [50] but further intensive preclinical research remains mandatory.

Several molecular targets, specific for brain tumors, are located in the cytoplasm or even the nucleus and are therefore difficult to reach. Virotherapy aims to target malignant glioma cells by use of conditionally replicative viruses. During virotherapy, oncolysis is achieved by intra-neoplastic cell virus replication mediated cell lysis [67]. Holzmüller *et al.* proved the feasibility of this strategy by using YB-1 dependent virotherapy in combination with temozolomide to treat malignant human glioma in mice [68]. The usage of viral particles in human patients remains however a controversial approach.

1.4.3 Gene therapy

Therefore, attention turned to gene therapy for delivery of therapeutic genes to the tumor site. This includes delivery of cytokine genes to activate and attract immune cells against the tumor, such as FMS-like tyrosine kinase 3 ligand (Flt3L), and interferon- β (IFN- β), delivery of tumor-suppressor genes, such as p53 to reprogram tumor cells into apoptosis and delivery of suicide genes such as cytosine deaminase and HSV-TK to convert prodrugs in the tumor and achieve tumor cell death [69]. The system most widely used in clinical trials however is the HSV-TK suicide gene therapy. This approach has resulted in very promising results in a pre-clinical setting but the therapeutic efficiency of this therapeutic approach has been rather disappointing however, which is generally accepted to be related to sub-optimal distribution of the gene throughout the tumor region [70]. Therefore, attention turned to carriers such as bacteria with a tropism for necrosis [71], liposomes, nanoparticles, and viral vector based carriers [69]. Unfortunately, even when employing viral vectors to carry the suicide gene to the tumor cells, distribution of the suicide gene remained limited.

Therefore, stem cells that are able to target tumor cells, thus ensuring a higher gene delivery efficiency and which carry these viral vectors, including the suicide gene, are also under investigation [72].

1.4.4 Stem cell based suicide gene therapy for glioblastoma

1.4.4.1 Expression of suicide genes in tumor tracking stem cells

In order to use tumor targeting stem cells to deliver a suicide gene to the tumor cells, therapeutic stem cells need to stably express the suicide gene. Introduction of foreign DNA into a certain cell type can be accomplished by two major approaches. Either through non-viral gene transfer or through virus mediated gene transfer.

The first approach uses components such as plasmids, Zinc finger nucleases, DNA liposomes complexes or PEI (polyethylenimine) for gaining excess to the cell. Advantages of this approach include the absence of an immune response and also no size constraints for the gene of interest [73].

Viral mediated gene transfer however uses the optimized infection capabilities of viruses to deliver genetic material. This results in augmented transduction efficiency but as viruses are small, there is however a size restriction coupled to their use. Furthermore, viral vectors can also be engineered to target specific cell types, for instance by using a specific promoter, such as nestin, or by pseudotyping in which peptides, such as the RGD peptide, are added to increase specificity. Some care should be taken however in regard to immune responses and destruction of cells due to replication of the viruses. In order to exclude these threats however, viral vectors have been engineered so that they cannot replicate and should not contain proteins that cause immune responses. Several types of viral vectors have been developed and these can be subdivided into non-integrating and integrating vectors. With non-integrating vectors, the genetic material is present as episomal DNA and will eventually be lost due to cell division. These include adenoviral vectors (AV), Adeno-associated vectors (AAV), and Herpes simplex vectors (HSV). The integrating vectors result in stable transduction with the genetic material incorporated in the DNA of the host cell. These include retroviral (RV) and lentiviral vectors (LV). Retroviral vectors are however only capable of transducing dividing cells which makes applications in non-dividing or slowly dividing cells, such as differentiated brain cells, or

irregular dividing cells such as stem cells very difficult or impossible. Lentiviral vectors, which are derived from HIV, are however capable of transducing both dividing and non-dividing cells. An overview of the general characteristics of these viral vectors is given in table 2.

Table 2: Overview of the general characteristics of viral vectors.

	Vector	Genetic material	Packaging capacity	Tropism	Inflammatory potential	Envelope
Non-integrating (episomal)	AV	DsDNA	8-30kb	Broad	High	-
	AAV	SsDNA	<5kb	Broad	Low	-
	HSV-1	DsDNA	40-150kb	Neurons	High	+
Integrating	RV	RNA	8kb	Dividing cells	Low	+
	LV	RNA	8kb	(non)dividing cells	Low	+

Vector	Main limitations	Main advantages
AV	Risk of potential inflammatory response No integration → transient expression	Extremely efficient transduction in most tissues High titers (10^{11} TU/ml) Pseudotyping renders vectors specific
AAV	Small packaging capacity 10% integration → insertional mutagenesis Needs helper virus Pre-existing immunity	Non-inflammatory, non-pathogenic Absence of gene silencing Very pure preps, high titers
HSV-1	Inflammatory response Transient expression Limited to neurons	Large packaging capacity Strong tropism for neurons
RV	Only dividing cells Insertional mutagenesis	Stable gene expression in dividing cells
LV	Insertional mutagenesis	Transduction of dividing and non-dividing cells Stable gene transfer in most cells

AV: adenoviral vector, AAV: adeno-associated vector, HSV-1: Herpes Simplex virus type 1, RV: retroviral vector, LV: lentiviral vector, TU: transducing units, ds DNA: dubbel stranded DNA, ss DNA: single stranded DNA

Incorporation of a suicide gene in these viral vectors enables tumor cell killing when the suicide gene is expressed [74]. As mentioned previously, viral vectors can be engineered to be specific, but for brain tumors, there is currently no specific promoter available. Therefore, tumor targeting stem cells are under investigation [72].

1.4.4.2 Stem cells

An extensive overview of stem cells would be beyond the scope of this thesis but a condensed overview will be provided. In short, stem cells display three main characteristics: 1. Ability of self – renewal without senescence, 2. Ability to give rise to differentiated progeny cells and 3. Ability to reconstitute a given tissue *in vivo* [75]. Stem cells are usually classified according to their differentiation potential. Stem cells derived from the zygote or morula stage are totipotent, which means they can give rise to a new individual. Stem cells derived from the inner cell mass (ICM), such as embryonic stem cells (ESC), are pluripotent as they can give rise to the three somatic germ layers (ectoderm, mesoderm and endoderm), germ cells and yolk sac cells. When development progresses, these pluripotent cells will be restricted and will generate multipotent stem cells, such as neural stem cells (NSC's) that can differentiate into all cells of a specific tissue or germ layer [76]. Due to the intrinsic properties of stem cells to form almost any type of tissue, stem cells have been investigated tremendously in regenerative medicine such as for stroke therapy [77], where differentiation of certain stem cells is supposed to support recovery either by cell replacement or indirectly by the release of neurotrophic factors to reduce detrimental effects and improve recovery [78].

Next to obvious ethical concerns, there are also safety issues related to working with totipotent or pluripotent stem cells as they can potentially form tumors. In adult tissue however, multipotent cells can also be found, which are responsible for tissue homeostasis and injury repair. Among these are mesenchymal stem cells (MSC's) and multipotent adult progenitor cells (MAPCs). MSC's can be isolated from the bone marrow, umbilical cord blood and adipose tissue and can differentiate *in vitro* into osteoblasts, adipocytes and chondrocytes. MAPCs are also isolated from bone marrow but show different characteristics compared to most adult stem cells. They can proliferate without senescence and can differentiate *in vitro* into cell lines of the three germ layers. Clinical trials using human MAPCs, also known as hMultistem[®], are currently ongoing for the assessment of beneficial effect in for instance graft versus host disease due to their immunomodulatory characteristics [79].

1.4.4.3 Stem cell based suicide gene therapy

Stem cells that are able to target tumor cells can in principle invade the bulk tumor mass but also track infiltrating tumor cells. The underlying mechanism of this migration of stem cells towards tumors is still elusive although the chemokine receptor, CXCR4 and its ligand SDF-1 have been suggested to be involved [80] for hMSC's, whereas, NSC tropism is most likely regulated by both chemo-attractant cytokines and extracellular matrix components [81].

Due to the presence of a suicide gene like HSV-tk, the stem cells can be killed selectively, in this example with the pro-drug ganciclovir, as mammalian brain cells display a 1000 fold lower affinity for GCV they are unable to efficiently transform ganciclovir into its highly toxic metabolite, ganciclovir phosphate [82]. Subsequently, cellular kinases will recognize the GCV-monophosphate and will generate GCV-triphosphate which is highly cytotoxic as GCV is a guanosine analogue which will participate in normal DNA replication, causing chain termination and subsequent cell death. Normal adult brain cells do not divide and are therefore insensitive to this treatment. Thus, the therapeutic stem cell can be eliminated. Moreover, this strategy also enables killing of tumor cells by formation of gap junctions between the administered stem cells and their neighboring cells [83]. Via these gap junctions, the toxic ganciclovir-phosphate can be transferred to the tumor cells, thus also killing the latter. This phenomenon is also called the bystander killing effect (Figure 1). In theory this method should be sufficient to remove not only the main tumor mass, but also quantitatively target any remaining (infiltrating) tumor cells, thus eliminating sources of possible recurrent tumors [82].

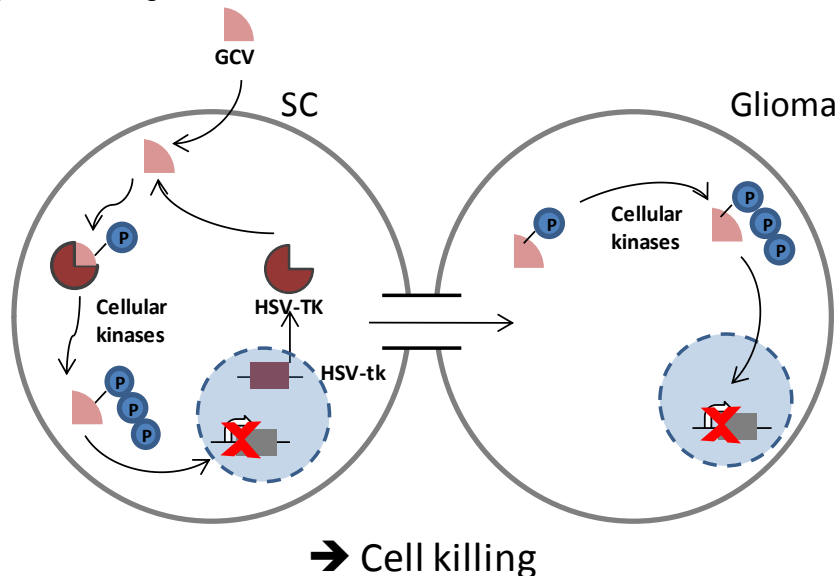
The feasibility of this strategy was demonstrated by several groups in both xenograft and syngeneic animal models. Li *et al* demonstrated a potent bystander killing effect of rNSC's on C6 rat gliomas [84], whereas Miletic *et al* [82] and Matuskova *et al* [85] obtained similar results for rMAPCs on 9L rat gliomas and hMSC's on the human glioblastoma cell lines 8-MG-BA, 42-MG-BA and U-118 MG respectively. Migration of hMSC's was furthermore optimized by Egea V [86] by preincubation with TNF- α . Treatment efficiency does, however, depend highly on the extent of gap junction communication between cells. As malignant gliomas

communicate poorly via these gap junctions, agents with the ability to augment gap junction formation provide a mean to optimize treatment. Paino *et al* demonstrated this by using Tolbutamide, a gap junction communication improver, which resulted in an augmented HSV-tk/GCV bystander effect in human U373 glioma cells [87].

However, *in vivo* imaging conducted on these animals is usually limited to assessing the outcome by a single modality, thus limiting the information that can be obtained. As the efficiency of this approach also depends on the administration of the co-drug at a time point of optimal stem cell distribution, longitudinal *in vivo* information on stem cell localization can be crucial. However promising some of these treatment modalities may be, assessment of tumor growth and treatment should be carefully monitored by one or more non-invasive imaging modalities such as MRI/MRS, PET, BLI, CT, or others [88].

Figure 1: Suicide gene therapy and bystander killing effect: mechanism.

HSV-TK expressing stem cells generate ganciclovir monophosphate which is recognized and phosphorylated by cellular kinases thus generating ganciclovir triphosphate. The latter is transported into the nucleus where it will act as a chain terminator, resulting in cell death of the therapeutic cells. Due to the formation of gap junctions between adjacent cells, ganciclovir phosphate passively diffuses into neighboring tumor cells, which will also be killed. This phenomenon is also called the bystander killing effect.



1.5 Imaging in experimental glioma therapies

As discussed previously, the most commonly used non-invasive techniques for imaging of brain tumors in preclinical animal models are comparable to the clinically applied methods, including MRI/MRS and PET. Moreover, additional imaging modalities, which are not yet available or not applicable in the clinic, can be used preclinically to augment information gained from preclinical rodent models and include near infrared (NIR) and bioluminescence imaging (BLI).

Multi-modal imaging is applied on a daily basis for diagnosis, grading, surgery planning, treatment follow-up and determination of tumor recurrence in a clinical setting. In preclinical animal models dedicated systems have been developed and allow similar imaging in rodents. For instance, BLI can give information on cell viability, PET on metabolism and MRI can enhance insights regarding anatomical position, necrosis/bleedings, tumor size, blood supply and blood brain barrier (BBB) disruption [16]. Molecular changes in both cancer tissue and surrounding microenvironment can be better analyzed by MRI/MRS [40, 89].

In a clinical setting, an anatomical T2 weighted MRI (T2W) image, which renders information on tumor size and presence of necrosis and/or bleedings, is combined with more functional information generated by diffusion weighted images (DWI) and diffusion tensor images (DTI) [90, 91]. During DWI, differences in diffusion of water molecules in different tissues are used to generate images. Tumors display an increased cellular density which results in a decreased apparent diffusion. Areas of necrosis however appear as regions with increased diffusivity as cell membranes are absent and no longer form barriers for diffusing water molecules. During DWI, apparent diffusion coefficient (ADC) maps can be generated which enables quantitative measurements [91].

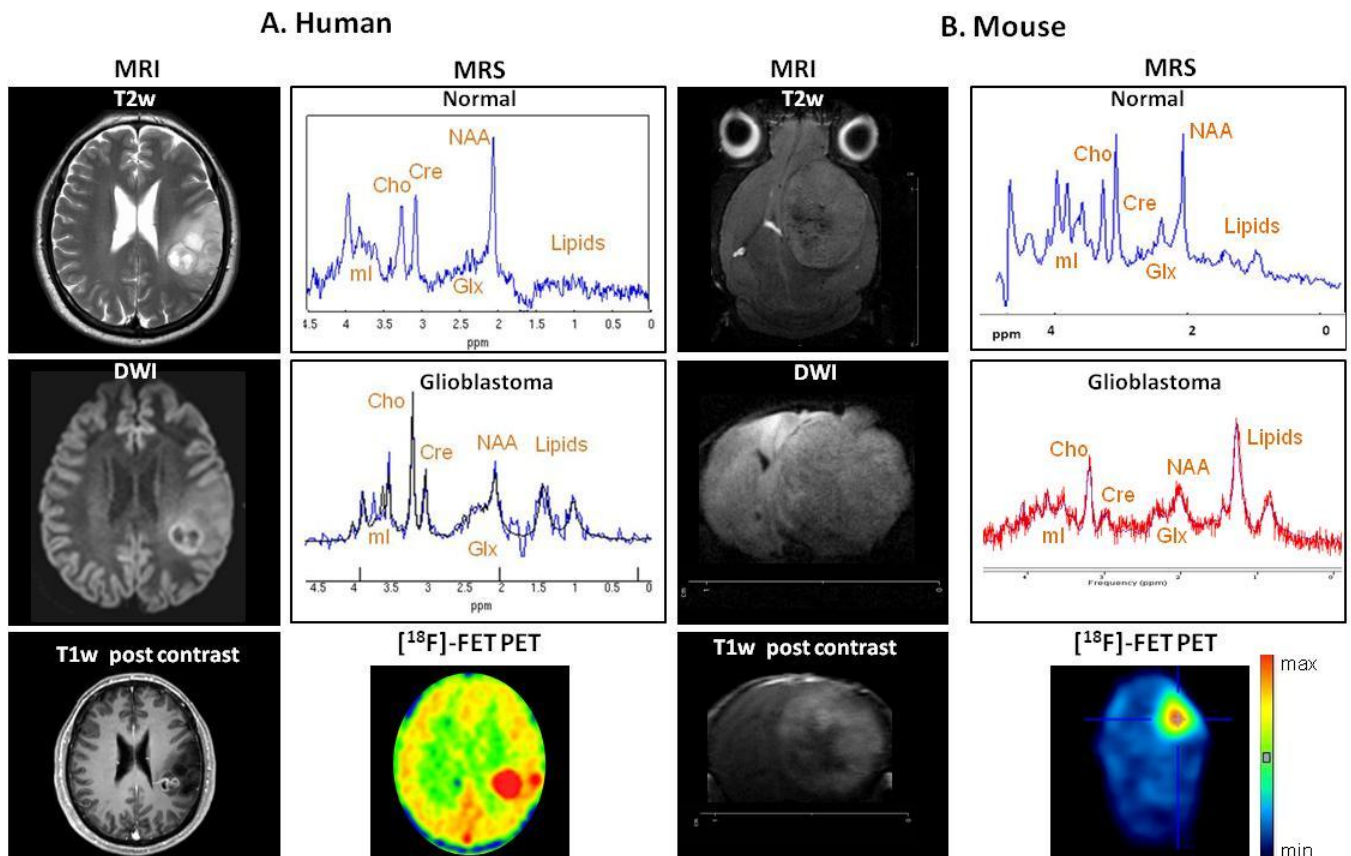
One of the most prominent features of GBM is the occurrence of the BBB disruption and their aggressive growth. BBB disruption can be monitored by contrast-enhanced MRI (CE-MRI) where a contrast agent, such as gadolinium chelates like Dotarem[®], which normally does not pass the BBB, are injected intravenously (*i.v.*). In GBM, the BBB is disrupted and T1 weighted MR images (T1W) show an increased signal from areas

with BBB disruption. Dynamic CE-MRI can be performed to derive blood volume, cerebral blood flow, vessel size, contrast agent arrival and transit times [92]. In a preclinical setting, similar MRI sequences for anatomical information and BBB disruption assessment [35, 93] are available and an extensive characterization of the tumor is also possible in living rodent models. With such advanced MRI methods, more specific information on blood flow changes, angiogenesis and regions of ischemia can be obtained by perfusion weighted MRI [36] or PET using [¹⁵O] radiolabeled water as a tracer [94], and a macroscopic view of the tumor blood vessels can be generated with MRI angiography as shown by Doblas *et al.* [36], while BBB disruption can be analyzed with CE-MRI. Brubaker *et al.* compared the number of terminal branches, the vessel count and the average vessel radius between tumor bearing mice and healthy controls [95]. Keunen *et al.* showed a reduced blood supply and an increased tumor cell invasion in glioblastoma after anti-VEGF treatment [96]. Mostly, these MRI sequences are applied after anti-angiogenic therapy. Although longitudinal studies that monitor the animals throughout therapy would be favorable, anti-angiogenic treatment may result in a less aggressive phenotype with normalized and less leaky blood vessels, thus decreasing the contrast-enhanced region, which is therefore not always indicative for the absence of tumor growth [43]. Furthermore, aggressively growing tumors display a higher metabolic activity which causes an increased demand of oxygen and nutrients and thus an increased blood flow. The higher metabolic rate is characterized in the clinic by PET imaging [25] or magnetic resonance spectroscopy (MRS) [43], which are also available preclinically. For instance Spaeth *et al.* showed high tumor uptake of [¹⁸F]-fluorocholine ([¹⁸F]-FCH), O-(2-[¹⁸F]-fluoro-ethyl-L-tyrosine ([¹⁸F]-FET) and 2-deoxy-2-[¹⁸F]-fluoro-D-glucose ([¹⁸F]-FDG) in a rat glioblastoma model [97]. Furthermore, Assadian *et al.* performed [¹⁸F]-FDG PET imaging [98], whereas Miletic *et al.* used methyl-L-[¹¹C]-Methionine ([¹¹C]-MET) PET [82] for follow-up of anti-glioma therapies. Several groups have also implemented MRS in preclinical brain tumor models, such as Hekmatyar *et al.* [99], Park *et al.* [100] and Simoes *et al.* [42] to characterize metabolic profiles of brain tumors. For an example of imaging approaches in glioma studies that are available both in a clinical setting and preclinically we refer to figure 2.

Figure 2: Comparison of imaging modalities for clinical and preclinical glioblastoma imaging.

- A. T2 weighted MR imaging and T1 weighted imaging post contrast administration in a 44-year old male patient diagnosed with a glioblastoma in the left frontal and temporal lobe, showed the tumor with central necrosis and perilesional edema. Diffusion weighted imaging (DWI) demonstrates high signal intensity (low diffusivity) in the solid contrast-enhancing part of the lesion (high cellularity), and low signal intensity (high diffusivity) in central necrotic parts. Furthermore, MRS with a spectrum obtained from tumor tissue showed an altered metabolism characterized by an increase in choline, NAA and lipids and a decrease in creatine. A MRS spectrum of normal appearing white matter is furthermore shown as a comparison. Furthermore, an [¹⁸F]-FET PET scan showed increased amino-acid metabolism within the glioblastoma.
- B. T2 weighted MRI and T1 weighted MRI post contrast administration in a mouse GL261 glioblastoma model, demonstrated a large tumor in the right side of the brain with central necrosis and mass effect. An MRS spectrum from normal and tumor tissue are furthermore demonstrated. The spectrum from tumor tissue showed an altered metabolism marked by an increase in choline, NAA and lipids and a creatine decrease. Finally, an [¹⁸F]-FET PET scan also demonstrated increased amino-acid metabolism in a mouse glioblastoma.

MRS: magnetic resonance spectroscopy, [¹⁸F]-FET: [¹⁸F]Fluorethyl-L-tyrosine, PET: positron emission tomography, MRI: magnetic resonance imaging, ml: myo-inositol (glial marker), Cho: choline (membrane turnover), Cre: creatine (energy metabolism), Glx: glutamine/glutamate (neurotransmitter metabolism), NAA: N-acetyl aspartate (marker of neural density), Lipids: mobile lipids/lactate (necrosis/ anaerobic glycolysis)



Additional to the imaging modalities used in a clinical setting, several exclusively preclinical imaging modalities exist such as near infrared (NIR) imaging, BLI and multi-photon laser scanning microscopy (MPLSM). Although fairly new, gold nanoparticles are under investigation for combined imaging and therapy purposes. These particles display surface plasmon resonance (SPR) which make them suitable for NIR imaging. Furthermore, they absorb laser irradiation in the near infrared region which means they can be used for photothermal therapy but also for photoacoustic imaging [101]. The size and shape of these gold nanoparticles can vary. Spherical, nanorod and branched particles have been described. Accumulation of these nanoparticles can be either passive, due to BBB disruption, or active, due to functionalization of the particles with tumor cell receptor targeting moieties. Van de Broek *et al.* and Day *et al.* showed the feasibility for the detection and therapeutic usage of these gold nanoparticles *in vitro* by conjugating them to anti-HER2 nanobodies in order to actively target breast cancer cells [102, 103]. Furthermore, Qian *et al.* and Yi *et al.* demonstrated the feasibility of detection and usage for therapy of these nanoparticles *in vivo* [104, 105]. Another preclinical multimodal imaging modality, BLI, can be used to assess cell viability and therefore therapeutic efficiency. As mentioned previously, cells need to be transduced with viral vectors which contain a reporter gene, such as the Firefly luciferase gene that enables bioluminescent imaging to assess tumor viability after treatment [106, 107]. Cells can also be transduced with fluorescent genes after which MPLSM or fluorescence imaging (FLI) can be performed on superficial tumors or animals adapted with cranial windows to look at glioma invasion as was shown by Winkler *et al* [108].

Finally, not only tumor growth, characteristics and viability can be monitored, but also therapeutic vehicles themselves. Using stem cells for brain tumor therapy can be followed with several imaging modalities. Migration of stem cells towards a tumor can be followed *in vivo* by *in vitro* labeling of the stem cells with micron-sized paramagnetic iron oxide particles (MPIO), superparamagnetic iron oxide particles (SPIO) or ultrasmall paramagnetic iron oxide particles (USPIO) [37]. These cause negative contrast enhancement on T2 and T2* MR images and thus darker areas in the regions of interest [109]. In mice, immunotherapy has been followed by labeling DC's *in vitro* and performing MRI. Tavare *et al* were able to locate DC's for up to 7 days

after injection [110]. Recently, also ^{19}F MRI has gained importance and has been utilized for tracking DC's *in vivo* [38].

When introducing a therapeutic gene, this can in some cases also be used for PET imaging. The HSV-TK gene can be imaged with specific radiotracers, such as ^{18}F FEAU (1-(2'-deoxy-2'-fluoro-beta-d-arabinofuranosyl)-5-ethyluridine), ^{18}F FFEAU (1-(2'-deoxy-2'-fluoro-beta-d-arabinofuranosyl)-5-(2-fluoroethyl)uridine) [111] or ^{18}F FHBG 9-(4- ^{18}F -fluoro-3-butyl)guanine [112].

Therapeutic genes can also be combined with an imaging reporter gene, such as the Firefly luciferase gene in multicistronic vectors or repeated cell transduction, which enables to determine the viability of therapeutic cells by BLI [93].

For an overview of available imaging techniques to assess specific characteristics of gliomas in small animals we refer to table 3.

Table 3: Overview of available imaging techniques to assess specific characteristics of gliomas in small animals.

Parameter	Imaging modality	Specifications	Limitations	Ref
Anatomy	MRI	T2 weighed images	Necrosis \leftrightarrow bleeding	[113]
Vasculature	MRI	BBB disruption: CE-MRI	Limited spatial resolution	[35, 96]
		MRI angiography	Needs anatomical imaging	[36]
Disruption of brain tracts	MRI	Diffusion tensor imaging	Limited info on tumor	[90]
Cellular composition	MRI	Diffusion weighted imaging	Limited spatial resolution	[91]
Invasiveness	MPLSM	Dynamic <i>in vivo</i> MPLSM	Cranial window requirement Superficial tumors	[108]
Metastasis	MRI/MRS	T2, CE-T1, DWI/ ^1H MRS		[42]
Viability	BLI		2D imaging modality Low spatial resolution	[16]
Metabolism	PET	^{18}F FDG/ ^{11}C acetate/ ^{18}F choline/ ^{18}F FET	Needs co-registration with MRI or CT Low spatial resolution in mice	[98, 114]
	MRS	^1H MRS/ ^{13}C MRS	Needs co-registration with MRI or CT	[99, 100]
Photothermal therapy	NIR	Golden nanoparticles	Limited penetration depth	[103, 105]

MRI: Magnetic resonance imaging, MPLSM: multiphoton laser scanning microscopy, MRS: magnetic resonance spectroscopy, BLI: Bioluminescence imaging, PET: Positron emission tomography, CT: computed tomography, CE-MRI: contrast enhanced –MRI, DTI: Diffusion tensor imaging, DWI: diffusion weighted imaging, ^{18}F FDG: ^{18}F -fluorodeoxyglucose, ^{18}F -FET: ^{18}F -Fluorethyl-L-tyrosine.

Even though there is a multitude of *in vivo* preclinical imaging modalities available, which can be combined, a Pubmed search, resulted in only a few multi-modal imaging applications in preclinical GBM research, which involved a combination of MRI/BLI [115], MRI/PET [116, 117] or BLI/CT [118]. Other papers regarding glioblastoma research applied a single imaging modality like MRI e.g.[119], BLI e.g.[120] or PET e.g.[121] but the majority of the published papers did not use any *in vivo* imaging to follow-up treatment response [122]. Most of the latter used size measurements on xenografts, symptomatic endpoints or survival combined with histological validation to assess treatment efficacy. Final outcome may thus be reconstructed but no information is recovered about initial tumor induction efficiency in orthotopic models or morphological or functional changes during therapy. In order to obtain this information, additional animals must be added and sacrificed at certain time points, thus increasing animal use and costs. Examples of multi-modal imaging applications in GBM research are provided in table 4.

Table 4: Examples of recent multi-modal imaging applications in rodents.

Author	Ref	Year	MRI	PET	BLI	CT	Other
Viel et al	[123]	2008	X	X			
Corroyer-Dulmont et al	[117]	2013	X	X			
Schwartz et al	[124]	2011	X	X		X	Ultrasound
Jarzabek et al	[115]	2012	X		X		
Baumann et al	[125]	2012	X		X	X	
Zhou et al	[126]	2009	X		X		NIR imaging
Dorsey et al	[127]	2009		X	X	X	Fluorescence
Cronin et al	[118]	2012			X	X	
Liu-Hua Wei et al	[128]	2008		X		X	
Wehrl et al	[28]	2013		X			MRS

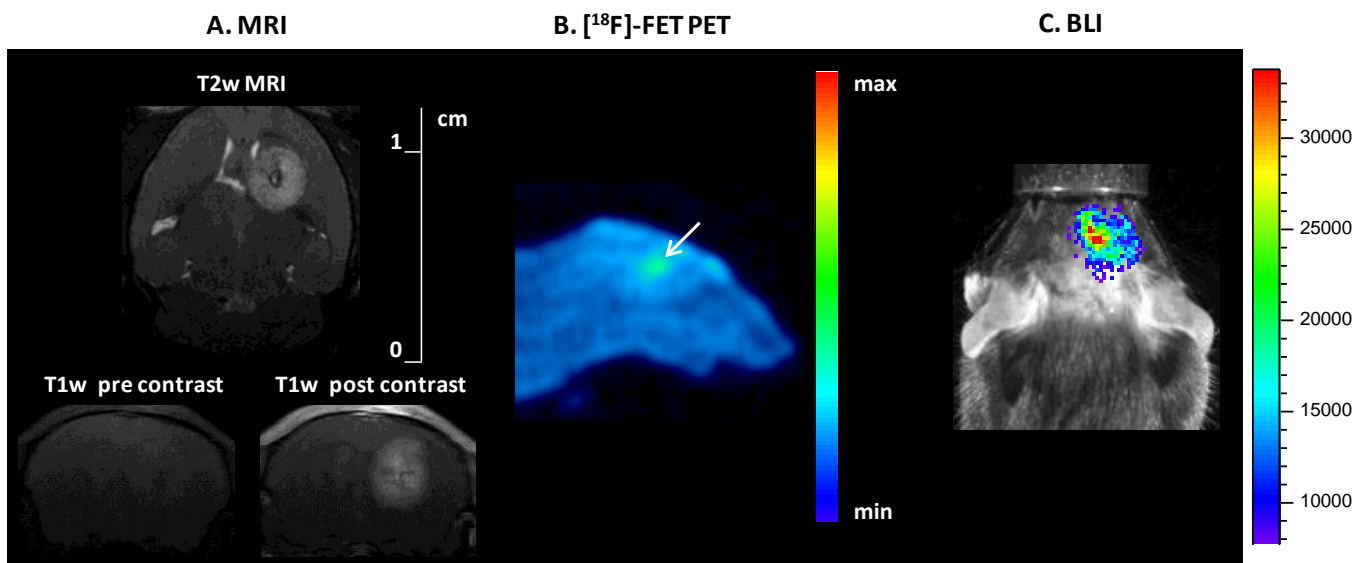
MRI: magnetic resonance imaging, PET: positron emission tomography, BLI: Bioluminescence imaging, CT: computed tomography, NIR: near infrared imaging, MRS: magnetic resonance spectroscopy.

The most frequently used combinations of preclinical imaging methods are MRI/PET [117, 123] and MRI/BLI [115] although combinations of these imaging modalities with other modalities, such as ultrasound [125], NIR imaging [126], MRS [28] and CT (PET/CT [128], BLI/CT [118], MRI/PET/CT [124] MRI/BLI/CT [125] and PET/BLI/CT [127]), have also been used. For an example of a multi-modal imaging approach using MRI, BLI and PET in mice performed in our centre, we refer to figure 3, showing an example for a glioma model used in this thesis.

Figure 3: Example of a multi-modal imaging approach in a GBM bearing mouse injected with fLuc expressing stem cells.

- A. T2 weighted MR imaging on a GL261 glioblastoma bearing C57BL6/J mouse was used to confirm the striatal location of the tumor and to determine the tumor size. Furthermore, T1 weighted imaging post contrast administration was performed in the same animal to confirm BBB disruption.
- B. Subsequently, a dynamic [^{18}F] FET PET scan was performed for 80 min which showed an increased amino-acid metabolism in the tumor.
- C. Finally, BLI was performed on the same animal to assess the viability of fLuc positive mMAPCs injected intratumorally 2 weeks prior to imaging. BLI confirmed that these stem cells were viable for at least 2 weeks in a glioblastoma environment.

MRI: Magnetic resonance imaging, [^{18}F] FET PET: [^{18}F] Fluorethyl-L-tyrosine positron emission tomography, BLI: Bioluminescence imaging, T1W: T1 weighted image, fLuc: Firefly luciferase.



1.6 Conclusion

The dismal prognosis faced by patients suffering from glioblastoma, has multiple causes. First, the aggressive nature and the presence of resistant stem cells and infiltrating tumor cells complicate treatment. Furthermore, early detection is usually impossible as symptoms are vague and MRI and / or PET scans are not routinely performed for screening. After treatment, it is difficult to discriminate tumor (re)growth from therapy induced edema and necrosis which complicates distinction between progression and pseudoprogression [129]. As a consequence, it becomes more difficult to distinguish responders from non-responders by using only conventional imaging techniques. Consistent combination of PET/BLI and MR spectroscopy [130] aids clinicians to identify true progression at an earlier time point and enable adaptations of treatment schedules when necessary. Current standard treatment remains however inefficient as indicated by the high mortality rate still experienced by patients suffering from high grade gliomas. Therefore, research should focus on the development and assessment of new treatment approaches. Extrapolation of the acquired data remains however difficult as no existing animal model recapitulates all aspects of a human brain tumor. Special efforts should therefore also be made to characterize models carefully before investigating new treatment modalities, which should be thoroughly followed by non-invasive imaging to assess treatment efficiency before proceeding to clinical settings. New treatment approaches not only have to focus on the main tumor mass but also on erasing tumor cells that infiltrate normal brain tissue as these cells are mainly responsible for relapse after therapy. Several imaging modalities are available to investigate different characteristics, each with their own strengths and limitations. Often, multi-modal imaging is required to answer specific research questions. Thus, imaging can aid researchers to guide therapy, better evaluate experimental treatment modalities, investigating factors such as treatment efficiency, progression free survival and possible side-effects more thoroughly before implementing experimental therapies in patients.

CHAPTER 2

Objectives and outline of this work

Chapter 2: Objectives and outline of this work

2.1 Outline of this work

During the last decades, new therapeutic approaches have resulted in decreased mortality rates for various tumor types. For glioblastoma patients, the prognosis remains however poor as innovative approaches derived from preclinical research models show unsatisfactory results when translated in a clinical setting. It is therefore crucial to thoroughly evaluate both preclinical models and the experimental therapy in order to maximize insights in treatment mechanisms and possible reasons for treatment failure. Unlike clinical practice where multi-modal imaging is applied frequently, preclinical research uses the abilities of *in vivo* multi-modal imaging, including magnetic resonance imaging (MRI), positron emission tomography (PET) and bioluminescence imaging (BLI), less extensively. These imaging modalities can however help researchers in assessing therapy mechanisms while reducing the number of animals, time and costs and increase statistical power of preclinical studies. In this study, preclinical *in vivo* multi-modal imaging techniques were used to study suicide gene therapy and the associated bystander killing effect in preclinical glioma models.

Although, the proof-of-principle for suicide gene therapy has been demonstrated before [82], imaging played a minor role in guiding therapy in this first study on the bystander-killing effect of tumor infiltrating, HSV-TK expressing stem cells.

2.2 Objectives

The first objective of this study was to label and transduce both stem cells and glioma cells to obtain cells with a therapeutic potential and that are traceable with non-invasive multi-modal imaging methods. For this purpose, several lentiviral vectors were designed. These vectors were designed to image both therapeutic and tumor cells and contained different fluorescent proteins (enhanced green fluorescent protein (eGFP) for stem cells, mCherry for glioma cells), and different luciferases (fLuc for stem cells, rLuc for glioma cells). Furthermore, stem cells were labeled with superparamagnetic iron oxide particles (SPIO's) for MR tracking (Figure 4).

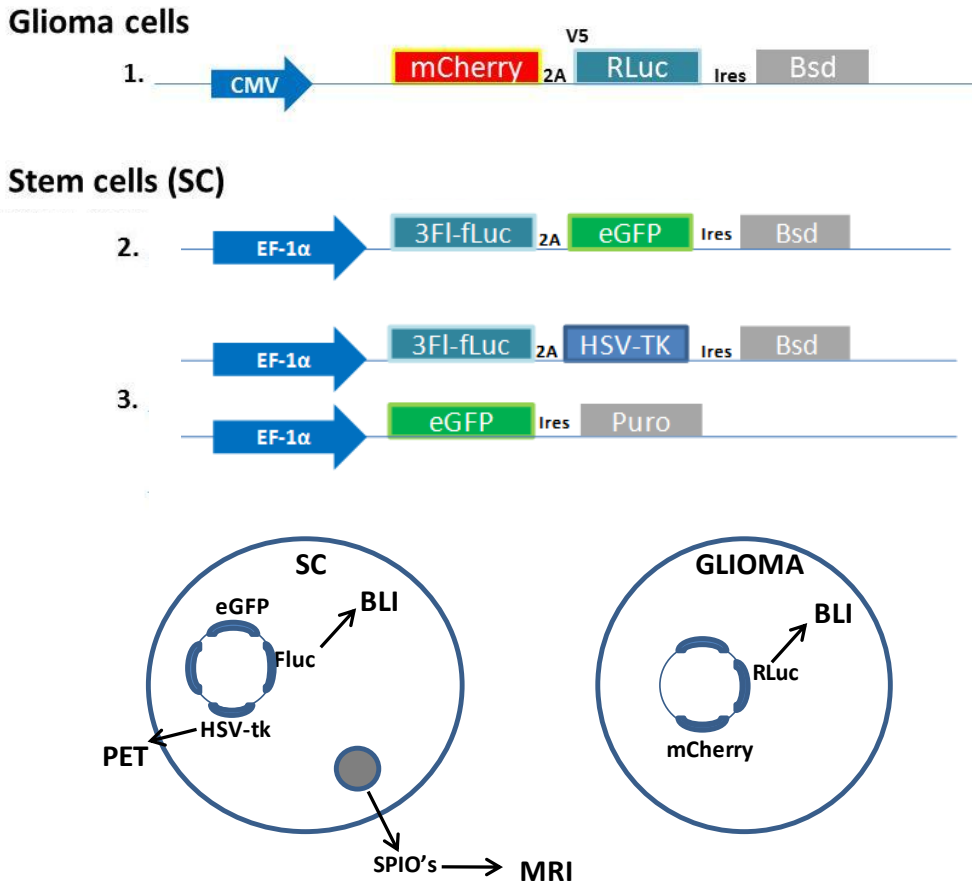
The second objective was to characterize and optimize different glioma models, both using mouse and human cell lines. The presence of BBB disruption and reproducibility were key indicators to select a model.

The third aim of this study was to conduct *in vivo* multi-modal imaging proof-of-principle experiments in order to generate a model for screening of stem cell mediated suicide gene therapy in different preclinical glioblastoma models. Therefore, eGFP-fLuc-HSV-TK positive cells were labeled with iron oxide particles and stereotactically injected into the brain of mice to optimize imaging protocols and define limits of the used methods. Repeated MRI provided detailed information on the biodistribution of the cells relative to the tumor. Thus, decisions could be made in regard to timing of ganciclovir administration. BLI (fLuc) or PET (^{18}F -FHBG) were assessed for their informative potential. Tumor formation and therapy assessment was performed by MRI (lesion size), PET (^{18}F -FET) and BLI (rLuc). *In vivo* findings were correlated to histology.

The final objective for this study was to assess stem cell mediated suicide gene therapy in different preclinical glioblastoma models using multi-modal small animal imaging, including MRI/BLI for follow-up of stem cell distribution and treatment response.

Figure 4: Overview of the developed lentiviral vectors for multi-modal imaging follow-up of suicide gene therapy.

For glioma cells, a lentiviral vector was produced carrying the mCherry and rLuc controlled by a cytomegalovirus promoter (CMV). For the stem cells, a control vector carrying the eGFP and fLuc genes was produced. Furthermore, two lentiviral vectors were designed to transduce cells with the eGFP, Fluc and HSV-TK genes. Stem cell lentiviral vectors were controlled by the elongationfactor 1 α (EF-1 α). Furthermore, blasticidine- or puromycine resistance genes were added for selection of the transduced cells. Following transduction, cell viability was assessed by BLI, using either fLuc (Stem cells(SC)) or rLuc (Glioma) and PET (HSV-tk / [116] FHBG). Finally, stem cells were labeled with SPIO's for MRI cell tracking.



CHAPTER 3

Generation & validation of cell lines for non-invasive imaging of suicide gene therapy

Chapter 3:
Generation & validation of cell lines for non-invasive imaging of suicide gene therapy

Chapter 3: Generation and validation of cell lines for non-invasive imaging of suicide gene therapy

3.1 Introduction

Over the past years, stem cells have gained interest as a mean for potential tumor treatment, where they can be used as cellular vehicles to deliver suicide genes to the malignant tissue [131]. Stem cells are also being considered in the broad field of regenerative medicine, such as in stroke [77], where differentiation of certain stem cells is supposed to support recovery either by cell replacement or indirectly by the release of neurotrophic factors [78]. Several types of stem cells are available and the selection of the most suitable stem cell type depends on the intrinsic stem cell characteristics and the anticipated results of the treatment. One type of stem cells that is currently being tested in a number of clinical trials are multipotent adult progenitor stem cells (MAPCs), which can be isolated from adult human bone marrow [132, 133] and display some unique features including the ability for self-renewal, which is shown by the observation that they can be cultivated for up to 70 passages [134].

In this study, we have assessed the transduction efficiency of a CMV promoter driven lentiviral vector encoding for either, eGFP and fLuc or eGFP, fLuc and HSV-TK on HEK293T cells and rOct4⁺ BM-HypoSCs. An EF1 α promoter driven lentiviral vector encoding for eGFP was assessed in order to increase the transduction stability and efficiency. In addition to the previously mentioned cell lines this vector was furthermore assessed in two additional, related mouse cell lines namely mOct4⁺ BM-HypoSCs and mMSC's. Subsequently, EF1 α promoter driven lentiviral vectors were produced which encoded for eGFP and fLuc (pCH-EF1a-3flag-fLuc-T2A-eGFP-Ires-Bsd) or eGFP, fLuc and HSV-TK (pCH-EF1a-eGFP-Ires-puro and pCH-EF1a-3flag-fLuc-T2A-HSVTK-Ires-Bsd).

After simultaneous preliminary *in vivo* experiments (see also chapter 4, 5), three different mouse cell lines (mOct4⁺ BM-HypoSCs, mOct4⁻ BM-MAPCs and mMSC's) and one human cell line (hMultistem) were transduced with these lentiviral vectors and labeled using in house fabricated SPIO's for MRI tracking. Subsequently, transduction efficiency was assessed using fluorescence activated cell sorting (FACS), BLI and a

GCV killing experiment. Furthermore, the effect of SPIO labeling (sensitivity, adverse effects, label stability, etc.) was assessed using, MRI, BLI, ICP and an MRI phantom.

Finally, a mouse (GL261-Glioblastoma) and human glioma xenograft (Hs683-oligodendroglioma and U87-MG -glioblastoma) models were selected for assessment of the bystander killing effect. Subsequently, these tumor cells were transduced using a CMV promoter driven lentiviral vector encoding for mCherry and rLuc. The expression of the rLuc gene was assessed by BLI using Coelenterazin-h as a substrate for rLuc.

3.2 Materials & methods

Cell lines

eGFP-fLuc + and eGFP-fLuc-HSVTK+ HEK 293T cells were acquired from the Laboratory of Molecular Virology and Gene Therapy, KU Leuven (also known as the Leuven Viral Vector Core) and were cultured using medium containing Dulbecco's Modified Eagle Media (DMEM) + Glutamax (Gibco®Invitrogen®Invitrogen, ThermoFisher Scientific, Waltham, MA USA) supplemented with 10% FCS and Gentamycin (50µg/ml, Gibco®Invitrogen).

Mouse and rat m/rOct4⁺ BM-HypoSCs and mOct4⁻ BM-MAPCs were obtained from the laboratory of Stem Cell Biology and Embryology at KU Leuven. Cells were cultured as described previously [135]. In short, culture dishes, coated with fibronectin were used to passage cells every 48 hours. Rat stem cell medium contained 60% low glucose DMEM (Gibco®Invitrogen BRL), 40% MCDB-201 (Sigma), 1 x insulin-transferrin-selenium (ITS) (Sigma), 1 x linoleic acid bovine serum albumin (LA-BSA) (Sigma), 10⁻⁹ M dexamethasone (Sigma), 10⁻⁴ M ascorbic acid 3-phosphate (Sigma), 100 units of penicillin, 1000 units of streptomycin (Cellgro), 2% fetal bovine serum (FBS; HyClone), 10 ng/mL human platelet-derived growth factor (R&D systems), 10 ng/mL mouse epidermal growth factor (Sigma), and 1000 units/mL mouse leukemia inhibitory factor (Esgro ESG, Chemicon). Mouse stem cell medium was similar with some modifications: 1 x selenium-insulin-transferrin-ethanolamine (SITE) (Sigma) was used instead of ITS, a combination of 0.2 mg/mL LA-BSA and 0.8 mg/mL powdered bovine serum albumin (BSA; Sigma) was added instead of using only LA-BSA, 1 x chemically defined lipid concentrate (Gibco®Invitrogen) was included, and dexamethasone was not included. Finally, b-mercaptoethanol (1 x; Gibco®Invitrogen) was added freshly to both types of media. Media was sterilized using a 22-mm filter (Millipore, USA).

mMSC's were also obtained from the laboratory of Stem Cell Biology and Embryology at KU Leuven and were cultured using medium containing Iscove's Modified Dulbecco's Medium (IMDM, Gibco®Invitrogen) supplemented with 10% FBS (Hyclone), 10% horse serum (Biochrom, Berlin, Germany), 1% L-glutamine (Gibco®Invitrogen) and 100 units of penicillin and 100µg of streptomycin (Cellgro). Cells were split every 60-72 hrs at 70-80% confluency.

hMultistem's and the U87-MG cell line were acquired from Regenesys (Leuven, Belgium) and the American Type Culture Collection (ATCC code HTB-14-Manassas, VA, USA) respectively and were cultured according to the manufacturer's guidelines.

The GL261 cell line, used as a mouse model for glioblastoma, and the Hs683 cell line, used as a human glioma xenograft model for oligodendroglioma, was obtained from the Laboratory of Clinical Immunology, at KU Leuven and the Laboratory for Toxicology at the Free University Brussels (ULB). Both cells were cultured as described previously [106].

The Hs683 cell line was obtained from the toxicology laboratory at the ULB and was cultured as described previously [136].

Genetic modification

CMV promoter driven lentiviral vectors encoding for eGFP-fLuc or eGFP-fLuc-HSVTK

eGFP-fLuc + and eGFP-fLuc-HSVTK + HEK 293T cells were obtained from the Laboratory of Molecular Virology and Gene Therapy, KU Leuven (Leuven Viral Vector Core) [137]. rOct4⁺ BM-HypoSCs were transduced using a CMV promoter driven lentiviral vector encoding for eGFP and fLuc or eGFP, fLuc and HSV-TK (20pg p24/cell). Subsequently, transduced cells were selected using puromycin (2-4 µg/ml) as the lentiviral vectors contained a puromycin resistance cassette. Samples for flow cytometric analysis were prepared using a final concentration of 2% paraformaldehyde and the percentage eGFP positive cells and the total eGFP expression (mean fluorescence intensity x %eGFP+ cells) were

measured using a FACSCanto system (BD Biosciences, Erembodegem, Flanders, Belgium) and analyzed with the FACSDiva software package provided with the instrument.

Evaluation of EF1 α promoter driven lentiviral vector encoding for eGFP for stem cell transduction

HEK293T cells and rOct4⁺ BM-HypoSCs were transduced with an EF1 α promoter driven lentiviral vector encoding for the eGFP gene and a puromycin resistance cassette (HEK 293T: 8pg p24/cell, rOct4⁺ BM-HypoSCs 20pg p24/cell). Furthermore, mOct4⁺ BM-HypoSCs (p24 = 20pg p24/cell), mOct4⁻ BM-MAPCs (p24 = 20pg p24/cell) and mMSC's (p24 = 8pg p24/cell) were transduced with the same lentiviral vector. Cells were subsequently selected with increasing puromycin concentration ranging from 2-4 μ g/ml (HEK293T, rOct4⁺ BM-HypoSCs, mOct4⁺ BM-HypoSCs, mOct4⁻ BM-MAPCs) or 4-6 μ g/ml (mMSC). Samples for flow cytometric analysis were prepared as described previously and the % of eGFP positive cells and the total eGFP expression (mean fluorescence intensity x %eGFP+ cells) were measured using a FACSCanto system (BD Biosciences) and analyzed with the FACSDiva software package provided with the instrument.

Viral vector construction, production and transduction

A control and two multicistronic HIV-based lentiviral vector transfer plasmids [137] were provided by the Molecular Virology and Gene Therapy, KU Leuven (Leuven Viral Vector Core) driving reporter gene expression from an EF1 alpha promoter. The first transfer plasmid was engineered to express a 3xflag tagged firefly luciferase (3flag-fLuc) together with Herpes simplex virus thymidine kinase (HSV-TK) and a blasticidin resistance cassette (BsdR) linked by a peptide2A sequence (T2A) and an internal ribosomal entry site (IRES), respectively (pCH-EF1a-3flag-fLuc-T2A-HSVTK-IRES-BsdR), whereas the second encoded enhanced green fluorescent protein (eGFP) and a puromycin resistance cassette (PuroR), linked by an IRES (pCH-EF1a-eGFP-IRES-PuroR). The control transfer plasmid was engineered to express 3xflag tagged derived firefly luciferase (3Flag-fLuc) together with eGFP and a blasticidin resistance cassette (BsdR) linked by a peptide 2A sequence (T2A) and a internal ribosomal entry site (IRES), respectively (pCH-EF1a-3flag-fLuc-T2A-eGFP-IRES-BsdR). LV vectors were produced by Molecular Virology and Gene Therapy, KU Leuven (Leuven Viral Vector Core) as previously described [137]. Filtered vector particles were concentrated with Vivaspin 15 columns (Vivascience, Hannover, Germany), aliquoted and stored at -80°C and are referred to as LV_EF1a-3flag-fLuc-T2A-HSVTK-IRES-BsdR, LV_EF1a-eGFP-IRES-PuroR and LV_EF1a-3flag-fLuc-T2A-eGFP-IRES-BsdR, respectively.

mOct4⁺ BM-HypoSCs (p24 = 20pg p24/cell), mOct4⁻ BM-MAPCs (p24 = 20pg p24/cell), hMultistem (p24 = 20pg p24/cell) and mMSC's (p24 = 8pg p24/cell) were consecutively transduced with the mentioned lentiviral vectors driven by an EF1 α promoter. First, LV_EF1a-eGFP-IRES-PuroR was used for transduction and cells were subsequently selected with puromycin (Invivogen, San Diego, USA) (2-4 μ g/ml, Sigma-Aldrich). Following selection, LV_EF1a-3flag-fLuc-T2A-HSVTK-IRES-BsdR was used to transduce the cells, which were subsequently selected with blasticidin (20-80 μ g/ml, Invivogen). Control cells were generated by adopting a similar strategy using the LV_EF1a-3flag-fLuc-T2A-eGFP-IRES-BsdR.

Evaluation of EF1 α promoter driven lentiviral vectors encoding for eGFP, fLuc (and HSV-TK) for stem cell transduction

eGFP expression was used for visual confirmation of transduction after which fLuc and HSV-tk expression were assessed. For fLuc expression, 1 x 10⁵ cells were seeded in triplicate in a 24 well plate and allowed to attach prior to fLuc BLI measurements. 75 μ g of D - luciferine (Promega, Madison, WI, USA) was added per well prior to placing the plates in the IVIS[®] 100 system (Perkin Elmer, Waltham, MA, USA) at 37°C. A scan was taken (medium binning, f stop = 1, time= 10s or 1 min) and acquired data were analyzed by the living image[®] 2.50.1 software.

Subsequently, HSV-tk expression was confirmed with a GCV killing experiment. Hereby, 2 x 10⁴ cells were seeded in a 24 well plate and allowed to grow. The following day, ganciclovir (GCV, Cymevene[®], Roche, Basel, Switzerland) was added in different concentrations, 100 μ M, 1 μ M and 0.01 μ M, for 4 consecutive days after which BLI was performed as described previously using the IVIS[®] 100 system (Perkin Elmer). Cells were subsequently collected and a BCA protein assay (ThermoScientific, Rockford, USA) was performed.

Stem cell characterization

Cell surface phenotype

The mOct4⁺ BM-HypoSCs and mOct4⁻ BM-MAPCs cells were trypsinized, washed with PBS and incubated for 15 min at room temperature with antibodies dissolved in staining buffer. Cells were washed once, resuspended in PBS and analyzed by flow cytometry.

Antibodies for mouse cell-surface markers were: CD140a-APC, CD31-APC, CD44-APC (eBioscience, San Diego, CA), c-Kit-APC (BDPharmingen, San Diego, CA), Sca1-APC (Abcam, Cambridge, UK).

Karyotyping

Two days after seeding mouse and rat Oct4⁺ BM-HypoSCs and mouse and rat Oct4⁻ BM-MAPCs were exposed to 0.1 µg/ml colcemid (Sigma) for 3 h, harvested, washed, and incubated with 75 mM KCl hypotonic solution for 9 min at 37°C. Cells were centrifuged and the pellet fixed for 10 min using 15 ml methanol/acetic acid (3:1). Subsequently, cells were again centrifuged and the pellet was resuspended in 0.15 ml methanol/acetic acid (3:1). Cells were put onto a hot glass slide. Chromosomes were stained using Wright's stain and seventeen chromosomal spreads were counted per population [138].

RNA isolation and qRT-PCR

Total RNA from (non-)transduced cells was extracted using the RNeasy microkit (Qiagen, Valencia, CA). mRNA was reverse transcribed using Superscript III reverse transcriptase (Invitrogen, Carlsbad, CA) and cDNA underwent 40 rounds of amplification (ABI PRISM 7700, Perkin Elmer/Applied Biosystems, Foster City, CA) as follows: 40 cycles of a two-step PCR (95°C for 15 sec, 60°C for 60 sec) after initial denaturation (95°C for 10 min) with 1 µl DNA solution, 1 × TaqMan SYBR Green Universal Mix PCR reaction buffer (Applied Biosystems). Primers used for amplification are shown in Supplementary Table 1. The mRNA levels were normalized using the housekeeping gene GAPDH and compared to the expression in embryonic stem cells.

SPIO labeling of stem cells

eGFP-fLuc-HSVTK expressing stem cells were seeded (1.2×10^3 cells/cm²: mOct4⁺ BM-HypoSCs, mOct4⁻ BM-MAPCs / 2×10^3 cells/cm²: hMultistem's / 2.1×10^4 cells/cm²: mMSC's) and labeled for 24 hours using in house fabricated SPIO's [139, 140] (20 µg Fe/ml: mOct4⁺ BM-HypoSCs, mOct4⁻ BM-MAPCs, hMultistem's or 10 µg Fe/ml: mMSC's) combined with 1.5 µg/ml poly-L-Lysin (PLL). Subsequently, cells were washed three times with PBS and incubated overnight in iron free medium. Afterwards, cells were trypsinized and counted prior to sample preparation for BLI to assess cell viability following labeling, MRI of phantoms and inductively coupled plasma optical emission spectrometry (ICP-OES) for the assessment of contrast generation and cellular iron content, respectively. For BLI, 1×10^5 cells were seeded in triplicates in 24 well plates and allowed to attach. The following day, BLI was performed. For MRI Phantom scanning, 1×10^5 cells were resuspended in 100 µl PBS (concentration: 1000cells/µl) and mixed with 1.5% agarose (Sigma-Aldrich) in a 1.1 ratio (final concentration: 500 cells/µl). All samples were subsequently transferred to a pre-made matrix made of 1.5% agarose [141]. Upon solidifying, the phantoms were scanned using a 9.4T Bruker Biospin MR scanner. For ICP-OES, triplicate samples of 5×10^4 cells were lysed with concentrated 37% HCL (Vel Labs, Leuven, Belgium). Samples were further homogenized with distilled water and the iron content per cell was determined using ICP-OES (Varian, 720ES, Santa Clara, USA).

Glioma cell transduction using a CMV promoter driven lentiviral vector encoding for mCherry and rLuc

1.25×10^4 /cm² tumor cells (GL261, Hs683, U87-MG) were seeded and allowed to attach prior to transduction. Cells were incubated (108 pg p24 /cell) for 24 hours with a CMV promoter driven lentiviral vector encoding for mCherry, rLuc and a blasticidin resistance cassette. Subsequently, cells were washed and expanded. Approximately one week post transduction, when mCherry expression became apparent, blasticidin selection was commenced and maintained for one week (40-60 µg/ml). 2.5×10^4 cells were seeded per well and allowed to attach after which rLuc BLI (IVIS® 100 system (Perkin Elmer)) was performed using Coelenterazin-h (Rediject Coelenterazin-h, Perkin Elmer, 0.25 µg / well) as a substrate.

Imaging:

Magnetic resonance imaging (MRI)

For scanning of agar phantoms containing labeled cells, a 9.4T Bruker Biospec small animal MR scanner (Bruker Biospin, Ettlingen, Germany; horizontal bore 20cm) equipped with actively shielded gradients (600mT m⁻¹) was used. A quadrature radio-frequency (rf) resonator (transmit/receive; inner diameter 7cm, Bruker Biospin) was used for image acquisition. Two dimensional multi-slice-multi-echo (MSME) scans were acquired for the calculation of T2 values (TR=2000ms, TE increments: 10.1ms, 16 echo's, number of slices: 8, slice thickness: 0.4mm, interslice distance: 0.6mm, matrix size: 200x200, in plane resolution: 100µm²). Furthermore, three dimensional, high resolution T2* weighted MR images were acquired using a gradient echo sequence (TR = 1500ms, first TE = 4.44ms with 8 increments of 6.75ms, matrix size 400 x 400, in plane resolution: 78µm², slice thickness: 0.35mm, number of slices: 12). Images were processed using the Paravision 5.0/5.1 software (Bruker Biospin).

Bioluminescence imaging (BLI)

For BLI, cells were seeded and allowed to attach. The following day, the substrate (D-luciferine (75µg/well, Promega) or Coelenterazin-h (0.25µg/well, Perkin Elmer) was added to each well, prior to imaging using an IVIS® 100 system (Perkin Elmer). A scan was taken (medium binning, f stop = 1, time= 10s or 1 min) and acquired data were analyzed by the living image® 2.50.1 software (Perkin Elmer).

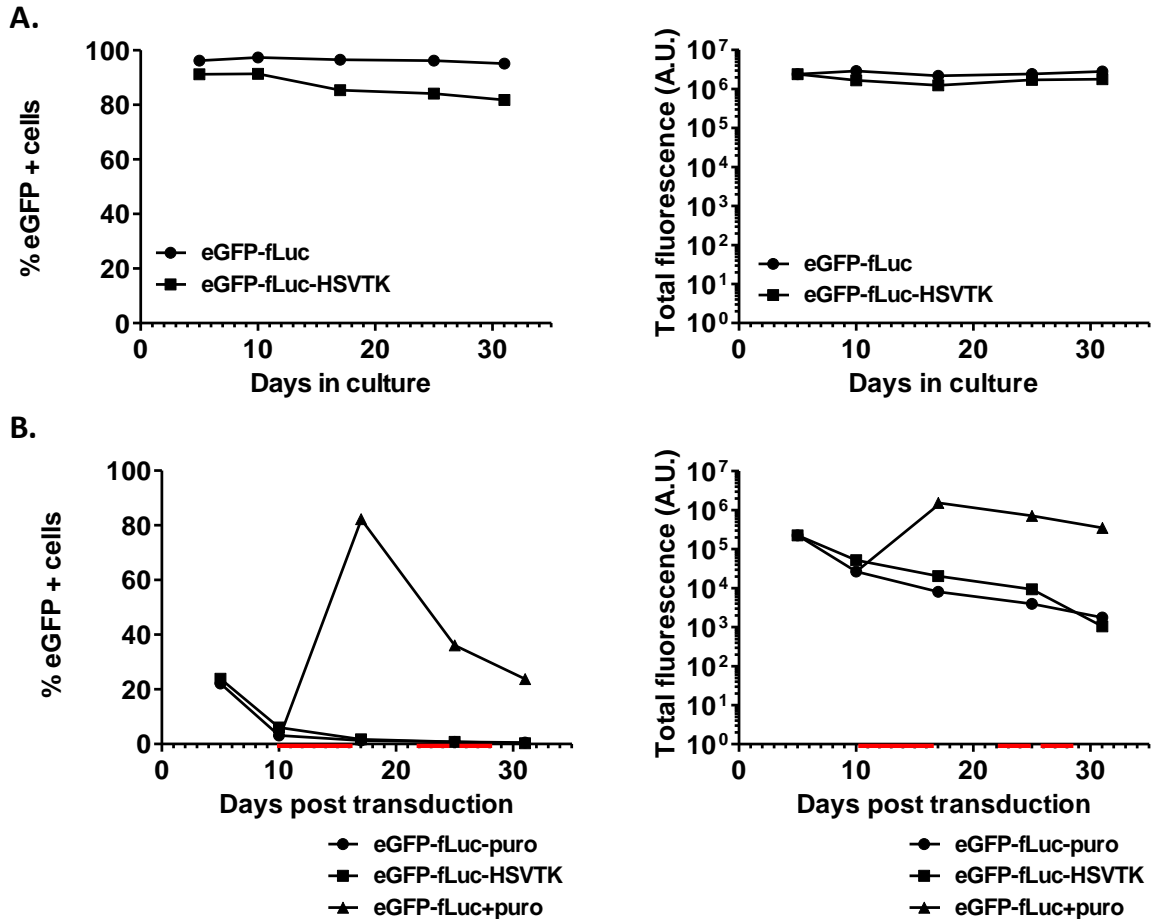
3.3 Results

3.3.1 Evaluation of transduction efficiency using a CMV promoter driven lentiviral vector

rOct4⁺ BM-HypoSCs transduced with a CMV promoter driven lentiviral vector encoding for eGFP-fLuc or eGFP-fLuc-HSVTK (20pg p24/cell) were compared to puromycin selected eGFP-fLuc + and eGFP-fLuc-HSVTK + HEK 293T cells (positive control). Transduction efficiency was assessed by FACS analysis (Figure 5). HEK 293T cells contained both, high percentages of positive cells (eGFP-fLuc: 96.3 ± 0.4%, eGFP-fLuc-HSVTK: 86.8 ± 1.9%) and high levels of fluorescence (eGFP-fLuc: $2.5 \times 10^6 \pm 1.4 \times 10^5$, eGFP-fLuc-HSVTK: $1.8 \times 10^6 \pm 1.8 \times 10^5$), for at least 30 days when keeping them in culture for both eGFP-fLuc and eGFP-fLuc-HSVTK + cell lines (Figure 5A). In rOct(+)-BM-HypoSCs, the transduction efficiency was much lower (eGFP-fLuc: 22.1%, eGFP-fLuc-HSVTK: 23.9%). Although puromycin selection increased the percentage of eGFP positive cells (eGFP-fLuc-puro: 82.3%), expression levels were not stable and both the number of eGFP+ cells and the total fluorescence decreased over time even when applying another puromycin selection regimen(Figure 5B).

Figure 5: HEK 293T and rOct4⁺ BM-HypoSCs transduction assessment using a CMV promoter driven lentiviral vector.

- A. eGFP expression analysis using FACS of HEK 293T cells showed efficient cell transduction that remained stable over time for both lentiviral vectors. Both the % eGFP⁺ cells and the total fluorescence remained high for at least 30 days when keeping them in culture.
- B. rOct4⁺ BM-HypoSCs displayed a less efficient gene transduction with approximately 20% eGFP⁺ cells, which increased up to 80% following puromycin selection. Unfortunately, this gene expression proved unstable and both the % of eGFP⁺ cells and the total fluorescence decreased over time even when applying another puromycin selection.



As transgene expression in rOct4⁺ BM-HypoSCs proved to be unstable using a CMV promoter, the EF1 α promoter was subsequently investigated in order to reach stable gene expression. As the insert size combined with the length of the EF1 α promoter would greatly diminish the packaging capacity of a lentiviral vector, one control vector (eGFP-fLuc-Blasticidin) and two treatment vectors (eGFP-Puromycin / fLuc-HSVTK-blasticidin) were produced. As an EF1 α promoter driven lentiviral vector encoding for eGFP and a puromycin selection cassette was available, proof of principle experiments were first conducted in order to assess the transduction efficiency of an EF1 α promoter driven lentiviral vector.

3.3.2 Evaluation of transduction efficiency using an EF1 α promoter driven lentiviral vector

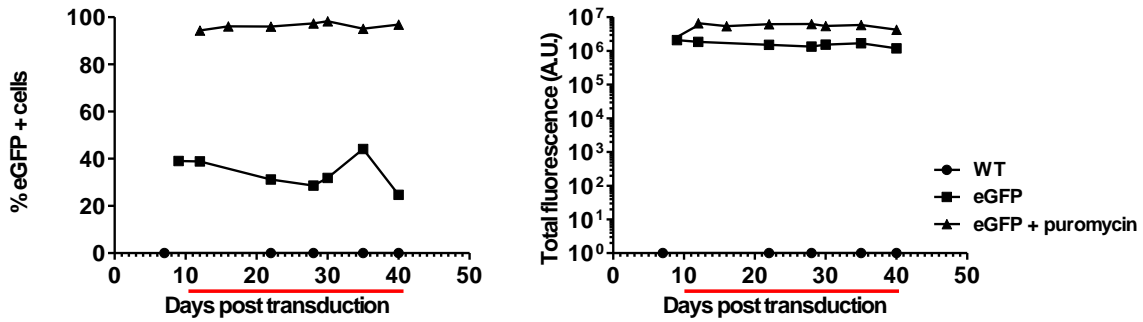
First, HEK293T cells and rOct4⁺ BM-HypoSCs were transduced using the EF1 α promoter driven lentiviral vector encoding for eGFP and a puromycin selection cassette after which eGFP expression was assessed by FACS. HEK 293T transduction was stable and following puromycin selection similar expression levels were obtained with the EF1 α promoter driven lentiviral vector as with the CMV promoter driven lentiviral vector. Both the percentage of eGFP⁺ cells and the total fluorescence remained stable in these cells over time (Figure 6A). In rOct4⁺ BM-HypoSCs higher expression levels were obtained using the EF1 α promoter driven lentiviral vector compared to transduction with the CMV promoter driven lentiviral vector. Furthermore, the percentage of eGFP⁺ cells and the total fluorescence remained more stable over time. FACS based cell sorting further increased the amount of eGFP⁺ cells (Figure 6B).

In addition to these cells, transduction of mOct4⁺ BM-HypoSCs was assessed in order to develop a syngeneic mouse model when combined with the GL261 glioblastoma mouse model. The transduction efficiency of these cells was acceptable and further increased by either puromycin selection or FACS based cell sorting. In both cases, expression levels remained stable for up to 25 days post transduction (Figure 6C). Finally, transduction of mMSC's was also assessed as Wolfs *et al* have shown that CMV promoter driven lentiviral vectors are unable to reach efficient transgene expression (personal communication). With the newly designed lentiviral vectors, the percentage of eGFP⁺ cells was initially rather low but increased significantly after puromycin selection. It remained stable for up to 40 days (Figure 6D). For an overview of the obtained FACS data we refer to table 5.

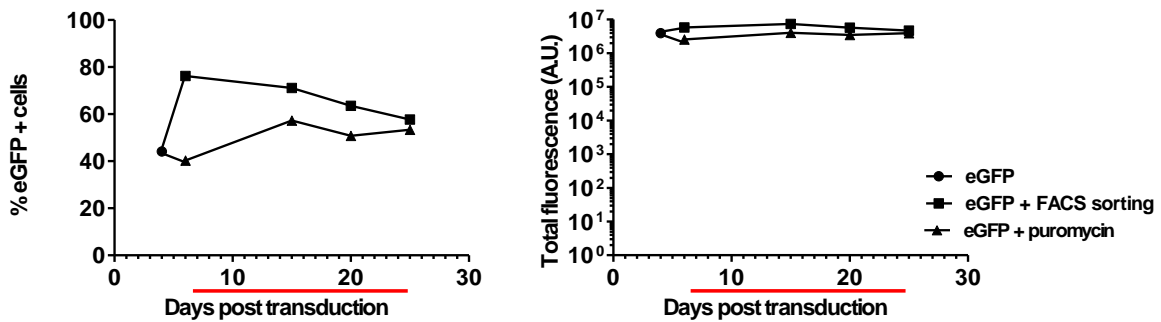
Figure 6: Transduction assessment using an EF1 α promoter driven lentiviral vector.

- A. FACS data of HEK 293T cells showed efficient transduction of the cells after selection using puromycin.
- B. FACS data of rOct4⁺ BM-HypoSCs showed increased transduction efficiency of the EF1 α promoter driven lentiviral vector compared to the CMV promoter driven lentiviral vector. The % of eGFP⁺ cells was further increased by puromycin selection
- C. FACS data of mOct4⁺ BM-HypoSCs showed similar transduction efficiency following puromycin selection and FACS based cell sorting.
- D. FACS data of mMSC's showed limited number of eGFP⁺ cells which increased substantially after puromycin selection.

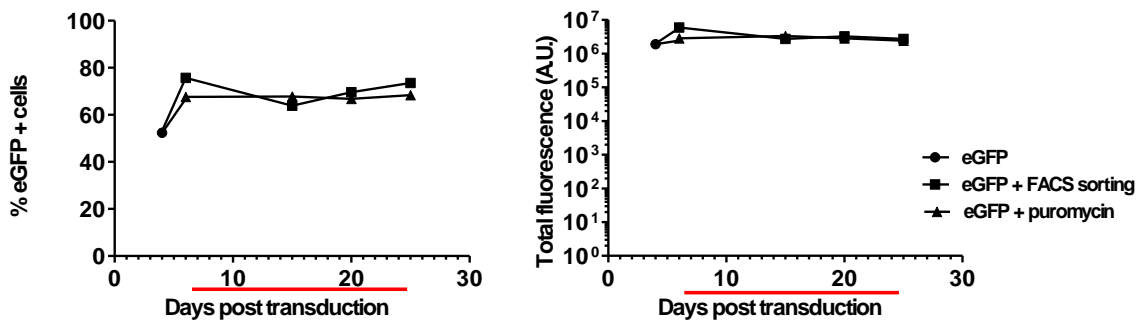
A.



B.



C.



D.

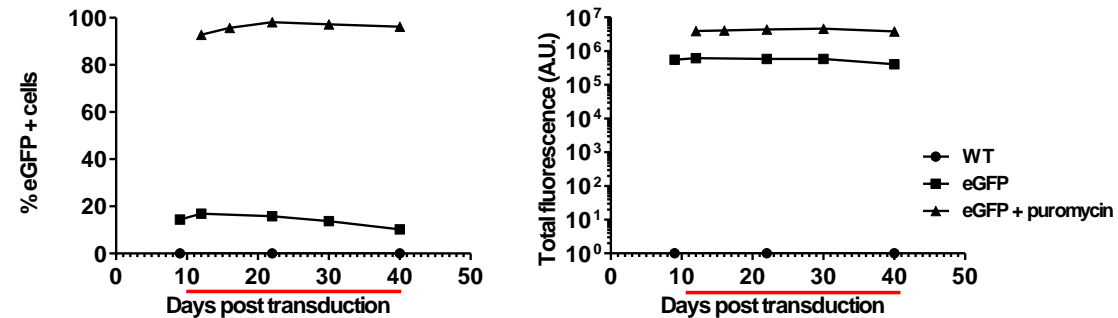


Table 5: FACS data after transduction of several cell lines using an EF1 α promoter driven lentiviral vector.

Cell line	Condition	% eGFP+ cells	Total fluorescence
293T	eGFP	34.1 \pm 2.6 %	1.6 x 10 ⁶ \pm 1.1 x 10 ⁵
	eGFP + puro	96.3 \pm 0.6%	5.7 x 10 ⁶ \pm 2.9 x 10 ⁵
rOct4 ⁺ BM-HypoSC	eGFP	44.1 %	3.9 x 10 ⁶
	eGFP + puro	50.5 \pm 3.6%	3.5 x 10 ⁶ \pm 3.4 x 10 ⁵
	eGFP + FACS sorting	67.1 \pm 4.1%	5.9 x 10 ⁶ \pm 5.6 x 10 ⁵
mOct4 ⁺ BM-HypoSC	eGFP	52.4%	1.9 x 10 ⁶
	eGFP + puro	67.7 \pm 0.3%	2.9 x 10 ⁶ \pm 1.9 x 10 ⁵
	eGFP + FACS sorting	70.7 \pm 2.6%	3.7 x 10 ⁶ \pm 7.7 x 10 ⁵
mMSC	eGFP	14.2 \pm 1.1%	5.5 x 10 ⁵ \pm 3.7 x 10 ⁴
	eGFP + puro	96.0 \pm 0.9 %	4.2 x 10 ⁶ \pm 1.5 x 10 ⁵

3.3.3 Evaluation of the transduction using lentiviral vectors encoding for eGFP, fLuc and HSV-TK

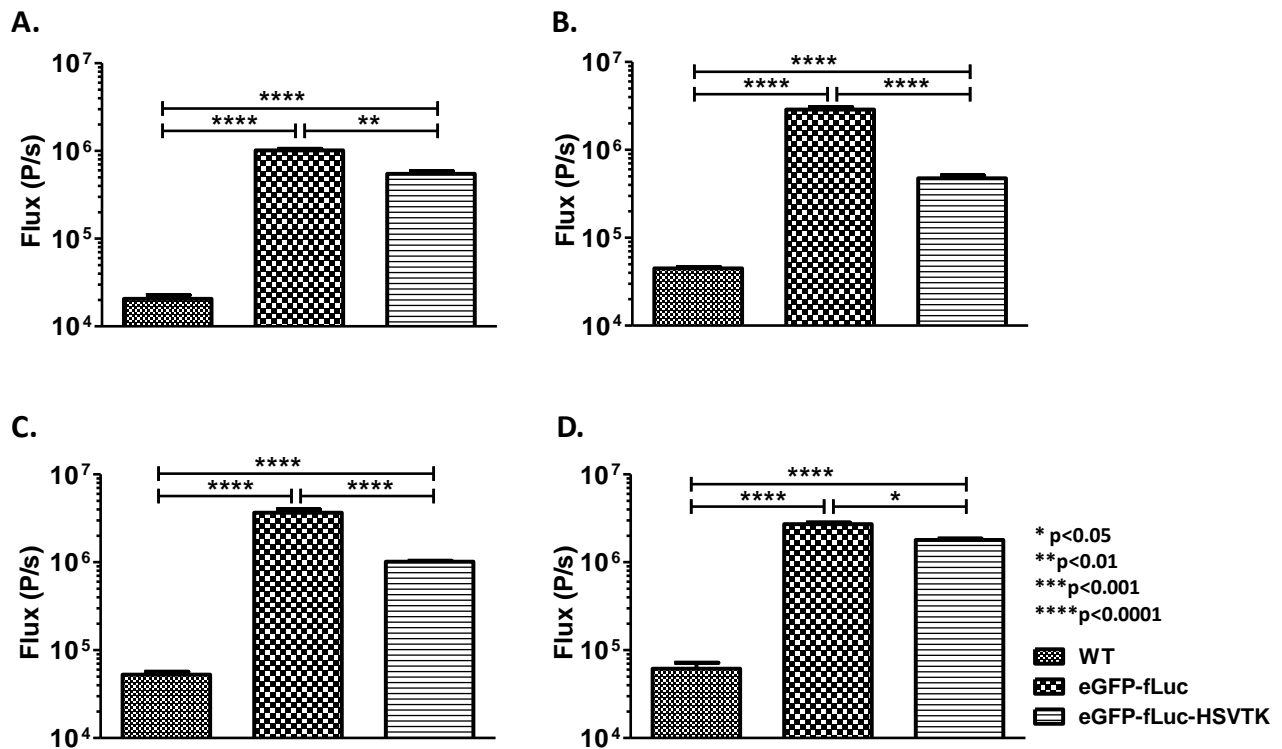
After simultaneous *in vivo* experiments (see chapter 4, 5), we chose to work with one mouse and two human glioma xenograft models. Therefore, three different mouse cell lines (mOct4⁺ BM-HypoSCs, mOct4⁻ BM-MAPCs and mMSC's) and one human cell line (hMultistem) were selected for assessment of suicide gene therapy in a mouse (GL261-Glioblastoma) and in two human glioma xenograft (Hs683-oligodendroglioma / U87-MG -glioblastoma) models.

For the mentioned stem cells, full transductions were subsequently performed, thus generating eGFP-fLuc or eGFP-fLuc-HSVTK positive cells, which were assessed for functional transgene (fLuc and HSV-TK) expression.

First, fLuc expression was assessed by BLI (Figure 7) which confirmed sufficient expression for *in vivo* validation of both the control vector (eGFP, fLuc) and the treatment vectors (eGFP, fLuc, HSV-TK).

Figure 7: Functional transgene expression: fLuc expression assessment using BLI.

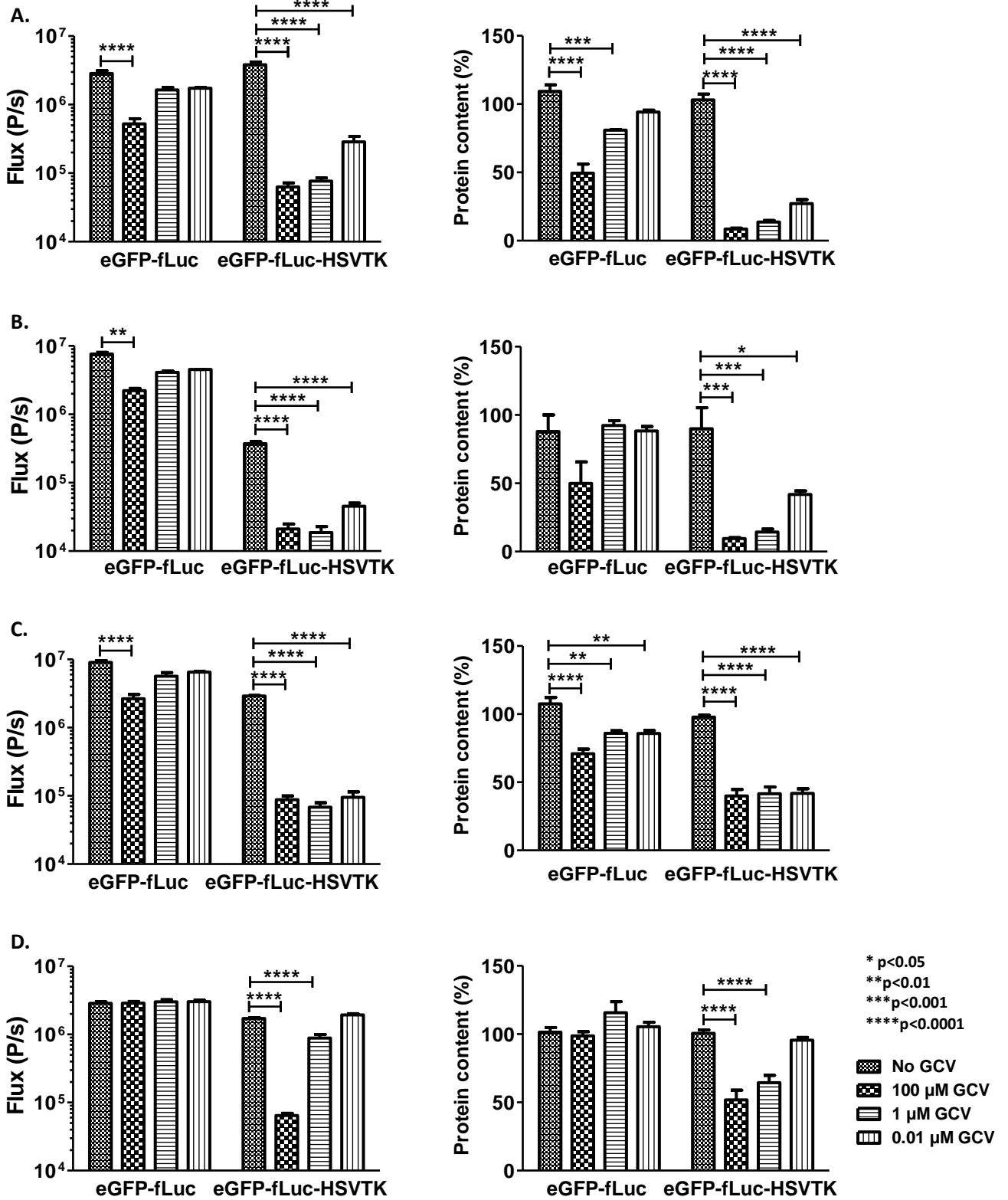
For all cell lines, fLuc expression was significantly different compared to WT cells for both eGFP-fLuc and eGFP-fLuc-HSVTK expressing cells although small differences were observed between eGFP-fLuc and eGFP-fLuc-HSVTK expressing cells. (A. mOct4⁺ BM-HypoSC, B. mOct4⁻ BM-MAPC, C. mMSC, D. hMultistem)



Subsequently, HSV-tk activity was assessed by a ganciclovir killing experiment, in which cells were subjected to different concentrations of GCV for four consecutive days after which BLI and a BCA protein assay were performed (Figure 8). BLI data showed that for all cell lines expressing eGFP and fLuc, a reduction in cell viability was only seen for the highest ganciclovir concentration which is probably due to cytotoxicity caused by GCV itself. Cells expressing eGFP, fLuc and HSV-TK however showed a dose-dependent cell killing even at concentrations as low as 0.01 μM of GCV. The BCA protein assay confirmed these results.

Figure 8: Functional transgene expression: HSV-TK expression assessment by using a GCV killing experiment.

BLI data (left) showed that for all cell lines expressing eGFP and fLuc, only a reduction in cell viability was seen for the highest ganciclovir concentration which is due to cell toxicity. Cells expressing eGFP, fLuc and HSV-TK however showed a dose-dependent cell killing with cell killing at concentrations as low as 0.01 μ M of GCV. The BCA protein assay (right) confirmed these results. (A. mOct4⁺ BM-HypoSC, B. mOct4⁺ BM-MAPC, C. mMSC, D. hMultistem)



3.3.4 Stem cell characterization and transduction related effects

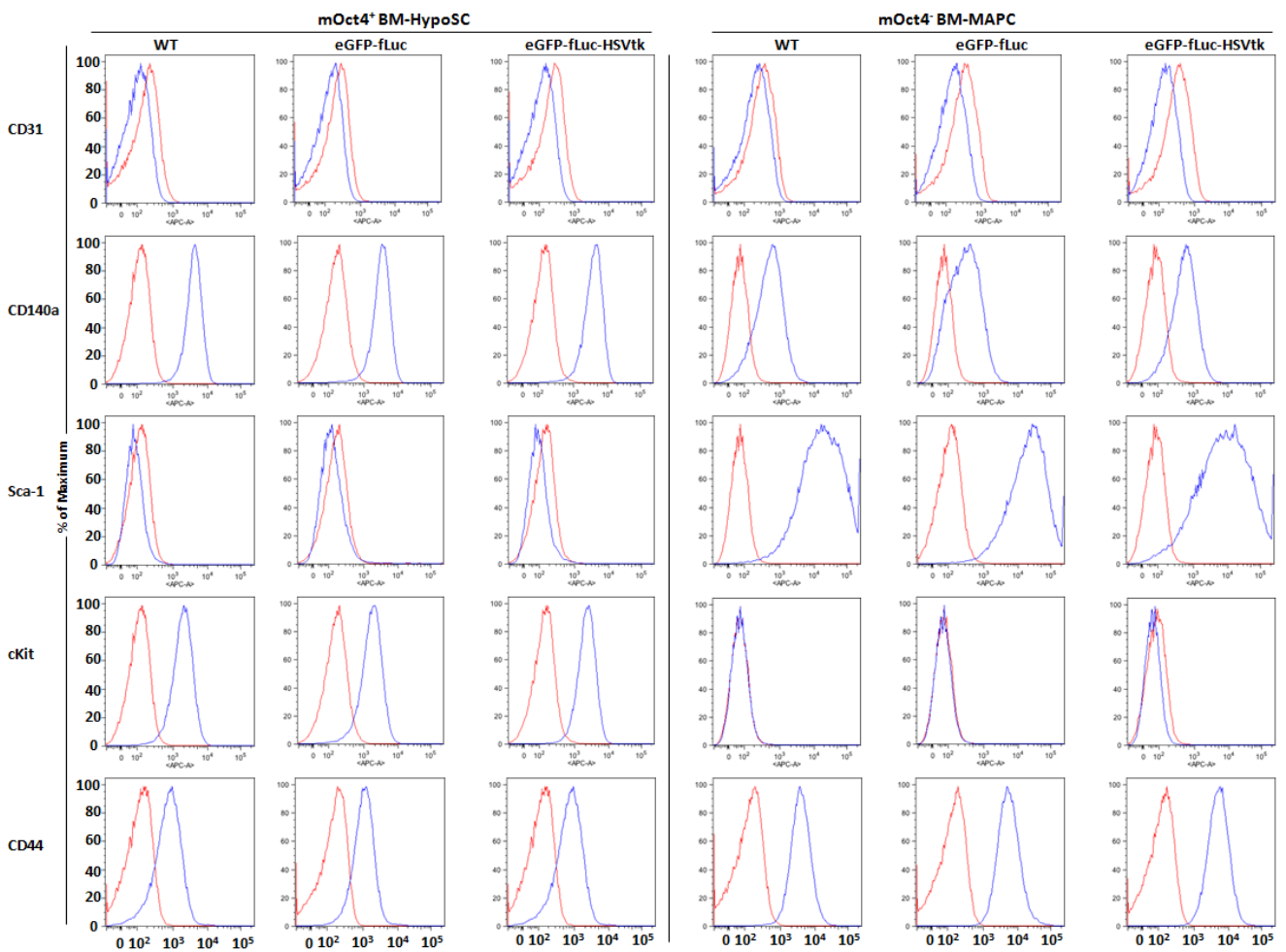
Stem cell characterization by flow cytometry showed that mOct4⁺ BM-HypoSCs were CD31, Sca-1 negative and CD140a, cKit, CD44 positive, whereas mOct4⁻ BM-MAPCs were CD31, cKit negative and CD140a, Sca-1, CD44 positive (Figure 9). For characterization of the rOct4⁺ BM-HypoSCs and rOct4⁻ BM-MAPCs, we refer to the work of Ulloa-Montoya *et al.*[132].

Figure 9: Cell-surface phenotype evaluated by flow cytometry

Left panel: Flow cytometry results for mOct4⁺ BM-HypoSCs.

Right panel: Flow cytometry results for mOct4⁻ BM-MAPCs.

From left to right are shown wt, eGFP-fLuc and eGFP-fLuc-HSVtk expressing cells. The histogram in each panel plots the number of cells (as a percentage of the maximum) on the vertical axis against the fluorescence intensity of the labeled antibody bound to the indicated protein (horizontal axis).



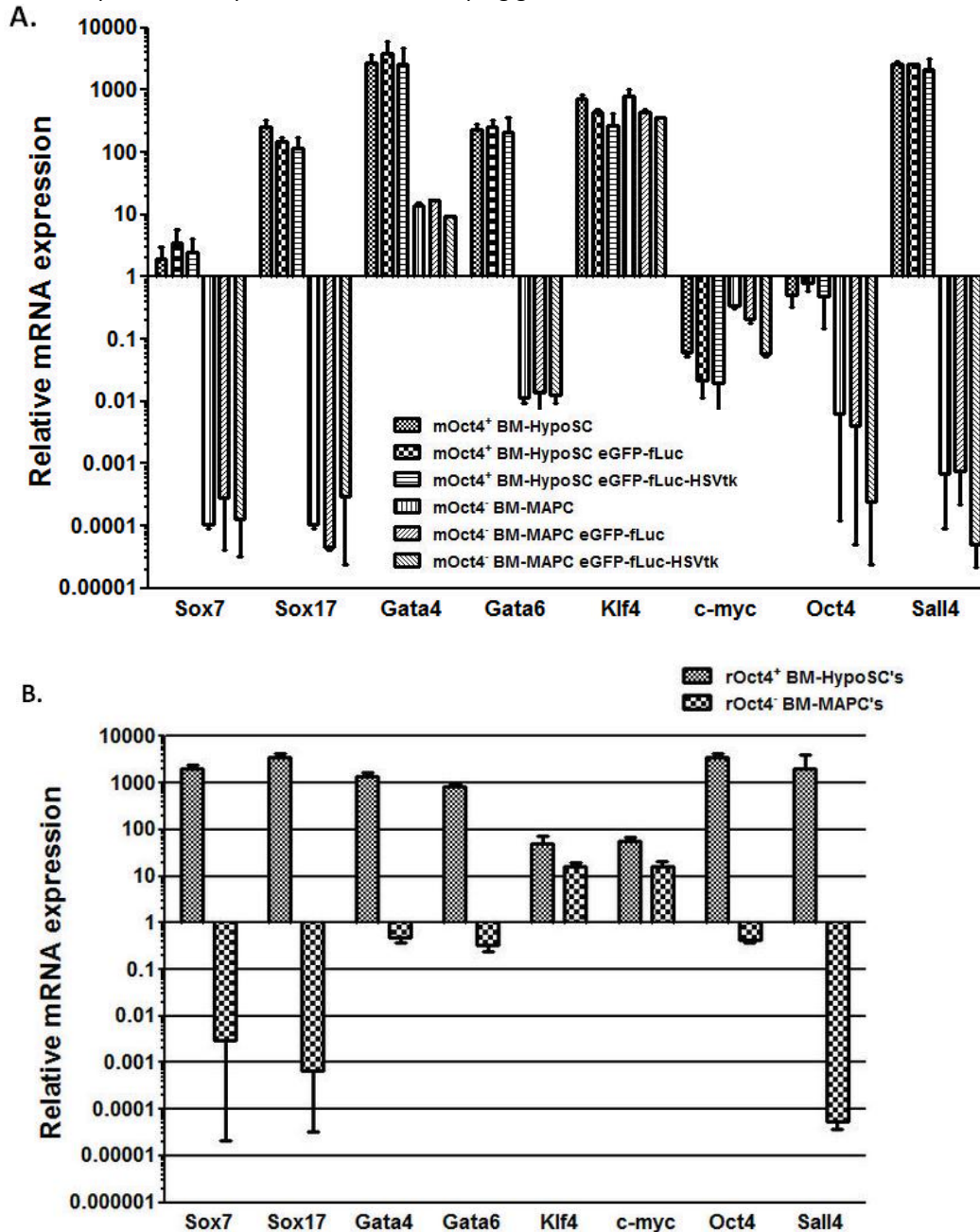
qRT-PCR (Figure 10) further showed a primitive endoderm gene expression pattern including high expression of Gata4, Gata6, Sox7 and Sox17 for mOct4⁺ BM-HypoSCs whereas mOct4⁻ BM-MAPCs showed very low expression of Gata4, Gata6, Sox7 and Sox17. Both cell lines were positive for c-Myc and Klf4. Oct4 and Sall4 were however expressed in mOct4⁺ BM-HypoSCs but not in mOct4⁻ BM-MAPCs. For rat cells, a similar pattern was observed with primitive endoderm gene expression in rOct4⁺ BM-HypoSCs but not in rOct4⁻ BM-MAPCs. Both cell lines expressed c-Myc and Klf4 but rOct4⁺ BM-HypoSCs expressed Oct4 and Sall4 whereas rOct4⁻ BM-MAPCs did not. Subsequently, the effect of transduction on stem cell characteristics, such as gene and cell surface marker expression was assessed using qRT-PCR and flow cytometry. Results indicate no pronounced differences in gene or cell surface marker expression between transduced and untransduced cells, neither for mOct4⁺ BM-HypoSCs nor for mOct4⁻ BM-MAPCs. Karyotyping revealed cytogenetic abnormalities in both rat and mouse cell lines, but this was not related to tumor growth or transduction status as wild-type lines also showed abnormalities. It is a well known phenomenon that long-term culture of bone marrow-derived stem cells (especially murine cells) induces chromosomal instability [142].

Supplementary Table 1: Overview of qRT-PCR primers.

Target Gene	Species	Forward (5'-3')	Reverse(5'-3')
GAPDH	Mouse/rat	AAGGGCTCATGACCACAGTC	GGATGCAGGGATGATGTTCT
Klf4	Rat	CAGGCTGTGGCAAAACCTAT	CGGTAGTGCCTGGTCAGTTC
c-myc	Rat	CTGACCCAACATCAGCGGTC	TGACTGTCCGGTTTTCCACCT
Oct4	Rat	CTGTAACCGGCGCCAGAA	TGCATGGGAGAGCCAGAA
Sox7	Rat	CAAGGATGAGAGGAAACGTC	CTCTGCCTCATCCACATAGG
Sox17	Rat	TGAGCAAGATGCTAGGCAAA	TAGTTGGGATGGTCTGCAT
Gata4	Rat	CTGTGCCAACTGCCAGACTA	AGATTCTGGGCTTCGTTT
Gata6	Rat	GTAAGATGAACGGCCTCAGC	GGTTGTGGTGTGACAGTTGG
Sall4	Rat	AGGAATTGGTGGCGGAGAAG	GAATCACTGGAACCCGGG
Klf4	Mouse	TGTGTCGGAGGAAGAGGAAGC	ACGACTCACCAAGCACCATCA
c-myc	Mouse	TGACCTAACTCGAGGAGGAGCTGGAATC	AAGTTTGAGGCAGTTAAAATTATGGCTGAAGC
Oct4	Mouse	CCAATCAGCTTGGGCTAGAG	CCTGGGAAAGGTGTCCTGTGA
Sox7	Mouse	TGTTGACAGATCCCCAAGAA	CTGGGCACCAGTCAATTACA
Sox17	Mouse	CACAACGCAGAGCTAAGCAA	TTGTAGTTGGGTTGGTCTCTG
Gata4	Mouse	TCTCACTATGGGCACAGCAG	GCGATGTCTGAGTGACAGGA
Gata6	Mouse	GCCAACTGTCACACCACAAC	TGTTACCGGAGCAAGCTTTT
Sall4	Mouse	AGAACTTCTCGTCTGCCAGTG	CTCTATGGCCAGTCTCCTTC

Figure 10: q-RT-PCR analysis

- A. qRT-PCR analysis for the expression of Sox7, Sox17, Gata 4, Gata6, Oct4, Sall4, Klf4 and c-Myc in mOct4⁺ BM-HypoSCs and mOct4⁻ BM-MAPCs showed a primitive endoderm gene expression pattern for mOct4⁺ BM-HypoSCs, including Gata4, Gata6, Sox7 and Sox 17 expression whereas mOct4⁻ BM-MAPCs showed very low expression of Gata4, Gata6, Sox7 and Sox17. Both cell lines were positive for c-Myc and Klf4. Oct4 and Sall4 were however expressed in mOct4⁺ BM-HypoSCs but not in mOct4⁻ BM-MAPCs. No profound alterations in gene expression could be detected following transduction for both mOct4⁺ BM-HypoSCs and mOct4⁻ BM-MAPCs. Relative mRNA expression compared to the housekeeping gene GAPDH is shown.
- B. qRT-PCR analysis for the expression of Sox7, Sox17, Gata 4, Gata6, Oct4, Sall4, Klf4 and c-Myc in rOct4⁺ BM-HypoSCs and rOct4⁻ BM-MAPCs showed also a primitive endoderm gene expression pattern for rOct4⁺ BM-HypoSCs, but not for rOct4⁻ BM-MAPCs. Both cell lines expressed c-Myc and Klf4 but rOct4⁺ BM-HypoSCs expressed Oct4 and Sall4 whereas rOct4⁻ BM-MAPCs did not. No profound alterations in gene expression could be detected following transduction for both mOct4⁺ BM-HypoSCs and mOct4⁻ BM-MAPCs. Relative mRNA expression compared to the housekeeping gene GAPDH is shown.



3.3.5 Labeling stem cells with SPIO's

As the previous results indicated that the stem cells are adequately transduced for *in vivo* validation, stem cells were subsequently labeled using in house fabricated superparamagnetic iron oxide particles (SMG²-mPEGSi) [143] for *in vitro* assessment of cell tracking by MRI.

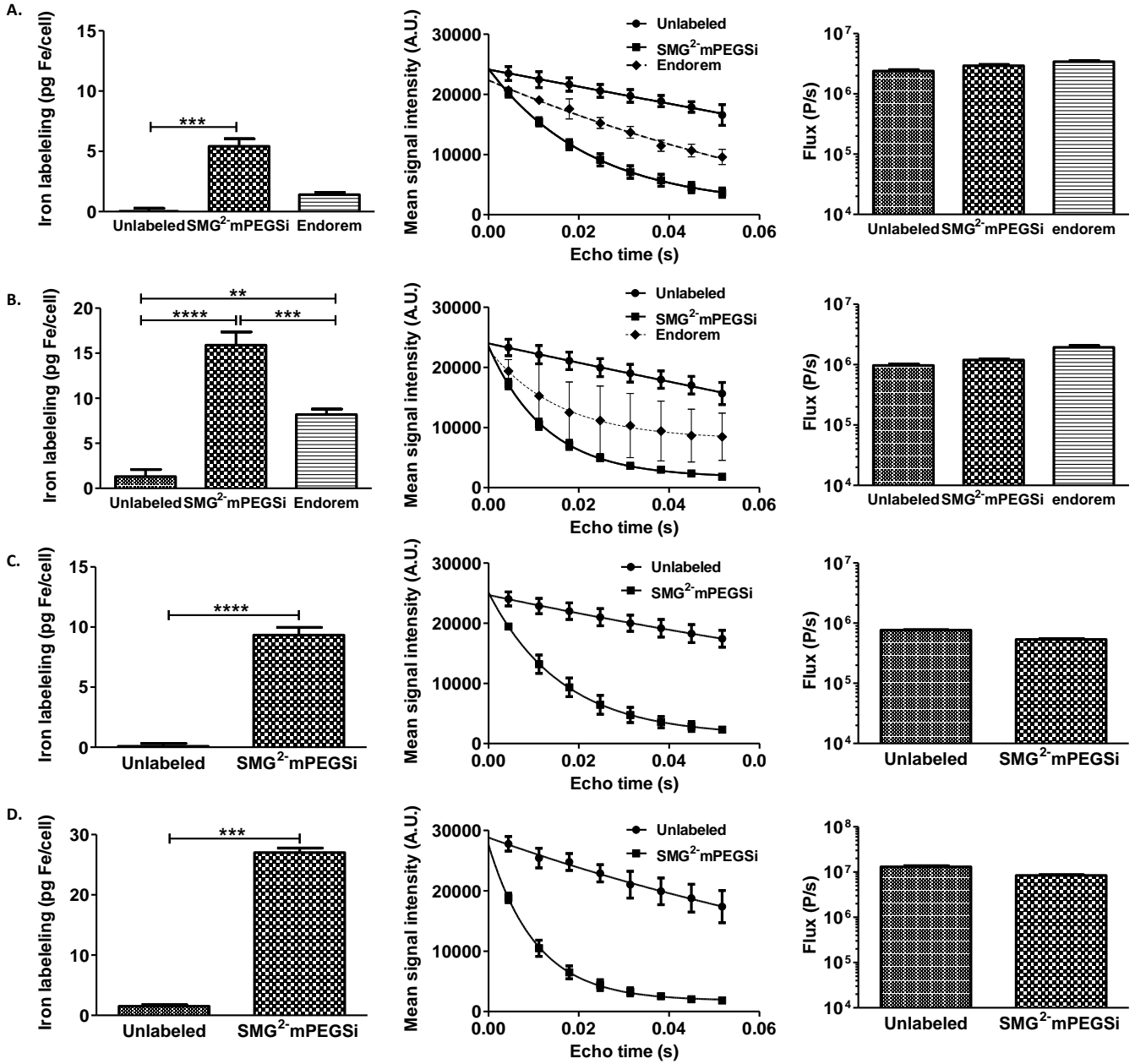
eGFP-fLuc-HSVTK expressing stem cells (mMSC's, mOct4⁻ BM-MAPCs, mOct4⁺ BM-HypoSCs, and hMultistem's) were labeled with SMG²-mPEGSi particles after which ICP-OES (left), an MRI of a cell containing phantom (middle) and BLI (right) were performed to assess labeling efficiency and stem cell viability (Figure 11). For mMSC's (Figure 11A), ICP-OES showed an iron uptake of 5.4 ± 0.6 pg iron/cell for SMG²-mPEGSi and 1.4 ± 0.2 pg iron/cell for Endorem[®] labeled cells. An MRI phantom showed contrast generation of SMG²-mPEGSi labeled cells while no marked differences in cell viability were observed between labeled and unlabeled cells as assessed by BLI. Similar results were obtained for mOct4⁻ BM-MAPCs, mOct4⁺ BM-HypoSCs, and hMultistem's, although the amount of iron / cell varied between different cell types. mOct4⁻ BM-MAPCs, mOct4⁺ BM-HypoSCs, and hMultistem's contained 15.9 ± 1.5 pg iron/cell, 9.3 ± 0.6 pg iron/cell and 27.0 ± 0.7 pg iron/cell, respectively, without significant differences in cell viability as assessed by BLI. Differences in the amount of iron / cell were represented in the contrast generation in the corresponding MRI phantoms, with higher amounts of iron generating a rapid and more profound hypointense contrast.

In conclusion, an adequate cell labeling was confirmed by ICP-OES and MRI of phantoms with no or very little effect on stem cell viability for all cell lines. Furthermore, mMSC's and mOct4⁻ BM-MAPCs were also labeled with Endorem[®] as a reference compound. These experiments indicate that the SMG²-mPEGSi particles displayed superior labeling characteristics.

Figure 11: *In vitro* assessment of stem cells labeling using SMG²-mPEGSi.

Left column contains ICP-OES acquired iron content per cell, middle column contains MRI acquired relaxation information and right column contains BLI acquired stem cell viability information.

ICP-OES (left) and MRI phantoms (middle) showed efficient stem cell labeling using SMG²-mPEGSi particles without significant effects on stem cell viability for mMSC's (A), mOct4⁻ BM-MAPCs (B), mOct4⁺ BM-HypoSCs (C) and hMultistem's (D). For mMSC's and mOct4⁻ BM-MAPCs Endorem[®] labeled stem cells were used as a reference.

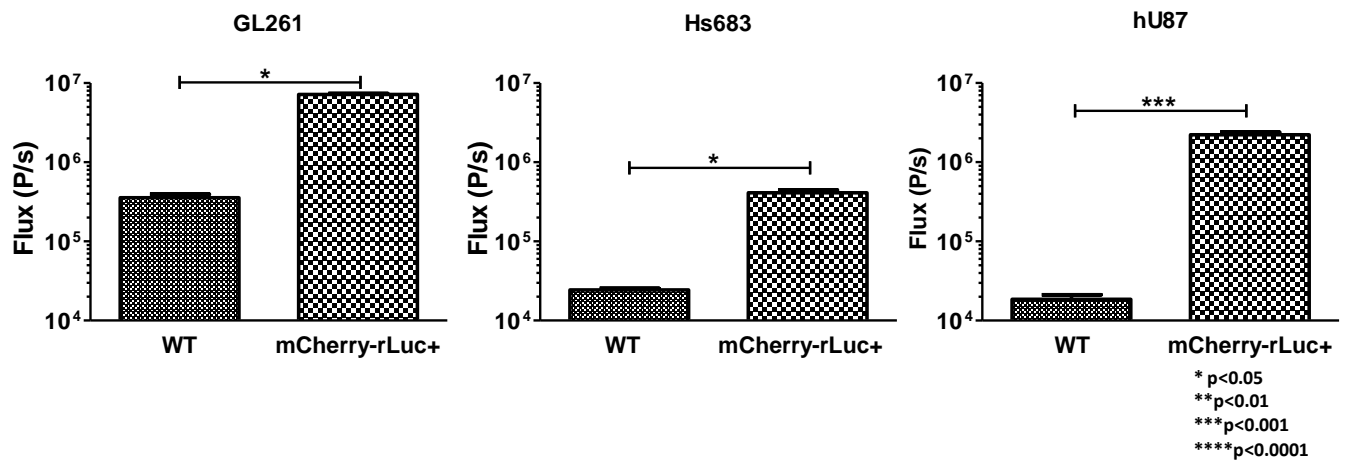


3.3.6 Transduction of glioma cells using a CMV promoter driven lentiviral vector encoding for mCherry and rLuc

Finally, also tumor cells were transduced with a lentiviral vector encoding for mCherry, rLuc and a blasticidin selection cassette of which the expression was driven by a CMV promoter in order to follow tumor viability *in vivo*. As mentioned earlier, one mouse (GL261-glioblastoma) and two human glioma xenograft (Hs683-oligodendroglioma / U87-MG -glioblastoma) models were selected. mCherry expression was used in order to visually confirm transduction by fluorescence microscopy. All three models showed rLuc expression *in vitro* when assessed by BLI using coelenterazin-h as a substrate (Figure 12).

Figure 12: rLuc expression evaluation using BLI.

All tumor cell lines (GL261, Hs683, U87-MG) showed rLuc expression when Coelenterazin-h was provided as a substrate.



3.4 Discussion

Due to their self-renewal, migration and differentiation capacity, stem cells are increasingly regarded as candidates in regenerative medicine or as cellular vehicles to deliver therapeutic molecules. Although pluripotent stem cells hold the greatest potential, their ability to form teratomas also hampers their clinical use [144]. Multipotent stem cells are more restricted in their differentiation potential and therefore less likely to form teratomas, although mass formation has been reported [145]. It is therefore crucial that the fate of stem cells is followed longitudinally *in vivo* to assess possible safety issues but also to monitor the therapeutic response. For this purpose, we have developed eGFP-fLuc and eGFP-fLuc-HSVTK+ stem cells, which were subsequently labeled with SPIO's in order to track them longitudinally *in vivo* with MRI and BLI while using them as cellular vehicles to carry the suicide gene (HSV-TK), to the tumor site. These cells were subsequently used to investigate suicide gene therapy for malignant gliomas. Transduction and labeling of cells has been applied previously in order to follow-up on cell behavior [146-148]. For instance Wolfs *et al.* showed that expression of the human sodium iodide symporter (hNIS) can be used to assess stem cells *in vivo* by using PET [148]. The low spatial resolution and the hardware (e.g. a cyclotron) required for production of radioactive tracers however means that application of PET is more cost and labor intensive compared to BLI.

Lentiviral vectors were used to obtain stable gene expression in stem cells. Lentiviral vectors driven by the most commonly used promoter, namely the cytomegalovirus (CMV) promoter resulted in stable gene expression levels in 293T cells but not in rOct4⁺ BM-HypoSCs which is concurrent with the observation that the CMV promoter is less suitable for stable stem cell transduction [149]. Wang *et al* showed that the human elongation factor 1 alpha (EF1 α) is better suited for stable gene transduction in stem cells [149]. Therefore, a lentiviral vector encoding for eGFP and a puromycin resistance cassette was used to transduce not only HEK 293T cells and rOct4⁺ BM-HypoSCs but also mOct4⁺ BM-HypoSCs and mMSC's. All cell lines showed efficient gene expression following puromycin selection when using the EF1 α promoter driven lentiviral vector. Furthermore, qRT-PCR and flow cytometry showed that transduction of mOct4⁺ BM-HypoSCs and for mOct4⁺ BM-MAPCs, did not result in genetic (Sox7, Sox17, Gata6, Gata4, Oct4, Sall4, Klf4 and c-myc) or cell surface

marker (CD31, CD140a, Sca-1, cKit and CD44) aberrations compared to WT cells. EF1 α promoter driven lentiviral vectors encoding for eGFP and fLuc or eGFP, fLuc and HSV-TK were assessed for functional gene expression in mOct4⁺ BM-HypoSCs, mOct4⁻ BM-MAPCs and mMSC's for glioma models in mice and in hMultistem's for human glioma xenograft models. In all cell lines expressing eGFP, fLuc and HSV-TK a dose dependant stem cell killing was observed both in BLI signal (cell viability) and a BCA protein assay (protein content) after GCV administration. This was not the case for cells that only expressed eGFP and fLuc, although some cell toxicity was observed with high concentrations of GCV which is concurrent with data published by Li *et al* [84]. Subsequently, eGFP-fLuc-HSVTK + mOct4⁺ BM-HypoSCs, mOct4⁻ BM-MAPCs, mMSC's and hMultistem's were labeled for MR imaging using in house fabricated SPIO's. Efficient cell labeling was confirmed using MRI phantoms and ICP-OES. Furthermore, stem cell viability was checked with BLI using D-luciferine as a substrate.

As such, we have shown that several different stem cells can be detected *in vitro* by MRI and BLI and therefore, *in vivo* assessment of stem cell localization prior to treatment initiation and stem cell viability follow-up can be commenced. In regard to suicide gene therapy, it is however also useful to investigate tumor viability following suicide gene therapy as tumor size alone might not be the most efficient readout for rapid validation of therapy. Therefore, three different tumor cell lines, namely GL261, Hs683 and U87-MG were also transduced using a CMV promoter driven lentiviral vector encoding for mCherry and rLuc in order to follow-up tumor cell viability. All three cell lines showed *in vitro* rLuc expression when BLI was performed using coelenterazin-h as a substrate.

These results indicate that subsequent *in vivo* assessment of both stem cells and tumor cell lines can be commenced.

Chapter 3:
Generation & validation of cell lines for non-invasive imaging of suicide gene therapy

CHAPTER 4

***In vivo* validation of cell lines for non-invasive imaging of suicide gene therapy**

Chapter 4:

In vivo validation of cell lines for non-invasive imaging of suicide gene therapy

Chapter 4:

***In vivo* validation of cell lines for non-invasive imaging of suicide gene therapy**

This chapter has been compiled based on the following publications:

Leten C., et al., *In vivo and ex vivo assessment of the blood brain barrier integrity in different glioblastoma animal models*. J Neurooncol, 2014.

Leten C., et al. Controlling and monitoring stem cell safety in vivo in an experimental rodent model. Stem cell, 2014.

Leten C., et al., Assessment of bystander killing mediated therapy of malignant brain tumors using a multimodal imaging approach. (Submitted to Stem cell research & therapy)

4.1 Introduction

Gliomas arise from the glial cells (astrocytes, oligodendroglial and ependymal cells) and are the most common brain tumors in humans. They comprise a broad range of lesions with distinct differences in malignancy, which is assessed according to the World Health Organization classification. Glioblastoma multiforme (GBM) is the most malignant glioma of the spectrum (WHO grade IV) [1]. The prognosis of patients diagnosed with GBM is still extremely poor with a 5-year survival of less than 3% despite a multimodal treatment approach consisting of surgery and concomitant radio- and chemotherapy[3]. Therefore, new treatment modalities are under investigation, among which therapy based on the bystander killing effect following suicide gene therapy [84, 150-152].

This therapeutic approach relies on administration of cells carrying a suicide gene, such as the gene encoding for the Herpes Simplex virus-thymidine kinase (HSV-TK). When the substrate for this enzyme, for instance ganciclovir (GCV) is provided, it enters the cell and is converted by HSV-TK into GCV-monophosphate. The HSV-tk displays a 1000 fold higher affinity for GCV than the mammalian thymidine kinase [152] and therefore this targeting approach limits systemic toxicity while the increased affinity boosts tumor therapy capabilities [152]. Subsequently, cellular kinases recognize the GCV-monophosphate and will create GCV-triphosphate, a guanine nucleoside analogue which causes DNA chain termination and subsequent cell death. Due to the formation of gap junctions between adjacent cells, ganciclovir monophosphate can passively diffuse into neighboring cells which will result in mostly tumor and therapeutic cell killing as normal

adult brain cells usually do not replicate. Thus, both tumor and therapeutic cells can be killed. This is also known as 'the bystander killing effect

When using stem cells that can track infiltrating tumor cells, this method can in theory be applied to remove not only the main tumor, but also destroy any remaining tumor cells, thus eliminating sources of possible recurrent tumors [152]. The feasibility of this strategy was demonstrated by several groups in both xenograft and syngeneic animal models. Miletic *et al.* [152] and Matuskova *et al.* [85] demonstrated a potent bystander killing effect of rMAPCs on 9L rat gliomas and hMSC's on the human glioblastoma cell lines 8-MG-BA, 42-MG-BA and U-118 MG respectively.

However suitable some stem cells might be, there is also a potential safety risk associated with stem cell therapies as the transplanted cells have the ability to proliferate longitudinally and can differentiate into several cell types of which some can result in unwanted side effects. Well known examples of this are embryonic stem cells (ESC) [153] and induced pluripotent stem cells (iPSC) which can form teratomas [125], hampering applications of those cells *in vivo* [90]. Lo Nigro *et al* recently demonstrated that rat bone marrow (BM) derived cells, expressing high levels of Oct4, generated *in vitro*, so called Hypoblast-like stem cells (BM-HypoSC) [145], share characteristics with blastocyst derived HypoSC including high levels of Oct4 expression as well as a compliment of primitive endoderm genes [133]. Other rodent cell lines [132] isolated under the identical condition as the Oct4⁺ cells (MAPC conditions), however do not express high levels of Oct4 and do not have the primitive endoderm gene signature (Oct4⁻ BM-MAPCs). To better illustrate this difference, the cells with high Oct4 expression are called BM-HypoSCs and the ones with no Oct4 expression MAPCs throughout the manuscript. Likewise, human Oct4^{low/no} MAPCs, currently used for clinical trials under the name Multistem, also do not express high levels of Oct4 nor do they display the endodermal gene signature. High levels of Oct4 in rat rOct4⁺ BM-HypoSCs [145] and mouse mOct4⁺ BM-HypoSCs (unpublished data) appear to be responsible for the formation of yolk-sac tumors when injected in animals while none of the ^{low/no} level Oct4 rodent or human MAPCs have generated yolk sac like tumors [154] as shown by transplantation of the cells under the kidney capsule or as xenografts.

Unfavorable safety profiles can hamper the application of stem cells, which might be otherwise very well suited for particular applications *in vivo*, for example the ability of stem cells to track infiltrating tumor cells and erase them by the expression of suicide genes [84, 150, 151]. Therefore, safety studies were performed using r and mOct4⁺ BM-HypoSCs, r and mOct4⁻ BM-MAPCs and mMSC's to assess possible tumor formation in the brain of syngeneic C57BL6/J mice.

In a clinical setting, patients are routinely followed up by non-invasive imaging such as magnetic resonance imaging (MRI). In a preclinical setting, these non-invasive imaging techniques are also available and should therefore, when possible, also be used to evaluate stem cell viability and treatment response. Therefore, stem cells expressing eGFP and fLuc or eGFP, fLuc and the HSV-TK suicide gene and labeled using in house fabricated SPIO's that were assessed previously *in vitro* (Chapter 3) were validated *in vivo* for multi-modal imaging follow-up. Thus, the HSV-TK gene can be used as a suicide gene for bystander mediated cell killing in tumor treatment but also as a safety switch for tumor forming stem cells.

Furthermore, animal models for glioblastoma were developed. These included one mouse glioblastoma model (GL261) in syngeneic C57BL6/j mice and two malignant glioma models (Hs683: oligodendroglioma / U87-MG: glioblastoma) in an immunodeficient Hsd:athymic Nude-Foxn1^{nu} mice. The GL261 model, a syngeneic model in a syngeneic (immunocompetent) host, has been characterized extensively [106, 155, 156] and is widely considered as the gold standard in glioblastoma research. The U87-MG and Hs683 models have been well described also and are often used as human glioma xenograft models [157, 158]. Subsequently, multi-modal imaging of suicide gene therapy for glioblastoma using stem cells as cellular vehicles was assessed using MRI, BLI and PET.

4.2 Materials & methods

Cell lines

Cells were cultured as described previously (Chapter 3).

Animals

All animal experiments were conducted according to the European Union Community Council guidelines and were approved by the local ethics committee of KU Leuven. C57BL6/j mice and Fisher 344 rats were used for experiments which required a syngeneic host whereas Hsd:athymic Nude-Foxn1^{nu} mice were used for the optimization of the human glioma xenograft models.

Stereotactic injection

For surgery, animals were anaesthetized by an *i.p.* injection with a mixture of Ketamine (Ceva, Pompidou, France) (mice: 4.5mg/kg; rats: 30 mg/kg) / medetomidin (Domitor®, Pfizer, New York, USA) (mice: 0.6 mg/kg, rats: 0.2 mg/kg). Local analgesia (2% xylocain, AstraZeneca, London, UK) and antibiotics (6mg/mouse, Ampiveto-20 (200mg/ml), VMD, New Haw, Surrey, UK) were administered prior to surgery. After fixation of the animals in a stereotactic frame adapted with a Quintessential stereotaxic injector (All from Stoelting, Wood Dale USA), cells were injected with a 10 µl Hamilton (total volume 5µl, infusion rate: 0.5 µl/min) syringe, equipped with a 22 G needle, into the right striatum of C57BL6/j mice or Fisher rats respectively. Coordinates for mice were 0.5 mm anterior and 2.0 mm lateral to bregma and 3.0 mm from the dura for mice. For rats, injection coordinates were 2.8 mm lateral to bregma and 5.5 mm from the dura. 2.5×10^5 or 5×10^5 stem cells were injected for *in vivo* proliferation experiments or ganciclovir killing experiments, respectively. Cell numbers were chosen based on previous experiments for stem cell therapy in the rat brain [152] and considerations regarding the cell yield.

In vivo proliferation experiment

2.5×10^5 m/rOct4⁺ BM-HypoSCs, m/rOct4⁻ BM-MAPCs, mMSC's or hMultistem's suspended in 5 µl PBS were injected stereotactically into the striatum, using the same device and coordinates as previously described, of C57BL6/J mice or Fisher rats. Animals were followed using MRI to assess possible tumor development.

In vivo ganciclovir treatment experiment

A total of 5×10^5 eGFP-fLuc-HSV-tk positive mOct4⁺ BM-HypoSCs, mOct4⁻ BM-MAPCs, mMSC's or hMultistem's suspended in 5µl PBS were injected stereotactically in the striatum of C57BL6/j mice, using the same device and coordinates as previously described,. The following day, MRI and BLI were performed to ascertain the site of injection and the cell viability after which, PBS or GCV (50mg / kg, intraperitoneally) was administered for 14 consecutive days. mOct4⁻ BM-MAPC (PBS: N = 2, GCV: N = 2), mMSC (PBS: N = 2, GCV: N = 2) and hMultistem (PBS: N = 3, GCV: N = 3) injected animals were sacrificed following MRI and BLI at the end of treatment (d15). Of the mOct4⁺ BM-HypoSC injected animals (PBS: N = 5, GCV: N = 5), three animals from the GCV treated group were followed up for 12 weeks by MRI and BLI to check for tumor regrowth.

In vivo validation of SPIO labeling of stem cells for MRI tracking

For each cell line (mMSC, mOct4⁻ BM-MAPCs), a similar approach was used. Four C57BL6/j mice were stereotactically injected with the following in opposing hemispheres: mouse 1: PBS and 3×10^5 unlabeled stem cells, mouse 2: 1×10^5 and 3×10^5 Endorem® labeled stem cells, mouse 3: 1×10^5 SMG²-mPEGSi labeled stem cells, mouse 4: 3×10^5 SMG²-mPEGSi labeled stem cells such that for each condition N = 2).

In vivo validation of mCherry rLuc transduction of malignant glioma cells

2.5×10^5 GL261, 5×10^4 Hs683 or 3×10^5 U87-MG cells (mCherry-rLuc +) were injected stereotactically into the striatum of C57BL6/j or Hsd:athymic Nude-Foxn1^{nu} mice brain as described previously and followed up once a week using MRI and BLI using coelenterazin-h (Rediject Coelenterazin-h, Perkin-Elmer, 15µg / animal, *i.v.*) as a substrate for rLuc. Subsequently, animals were sacrificed, 1 mm brain slices were cut and *ex vivo* BLI scans were taken for one representative mCherry-rLuc + GL261 and one Hs683 tumor bearing animal (one drop of Rediject Coelenterazin-h/slice, Perkin-Elmer).

Imaging:Magnetic resonance imaging (MRI)

All MR images were acquired with a 9.4T Biospec small animal MR scanner (Bruker Biospin, Ettlingen, Germany) equipped with a horizontal bore magnet and an actively shielded gradient set of 600mT m^{-1} (117 mm inner diameter) using a 7 cm linearly polarized resonator for transmission and an actively decoupled dedicated mouse or rat surface coil for receiving (Rapid Biomedical, Rimpar, Germany). MRI was performed once per week to assess the proliferation potential *in vivo*. Prior to scanning, mice and rats were anaesthetized with 2% or 4% isoflurane for induction and 1.5% or 2% isoflurane for maintenance, respectively. Temperature and respiration were monitored throughout the experiment and maintained at 37°C and 100-120 breaths / minute for mice and 70-90 breaths / minute for rats, respectively.

T2 weighted (rapid acquisition with refocused echoes (RARE) sequence, repetition time (TR):3157.6 ms; echo time (TE):48.8 ms; matrix size: 256×256 , FOV: 2.5×2.5 cm, in plane resolution: $78 \mu\text{m}^2$, number of continuous slices 24 / 12 in mouse/rat, slice thickness 0.5mm, slice orientation: axial) and T2 weighted (RARE sequence, TR: 3000ms, TE: 50.2ms, matrix size: 256×256 , FOV: 2×2 cm, number of slices: 16 / 9 in mouse/rat, slice thickness: 0.5mm, interslice distance: 0.5mm in rat, slice orientation: coronal, in plane resolution: $78 \mu\text{m}^2$) MRI scans were acquired to establish graft sizes. The area of the graft was determined by delineating it manually on all slices of the T2 weighted coronal MR images using the 5.1 Paravision software (Bruker, Biospin). The mean of the cross sectional area was used to determine the total graft volume. An ANOVA test (GraphPad PRISM, GraphPad Software, La Jolla, CA, USA) was used to determine significant differences with $p < 0.05$. In case of tumor formation, further characterizations were performed using T2 maps (multi slice multi echo (MSME) experiments, TR: 2000ms, TE increments: 10.1ms, 16 echo's, number of slices: 8, slice thickness: 0.4mm, slice thickness: 0.6 mm, matrix size: 200×200 , in plane resolution: $100 \mu\text{m}^2$) and diffusion weighted MRI (echo planar imaging (EPI) with spin echo read out, TR: 300ms, TE: 25.4ms, B-values: 250, 500, 1000, 1400 s/mm^2 , matrix size: 96, FOV: 2×2 cm, number of slices: 8, in plane resolution: $208 \mu\text{m}^2$). For quantification, regions of interest (ROIs) were defined by placing a ROI over the tumor area followed by placing a ROI of identical size on the striatum (the site of cell engraftment) of the contralateral hemisphere. Subsequently, T2- and ADC maps were generated and T2 and ADC values were extrapolated for analysis using the Paravision 5.1. software. To validate the integrity of the blood brain barrier, pre- and post-contrast (gadolinium (Dotarem®), Guerbet, Villepinte, France, dosage: $100 \mu\text{l}$ / mouse of 0.05 mmol/ml, *i.v.*) T1 weighted MR images were acquired (RARE sequence, RARE factor: 4, TR: 819ms, TE: 7.6ms, matrix size: 256×256 , FOV: 2×2 cm, number of continuous slices: 20, slice thickness: 0.5mm, slice orientation: axial, in plane resolution: $78 \mu\text{m}^2$). The relative signal intensity of the tumor region showing the strongest contrast enhancement (relative to surrounding brain tissue) was determined by placing ROI over the tumor and normal brain tissue areas using the Paravision 5.1. software. For statistical analysis of the BBB integrity, pre-contrast scans were subtracted from post-contrast scans after which the percent increase following gadolinium injection was calculated for the contralateral hemisphere (negative control set to 100%), tumor tissue and extracranial muscle tissue (positive control) for each animal.

Significance of relative differences was determined by using ANOVA test (GraphPad PRISM, GraphPad Software, La Jolla, CA, USA) with $p < 0.05$.

For *in vivo* tracking of the SPIO labeled stem cells 3D T2* (FLASH sequence, TR: 100ms, TE: 12 ms, flip angle: 20° , resolution: $78 \mu\text{m}^2$, field of view: $2.0 \times 1.5 \times 0.75$ cm) MR images were acquired and analyzed with the Image J software (National institute of health, Bethesda, Maryland, USA) to calculate the hypointense voxel volume.

Bioluminescence imaging (BLI)

Mice were anesthetized with isoflurane (2% induction, 1.5% maintenance) and placed in the IVIS® 100 system (Perkin Elmer, Waltham, MA, USA), maintaining the body temperature at 37°C . Subsequently, D-Luciferin (126mg/kg) (Promega, Madison, WI, USA) was injected intravenously and bioluminescent images were acquired for 1 minute with medium binning and f stop = 1. Data were analyzed for maximum intensity of the photon flux by the living image® 2.50.1 software (Perkin Elmer). Animals were imaged before and after GCV treatment, after which 3 GCV treated mOct4+ BM-HypoSC bearing animals were imaged every other week for another 12 weeks.

Positron emission tomography (PET)

For xenograft experiments, 5×10^5 or 1×10^6 HEK293T cells were injected. The following day, BLI and an 80 min dynamic [^{18}F] FHBG scan were performed. Mice were anesthetized with isoflurane (2% induction, 1.5% maintenance) and placed in a Focus 220 microPET system (Siemens Medical Solutions USA) after which $300 \mu\text{Ci}$ activity was injected *i.v.* Images were reconstructed using an iterative maximum a posteriori probability algorithm with ordered subsets (MAP; 18 iterations, 9 subsets, fixed resolution: 1.5 mm) and analyzed in PMODv.3.1 (PMOD Inc, Zurich, Switzerland). Summed images of the 80-min acquisition time were used for the analysis.

Statistical analysis

Values are represented as the mean \pm SEM. Analysis were performed using GraphPad PRISM 5 software (GraphPad, California, USA). The degree of significance is indicated where necessary (*: $p < 0.05$, **: $p < 0.01$, ***: $p < 0.001$, ****: $p < 0.0001$).

***In vivo* proliferation experiment**

2.5×10^5 m/rOct4⁺ BM-HypoSCs or m/rOct4⁻ BM-MAPCs suspended in 5 μ l PBS were injected stereotactically into the striatum, using the same device and coordinates as previously described, of C57BL6/J mice or Fisher rats. Animals were followed using MRI to assess possible tumor development.

Ganciclovir treatment experiment

A total of 5×10^5 eGFP-fLuc-HSV-tk positive mOct4⁺ BM-HypoSCs or mOct4⁻ BM-MAPCs suspended in 5 μ l PBS were injected stereotactically in the striatum, using the same device and coordinates as previously described, of C57BL6/j mice. The following day (day 1 post injection), MRI and BLI were performed to ascertain the site of injection and the cell viability after which, PBS or GCV (50mg / kg, intraperitoneally) was administered for 14 consecutive days. mOct4⁻ BM-MAPC injected animals (PBS: N = 6, GCV: N = 6) were sacrificed following MRI and BLI at the end of treatment (d15 post injection). Of the mOct4⁺ BM-HypoSC injected animals (PBS: N = 5, GCV: N = 5), three animals from the GCV treated group were followed up for 12 weeks by MRI and BLI to check for tumor regrowth. Anova tests were used to perform statistical analysis.

Furthermore, C57BL6/j mice were stereotactically injected in the brain with eGFP-fLuc expressing mOct4⁺ BM-HypoSCs and treated with PBS or GCV (N = 3 for each group). Significant differences in tumor growth and cell viability were determined using a Kruskal-Wallis test using Dunn's correction using GraphPad PRISM.

Endpoints

For mass forming experiments, rats stereotactically injected with rOct4⁺ BM-HypoSCs were sacrificed when symptoms reached grade 3 out of 4 (grade 0 for healthy rats, grade 1 for slight unilateral paralysis, grade 2 for moderate unilateral paralysis and/or beginning hunchback, grade 3 for severe unilateral or bilateral paralysis and pronounced hunchback, and grade 4 for moribund rats) [66].

In mice, mOct4⁺ BM-HypoSCs mass formation reached an equilibrium after approximately 25 days, after which one mouse was sacrificed at 53 days (n = 1) post injection and the remaining mouse at 104 days (n = 1) post injection.

For the m/rOct4⁻ BM-MAPCs, animals were followed for 110 days, mMSC's for 63 days and hMultistem's for 14 days, after which they were sacrificed.

For the GCV treatment experiment, two animals stereotactically injected with mOct4⁺ BM-HypoSCs of each group (PBS-GCV) were sacrificed on the last day of GCV treatment (= day 15 post injection) whereas three animals were followed up by MRI and BLI every other week for up to 12 weeks to validate tumor regrowth.

Histology

Animals were sacrificed by an *i.p.* overdose of Nembutal (300 μ l; Ceva) and subsequently perfused with 4% ice-cold paraformaldehyde (PFA) solution (Sigma-Aldrich). After overnight post fixation in 4% PFA, the brain tissue was stored in a 0.1% sodium azide solution (Fluka, Sigma-Aldrich) at 4°C. Brains were embedded in paraffin and 50 μ m vibratome or 5 μ m paraffin sections were sliced and a Masson's trichrome staining was performed. Sections were deparaffinized in xylol, followed by rehydration through ethanol. Subsequently, sections were stained with hematoxylinen ponceau/fuchine and aniline blue. Finally, sections were dehydrated and mounted with di-n-butylPhthalate in xylene (Sigma-Aldrich). Furthermore, brain slices of animals injected with m/rOct4⁺ BM-HypoSCs were stained for H&E, Periodic acid Schiff (PAS), and laminine [145]. Finally, brain slices of mOct4⁺ BM-HypoSCs or mOct4⁻ BM-MAPC bearing animals were stained using an anti-FLAG antibody (Sigma F1804).

For confirmation of MRI obtained results from SPIO labeled stem cells a prussian blue staining was performed to stain for iron present in the brain by combining a 20% aqueous solution of hydrochloric acid and a 10% aqueous solution of potassium ferrocyanide and counterstained with nuclear fast red staining. Slices were scanned with a Mirax desk (Carl Zeiss, Oberkochen, Germany) and microscopic images were taken with the Mirax viewer software.

4.3 Results

4.3.1 Safety studies m and rOct4⁺ BM-HypoSCs, m and rOct4⁻ BM-HypoSCs, mMSC's and hMultistem's

4.3.1.1 m and rOct4⁺ BM-HypoSCs

Intracranial engraftment of m/rOct4⁺ BM-HypoSCs was performed on C57Bl6/J mice and Fisher rats respectively. Mass formation was monitored by weekly MR imaging.

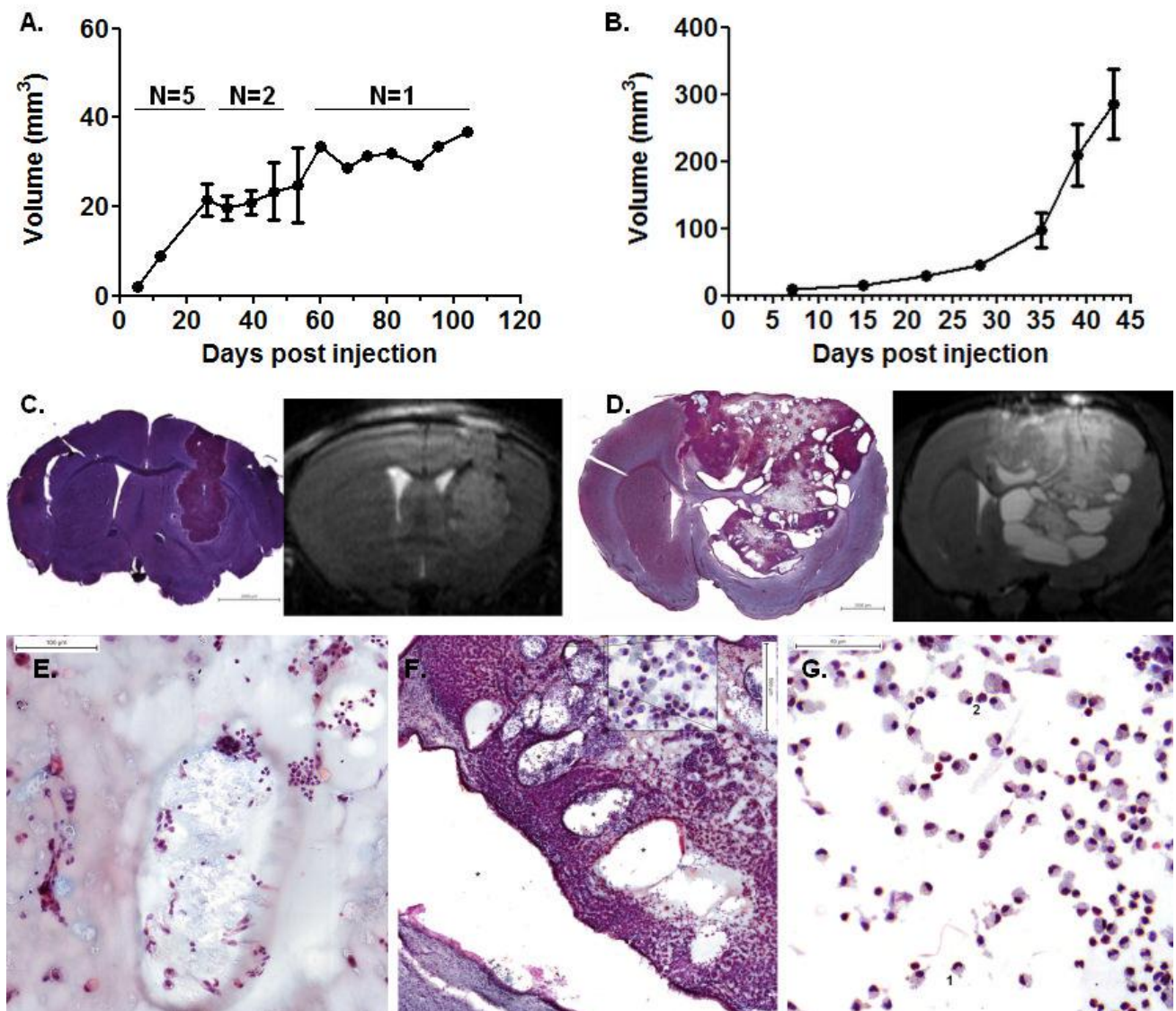
In mice (N = 5), masses developed without obvious symptoms reaching a relative plateau at 26 days post injection ($21 \pm 4 \text{ mm}^3$) after which, three animals were sacrificed. One more animal was sacrificed at 53 days post injection when the average mass size was $25 \pm 8 \text{ mm}^3$. The final animal was sacrificed at 104 days post injection and showed a mass of 37 mm^3 (Figure 13A).

Rats (N = 6) also developed masses reaching an average size of $286 \pm 52 \text{ mm}^3$ at 43 days post injection as shown in Figure 13B after which they were sacrificed as grade 3 symptoms emerged. *In vivo* MRI data suggest that after an initial formation of some solid tumor parts, heterogeneous, cyst like (fluid filled) structures formed. Hereby, masses were more heterogeneous in rats when compared to mice (see also Figure 13C).

After sacrificing the animals, trichrome stainings were performed on vibratome sections of the brain and compared to the MRI scans of the last time point. Histology on mouse brain sections confirmed intracerebral mass formation and showed a solid pattern for the mice injected with mOct4⁺ BM-HypoSCs (Figure 13C).

Figure 13: Mass formation of m/rOct4⁺ BM-HypoSCs in mouse and rat brain monitored by *in vivo* MRI.

- A. Mass formation in the mouse brain (N = 5) following intracranial cell engraftment. After 26 days, three mice were sacrificed. Another mouse was sacrificed 53 days post injection. The final mouse was monitored until day 104 post injection.
- B. Mass formation in the rat brain following intracranial cell engraftment. Rats (n = 6) developed large masses reaching an average size of $286 \pm 52 \text{ mm}^3$ at 43 days post injection.
- C-D. Masson's trichrome stained brain slices of mice (C) and rats (D) were concurrent with the obtained MRI data. (scale bar: 2000 μm)
- E-G. Histology of rOct4⁺ BM-HypoSC masses showed a microcystic pattern with wisps of myxoid material in cystic spaces (e. 10x scale bar: 100 μm), fluid filled cyste formation (f. 5x *, scale bar: 500 μm) and immune cell infiltration caused by necrosis (characterized by a loss of cell membrane integrity and an uncontrolled release of cell death products into the intracellular space) (f. 40x). g: 40x magnification image of fluid filled cyst with immune cell infiltration including 1. Lymphocyte (small, round cell with a very large nucleus and barely any cytoplasm), 2. Macrophage (very large, irregularly shaped cells with a small nucleus in comparison to the amount of cytoplasm) (scale bar: 50 μm)



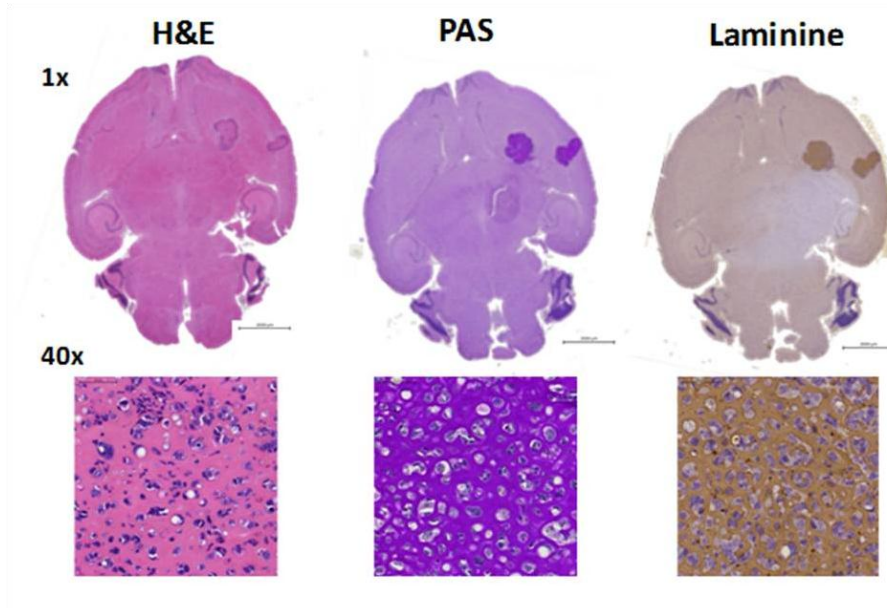
Chapter 4:

In vivo validation of cell lines for non-invasive imaging of suicide gene therapy

Histological analysis showed yolk sac tumor characteristics, like Periodic acid Schiff (PAS) and laminin positive staining (Figure 14) [145]. Histology on rat brain sections also showed mass formation but with a microcystic pattern (Figure 13D-G) with wisps of myxoid material in cystic spaces, fluid filled cyst formation and immune cell infiltration caused by necrosis. The histological data were therefore concluded to be concurrent with the MRI images obtained before sacrificing the animals.

Figure 14: Histological analysis of mOct4⁺ BM-HypoSC tumors.

Histological analysis of mOct4⁺ BM-HypoSC tumors revealed yolk sac tumor characteristics like Periodic Acid Schiff (PAS) and laminine positive staining (scale bar overview: 2000 μ m, 40x: 50 μ m).



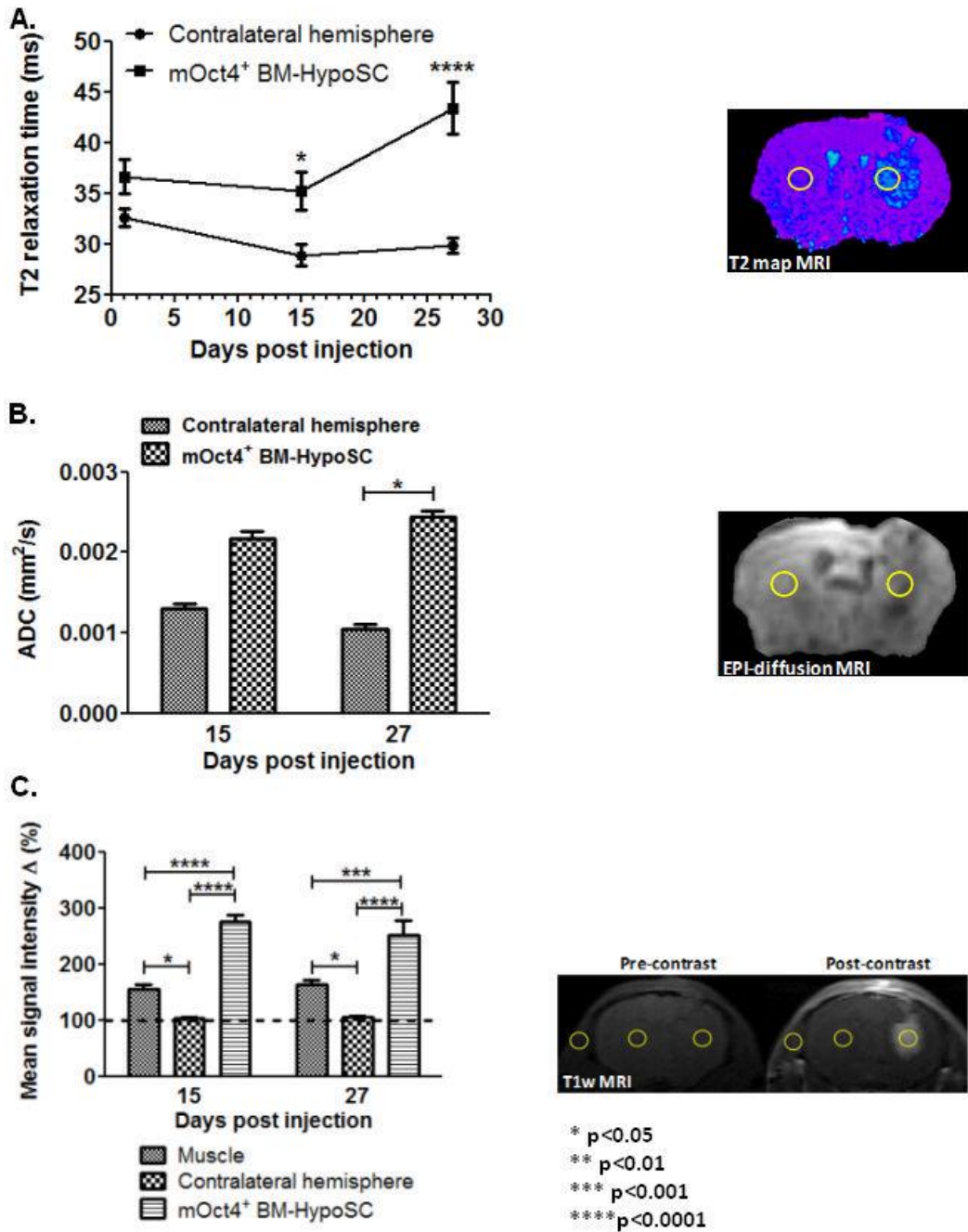
Mass formation following mOct4⁺ BM-HypoSC engraftment was subsequently further characterized by MR imaging (Figure 15). MRI analyses on mOct4⁺ BM-HypoSC masses on day 15 and day 27 post injection showed elevated T2 relaxation times (N = 6, 39.3 ± 4.1 ms) (Figure 15A) and increased diffusion (N = 3, 0.002 ± 0.00009 mm²/s) (Figure 15B) compared to the contralateral hemisphere (T2 relaxation time: 29.4 ± 0.55 ms / ADC values: 0.001 ± 0.000055 mm²/s). Furthermore, BBB integrity loss was apparent on day 15 and 27 (N = 6, see Figure 15C). Hereby, larger tumors displayed a more heterogeneous BBB disruption pattern.

Figure 15: MRI analysis of mass formation after engraftment of mOct4⁺ BM-HypoSCs.

- A. T2 relaxation time of masses formed by mOct4⁺ BM-HypoSCs increased compared to the contralateral hemisphere on day 15 ($p < 0.05$) and day 27 ($p < 0.0001$) post injection, indicating an increased fluid content in the masses. (N = 6)
- B. The apparent diffusion coefficient (ADC) of masses formed by mOct4⁺ BM-HypoSCs was also elevated compared to the contralateral hemisphere on day 15 ($p < 0.0001$) and day 27 ($p < 0.0001$) post injection, indicating an increase of the intercellular space [26]. (N = 3)
- C. BBB disruption was shown by an increased signal intensity at the mass site after Dotarem injection. (N = 6)

For each graph, one representative analysis is shown (ROI = yellow circle). Graft sites of mOct4⁺ BM-MAPCs were characterized by decreased signal intensities, T2 and ADC values in comparison to the contralateral hemisphere which is concurrent with damage caused by cell injection (data not shown).

The significance for all graphs refers to * $p < 0.05$, ** $p < 0.01$, *** $p < 0.001$, **** $p < 0.0001$.

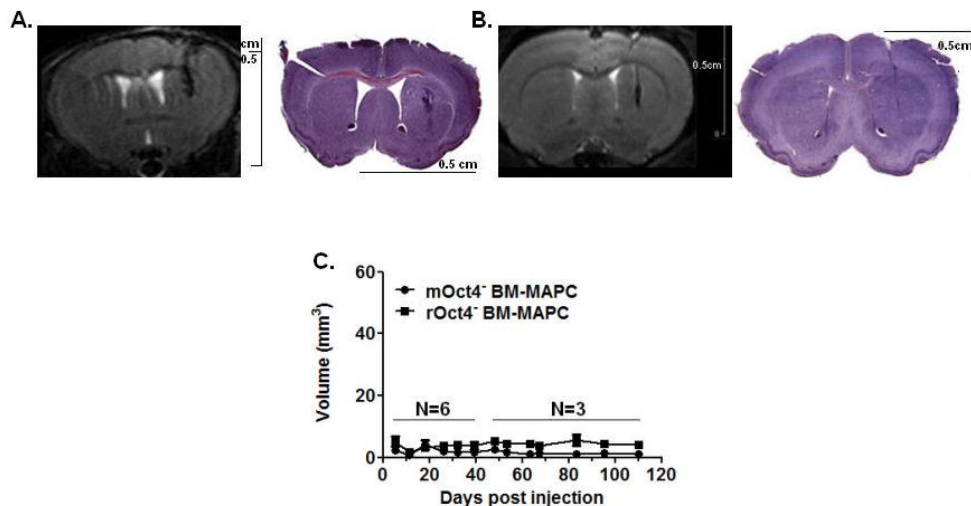


4.3.1.2 m and rOct4⁻ BM-MAPCs

As Oct 4 is a marker for pluripotency [159], we wanted to assess the hypothesis that stem cells, not expressing Oct4 might not give rise to mass formation. Therefore, m/rOct4⁻ BM-MAPCs, were injected in the striatum of C57BL6/j mice (N=6) and Fisher rats (N=6), respectively. MRI of the remaining animals (N=3) did not indicate mass formation even after 110 days. The absence of mass growth was subsequent confirmed by histology, which neither revealed intracerebral mass formation in mice (Figure 16A) nor in rats (Figure 16B). In rats, grafts were rather difficult to locate as graft sizes seemed to be limited to the needle tract made by the initial injection. In mice, grafts were more easily detected as cells seemed to have persisted at the graft location without causing tumor formation. Hypointense contrast was obvious from the first MRI post cell engraftment, indicating minor injury/bleeding. This contrast did not change over time, resulting in volumes of $0.8518 \text{ mm}^3 \pm 0.0684$ for mOct4⁻ BM-MAPCs injected in mice and $0.7217 \text{ mm}^3 \pm 0.1323$ for rOct4⁻ BM-MAPCs injected in rats, respectively (Figure 16C).

Figure 16: Histology and MRI data obtained for animals injected intracranially with m/rOct4⁻ BM-MAPCs.

- A-B. MRI scans and subsequent histology showed a minor injury due to the engraftment of stem cells but did not reveal mass development neither in mice (A) nor in rats (B).
 C. Statistical analysis of the data obtained by MRI resulted in hypointense volumes of $1.2 \pm 0.2 \text{ mm}^3$ and $2.0 \pm 0.2 \text{ mm}^3$ for mouse and rat stem cells respectively at 110 days post injection. These volumes did not significantly change in size over the course of the experiment (day 1 tot 110)

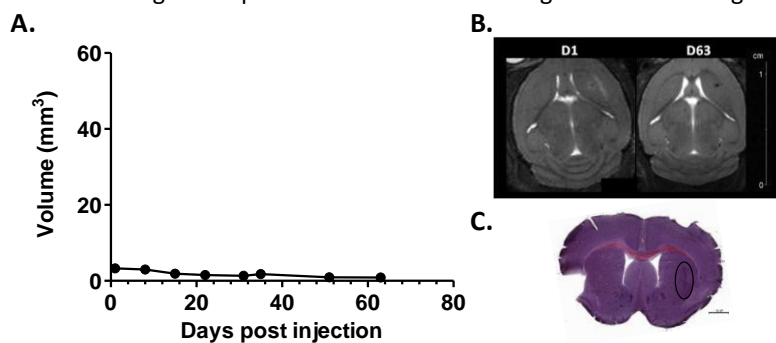


4.3.1.3 mMSC's

Subsequently, mMSC's were injected stereotactically in the striatum of syngeneic C57BL6/j mice. MRI of these animals did not indicate mass formation even after 63 days as lesion sizes remained small at $1.81 \text{ mm}^3 \pm 0.32 \text{ mm}^3$ over the entire duration of follow-up (Figure 17A) as assessed by T2 weighted MR images (Figure 17B). Subsequent histology did also not reveal intracerebral mass formation (Figure 17C).

Figure 17: Histology and MRI data obtained from animals injected intracranially with mMSC's

- Lesion size in the brain (N = 4) following intracranial mMSC engraftment. Mice were followed for 63 days after which they were sacrificed for Masson's trichrome staining.
- Example of T2 weighted coronal images on day 1 and day 63 post injection of a representative animal.
- Masson's trichrome staining of a representative animal showing a lesion in the right hemisphere.

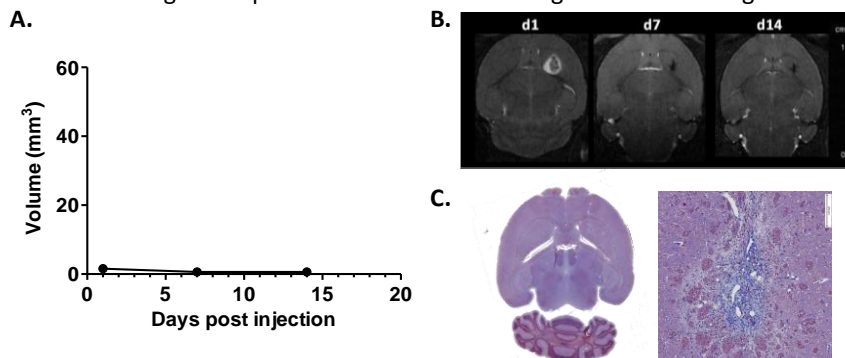


4.3.1.4 hMultistem's

Finally, also human Multistem's were stereotactically injected in the healthy brain of Hsd:athymic Nude-Foxn1^{nu} mice. MRI showed no mass formation (Figure 18A) but rather a decrease of the graft, indicative of cell death at 14 days post injection. Lesion sizes were assessed by T2 weighted MR images (Figure 18B). Subsequent histology did also not reveal intracerebral mass formation (Figure 18C).

Figure 18: Histology and MRI data obtained from animals injected intracranially with hMultistem's

- Lesion size in the brain (N = 4) following intracranial hMultistem engraftment. Mice were followed for 63 days after which they were sacrificed for Masson's trichrome staining.
- Example of T2 weighted coronal images on day 1 and day 63 post injection of a representative animal.
- Masson's trichrome staining of a representative animal showing a lesion in the right hemisphere.



4.3.2 *In vivo* validation of fLuc and HSV-TK expression in eGFP-fLuc-HSVTK transduced stem cells

4.3.2.1 mOct4⁺ BM-HypoSCs and mOct4⁻ BM-MAPCs

The data above suggest that using Oct4⁻ stem cells would greatly improve the safety profile of these stem cells. However, as some 'therapeutic' properties of those cells might be different to cells expressing higher Oct4 levels, we investigated an additional safety measure for the mouse stem cells, namely transducing both mOct4⁺ BM-HypoSCs and mOct4⁻ BM-MAPCs with a lentiviral vector containing the HSV-TK gene, which makes these cells susceptible for ganciclovir treatment and subsequent formation of cytotoxic phosphorylated ganciclovir.

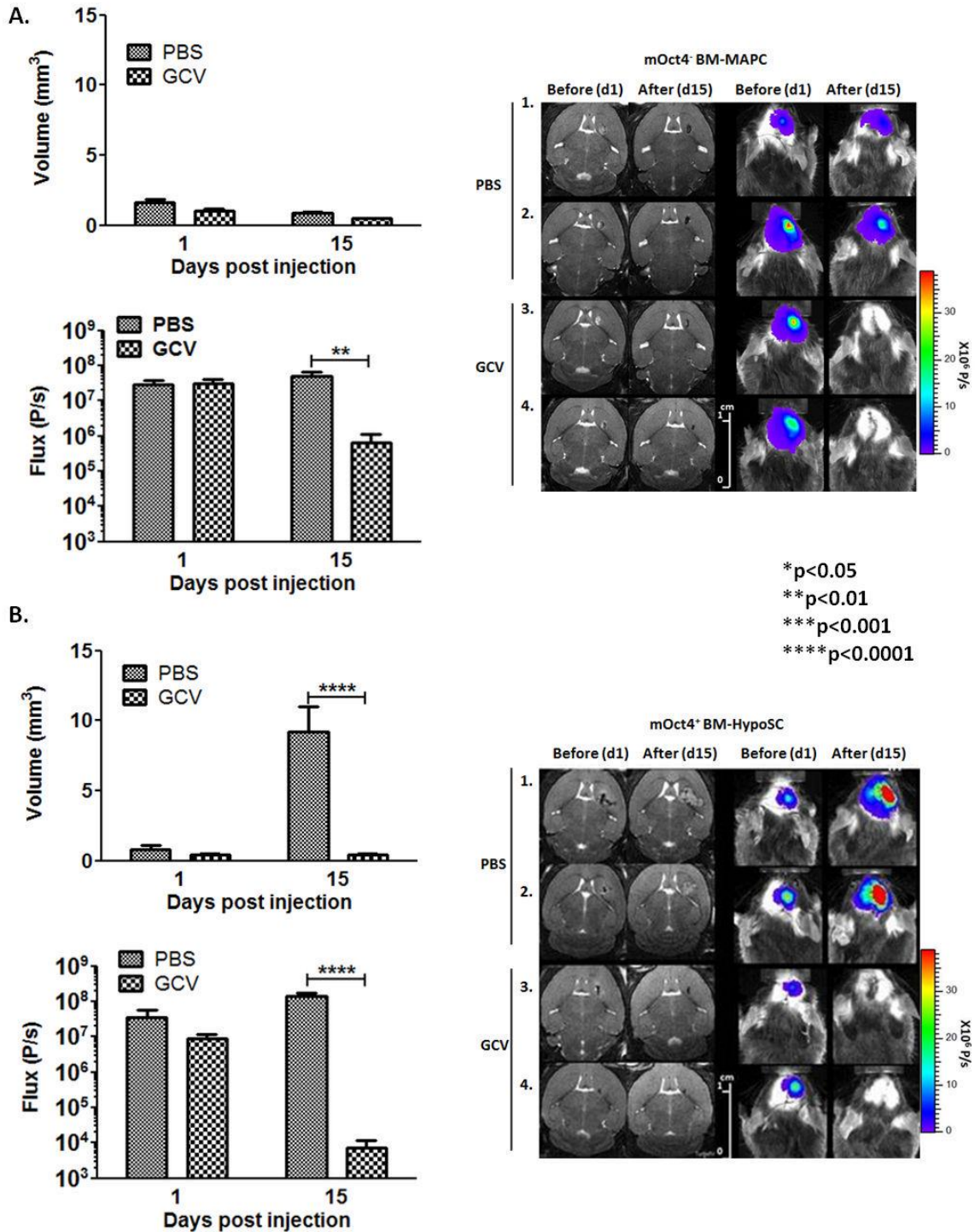
mOct4⁻ BM-MAPC graft volumes of PBS and GCV treated animals were not significantly different on MRI although BLI signal intensity of GCV treated animals injected with transduced cells did show a significant decrease over time indicating a cytotoxic effect (Figure 19A). Injection of 5×10^5 cells generates a rather small graft which explains the lack of difference on MRI.

Masses formed in mice implanted with eGFP-fLuc-HSVtk expressing mOct4⁺ BM-HypoSCs and treated with GCV (N = 5) showed a significant difference in both graft size (MRI) and cell viability (BLI) when compared to PBS control animals (N = 5, day 15, see Figure 19B). Observations made by *in vivo* imaging were confirmed with histology (Figure 19C) and the more specific anti-FLAG staining, in order to specifically stain for fLuc expression (Figure 20). This specific staining showed eGFP-fLuc-HSVtk expressing cells at the graft site for mOct4⁻ BM-MAPC (Figure 20A) and mOct4⁺ BM-HypoSC (Figure 20B) bearing animals treated with PBS for 14 days (=15days post injection). In GCV treated animals, only few fLuc positive cells were detected in both mOct4⁻ BM-MAPC (Figure 20C) and mOct4⁺ BM-HypoSC (Figure 20D) bearing animals, which is concurrent with the results obtained by MRI, BLI and Masson's trichrome staining.

Three GCV treated animals implanted with eGFP-fLuc-HSVtk expressing mOct4⁺ BM-HypoSCs were maintained to assess delayed cell growth but both MRI and BLI confirmed that there was no mass formation or increased BLI signal intensity for up to 12 weeks post GCV treatment. For an overview of both MRI and BLI measurements see Table 6. In contrast, animals implanted with eGFP-fLuc expressing mOct4⁺ BM-HypoSCs and treated with GCV (N=3) did not show significant differences to PBS treated animals (N=3, Figure 21).

Figure 19: *In vivo* transgene expression assessment of eGFP-fLuc-HSV-TK + mOct4⁻ BM-mMAPCs and mOct4⁺ BM-HypoSCs.

- A. For mice injected with mOct4⁻ BM-mMAPCs, no significant change in mass volume could be detected by MRI. However, a decrease in BLI signal intensity and hereby of cell viability was detected after GCV treatment but not in PBS control animals.
 - B. GCV treatment resulted in significant differences of both mass volume (MRI) and viability (BLI) after GCV treatment between PBS and GCV treated mice injected with mOct4⁺ BM-HypoSCs.
 - C. Histology: Masson's trichrome staining on animals killed at the end of GCV treatment confirmed MRI and BLI data (scale var overview: 200µm, 20x:100µm).
- The significance for all graphs refers to *p<0.05, **p<0.01, ***p<0.001, ****p<0.0001



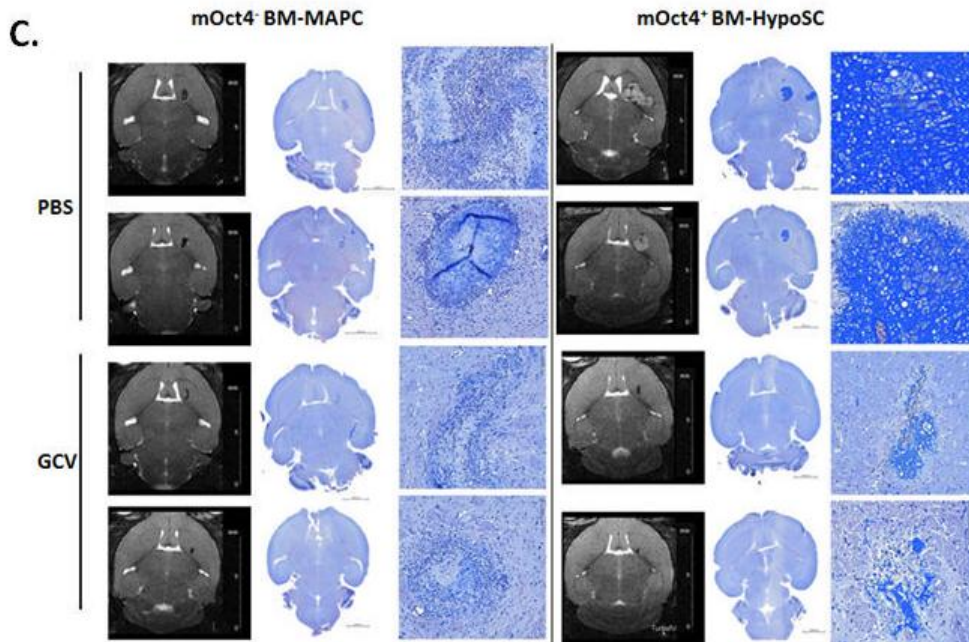


Figure 20: Anti-FLAG staining on eGFP-fLuc-HSVtk expressing stem cells after treatment.

- mOct4⁻ BM-MAPC bearing mice showed a high abundance of fLuc expression at the graft site following PBS treatment (day 15 post injection).
 - mOct4⁺ BM-HypoSC bearing mice also showed fLuc expression at the graft site following PBS treatment (day 15 post injection). Here however, masses developed as described previously.
 - mOct4⁻ BM-MAPC bearing mice treated with GCV showed less fLuc expression compared to the PBS treated group (A) at the end of treatment, which is consistent with the decreased viability observed by BLI.
 - mOct4⁺ BM-HypoSC bearing mice treated with GCV also showed a decrease in fLuc expression at the graft site (black circle) following treatment (day 15 post injection) in comparison to the PBS treated group. Furthermore, mass development was absent which is concurrent with the results obtained by MRI and BLI.
- (images: magnification: 10x, scale bar: 200 μ m)

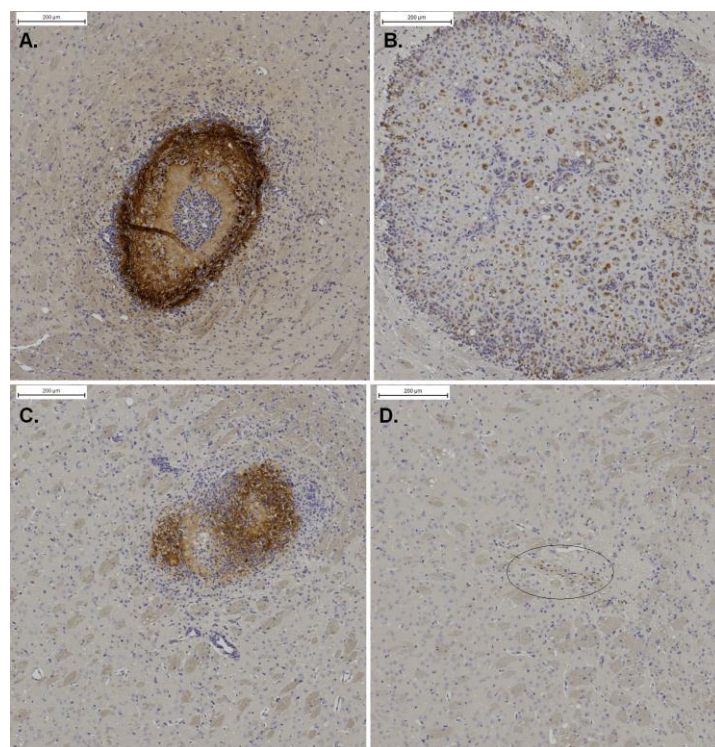
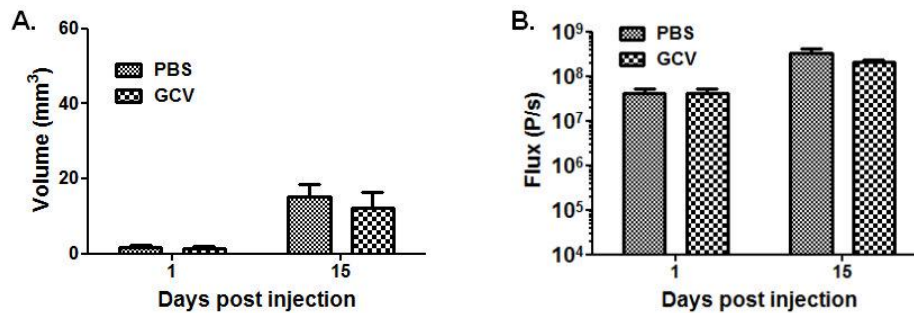


Table 6: Quantitafication of mass volumes (MRI) and cell viability (BLI) of mOct4⁺ BM-HypoSCs *in vivo*.

	MRI (mm ³)		BLI (Flux: P/s)	
	PBS	GCV	PBS	GCV
Before therapy	0.91 ± 0.37 (N=5)	0.44 ± 0.08 (N=5)	3,67 × 10 ⁷ ± 2.22 × 10 ⁷ (N=5)	8.78 × 10 ⁶ ± 2.82 × 10 ⁶ (N=5)
After therapy	9.23 ± 1.76 (N=5)	0.43 ± 0.06 (N=5)	1.38 × 10 ⁸ ± 3.06 × 10 ⁷ (N=5)	7.24 × 10 ³ ± 4.15 × 10 ³ (N=5)
2 weeks post GCV		0.63 ± 0.19 (N=3)		5.53 × 10 ³ ± 4.57 × 10 ³ (N=3)
4 weeks post GCV		0.45 ± 0.10 (N=3)		4.01 × 10 ³ ± 2.42 × 10 ³ (N=3)
6 weeks post GCV		0.46 ± 0.15 (N=3)		1.78 × 10 ⁴ ± 7.35 × 10 ³ (N=3)
8 weeks post GCV		0.44 ± 0.10 (N=3)		9.01 × 10 ³ ± 6.20 × 10 ³ (N=3)
10 weeks post GCV		0.42 ± 0.08 (N=3)		1.68 × 10 ⁴ ± 6.81 × 10 ³ (N=3)
12 weeks post GCV		0.49 ± 0.15 (N=3)		4.64 × 10 ³ ± 1.92 × 10 ³ (N=3)

Figure 21: Suicide gene therapy in eGFP-fLuc expressing mOct4⁺ BM-HypoSCs

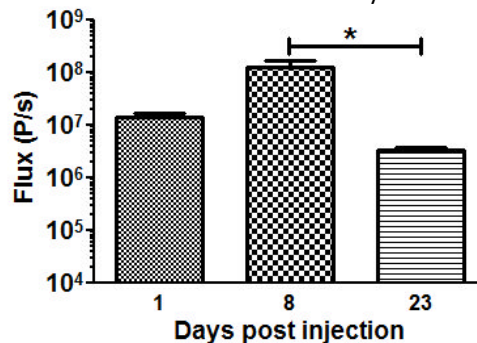
- A. MRI data showed no statistically significant difference in tumor growth between mOct4⁺ BM-HypoSC bearing mice treated with PBS (day 1: 1.8 ± 0.5mm³-day 15: 15.3 ± 3.3mm³) or GCV (day1: 1.5 ± 0.4mm³-day 15: 12.2 ± 4.3mm³).
- B. BLI data also did not show a statistical significant difference between PBS (day 1: 4.1x10⁷ ± 1.2x10⁷ P/s – day 15: 3.2x10⁸ ± 9.0x10⁷ P/s) and GCV treated (day1: 4.2x10⁷ ± 9.7x10⁶ P/s - day 15: 2.1x10⁸ ± 2.4x10⁷ P/s) mOct4⁺ BM-HypoSCs in cell viability.



Finally, mice injected with eGFP-fLuc-HSVtk expressing mOct4⁺ BM-HypoSCs (N = 3) were treated with GCV starting 8 days after injection. At the end of GCV treatment, BLI showed a reduced viability of the stem cells (Figure 22). However, this did not result in complete removal of the tumor.

Figure 22: Suicide gene therapy in eGFP-fLuc expressing mOct4⁺ BM-HypoSCs

BLI data obtained from mice in which eGFP-fLuc-HSVtk expressing mOct4⁺ BM-HypoSC were allowed to grow for 8 days prior to commencing GCV treatment showed a reduction in cell viability at the end of treatment.

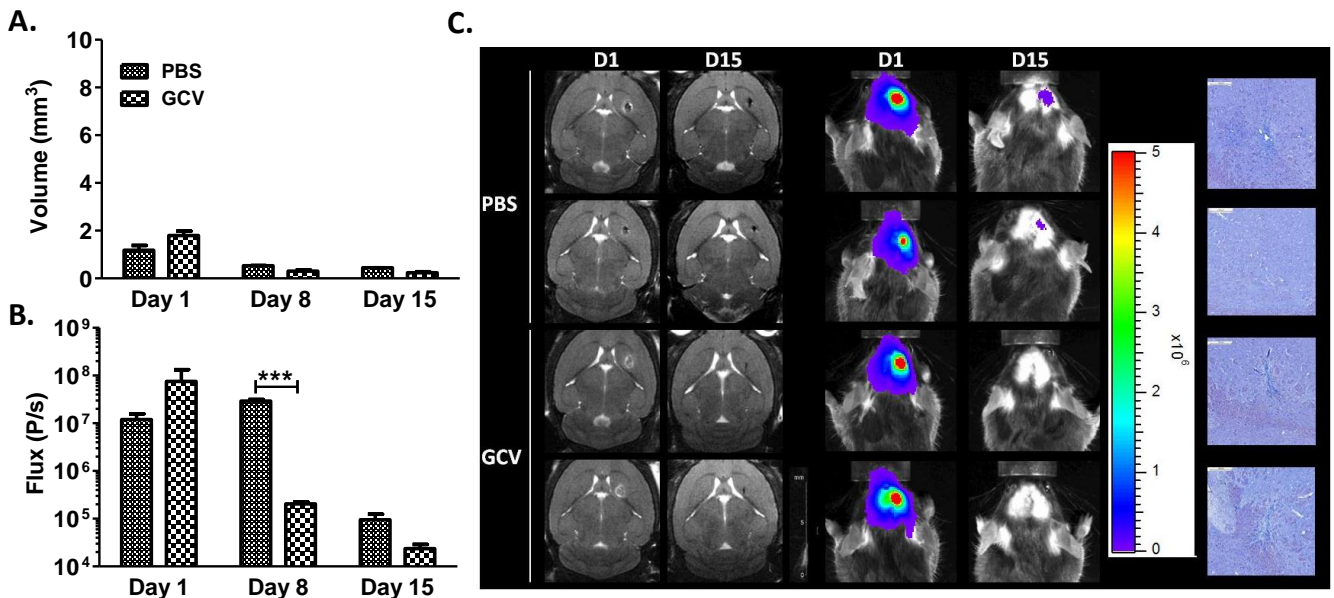


4.3.2.2 mMSC's

Subsequently, eGFP-fLuc-HSVTK expressing mMSC's were evaluated *in vivo* for stem cell detectability and HSV-tk killing potential. On MRI, eGFP-fLuc-HSVTK expressing mMSC lesion volumes of both PBS control and GCV treated animals decreased over time (Figure 23A). On day 8 post stem cell injection, a significant decrease in viability was seen between PBS control (N = 2) and GCV treated (N = 2) animals indicating cell killing after 7 days of GCV treatment. This difference could not be demonstrated at the end of the GCV treatment as the viability of the stem cells in animals treated with PBS also decreased indicating a poor survival of the stem cells *in vivo*. (Figure 23B). An overview of MRI and BLI images generated on prior to (day 1) and at the end of GCV treatment (day 15) are depicted in Figure 23C. Furthermore, histology confirmed the obtained data although the graft proved difficult to locate in some mice (Figure 23C).

Figure 23: *In vivo* transgene expression evaluation of eGFP-fLuc-HSVTK + mMSC's.

- For mice injected with mMSC's, lesion volumes decreased over time.
- Stem cell viability assessment using BLI (fLuc) showed a statistically significant difference between PBS control and GCV treated animals at day 8. However, PBS control animals also showed a decrease in stem cell viability indicating poor survival of the stem cells in the brain of healthy mice. *** $p < 0.001$
- Overview of MRI and BLI images generated before (day 1) and after (day 15) treatment. Furthermore, a Masson's trichrome staining confirmed the results obtained by MRI and BLI although in one animal the graft could not be localized (PBS control animal 2).



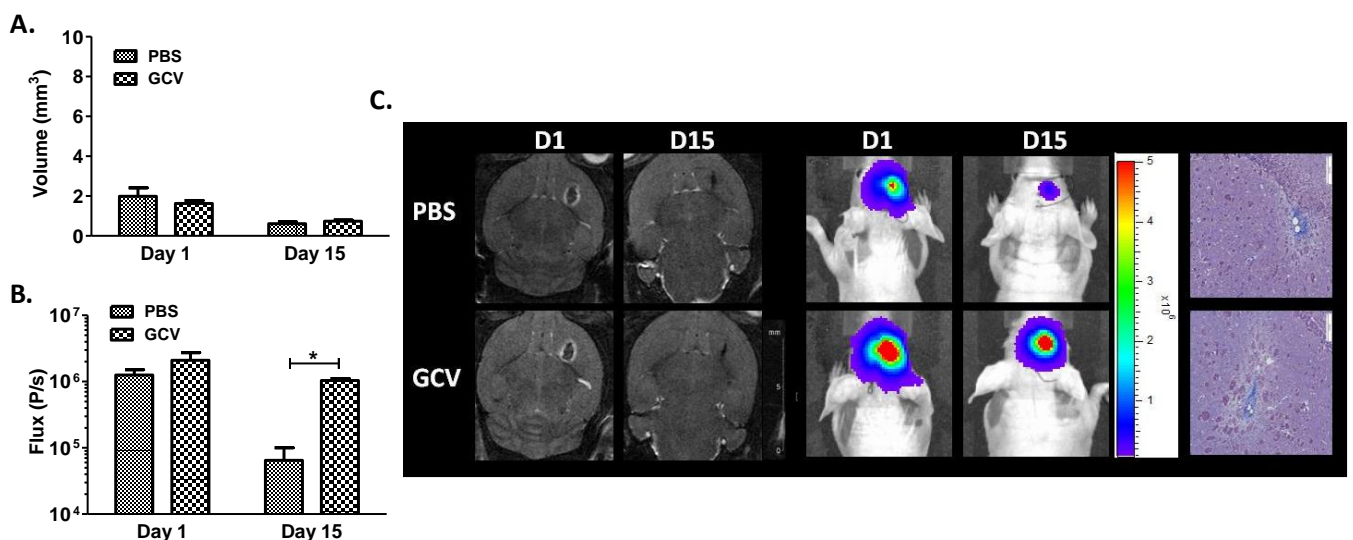
4.3.2.3 hMultistem's

Finally, also eGFP-fLuc-HSVTK expressing human Multistem's were assessed *in vivo* for their transgene expression. On MRI, eGFP-fLuc-HSVTK expressing hMultistem lesion volumes of PBS control and GCV treated animals were not significantly different due to the small lesion sizes caused by the injection of 5×10^5 cells (Figure 24A).

At the end of treatment (day 15), a significant decrease in stem cell viability was observed between PBS control (N = 3) and GCV treated (N = 3) animals. Stem cell viability in the GCV treated group remained high, indicating no significant toxicity of the GCV on the stem cells (Figure 24B), which might be related to insufficient levels of GCV in the brain, with limited BBB disruption. An overview of MRI and BLI images generated prior to (day 1) and at the end of GCV treatment (day 15) are depicted in Figure 24C. Furthermore, histology confirmed the obtained data (Figure 24C).

Figure 24: *In vivo* transgene expression evaluation of eGFP-fLuc-HSVTK + hMultistem's.

- For mice injected with hMultistem, lesion volumes were not statistically significantly different between PBS control (N = 3) and GCV treated animals (N = 3).
- Stem cell viability assessment using BLI (fLuc) showed significantly less viable hMultistem's in the PBS control group compared to the GCV treated group at the end of treatment (day 15). However, GCV treated animals did not show a decrease in stem cell viability at the end of GCV treatment. * $p < 0.05$
- Overview of MRI and BLI images generated before (day 1) and after (day 15) treatment. Furthermore, a Masson's trichrome staining confirmed the results obtained by MRI and BLI.

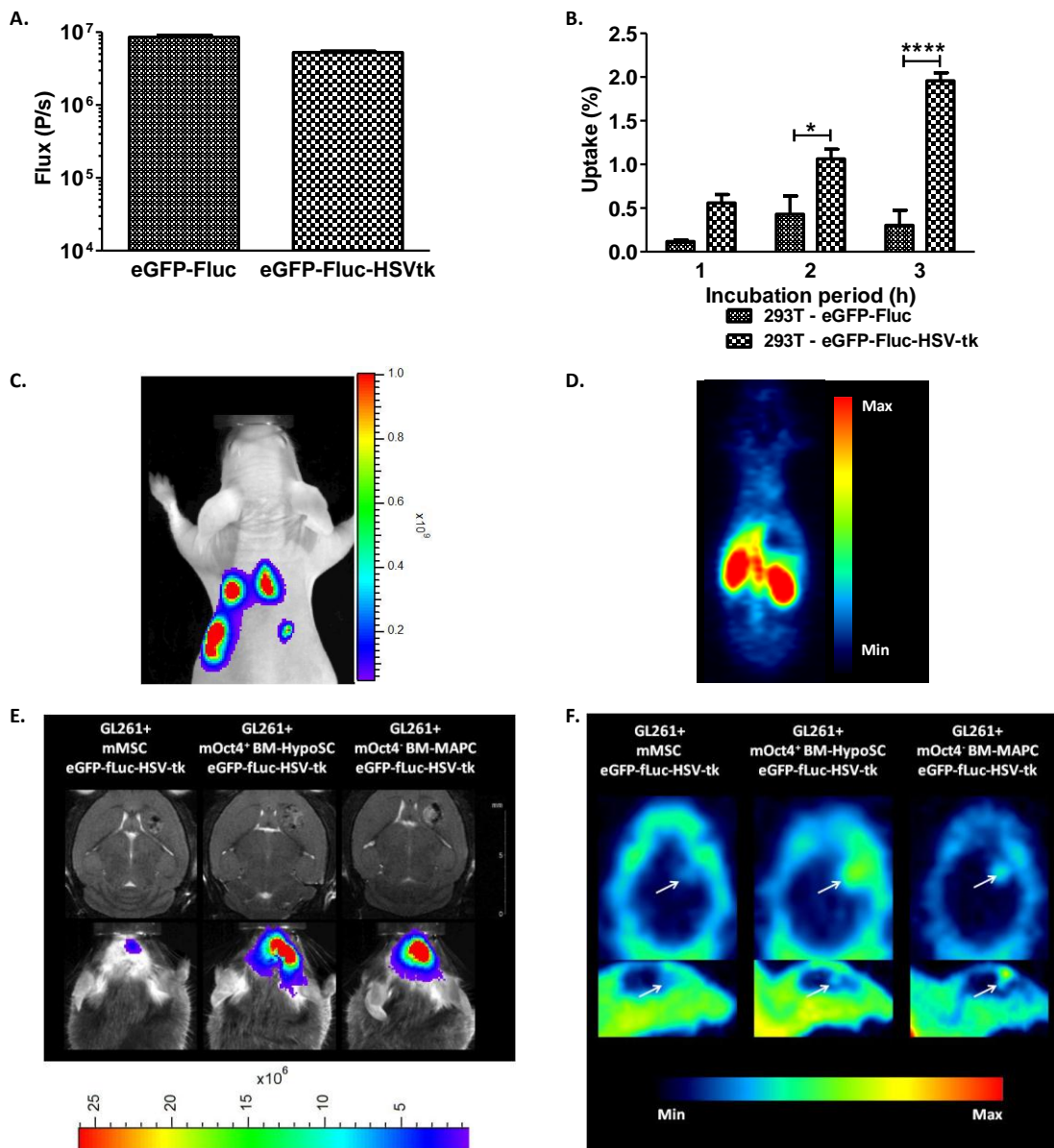


In conclusion, we were able to detect all eGFP-fLuc-HSVTK expressing stem cells by BLI (fLuc) *in vivo* one day after stereotactical injection into the healthy mouse brain. mOct4⁺ BM-HypoSCs and mOct4⁻ BM-MAPCs survived well *in vivo* for at least two weeks, whereas the majority of the mMSC's and hMultistem's showed signs of profound cell death after two weeks, which was irrespective to assignment of the animals to the PBS control or GCV treated group.

Furthermore, we attempted to detect eGFP-fLuc-HSVTK expressing cells by using [¹⁸F] FHBG PET imaging. Therefore, eGFP-fLuc-HSVTK expressing HEK 293T cells were assessed *in vitro* (Figure 25A) and *in vivo* (Figure 25B) for BLI expression (*in vitro*: Figure 25A, *in vivo*: Figure 25C) and [¹⁸F] FHBG tracer uptake (*in vitro*: Figure 25B, *in vivo*: Figure 25D). BLI showed sufficient fLuc expression both *in vitro* and *in vivo* for detection. [¹⁸F] FHBG tracer uptake was proven to be significant elevated *in vitro* at two hours and three hours post tracer injection compared to eGFP-fLuc transduced HEK 293T cells. Unfortunately, 5 x 10⁵ eGFP-fLuc-HSVTK expressing HEK293 T cells could not be detected in a xenograft. A plausible explanation for this is the partial volume effect which makes it impossible to distinguish the signal from the background. Subsequently, eGFP-fLuc-HSVTK expressing mMSC's, mOct4⁻ BM-MAPCs and mOct4⁺ BM-HypoSCs cells were assessed in a syngeneic mouse glioblastoma (GL261) model for cell viability (fLuc) and HSV-tk driven [¹⁸F] FHBG tracer uptake. BLI and MRI showed the presence and viability of the stem cells inside the tumor area (Figure 25E), whereas stem cells could be detected with some difficulty by an [¹⁸F] FHBG PET scan (Figure 25 F).

Figure 25: *In vivo* HSV-tk imaging assessment using [^{18}F] FHBG PET imaging.

- HEK 293T fLuc expression assessment using BLI showed no statistically significant differences *in vitro* between eGFP-fLuc and eGFP-fLuc-HSVTK expressing cells.
- Gamma counter measurements on HEK 293T cells showed significantly more [^{18}F] FHBG tracer uptake in eGFP-fLuc-HSVTK expressing cells compared to eGFP-fLuc expressing cells.
- In vivo* BLI on HEK293T xenografts in Hsd:athymic Nude-Foxn1^{nu} mice showed sufficient expression of fLuc for *in vivo* detection of the cells.
- [^{18}F] FHBG PET scan of the same animal mentioned in C could not show presence of the stem cells *in vivo*. The partial volume effect explains is believed to be responsible for this result as it makes it impossible to distinguish the signal from the background.
- MRI and BLI measurements on GL261 tumor bearing animals injected with 5×10^5 mMSC's, mOct4⁺ BM-HypoSCs or mOct4⁻ BM-MAPCs showed that stem cells could be easily detected by MRI (SMG²-mPEGSi) and BLI (fLuc).
- [^{18}F] FHBG PET scan on the same animals mentioned in E showed that HSV-TK expressing stem cells could also be detected using PET although this proved more challenging.

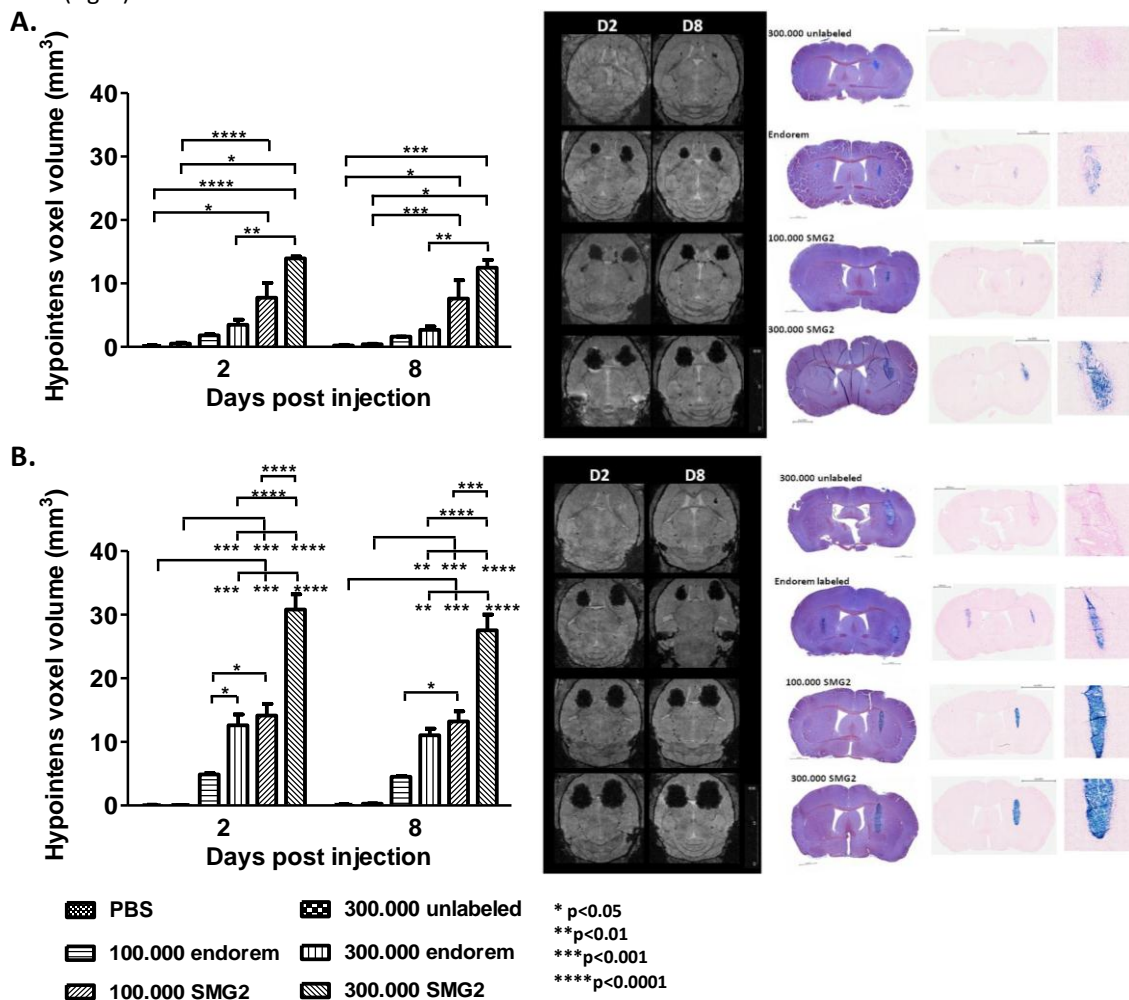


4.3.3 *In vivo* assessment of stem cells labeled with SPIO's using MRI

Subsequently, stem cells labeled with in house fabricated SPIO's (see Chapter 3) were compared to Endorem® labeled cells for *in vivo* MR tracking. Therefore, a set number (1×10^5 or 3×10^5) of labeled mMSC's (Figure 26A) and mOct4⁻ BM-MAPCs (Figure 26B) were stereotactically injected into the right striatum of C57BL6/j mice and followed by MR imaging. Places that contained labeled stem cells created a signal void on 3D T2* MR images, which were quantified by using the software program Image J. Only slight differences were observed when imaging two or eight days post injection. Animals were sacrificed and trichrome and Prussian blue staining were performed to confirm the data obtained by MR imaging.

Figure 26: *In vivo* SPIO labeling evaluation of mMSC's and mOct4⁻ BM-MAPCs.

- A. Hypointense voxel volume analysis caused by stereotactical injection of SPIO labeled mMSC's (left) on 3D T2* MR images (middle). MRI results were confirmed with histology (Masson's Trichrome and Prussian blue (right)).
- B. Hypointense voxel volume analysis caused by stereotactical injection of SPIO labeled mOct4⁻ BM-MAPCs (left) on 3D T2* MR images (middle). MRI results were confirmed with histology (Masson's Trichrome and Prussian blue (right)).



4.3.4 *In vivo* assessment of mCherry-rLuc transduction of malignant glioma cells using MRI and BLI

Finally, *in vivo* expression of mCherry and rLuc in all three tumor cell lines was investigated using BLI. 2.5×10^5 GL261, 5×10^4 Hs683 or 3×10^5 U87-MG cells (mCherry-rLuc +) were injected stereotactically into the brain and followed up using MRI and BLI. For the GL261 cell line, MR images showed a slight growth difference between WT cells and mCherry rLuc + cells (Figure 27A1). Although tumors grew exponentially, this was not reflected in the BLI signal originating from the tumor cells (Figure 27 A2). BLI and MR images for one representative mCherry-rLuc+ GL261 tumor bearing animal are shown in figure 27A3.

mCherry-rLuc + Hs683 tumors also showed a marked growth delay compared to WT Hs683 tumors on week 4; 5 and 6 post injection (Figure 27B1). Although a BLI signal could be observed from the mCherry-rLuc+ Hs683 tumors, it was very small and not proportional to the actual tumor size (Figure 27B2). BLI and MR images for one representative mCherry-rLuc+ Hs683 tumor bearing animal are shown in figure 27B3.

Finally, mCherry-rLuc + U87-MG tumors were assessed for *in vivo* rLuc expression. These tumors did not show a growth delayed on MRI compared to WT tumors (Figure 27C1). As tumors grew larger, BLI signal became apparent which was significantly different compared to the first timepoint (Figure 27C2). BLI and MR images for one representative mCherry-rLuc+ U87-MG tumor bearing animal are shown in figure 27C3.

Since mCherry-rLuc expressing GL261 and Hs683 cells showed a detectable *in vitro* but not *in vivo* rLuc expression *ex vivo* BLI scans from brain slices were also taken (Figure 28). These *ex vivo* measurements showed that although rLuc expression is present in both cell lines, very little signal can be detected *in vivo*.

Figure 27: *In vivo* validation of mCherry-rLuc transduction of malignant glioma cell lines.

- A. mCherry-rLuc expression in the GL261 model
 - 1. MRI showed a slight difference in growth delay of transduced GL261 cells *in vivo*.
 - 2. BLI using Coelenterazin-h as a substrate for rLuc did not show significant rLuc signal originating from the tumor cells.
 - 3. Example of BLI and MR images of one representative mCherry-rLuc + GL261 tumor bearing animal.
- B. mCherry-rLuc expression in the Hs683 model
 - 1. MRI showed a significant growth delay of transduced Hs683 cells *in vivo*.
 - 2. BLI using Coelenterazin-h as a substrate for rLuc showed a slight but insignificantly different from WT cells rLuc signal originating from the tumor cells.
 - 3. Example of BLI and MR images of one representative mCherry-rLuc + Hs683 tumor bearing animal.
- C. mCherry-rLuc expression in the U87-MG model
 - 1. No difference could be shown in growth characteristics between WT and mCherry-rLuc transduced cells *in vivo*.
 - 2. BLI using Coelenterazin-h as a substrate for rLuc showed an increasing BLI signal originating from the tumor.
 - 3. Example of BLI and MR images of one representative mCherry-rLuc + U87-MG tumor bearing animal.

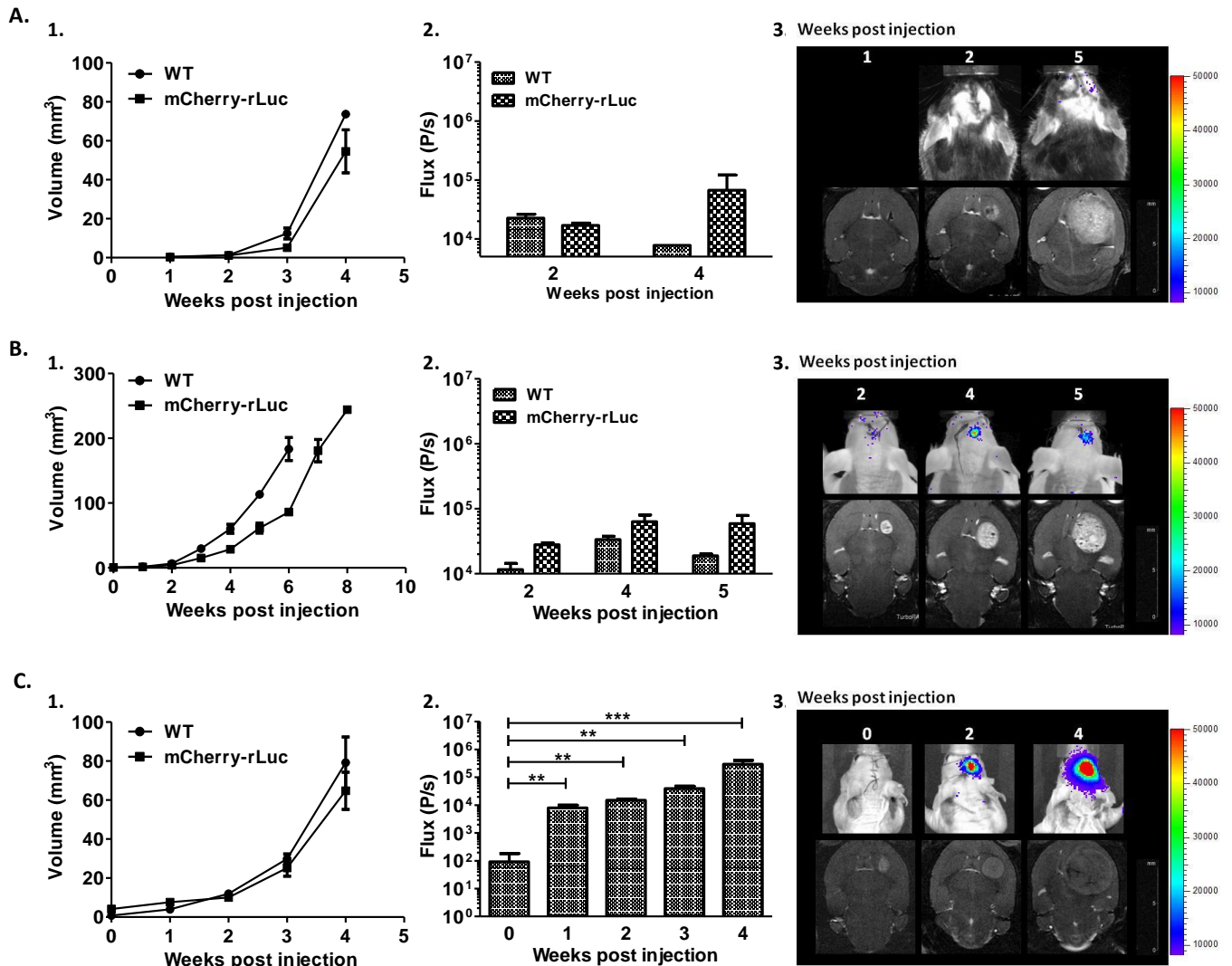
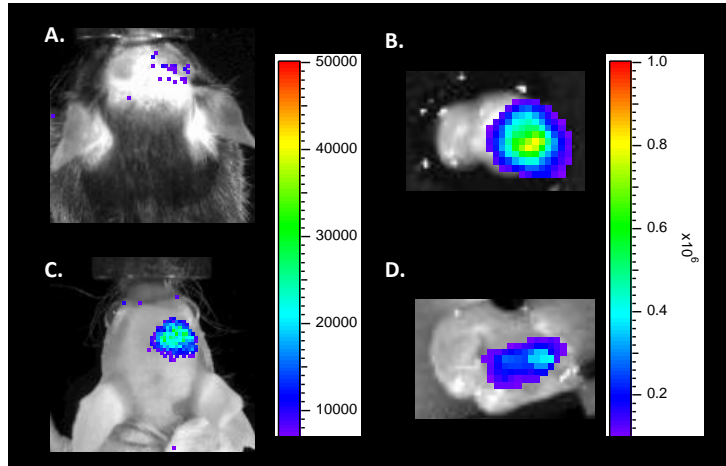


Figure 28: *Ex vivo* validation of mCherry-rLuc expression in GL261 and Hs683 tumors.

- A. *In vivo* BLI of a mCherry-rLuc + GL261 tumor bearing animal showing very little signal originating from the tumor site.
- B. *Ex vivo* BLI of the animal in A did however show that there is rLuc expression present in the GL261 cells.
- C. *In vivo* BLI of a mCherry-rLuc + Hs683 tumor bearing animal showing some signal originating from the tumor site.
- D. *Ex vivo* BLI of the animal in C confirmed rLuc expression in Hs683 cells.



4.4 Discussion

In this study we have evaluated the cells generated in Chapter 3 *in vivo* by MRI, BLI and PET. Due to their self renewal, migration and differentiation capacity, stem cells are increasingly regarded as candidates in regenerative medicine or as cellular vehicles to deliver therapeutic molecules. Although pluripotent stem cells hold the greatest potential, their ability to form teratomas also hampers their clinical use [144]. Multipotent stem cells are more restricted and therefore safer to work with but some may still give rise to mass formation [145]. Before considering stem cells as possible therapeutic agents, it is therefore crucial to investigate the safety of the therapeutic cells.

In this study, we have shown that m/rOct4⁺ BM-HypoSCs are characterized *in vivo* by the formation of masses that show a disrupted BBB integrity, an elevated diffusivity and T2 relaxation times, when engrafted into the healthy rodent brain which is concurrent with data obtained by Lo Nigro *et al* [145] and Burns *et al* (unpublished data) in xenograft and stroke models. These tumors were characterized as yolk sac tumors by H&E staining combined with positive laminin, periodic acid Schiff (PAS), α -fetoprotein (AFP) and cytokeratin staining [145]. Furthermore, it has been shown in our laboratory that even 5×10^4 engrafted cells can give rise to yolk sac tumor formation whereas systemic, intracardiac injection did not result in mass formation (unpublished data). In rats, Oct4⁺ BM-HypoSCs gave rise to large masses characterized by the formation of large fluid filled cysts, wisps of myxoid material in these cystic spaces, necrosis and the consequential immune cell infiltration, characterized mostly by macrophages and lymphocytes. In mice, solid masses developed more slowly over time.

As Oct 4 is a marker of pluripotency [159] we hypothesized that the absence of Oct 4 would reduce the mass forming capacity in the brain as was shown for m/rOct4⁻ BM-MAPCs. We have shown that at least some mOct4⁻ BM-MAPCs survive well *in vivo* without causing masses even when followed for several weeks. Even 110 days after engraftment into healthy rodent brains, no mass formation could be detected, indicating that m/rOct4⁻ BM-MAPCs, like human MAPCs are safe for *in vivo* use confirming the results obtained previously in

a stroke model in our laboratory (unpublished data). Furthermore, mMSC's and hMultistem's do not show tumor formation.

Although one should aim to select stem cells that are safe, stem cells with the required characteristics for stem cell therapy do not always have a favorable safety profile. One novel experimental cancer therapy approach is based on suicide gene expression, where stem cells expressing a suicide gene, such as HSV-TK, are used to kill cancer cells after administration of the substrate ganciclovir. This therapy has been investigated for the treatment of several cancers including glioblastoma [152]. First, we applied the suicide gene therapy approach to HSV-tk positive, mOct4⁻ BM-MAPCs. Ganciclovir treated animals bearing these cells did not show a significant difference in graft volume (MRI) after ganciclovir treatment compared to PBS treated animals as the graft size caused by minor injury related to the injection of 5×10^5 cells is relatively small. The cells did however show a decrease in viability after ganciclovir treatment compared to PBS control animals, proving that the stem cells could be killed selectively.

Next, the yolk-sac tumor forming mOct4⁺ BM-HypoSCs were investigated in order to augment their safety profile. Mice injected with HSV-tk positive mOct4⁺ BM-HypoSCs and treated with PBS grew masses over time as measured by MRI. In contrast, ganciclovir treated animals did not display mass development and even more, the stem cell viability (BLI) decreased until the cells could no longer be detected. Even 12 weeks after the end of the ganciclovir treatment, mass growth could not be detected neither by MRI nor BLI, indicating that GCV concentrations in the brain were sufficiently high for efficient killing of the stem cells.

When allowing masses to form, for 8 days prior to GCV administration cell viability decreased after GCV treatment as assessed by BLI. However, treatment did not result in complete removal of the tumor mass. This is possibly due to the fact that GCV does not reach all tumor cells in a larger mass after a single administration. Further studies concerning repeated GCV administration are required.

Furthermore, animals injected with eGFP-fLuc expressing mOct4⁺ BM-HypoSCs, treated with GCV did not show a reduction in tumor growth or stem cell viability indicating that the cell death described here for GCV

treated animals injected with eGFP-fLuc-HSV-tk positive mOct4⁺ BM-HypoSCs is due to expression of HSV-tk and not by cytotoxic effects of GCV alone.

mMSC's failed to survive for the duration of the treatment (two weeks) in the healthy brain whereas hMultistem's did not seem to respond to GCV treatment *in vivo*. This however might be due to incomplete BBB disruption, which might cause suboptimal GCV concentrations in the healthy brain. Furthermore, *in vitro* data suggested that hMultistem's might be slightly more resistant to GCV treatment compared to mOct4⁺ BM-HypoSCs.

The mechanism of cell killing is still under investigation but the following hypothesis is generally accepted. When the substrate for the suicide gene, e.g. ganciclovir (GCV) / HSV-tk, is provided, GCV enters the cell and is converted by HSV-TK into GCV-monophosphate [82]. The HSV-tk displays a 1000 fold higher affinity for GCV than the mammalian thymidine kinase and therefore, limited side effects are expected. Subsequently, cellular kinases recognize the GCV-monophosphate and will create GCV-triphosphate, a highly toxic guanine nucleoside analogue which causes DNA chain termination and subsequent cell death, which can occur through both apoptotic and non-apoptotic mechanisms [160]. Due to the formation of gap junctions between adjacent cells, ganciclovir monophosphate can passively diffuse into neighboring cells. This phenomenon is also called the bystander killing effect and has already been used for stem cell mediated glioma therapy [82]. Furthermore, results from the suicide gene therapy field suggest that besides this bystander killing effect, a Th1 response might also be generated by necrotic cell death which releases immunostimulatory molecules [161-163]. Thus, a more efficient cell killing can be achieved.

Furthermore, we would also like to point out that although selection of HSV-tk positive cells is very important in order to maximize the suicide gene therapy, non-transduced cells should also be killed as the bystander killing effect, which is well described for suicide gene therapy, also kills neighboring fast growing cells [84, 150-152]. These HSV-tk positive cells therefore have a dual potential purpose. They can be used as vehicles to deliver suicide gene therapy for anti-neoplastic therapy but the system can also be used as a 'safety switch' in case of unwanted and uncontrolled growth of therapeutic cells opening the way for use of

stem cells with an unfavorable safety profile. For the latter application, further research regarding safety and applicability is however mandatory.

Finally, also the mCherry-rLuc⁺ malignant glioma cells were evaluated *in vivo*. Although all cell lines generated a BLI signal *in vitro*, GL261 and Hs683 tumors could only be detected when tumors grew very large and even then, detection was not always straightforward. Therefore, *ex vivo* scans were performed which showed that both tumor cells still expressed the rLuc. In contrast, U87-MG tumors were already detectable at 1 week post injection by using BLI for rLuc.

Several factors may be responsible for the unexpected GL261 and Hs683 results. First, rLuc emits light at 480nm (blue light). At this wavelength, much more absorption occurs by the animals' skin, skull, brain tissue and blood (albumin) compared to eGFP which emits at 560nm (green light). Therefore, less light is available for *in vivo* detection. Furthermore, in Hs683 tumors, BBB disruption is incomplete (see Chapter 5), which might cause insufficient high levels of Coelenterazin-h to enter the brain as it does not pass the BBB easily. GL261 tumors do however display a BBB integrity loss (Chapter 3), so it does not explain the discrepancy between the *in vitro* and *in vivo* data for this cell line. Another reason could be the presence of efflux pumps, which are present on tumor cells [164]. Also, the human glioma xenograft tumor models that we used are generated in Hsd:athymic Nude-Foxn1^{nu} mice. These mice do not synthesize melanin, which also absorbs light. The GL261 model however has a syngeneic host, namely C57BL6/j mice, which do produce melanin that can therefore further absorb the signal coming from the brain. We would like to stress that it is possibly a combination of all these factors which results in the unexpected failure to detect GL261 and Hs683 tumor cells *in vivo*.

As a final remark, we would like to point out that increasing the rLuc expression could possibly overcome the issues with the detection of these tumors. This is however not recommendable as both the GL261 and Hs683 cell lines transduced with mCherry and rLuc already displayed a growth delay *in vivo*.

Chapter 4:

In vivo validation of cell lines for non-invasive imaging of suicide gene therapy

In conclusion, we have shown that at least a fraction of the mOct4⁻ BM-MAPCs remains *in vivo* without causing unwanted side-effects, even when followed for several weeks. This hypothesis is supported by BLI and histological findings where a small but apparent cell graft is still present.

In contrast, mOct4⁺ BM-HypoSCs formed yolk sac tumors. Both stem cell types can however be selectively killed after suicide gene expression making them safer for *in vivo* applications. This approach can also be applied to other, very promising but tumor forming stem cells to augment their safety profile and increase their applicability *in vivo*.

Furthermore, we have validated both tumor transduction and stem cell transduction and labeling *in vivo*. All stem cells were easily detectable by MRI and BLI (fLuc – D-luciferin) but not PET ([¹⁸F] FHBG) whereas for the tumor cells, only the U87-MG could be followed using BLI (rLuc – coelenterazin-h) for the hU87-MG from week 1 post injection.

Chapter 4:

In vivo validation of cell lines for non-invasive imaging of suicide gene therapy

CHAPTER 5

Malignant glioma development

Chapter 5: Malignant glioma model development

This chapter has been compiled based on the following publication:

Leten, C., et al., *In vivo and ex vivo assessment of the blood brain barrier integrity in different glioblastoma animal models*. J Neurooncol, 2014.

5.1 Introduction

One of the characteristics of high grade gliomas is angiogenesis as tumors rely on both co-option of existing blood vessels and neovascularization to meet their oxygen and nutrient requirements [165]. Only specific, carrier mediated transport is possible in the normal brain. Under pathological conditions, both transcellular and paracellular transport increase, thus allowing passage of substances into the brain that normally do not cross an intact blood brain barrier (BBB) [166, 167].

In humans, neovascularization is correlated with tumor grade and malignancy. Therefore, T1 weighted (T1W) magnetic resonance imaging (MRI) after injection of contrast agents like gadolinium chelates, such as Dotarem® (MW 562Da) is performed on a regular basis to assess the BBB integrity and diagnose high-grade gliomas [168]. Accumulation of these chelates in the brain indicates loss of BBB integrity as they normally do not cross the BBB. Contrast enhanced MRI (CE-MRI) has mostly replaced CT for non-invasive BBB integrity assessment as MRI shows higher soft tissue contrast compared to CT [169, 170].

In a preclinical setting, several low and high molecular weight vascular permeability markers are available to assess the BBB integrity [167]. Both radiolabeled markers including alpha-aminoisobutyric acid, sucrose and inulin [171, 172] and non-radioactive low molecular markers such as sodium fluorescein were developed for *ex vivo* assessment of the BBB integrity. Radiolabeled markers can be used for PET/SPECT imaging. Furthermore, high molecular weight markers were developed including horseradish peroxidase, dextran and Evans blue [167]. The non-toxic Evans blue (MW 961) binds to albumin (Evans blue-Albumin: MW 69kDa) directly after intravenous injection and is therefore contained to the blood stream. When sites of BBB disruption are present, Evans blue crosses the BBB, thus resulting in site-specific accumulation [167]. Unfortunately, to assess the BBB disruption with such low or high molecular weight dyes, animals need to be sacrificed and brain sections analyzed, which is labor intensive and requires large number of animals as longitudinal studies on individual animals are impossible. In addition to histological methods, non-invasive

CE-MR imaging protocols using injection of gadolinium chelates, similar to the protocols used in humans have been developed for dedicated small animal MR imaging [35, 168, 173] hereby, facilitating longitudinal studies on a small number of animals.

The loss of the BBB integrity is both in humans and experimental glioma models one of the characteristics used to assess and follow-up therapeutic response of glioblastoma. Furthermore, the effectiveness of some experimental treatments, such as systemic delivery of cells [174, 175] or administration of large or hydrophilic compounds [176] usually depends on the disruption of the BBB. It is therefore crucial to characterize the vascular integrity of tumor models very carefully before assessing novel treatment approaches.

In this study we compared two brain tumor models for the disruption of the BBB. The most frequently used glioblastoma mouse model is the GL261 model, which has been well described [155] with a documented BBB disruption [35]. Furthermore, two human malignant glioma xenograft models, namely the Hs683 oligodendroglioma model [136] and the U87-MG glioblastoma were selected to validate to what extent they meet the hallmarks of glioblastoma models like the disruption of the BBB integrity and for *in vivo* characterization.

5.2 Materials and methods

Cell lines

The GL261 cell line, a mouse glioblastoma model, was obtained from Dr S. Van Gool, University of Leuven, Belgium and cultured as described previously [106]. The Hs683 cell line, derived from a human oligodendroglioma, was obtained from Dr R. Kiss, University of Bruxelles, Belgium and cultured as described previously [136]. U87-MG cells were obtained from the American Type Culture Collection (ATCC, Manassas, VA, USA) and cultured according to the manufacturer's instructions.

Stereotactical injections

All animal experiments were conducted according to the European Union Community Council guidelines and were approved by the local ethics committee of KU Leuven. Animals were anaesthetized by an *i.p.* injection of a Ketamine (Ceva, Pompidou, France, 4.5mg/kg)/medetomidin (Domitor®, Pfizer, New York, USA, 0.6 mg/kg) mixture. Local analgesia (2% xylocain, AstraZeneca, Londen, UK) and antibiotics (6mg/mouse, Ampiveto-20 (200 mg/ml), VMD, New Haw, Surrey, UK) were administered prior to surgery. After fixation of the animals in a stereotactic frame adapted with a Quintessential stereotaxic injector (both from Stoelting, Wood Dale USA), cells were injected (speed: 0.5 $\mu\text{l}/\text{min}$) into the right striatum of C57Bl6/j mice at the following coordinates: 0.5 mm anterior and 2.0 mm lateral to bregma and 3.0 mm from the dura using a 10 μl Hamilton syringe, equipped with a 22 G needle. 2.5×10^5 GL261 cells, 5×10^4 Hs683 cells or 3×10^5 U87-MG cells were injected in C57Bl6/j or Hsd:athymic Nude-Foxn1^{nu} mice (Harlan Laboratories, Indianapolis, Indiana, USA) respectively.

Imaging:

Magnetic resonance imaging (MRI)

All MR images were acquired with a 9.4T Biospec small animal MR scanner (Bruker Biospin, Ettlingen, Germany) equipped with a horizontal bore magnet and an actively shielded gradient set of 600mT m^{-1} (117 mm inner diameter) using a 7cm linearly polarized resonator for transmission and an actively decoupled dedicated mouse surface coil for receiving (Rapid Biomedical, Rimpf, Germany). MRI was performed once per week to follow-up tumor growth and BBB integrity. Prior to scanning, mice were anaesthetized with 2% isoflurane for induction and 1.5% isoflurane for maintenance, respectively. Temperature and respiration were monitored throughout the experiment and maintained at 37°C and 100-120 breaths min^{-1} . T2 weighted MRI scans (RARE sequence, TR:3000 ms; TE:50.2 ms, RARE factor: 9, matrix size 256 x 256, FOV: 2 x 2 cm, number of continuous slices:16, slice orientation: coronal, in plane resolution: $78 \mu\text{m}^2$) were used to monitor tumor growth. The area of the tumor was determined by outlining it manually on all slices of the T2 weighted MR images with coronal orientation using the 5.1 Paravision software (Bruker, Biospin). The sum of the cross sectional discs was used to determine total tumor volume. To validate the integrity of the blood brain barrier, pre- and post-contrast (gadolinium (Dotarem®, Guerbet, Villepinte, France, dosage: 100 μl / mouse of 0.05 mmol/ml, *i.v.*) T1 weighted MR images were acquired (RARE sequence, RARE factor: 4, TR: 819ms, TE: 7.6ms, matrix size: 256 x 256, FOV: 2 x 2 cm, number of slices: 20, slice thickness, 0.5mm, orientation: axial, in plane resolution: $78 \mu\text{m}^2$). The relative signal intensity of the tumor region showing the strongest contrast enhancement (relative to surrounding brain tissue) was determined by placing a region of interest (ROI) over the area using the Paravision 5.1 software. To avoid influences from strong tumor heterogeneity (necrosis), we only analyzed tumor regions with strong contrast enhancements by manual delineation. For statistical analysis of the BBB integrity, pre-contrast scans were subtracted from post-contrast scans after which the procentual increase following gadolinium injection was calculated for the contralateral hemisphere (negative control set to 100%), tumor tissue and extracranial muscle tissue (positive control) for each animal. Significant differences were determined by ANOVA testing (GraphPad PRISM, GraphPad Software, La Jolla, CA, USA) with $p < 0.05$.

Evans Blue Staining

A phototrombotic stroke was induced as described previously [177] as a positive control for Evans blue uptake and the disruption of the BBB. In short, the animal was sedated with isoflurane (2% induction-1.5% maintenance). After exposing the skull, the photosensitizer rose bengal (20 mg/kg, Sigma-Aldrich, St. Louis, MO, USA) was injected intravenously followed by photo-illumination of the right motor cortex with green light (wave length, 540 nm; bandwidth 80nm) from a xenon light (model L-4887; Hamamatsu Photonics, Hamamatsu City, Japan) for 20 min with an irradiation intensity of $0.68 \text{ W}/\text{cm}^2$. Focal activation of the photosensitive dye results in local endothelial cell injury leading to microvascular thrombosis and circumscribed cortical infarctions. Afterwards, the mouse was allowed to recover. Within 24 hours, Evans blue (4 μl / g of body weight of a 2% Evans blue solution [167]) was administered *i.v.*

and the mouse was perfused approximately 25 minutes post injection. At several time points, one animal from the GL261 tumor bearing group (week 2 and 4) and one animal from the Hs683 tumor bearing group (week 2, 4 and 5) was sacrificed similarly.

Endpoints

Animals were sacrificed when symptoms reached grade 3 out of 4 (grade 0 for healthy mice, grade 1 for slight unilateral paralysis, grade 2 for moderate unilateral paralysis and/or beginning hunchback, grade 3 for severe unilateral or bilateral paralysis and pronounced hunchback, and grade 4 for moribund mice) [66].

Histology

Animals were sacrificed by an overdose of Nembutal (250µl, *i.p.*, Ceva, Libourne, France) and subsequently perfused with 4% ice-cold paraformaldehyde (PFA) solution (Sigma-Aldrich). After overnight post-fixation in 4% PFA, the brain tissue was kept in a 0.1% sodium azide solution (Fluka, Sigma-Aldrich, Belgium) at 4°C. Paraffin sections (5µm thickness) were sliced and a Masson's trichrome staining and a GFAP staining were performed. In short, for the Masson's staining, sections were deparaffinized and rehydrated prior to hematoxylin, ponceau / fuchsine and aniline blue staining after which they were dehydrated and mounted with DPX (Sigma-Aldrich). For the GFAP staining, which was kindly provided by Professor Verfaillie from the Stem cell Institute, KU Leuven, sections were also deparaffinized and rehydrated prior to staining. Subsequently, antigen retrieval was performed and sections were incubated overnight at 4°C with the primary polyclonal rabbit anti-glial fibrillary acidic protein (GFAP) antibody (1/250, Dako – Z0334), followed by staining with the secondary Alexa Fluor® 488 goat anti-rabbit IgG antibody (1/500, Invitrogen, A11034) for 30 min at room temperature and Hoechst (1/1000, Sigma-Aldrich, 33258) after which they were also dehydrated and mounted with Prolong® Gold antifade reagent(Invitrogen, P36930).

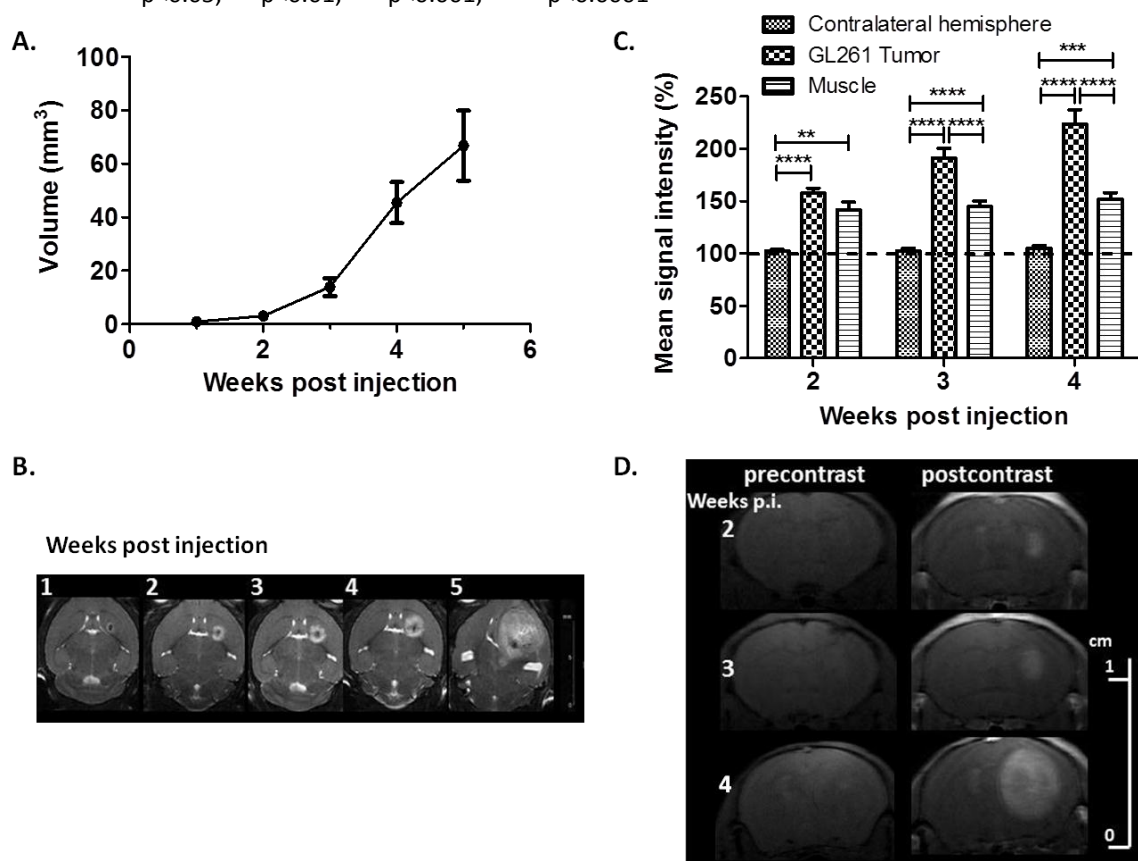
5.3 Results

5.3.1 Mouse glioblastoma model (GL261)

Injection of 2.5×10^5 GL261 cells in the striatum of C57BL6/J mice resulted in tumors with an average size of $76 \pm 14 \text{ mm}^3$ at 5 weeks post injection Figure 29A. MR images of a representative GL261 tumor bearing animal are shown in Figure 29B. Weekly MRI sessions showed an increased BBB disruption over time (Figure 29C, D), starting already from week 2 post glioma injection. The relative signal intensity increased over time indicating progressing BBB disruption with tumor growth.

Figure 29: BBB integrity assessment by contrast enhancement in T1W MRI for GL261 tumors.

- Tumors grow gradually over time until they reach an average size of $76 \pm 14 \text{ mm}^3$ at 5 weeks post injection (N = 12).
 - Example of tumor growth in a representative animal (T2W MR image, coronal orientation).
 - Intravenous injections of gadolinium showed a loss of BBB integrity, which deteriorates over time (N = 11).
 - Example of contrast enhancement on T1W MR images in the same animal mentioned in C over time.
- * $p < 0.05$, ** $p < 0.01$, *** $p < 0.001$, **** $p < 0.0001$

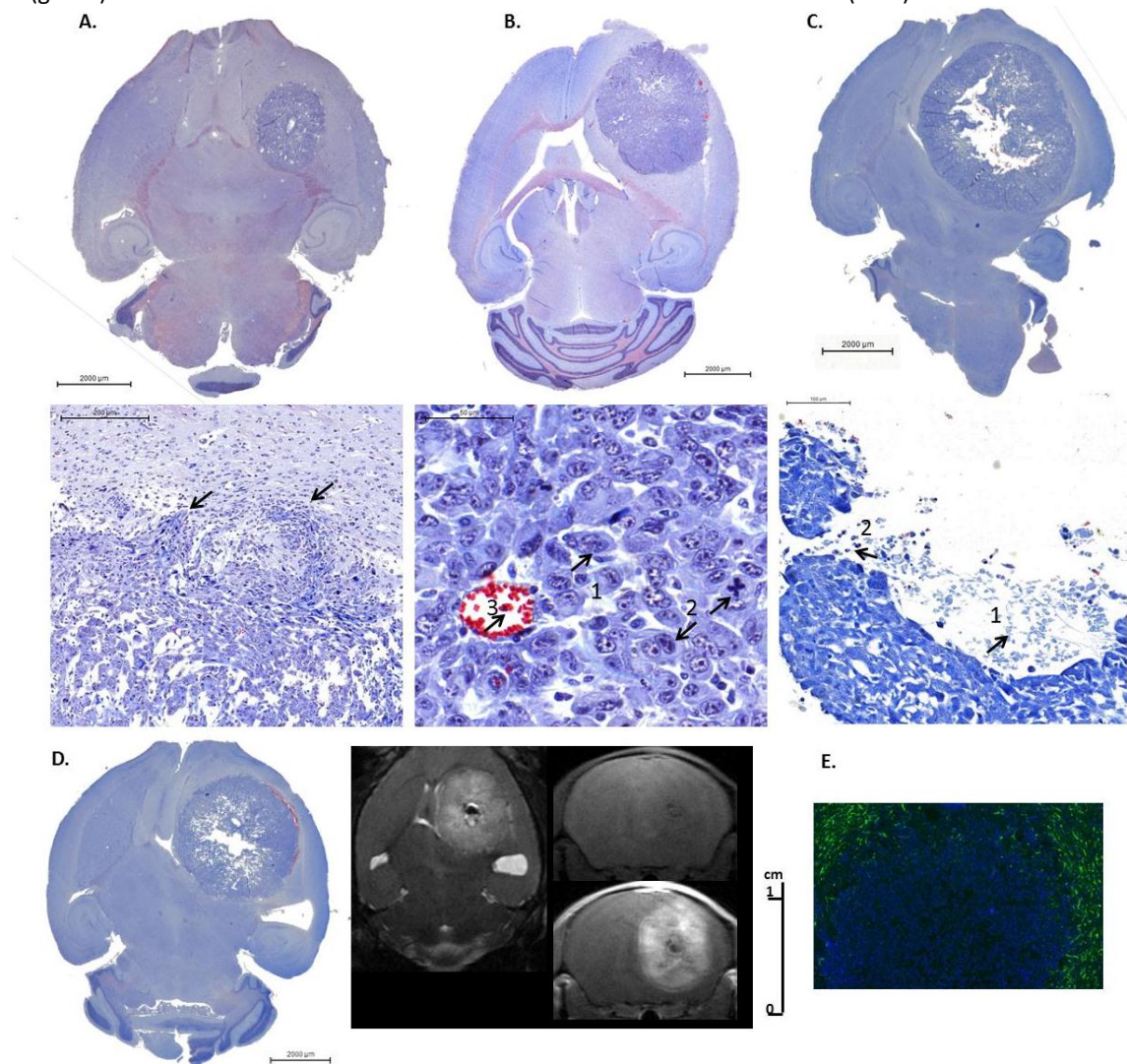


Furthermore, histological analysis (Figure 30) was performed to evaluate the characteristics of the developing tumor more elaborately. Masson's trichrome staining revealed tumor infiltration of small tumors into the normal brain parenchyma (Figure 30A) whereas this was less apparent in larger tumors. Also nuclear

atypia (Figure 30B1), mitosis (Figure 30B2) and the presence of extensive vascularization (Figure 30B3), all characteristics of glioblastoma were detected. Furthermore, histology showed both necrosis and apoptosis as tumors grew larger (Figure 30C), which correlated with non-enhancing regions on MRI after gadolinium injection (Figure 30D). Also a midline shift caused by the aggressive growth of the tumor was observed both on MRI and histology. Finally, GFAP staining proved negative (Figure 30E).

Figure 30: Histological analysis of the GL261 tumors.

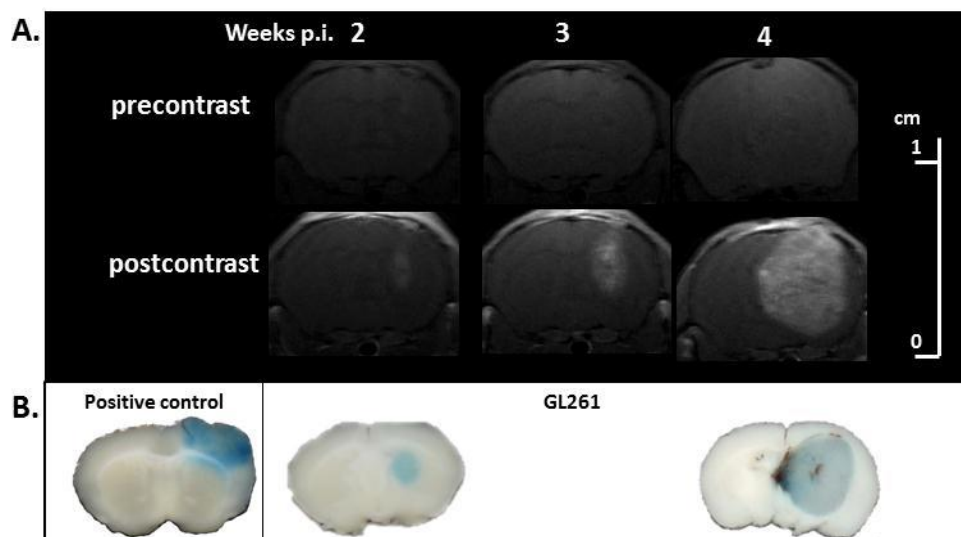
- Infiltration of the tumor cells into normal brain parenchyma was observed mainly for smaller tumors, whereas this was less apparent in larger tumors.
- Several typical characteristics of glioblastoma were detected, such as nuclear atypia (1), mitosis (2) and the presence of extensive vascularization (3).
- In very large tumors, necrosis (1) and apoptosis (2) became apparent in the centre of the tumors.
- Central necrosis correlated with non-enhancing regions on MRI after gadolinium injections. Both on MRI and histology, a midline shift became apparent as tumors grew larger.
- GFAP staining showed that the tumor is negative for the glial fibrillary acidic protein as no GFAP staining (green) could be detected in the tumor whereas it was stained with Hoechst (blue).



Subsequently, one animal was sacrificed on week 2 and 4 post tumor cell injection after Evans blue injection to confirm loss of BBB integrity (Figure 31). Infiltration of the Evans blue solution into the tumor confirmed the BBB disruption observed on MR images as early as week 2 post glioma initiation.

Figure 31: BBB integrity assessment using Evans blue staining.

- A. Contrast enhancement in T1w MRI before and after gadolinium injection showed a loss of the BBB integrity.
- B. Sliced brains of Evans blue perfused animals confirmed BBB disruption on both week 2 and week 4 post tumor cell injection. A phototrombotic stroked animal was used as a positive control for BBB disruption.



5.3.2 Human malignant glioma xenograft models

5.3.2.1 Human glioma xenograft (oligodendroglioma) model (Hs683)

Injection of 5×10^4 Hs683 cells in the striatum of Hsd:athymic Nude-Foxn1^{nu} mice resulted in tumor formation with an average tumor volume of $244 \pm 0.3 \text{ mm}^3$ at 8 weeks post injection (Figure 32A) with animals developing symptoms between week 6 and 8. MR images of a representative Hs683 tumor bearing animal are shown in Figure 32B. T1 weighted MR imaging following *i.v.* injection of gadolinium showed loss of the BBB integrity compared to the contralateral hemisphere (Figure 32C). However, the relative changes in signal intensity compared to the contralateral hemisphere and extracranial muscle tissue were much smaller than those observed for the GL261 tumors.

In contrast to the GL261 glioblastoma model, extensive heterogeneity was evident on T1 weighted post-contrast MR images in large Hs683 model (Figure 32D), which was confirmed by T2 weighted MR images (Figure 33A) and histological analysis (Figure 33B and C) of Hs683 tumors. Masson's trichrome staining of

paraffin embedded brains revealed large fluid filled cysts but no regions of pronounced necrosis or apoptosis. Many of the large fluid filled cysts also contained blood. Finally, GFAP staining was also negative for Hs683 tumors (Figure 33D).

Figure 32: BBB integrity assessment by MRI for the Hs683 tumor model.

- A. Tumors grew gradually over time until they reached an average size of $244 \pm 0.3 \text{ mm}^3$ at 8 weeks post injection (N = 22).
- B. Example of Hs683 tumor growth in a representative animal (T2W MR images, coronal orientation).
- C. Intravenous injections of gadolinium showed a loss of BBB integrity starting from week 2 post tumor initiation (N = 22).
- D. Intratumoral heterogeneity of the integrity of the BBB causes differences in maximal signal intensity on later time points. Areas with high (red arrows) and low signal intensities can be seen within a single tumor.

* $p < 0.05$, ** $p < 0.01$, *** $p < 0.001$, **** $p < 0.0001$

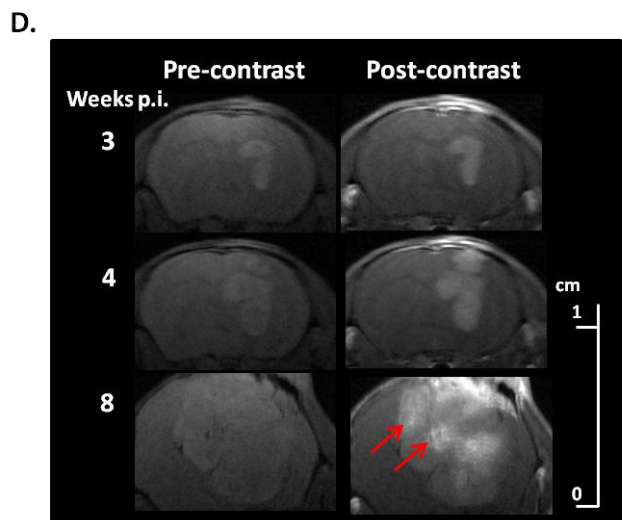
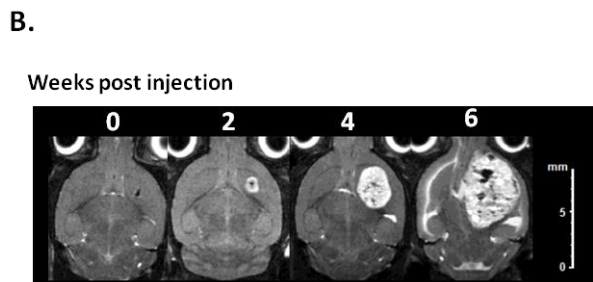
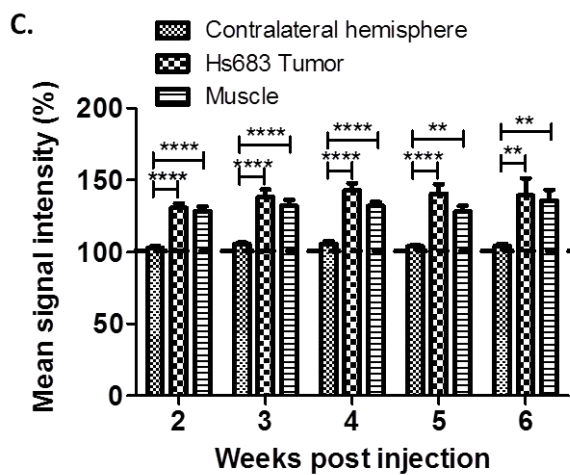
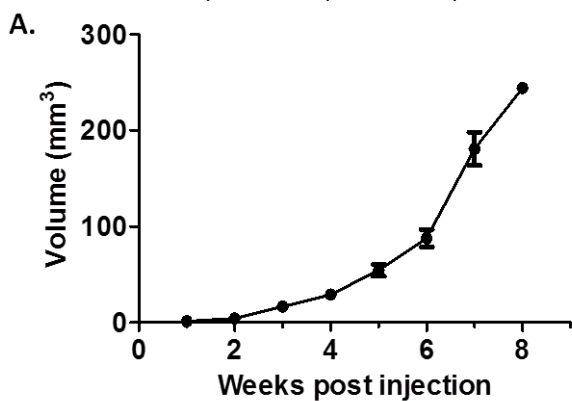
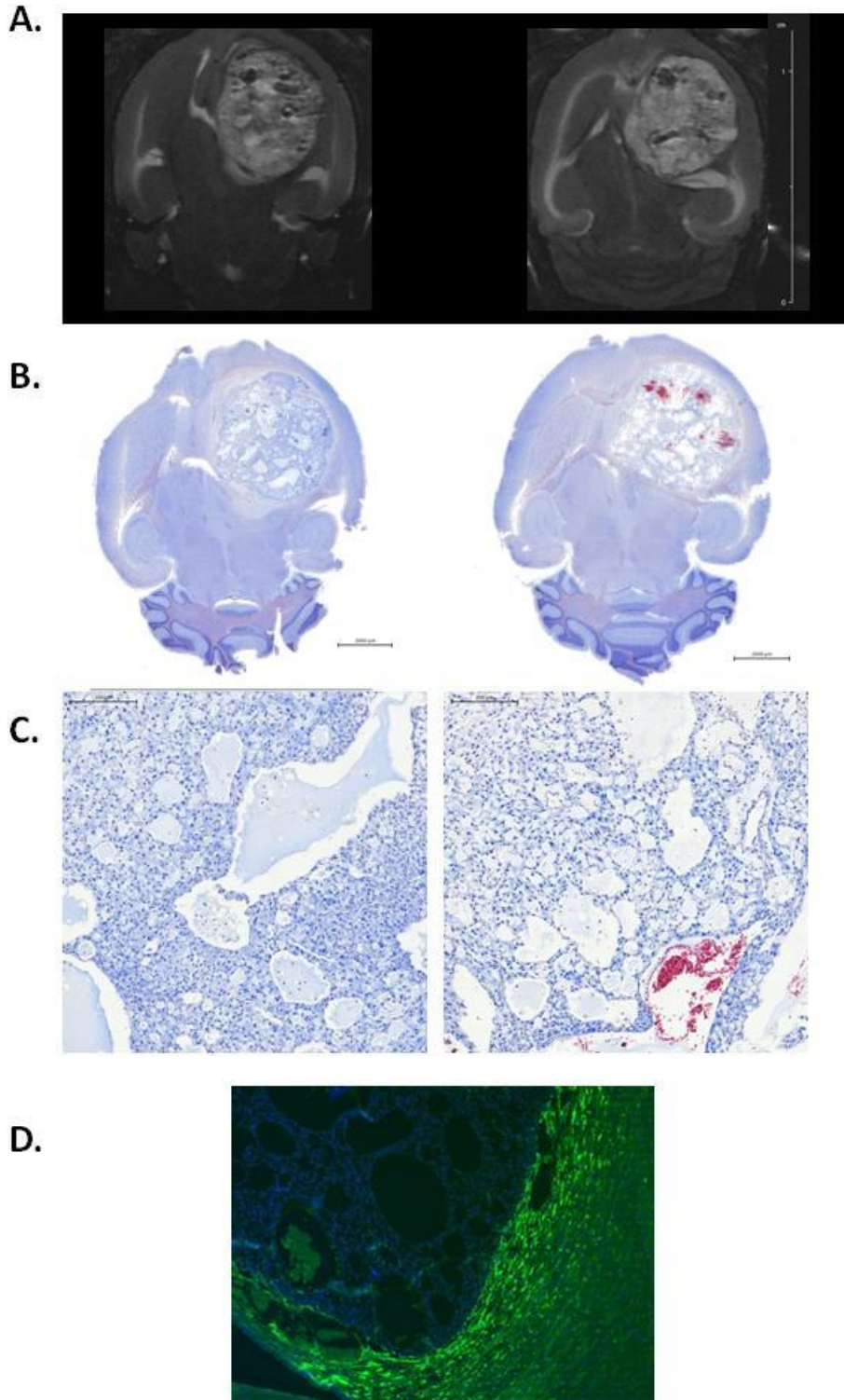


Figure 33: Histological analysis of the human glioma xenograft (oligodendroglioma - Hs683) model.

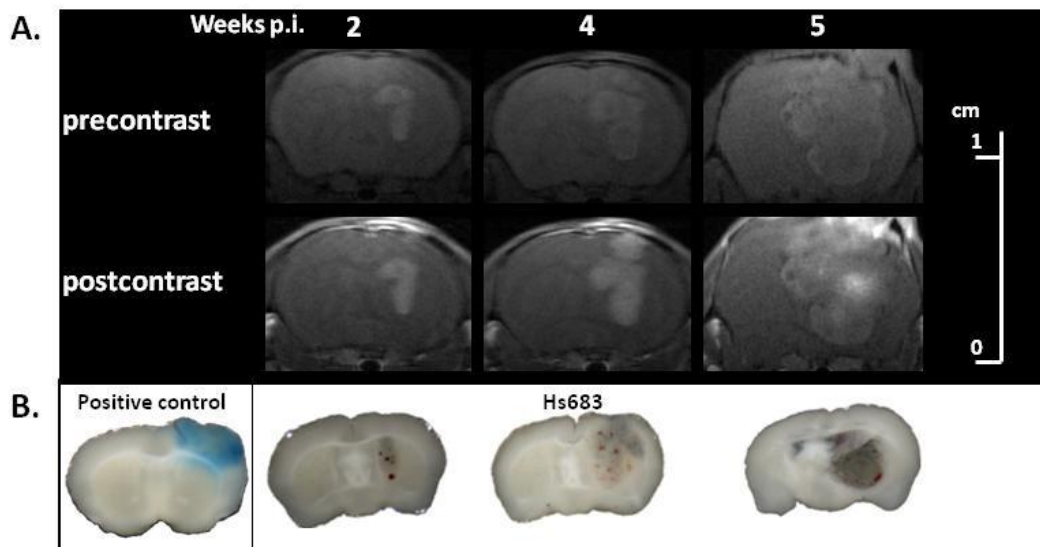
- A. T2W MR images (coronal orientation) of Hs683 tumor bearing animals at week 6 post tumor initiation.
- B. Corresponding 5 μm thick paraffin embedded brain sections stained with a Masson's trichrome staining showed large fluid filled cyst formation and blood vessels which corresponded to respectively hyper-and hypointense areas on T2W MR images shown in A.
- C. Examination of the tumors did not show pronounced necrosis/apoptosis (10x).
- D. GFAP staining was negative for Hs683 tumors (5x). (Hoechst = blue)



Subsequently, animals were sacrificed following Evans blue injections on weeks 2, 4 and 5 post tumor initiation to confirm the observations made by T1 weighted post-contrast MR images (Figure 34). Loss of BBB integrity in the Hs683 model could however not be shown at any of the mentioned time points by Evans blue, which is in line with the relatively small changes in the T1 weighted post-contrast MR images.

Figure 34: Assessment of the BBB integrity using Evans blue staining in the Hs683 tumor model.

- A. Contrast enhancement on T1W MRI before and after gadolinium injection showed BBB disruption..
 - B. Sliced brains of animals receiving Evans blue prior to perfusion did not show BBB integrity loss for any of the animals on weeks 2, 3, 4 or 5 post tumor cell injection.
- A phototrombotic stroked animal was used as a positive control for BBB disruption.



5.3.2 Human glioma xenograft (glioblastoma) model (U87-MG)

The second human malignant glioma model that was selected was the U87-MG cell line which is classified as a human glioblastoma by the supplier. Injection of 3×10^5 U87-MG cells in the striatum of Hsd:athymic Nude-Foxn1^{nu} mice resulted in tumors with an average size of $65 \pm 10 \text{ mm}^3$ at 4 weeks post injection (Figure 35A) with animals developing symptoms at a very late stage. T1 weighted MR imaging following *i.v.* dotarem injections showed BBB integrity loss (Figure 35B). T2 weighted anatomical MR images of a representative U87-MG tumor bearing animal are shown in Figure 35C. These tumors seemed rather homogeneous on anatomical scans, which was confirmed by T1 weighted pre- and post-contrast MR images (Figure 35D) showing a homogenous BBB integrity loss.

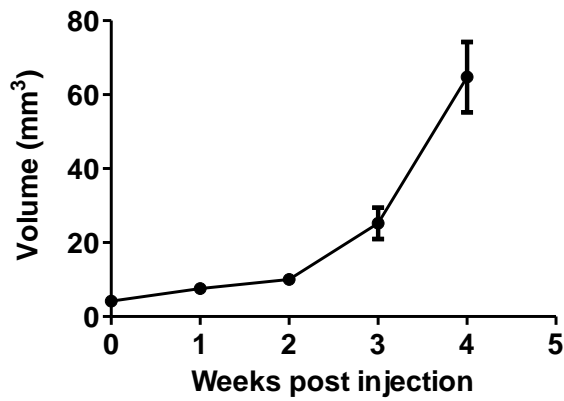
Histological analysis (Figure 36) was performed which confirmed the results obtained by MRI. A general overview showed a homogeneous tumor environment with some bleedings at the tumor border (Figure

36A). Further analysis revealed several characteristics of glioblastoma including mitosis and nuclear atypia (Figure 36B: 1, 2). Also striking in this tumor model was the presence of connective tissue in the tumor region which was predominantly present in the central part of the tumor but not so much in the tumor border (Figure 36C: 3). Finally, microbleedings were also apparent on histological sections (Figure 36C: 4).

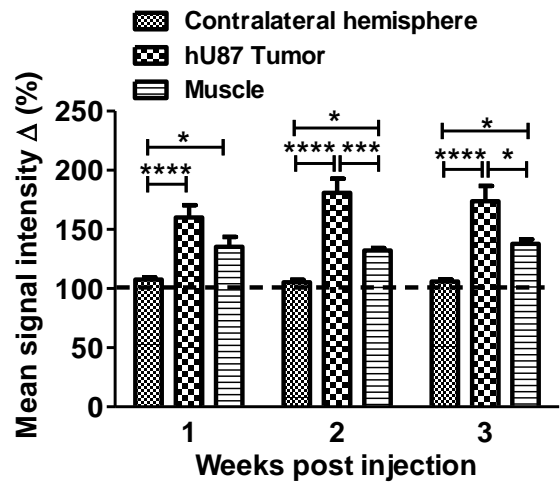
Figure 35: Human glioma xenograft (glioblastoma - U87-MG) model characterization.

- A. Tumors grew gradually over time until they reached an average size of $65 \pm 10 \text{ mm}^3$ at 4 weeks post tumor cell injection (N = 3).
- B. Example of U87-MG tumor growth in a representative animal (T2 weighted MR images, coronal orientation)
- C. Intravenous injections of gadolinium showed a loss of the BBB integrity starting from week 2 post tumor initiation (N = 3).
- D. Contrast enhancement on T1 weighted post-contrast MR images showed a rather homogeneous tumor environment.

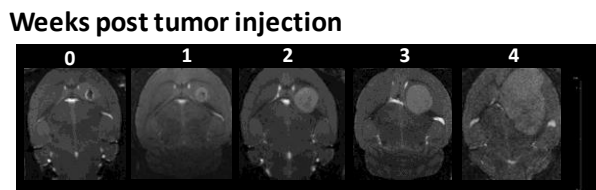
A.



C.



B.



D.

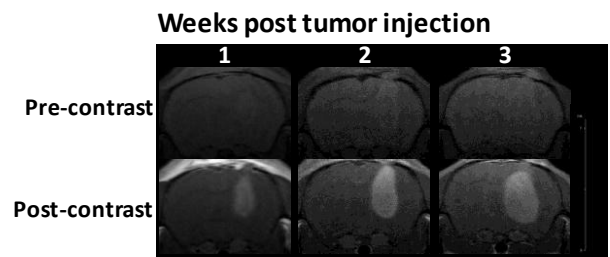
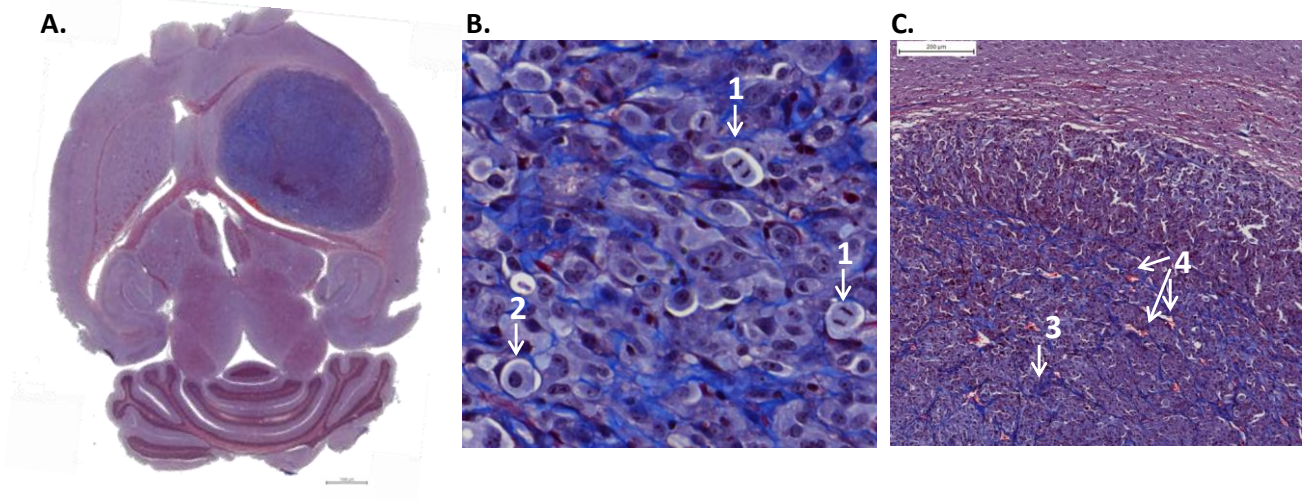


Figure 36: Histological analysis of the human glioma xenograft (glioblastoma - U87-MG) model.

- A. General overview of a paraffin section stained using a Masson's trichrome staining from the brain of a representative U87-MG tumor bearing animal, sacrificed at week 4 post injection when symptoms became apparent. Tumors appeared rather homogenous which corresponded with the obtained MR images.
- B. Analysis of the tumors revealed glioblastoma characteristics such as mitosis (1) and nuclear atypia (2). Furthermore, the presence of connective tissue was observed (blue lines). (40x)
- C. The connective tissue seemed to be mainly present in the tumor bulk (3) but not so much in the tumor border. (10x). Microbleedings (4) were observed both in the tumor itself and at the tumor border (10x).



5.4 Discussion

In this study, the BBB integrity was assessed in one mouse glioblastoma model (GL261) and two high grade human glioma xenograft mouse models (Hs683 and U87-MG). One of the hallmarks of high grade gliomas is neovascularization [178], characterized by severe leakiness [179], which is correlated with tumor grade and malignancy [168]. Furthermore, some experimental brain tumor treatments, using for instance systemically injected stem cells [174, 175] or administration of large or hydrophilic therapeutic molecules [176], could be hampered by incomplete BBB disruption, which might decrease treatment efficacy. It is therefore crucial to characterize tumors models very carefully before considering the assessment of possible treatment regimes. Here, we compared the assessment of the BBB disruption by using CE-T1W MRI and the high molecular weight marker, Evans blue. While CE-T1W MRI is common practice in the clinic, we have used MRI and Evans blue staining for the comparison of a frequently used experimental model (GL261) with the less frequently used, human glioma xenograft models (Hs683, hU87).

One of the most used glioblastoma models in preclinical research is the GL261 model as it is a syngeneic and well characterized model with a very reproducible growth. In this model, BBB disruption was shown as soon as 2 weeks post tumor cell injection (2.5×10^5). Hereby, we confirmed the results obtained previously by Cha *et al* [35] and proved that the applied methodology can be used to assess BBB disruption. Furthermore, we showed infiltration, mitosis, nuclear atypia and the presence of blood vessels in these tumors. Extensive central necrosis was however only observed in the GL261 model but not the U87-MG nor the Hs683 model. Also a midline shift due to the aggressive growth of the tumor, causing elevated intracerebral pressure, was apparent both on MRI and histological analysis. GFAP staining was negative, which is consistent with previously published reports [155].

Translation of the results obtained in preclinical animal research is however not straight forward [70]. We have used human glioma xenograft animal models, (transplantation of human tumor cells (Hs683) in an immune-suppressed animal), which is less extensively characterized.

The BBB integrity of the GL261 model was compared with the Hs683 model. These tumors grew very large before resulting in grade 3 symptoms. Furthermore, large fluid filled cysts appeared both on MRI and BLI.

These tumors were also GFAP negative which is consistent with previous reports from Belot *et al*, who observed very low levels of GFAP mRNA [180]. Lamoral-Theys *et al* proposed that this oligodendroglioma model could represent a glioblastoma with an oligodendroglial origin [181]. To our knowledge there are however no reports on the BBB status in this model. CE-T1W MRI showed a heterogeneous contrast enhancement of lower relative signal intensity changes in the tumor region when compared to the GL261 model. In contrast, Evans blue did not give evidence for BBB disruption at any time point. Although loss of BBB integrity is a general characteristic of glioblastoma, little is known about the actual mechanisms involved in the BBB disruption. One hypothesis is however that increased MMP3 activity, followed by agrin degradation results in loss of astrocyte polarity causing BBB integrity loss [182]. BBB disruption on MRI but not after Evans blue injection could be explained by an incomplete BBB disruption as gadolinium chelates (Dotarem®) and Evans blue bound to albumin have different molecular weights of 562 Da and 69 kDa, respectively. If the BBB is not fully disrupted, larger molecules would have more difficulty passing the BBB, which would explain the negative Evans blue staining.

These results might aid researchers to assess mechanisms of novel therapeutic approaches where the breakdown of the BBB might be of importance. For example, Mathieu *et al.* studied the combination of chemotherapeutics (Temozolomide) and anti-angiogenic compounds (Bevacuzimab) where Temozolomide is able to cross the BBB (MW Temozolomide: 149 Da, MW Dotarem: 562Da) but Bevacuzimab would not be able to cross the BBB (MW Bevacuzimab: 149 kDa, MW albumin-bound Evans blue: 69 kDa) but may still exert its anti-angiogenic effect from within the tumor vessels [183]. In conclusion, the Hs683 model should be used with caution when using therapeutic products that normally do not pass the BBB easily.

The third model that was characterized was the U87-MG model. MRI showed a homogenous loss of BBB integrity as early as one week post injection which remained present until grade 3 symptoms occurred. Further histological analysis confirmed the homogenous nature of these tumors and several glioblastoma characteristics such as mitosis, nuclear atypia and the presence of blood vessels were observed. The formation of connective tissue in the U87-MG tumors was also very striking on Masson's trichrome staining.

Finally, a difference in heterogeneity of the BBB disruption was observed by CE-T1W MR imaging of these glioblastoma models. Glioblastomas are known for their inter- and intratumoral heterogeneous nature [184, 185], which logically results in regional differences in contrast enhancement. Therefore, we have analyzed only enhancing regions for our semi-quantitative assessment of the BBB disruption, which are also the regions selected in the clinic for histopathological evaluation [186]. The GL261 and U87-MG tumors appeared relatively homogenous on CE-T1W MR imaging, even as tumors grew very large. Only very few regions did not enhance on T1W MRI, representing necrotic regions, which was also confirmed on histological sections. The Hs683 tumors became however increasingly heterogeneous over time, with the presence of very large fluid filled cysts and microbleedings shown both on T2 weighted images and histological sections, which also explains their heterogeneous contrast enhancement on CE-T1W MR images. Recently, macromolecular Gadolinium-chelates, such as albumin bound chelates, have been investigated as contrast agents for BBB disruption [187]. Although promising results have been reported, further feasibility studies are required as preliminary results show that longer delay times of up to 4 hours are required prior to imaging for obtaining reliable results [187].

In conclusion, in this study the BBB integrity was assessed by means of CE-T1W MR imaging and Evans blue assessment. The BBB integrity data from both methods was concurrent for the GL261 glioblastoma model, clearly indicating BBB integrity loss as soon as 2 weeks post tumor cell injection. In contrast, the data obtained for the Hs683 oligodendroglioma model showed a limited BBB disruption based on the high molecular weight Evans blue staining and a reduced uptake of low molecular weight gadolinium chelates as indicated by CE-T1W MRI. These results clearly indicate the importance of checking the BBB integrity status using different methods. This is in particular of importance for the assessment of therapeutic molecules and the selection of appropriate animal models. Care should be taken with the appropriate assessment of the BBB disruption prior to commencing therapeutic investigations.

Chapter 6

Multi-modal imaging of the bystander killing effect in malignant brain tumors

Chapter 6:
Multi-modal imaging of the bystander killing effect in malignant brain tumors

Chapter 6:

Multi-modal imaging of the bystander killing effect in malignant brain tumors

This chapter has been compiled based on the following publication:

Leten C., et al., Assessment of bystander killing mediated therapy of malignant brain tumors using a multi-modal imaging approach. (Submitted to Stem cell research & therapy)

6.1 Introduction

Gliomas arise from glial cells (astrocytes, oligodendroglial and ependymal cells) and are the most common brain tumors in humans. They comprise a broad range of lesions with distinct differences in malignancy, which is classified according to the World Health Organization [5]. Glioblastoma multiforme (GBM) is the most malignant tumor (WHO grade IV) in the spectrum of brain tumors [1]. The prognosis of patients diagnosed with GBM is still extremely poor with a 5-year survival of less than 3% of patients despite multimodal treatment approaches consisting of surgery and concomitant radio- and chemotherapy [188]. Therefore, new treatment modalities are under investigation, among which therapy based on the bystander killing effect following suicide gene therapy [84, 150-152].

Previously, several clinical trials have attempted to treat glioblastoma patients using viral vectors encoding for HSV-TK to directly introduce the suicide gene within the tumor cells, with usually poor results [70]. This is generally believed to be caused by insufficient distribution of the viral vectors throughout the tumor [189]. Therefore, attention turned to carriers such as bacteria [71, 190] and tumor tracking stem cells [191] to enhance delivery of the suicide gene. Stem cells that are capable of forming gap junctions with infiltrating tumor cells will allow transfer of the GCV-phosphate into neighboring cells, which results in bystander mediated tumor cell killing [192, 193]. This approach can in theory eliminate both the primary tumor and the infiltrating tumor cells, thus eliminating sources of possible recurrent tumors [82].

The feasibility of this strategy was demonstrated by several groups in both xenograft and syngeneic animal models [82, 84, 93, 151, 174, 194]. Miletic *et al.* [82, 152] and Matuskova *et al.* [85] demonstrated a potent bystander killing effect of HSV-TK expressing rat bone marrow-derived tumor-infiltrating progenitor cells on

Chapter 6:
Multi-modal imaging of the bystander killing effect in malignant brain tumors

9L rat gliomas and human mesenchymal stem cells (hMSC's) on the human glioblastoma cell lines 8-MG-BA, 42-MG-BA and U-118 MG respectively.

In previous reports, different imaging modalities have been used mainly for the assessment of the treatment rather than for guidance of the therapy [194]. In a clinical setting, patients are routinely followed up by non-invasive imaging such as magnetic resonance imaging (MRI) and positron emission tomography (PET) [195, 196]. In a preclinical setting, these non-invasive imaging techniques are also available and should therefore, when possible, also be used to guide therapy and evaluate treatment response. Furthermore, additional preclinical imaging modalities such as bioluminescence imaging (BLI) are available to further optimize the acquired information prior to treatment initiation and follow-up of therapeutic efficacy [197]. In addition, molecular imaging methods could also be used to monitor the location of therapeutic cells [198].

In this chapter, the therapeutic potential of these mOct4⁻ BM-MAPCs was assessed in a mouse glioma model and in particular, the guidance of this therapy by *In vivo* multi-modal imaging methods (MRI, BLI and PET) for optimization of the therapeutic response and for identification of therapeutic windows. In short, therapeutic eGFP, fLuc and HSV-tk expressing mMSC's, mOct4⁺ BM-HypoSCs and mOct4⁻ BM-MAPCs were assessed in GL261 tumor bearing C57BL6/j mice while therapeutic hMultistem's were assessed in human malignant glioma xenograft models (Hs683/U87-MG) for cell tracking properties and their tumor killing capabilities.

6.2 Materials and Methods

Cell culture

All cell lines (mMSC's, mOct4⁻ BM-MAPCs and mOct4⁺ BM-HypoSCs, GL261, U87-MG, Hs683) were cultured as described previously (Chapter 3).

Stereotactical tumor and/or stem cell injections

All animal experiments were conducted according to the European Union Community Council guidelines and were approved by the local ethics committee of the KU Leuven. Before surgery, animals were anaesthetized by an *i.p.* injection with a mixture of ketamine (Ketamine1000, 4.5mg/kg, Ceva, Pompidou, France)/medetomidin (0.6 mg/kg, Domitor®, Pfizer, New York, USA). Local analgesia (2% xylocain, AstraZeneca, London, UK) and antibiotics (6mg/mouse, Ampiveto-20, 200mg/ml, VMD, New Haw, Surrey, UK) were administered prior to surgery. After fixation of the animals in a stereotactic frame adapted with a stereotaxic injector (both from Stoelting, Wood Dale USA), cells were suspended in 5µl PBS and injected (0.5 µl/min) with a 10 µl Hamilton syringe, equipped with a 22 G needle, into the right striatum of C57BL6/j mice at the following coordinates 0.5 mm anterior and 2.0 mm lateral to bregma at 3.0 mm from the dura.

Glioblastoma mouse model (GL261): Suicide gene therapy

2.5×10^5 GL261 were stereotactically injected in the striatum of C57BL6/j mice and allowed to grow for two weeks prior to intratumoral stereotactical injection of 5×10^5 labeled and transduced mOct4⁻ BM-MAPCs. [155] All animals received tumor induction followed by the generation of three treatment groups two weeks after tumor cell injection. As such, SHAM operated animals, which received a PBS injection, PBS treated animals which received 5×10^5 mOct4⁻ BM-MAPCs and that were treated with PBS and GCV treated animals, which also received 5×10^5 mOct4⁻ BM-MAPCs but were treated with GCV, were distinguished. To reduce the blooming effect and the possible negative effects on stem cell behavior, only a limited % of cells were labeled prior to injection. (mMSC's and mOct4⁺ BM-HypoSCs: 1%, mOct4⁻ BM-MAPCs: 1 or 10%). Imaging was performed prior to (MRI) and following (MRI/BLI) stem cell injection (1 day and 5 days post stem cell injection for mMSC's and mOct4⁺ BM-HypoSCs and 1 day after stem cell injection for mOct4⁻ BM-MAPCs) and after which GCV (50mg/kg) or PBS was administered for 14 consecutive days. At the end of treatment both MRI and BLI were performed to assess tumor response and mOct4⁻ BM-MAPC viability. Responding animals were defined as animals with tumors smaller than 5 mm^3 at the end of GCV treatment. Some animals were followed up after the end of treatment for progression free survival analysis.

Human glioma xenograft models (Hs683-U87-MG): Suicide gene therapy

3×10^5 U87-MG or 5×10^4 Hs683 cells were stereotactically injected in the striatum of Hsd:athymic Nude-Foxn1^{nu} mice and allowed to grow for one (U87-MG) or two (Hs683) weeks prior to intratumoral stereotactical injection of 5×10^5 labeled and transduced hMultistem's. All animals received tumor induction followed by the generation of three treatment groups at the time of stem cell injection. As such, SHAM operated animals, which received a PBS injection, PBS treated animals which received 5×10^5 hMultistems and that were treated with PBS and GCV treated animals, which also received 5×10^5 hMultistems but were treated with GCV, were distinguished. To reduce the blooming effect and the possible negative effects on stem cell behavior, only 1% labeled hMultistems were injected. Imaging was performed prior to (MRI) and following (MRI/BLI) hMultistem injection after which GCV (50mg/kg) or PBS was administered for 14 consecutive days. At the end of treatment both MRI and BLI were performed to assess tumor response and hMultistem viability. Responding animals were defined as animals with tumors smaller than 5 mm^3 at the end of GCV treatment. For GL261 bearing animals treated with mOct4⁻ BM-MAPCs, some animals were followed up after the end of treatment for a progression free survival analysis. Two GCV treated animals were followed for 184 days without tumor regrowth after which, animals were sacrificed. A progression free survival curve analysis was performed using GraphPad PRISM (GraphPad Software PRISM, La Jolla, CA, USA).

Imaging:

Magnetic resonance imaging (MRI): Suicide gene therapy

All MR images were acquired with a 9.4 T Biospec small animal MR scanner (Bruker Biospin, Ettlingen, GE) equipped with a horizontal bore magnet and an actively shielded gradient set of 600 mT m^{-1} (117 mm inner diameter) using a 7cm linearly polarized resonator or a quadrature decoupled resonator for transmission and an actively decoupled dedicated mouse surface coil for receiving (Rapid Biomedical, Rimpfing, Germany).

For the GL261 model, MRI was performed after GL261 tumor induction, prior (=d14 post glioma injection) and following stem cell injection but before treatment initiation (=d16 post glioma injection) and at the end of the treatment (=d30

post glioma injection), whereas for the human glioma xenograft models MRI was performed before (d15/d7 post tumor injection) and after (d17/d9 post tumor injection) stem cell injection but before treatment initiation and at the end of treatment (d31/d24 post tumor injection) for Hs683/hU87 respectively. Mice were anaesthetized with 2% isoflurane in oxygen for induction prior to scanning and 1.5% isoflurane in oxygen for maintenance. Temperature and respiration were monitored throughout the experiment and maintained at 37°C and 100-120 breaths / minute. For *in vivo* tracking of the SMG²-mPEGSi labeled mOct4⁻ BM-MAPCs 3D T2*-weighted MR images were acquired (parameters: 3D FLASH sequence, TR= 100ms, TE= 12 ms, flip angle= 20°, isotropic resolution: 78 μm³, field of view: 2.0 x 1.5 x 0.75 cm) and analyzed with the Image J software using a semi-automated method (National Institute of Health, Bethesda, Maryland, USA) to calculate the hypointense pixel volume. Furthermore, 2D T2 weighted axial (parameters: RARE sequence, TR=3157.6 ms, TE=48.8 ms, matrix size= 256 x 256, FOV= 2.5 x 2.5 cm, in plane resolution= 78 μm², number of slices= 24, slice thickness= 0.5 mm) and coronal MRI scans (parameters: RARE sequence, TR=3000 ms, TE=50.2 ms, matrix size=256 x 256, FOV= 2.5 x 2.5 cm, number of slices= 16, slice thickness= 0.5 mm, in plane resolution: 78 μm²) were acquired to follow-up the tumor size. The area of the lesion was determined by outlining it manually on all slices using the 5.1 Paravision software (Bruker, Biospin). The sum of the cross sectional area was used to determine the total tumor size. An ANOVA test (GraphPad PRISM, GraphPad Software, La Jolla, CA, USA) was used to determine significant differences with $p < 0.05$. To validate the integrity of the blood brain barrier, pre- and post-contrast (gadolinium (Dotarem®) (100μl / mouse of 0.05 mmol/ml, *i.v.*), Guerbet, Villepinte, France) T1 weighted MR images were acquired (RARE sequence, TR: 819ms, TE: 7.6ms, matrix size: 256 x 256, FOV: 2 x 2 cm, number of slices: 20, in plane resolution: 78μm²). The relative signal intensity of the tumor region showing the strongest contrast enhancement (relative to surrounding brain tissue) was determined by placing a region of interest (ROI) over the area using the Paravision 5.1 software. To avoid influences from strong tumor heterogeneity (necrosis), we only analyzed tumor regions with strong contrast enhancements by manual delineation. For statistical analysis of the BBB integrity, pre-contrast scans were subtracted from post-contrast scans after which the procentual increase following gadolinium injection was calculated for the contralateral hemisphere (negative control set to 100%), tumor tissue and extracranial muscle tissue (positive control) for each animal. Significant differences were determined by ANOVA testing (GraphPad PRISM, GraphPad Software, La Jolla, CA, USA) with $p < 0.05$.

Bioluminescence imaging (BLI)

Mice were anesthetized with isoflurane (2% induction, 1.5% maintenance) and placed in the IVIS® 100 system (Perkin Elmer, Waltham, MA, USA) or an IVIS Spectrum (Hs683/U87-MG) (Perkin Elmer), maintaining the body temperature at 37°C. Subsequently, D-Luciferin (126mg/kg in PBS, Promega) or coelenterazin-h (15μg/mouse) were injected intravenously to assess stem cell or U87-MG tumor viability respectively. Subsequently, bioluminescent images were acquired. Data were analyzed (living image® 2.50.1 software, Perkin Elmer) for maximum intensity of the photon flux.

Positron emission tomography (PET)

Mice were anesthetized with isoflurane (2% induction, 1.5% maintenance) and placed in a Focus 220 microPET system (Siemens Medical Solutions USA) after which 300μCi activity was injected *i.v.* and an 80 min dynamic PET scan was performed. Images were reconstructed using an iterative maximum a posteriori probability algorithm with ordered subsets (MAP; 18 iterations, 9 subsets, fixed resolution: 1.5 mm) and analyzed in PMODv.3.1 (PMOD Inc, Zurich, Switzerland). Summed images of the 80-min acquisition time were used for the analysis.

Humane endpoints

Animals were sacrificed when symptoms reached grade 3 out of 4 (grade 0 for healthy mice, grade 1 for slight unilateral paralysis, grade 2 for moderate unilateral paralysis and/or beginning hunchback, grade 3 for severe unilateral or bilateral paralysis and pronounced hunchback, and grade 4 for moribund mice) according to [4].

Histology

Animals were sacrificed by an *i.p.* overdose of Nembutal (300μl, Ceva) and subsequently perfused with 4% ice-cold paraformaldehyde (PFA) solution (Sigma-Aldrich). After overnight post fixation in 4% PFA, the brain tissue was stored in a 0.1% sodium azide solution in PBS (Fluka, Sigma-Aldrich) at 4°C. 5 μm paraffin sections were sliced and a Masson trichrome staining, a Prussian blue staining (see Chapter 5) and an Iba 1 staining were performed. For the latter, sections were stained with an Iba1 antibody (1/250). Visualization was achieved by using the Dako EnVision + system-HRP (DAB) kit (Dako, Glostrup, Denmark).

Statistical analysis

Statistical analysis was performed using GraphPad Prism (GraphPad Software PRISM, La Jolla, CA, USA). Significant differences between GCV and PBS-treated animals regarding total tumor volumes (MRI: mm³) and cell viability (BLI: P/s) were determined by means of an ANOVA test with $p < 0.05$ regarded significant. Figures show means \pm SEM.

6.3 Results

6.3.1 Bystander killing effect assessment in a mouse glioblastoma (GL261) model

6.3.1.1 mMSC's

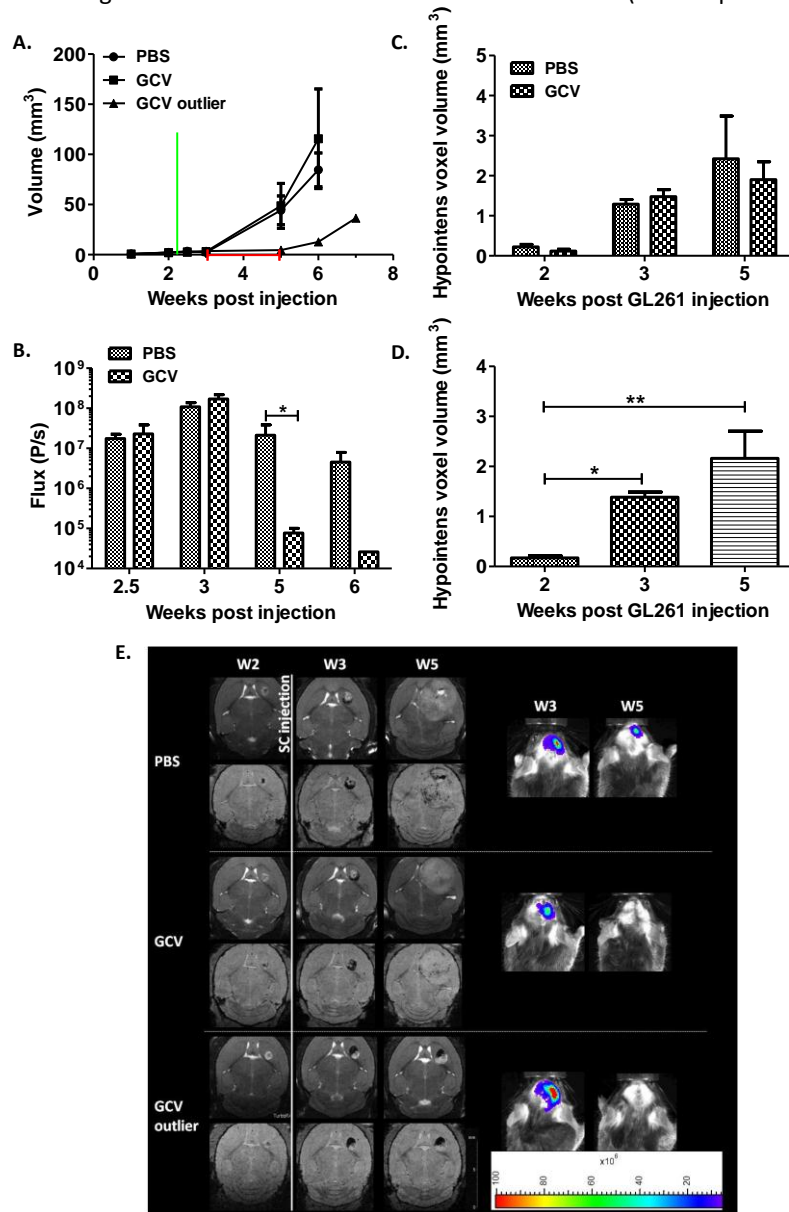
5×10^5 eGFP-fLuc-HSVTK transduced and SMG²-mPEGSi labeled (1%) mMSC's were injected stereotactically in the striatum of GL261 tumor bearing C57BL6/j mice, after which PBS or GCV (50mg/kg) treatment was administered for 14 consecutive days. GL261 tumor sizes were comparable before mMSC injection as assessed by T2 weighted MRI. Furthermore, PBS treated animals (N = 4) (44.3 ± 14.3 mm³) and most GCV treated (N = 3) (48.7 ± 22.4 mm³) animals did not show a significant difference in tumor size by the end of treatment (week 5 post injection of GL261 cells) (Figure 37A). One GCV treated animal however showed a slight delay in tumor growth at the end of treatment (4.6 mm³). Furthermore, BLI was performed to assess stem cell viability, which showed a decreased viability for GCV treated animals but not for PBS control animals at the end of treatment (PBS: $2.1 \times 10^7 \pm 1.7 \times 10^7$, GCV: $7.7 \times 10^4 \pm 2.4 \times 10^4$), indicating mMSC response to GCV treatment (Figure 37B). Hypointense voxel volume determinations showed no statistical difference at any time point (prior/after mMSC injection, at the end of treatment) between PBS or GCV treated groups (Figure 37C). When comparing different time points, a statistical difference was found between prior to and after mMSC injection (2 weeks and 3 weeks post GL261 injection), indicating that labeling only 1% of the injected mMSC's is sufficient for *in vivo* cell distribution follow-up (Figure 37D).

Furthermore also the MRI and BLI images of one representative animal are shown for each group in Figure 37E. 3D T2*W MR images show the distribution of the mMSC's surrounding the tumor prior to treatment initiation.

Furthermore, histological analysis was performed to assess tumor characteristics *in vivo* which revealed a high similarity between the tumors growing in mMSC-treated and untreated GL261 bearing animals.

Figure 37: Bystander killing effect assessment exerted by mMSC's on the GL261 glioblastoma model.

- Anatomical T2 weighted MR images revealed no statistically significant difference in tumor size following treatment (week 5 post GL261 injection) between PBS (N= 4) and most GCV treated animals (N = 3). Only one GCV treated animal displayed a delayed tumor growth.
- BLI analysis showed a decrease in stem cell viability for GCV treated animals (N=4) compared to PBS control animals (N = 4).
- Hypointense voxel determinations from 3D T2* MR images showed no statistical difference between PBS and GCV treated groups prior to (2 weeks post GL261 injection) or after stem cell injection (3 weeks post GL261 injection) nor at the end of treatment (5 weeks post GL261 injection).
- Statistical analysis of the hypointense voxel volume on different time points showed that 1% labeled mMSC's were sufficient for *in vivo* detection following injection (week 2 versus week 3 post GL261 injection) (N = 8 at each time point).
- MRI images (left) of animals from PBS and GCV treated groups show a comparable tumor growth prior to mMSC injection on T2 weighted coronal MR images (upper row for each group) whereas there is little hypointense contrast visible on 3D T2* MR images (lower row for each group). Stereotactically injected mMSC's could be detected by 3D T2* MRI on day 4 after injection. When tumors grew larger, the hypointense voxels got more dispersed over time, whereas the mouse (outlier) that showed a delay in tumor growth still showed hypointense signal from the stem cells at the end of treatment (week 5 post GL261 injection).



6.3.1.2 mOct4⁺ BM-HypoSCs

Subsequently, 5×10^5 eGFP-fLuc-HSVTK transduced and SMG²-mPEGSi labeled (1%) mOct4⁺ BM-HypoSCs were injected stereotactically in the striatum of GL261 tumor bearing C57BL6/j mice, after which PBS or GCV (50mg/kg) treatment was administered for 14 consecutive days. GL261 tumor sizes were also comparable prior to mOct4⁺ BM-HypoSC injection as assessed by T2 weighted MRI. Furthermore, PBS treated animals (N = 4) ($44.5 \pm 14.9 \text{ mm}^3$) and GCV treated (N = 4) ($30.3 \pm 16.7 \text{ mm}^3$) animals did not show a significant difference in tumor size by the end of treatment (week 5 post injection of GL261 cells) (Figure 38A). Furthermore, BLI was performed to assess stem cell viability, which showed a decreased viability for GCV treated animals but not for PBS control animals at the end of treatment (PBS: $2.2 \times 10^8 \pm 4.3 \times 10^7$, GCV: $7.1 \times 10^5 \pm 5.3 \times 10^5$). Although mOct4⁺ BM-HypoSCs seem to be responding to GCV treatment, background level could not be reached (Figure 38B).

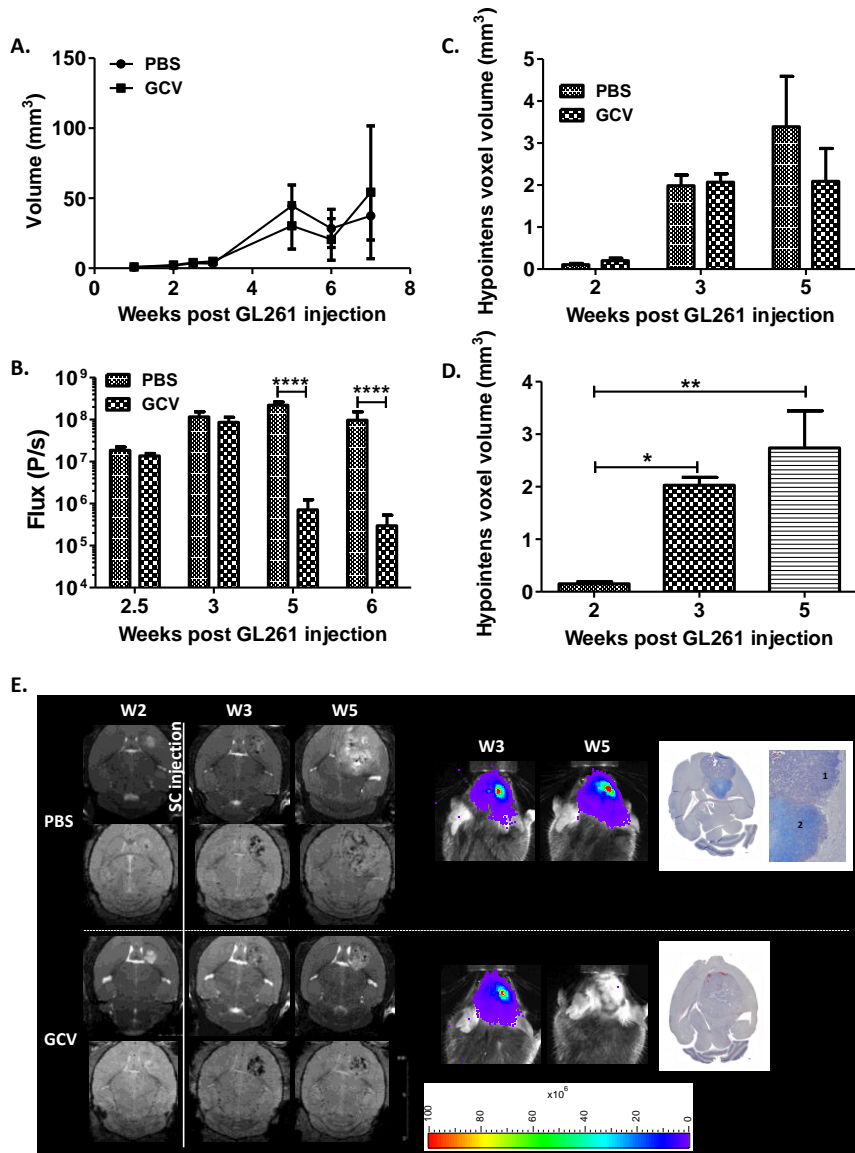
Hypointense voxel volume determinations showed no statistical difference at any time point (prior/after mMSC injection, at the end of treatment) between PBS or GCV treated groups (Figure 38C).

When comparing different time points, a statistical difference was found between prior to and after mOct4⁺ BM-HypoSC injection (2 weeks and 3 weeks post GL261 injection), indicating that labeling only 1% of the injected mOct4⁺ BM-HypoSCs is sufficient for *in vivo* cell distribution follow-up (Figure 38D).

The MRI and BLI images of one representative animal per group are shown in Figure 38E. 3D T2*W MR images show the distribution of the mMSC's surrounding the tumor prior to treatment initiation. BLI images show mOct4⁺ BM-HypoSC killing in the GCV but not in the PBS treated group, which was also apparent from histological analysis where Masson's trichrome staining showed that PBS treated animals developed masses that consisted of both GL261 tumors and mOct4⁺ BM-HypoSC masses whereas GCV treated animals only showed evidence of GL261 tumor growth and not mOct4⁺ BM-HypoSC mass growth.

Figure 38: Bystander killing effect assessment exerted by mOct4⁺ BM-HypoSCs on the GL261 glioblastoma model.

- A. Anatomical T2 weighted MR image analysis revealed no statistically significant difference in tumor size following treatment (week 5 post GL261 injection) between PBS treated animals (N= 4) and GCV treated animals (N = 4).
- B. BLI analysis showed a decrease in stem cell viability for GCV treated animals compared to PBS control animals.
- C. Hypointense voxel determinations from 3D T2* MR images showed no statistical difference between PBS and GCV treated groups prior to (2 weeks post GL261 injection) or after stem cell injection (3 weeks post GL261 injection) nor at the end of treatment (5 weeks post GL261 injection).
- D. Statistical analysis of the hypointense voxel volume on different time points showed that 1% labeled m Pct4(+) BM-HypoSCs were sufficient for *in vivo* detection following injection (week 2 versus week 3 post GL261 injection) (N = 8 at each time point).
- E. MRI (left) and BLI (middle) images of one representative animal from PBS and GCV treated groups show a comparable tumor growth prior to mMSC injection on T2 weighted coronal MR images (upper row for each group) whereas there is little hypointense contrast visible on 3D T2* MR images (lower row for each group). Stereotactically injected SMG²-mPEGSi labeled mMSC's could be detected by 3D T2* MRI on day 4 after injection. When tumors grew larger, the hypointense voxels got more dispersed over time. Furthermore Masson's trichrome staining revealed tumor growth from both GL261 (1) and mOct4+ BM-HypoSCs (2) in the PBS treated group whereas only GL261 tumor growth could be detected in the GCV treated group.



6.3.1.3 mOct4⁻ BM-MAPCs

5×10^5 mOct4⁻ BM-MAPCs were engrafted, of which only a fraction (1 or 10%) of the injected cells was labeled using SMG²-mPEGSi particles, as

Subsequently, stereotactical injection of 5×10^5 mOct4⁻ BM-MAPCs, of which only a fraction (1% or 10%) of the injected cells was labeled using SMG²-mPEGSi particles, as 3×10^5 cells already generated extensive hypointense contrast (Figure 26). Evaluation of the grafted cells by MRI showed that when 10% (Figure 39B), but not 1% (Figure 39A) of the stem cells were labeled with SMG²-mPEGSi particles, it was possible to follow them by MRI as indicated by the hypointense signal, with one representative animal shown in Figure 39C.

Subsequently, 5×10^5 eGFP-Fluc-HSVtk expressing cells of which only a fraction (10%) was labeled using SMG²-mPEGSi particle (10%) were stereotactically injected into GL261 tumor bearing animals (= d15 post GL261 injection). The following day (= d16) MRI and BLI were performed to ascertain stem cell location in and surrounding the tumor. Using T2* weighted MR images, we were able to demonstrate for all animals receiving 10% labeled mOct4⁻ BM-MAPCs, that the tumors contained and were surrounded by SMG²-mPEGSi labeled mOct4⁻ BM-MAPCs from the first imaging time point post engraftment (= day 16 post injection).

Subsequently, PBS or GCV (50mg/kg) administration was commenced for 14 consecutive days (i.e. until d30 following GL261 tumor induction). At d30 post GL261 injection, sham operated animals and some PBS treated animals started to develop grade 3 symptoms that were related to tumor growth, and needed to be sacrificed. Analysis of MR images results showed that there was no statistically significant difference in tumor volume prior to (= d14) and following (= d16) stereotactical injection of the mOct4⁻ BM-MAPCs. At the end of treatment however smaller tumor sizes were observed in GCV treated animals compared to Sham operated and PBS treated animals (Figure 40A). Viability data from mOct4⁻ BM-MAPCs indicated that GCV (N=18) administration resulted in a viability reduction of the mOct4⁻ BM-MAPCs, which was not the case for the PBS-treated (N=12) and the Sham operated group (N=5) (Figure 40B) as assessed by BLI. During this analysis, a heterogenic response was observed for GCV- and PBS treated animals. Therefore, additional sub-analyses were performed to assess therapeutic responses.

Figure 39: Analysis of eGFP-fLuc-HSVTK (+), SMG²-mPEGSi labeled mOct4⁻ BM-MAPCs tracking in a mouse glioblastoma model (GL261).

- A. Hypointense signal volume determination (3D T2* MRI) on 1% labeled mOct4⁻ BM-MAPCs did not show statistically significant differences between stem cell injected animals (PBS/GCV) and sham operated animals one day after surgery (day 16). At the end of treatment (day 30), there was however a significant difference between sham operated animals and GCV-treated animals. due to the smaller tumor sizes in the GCV-treated group. In the sham operated and PBS-treated group, tumor formation was present which is accompanied with necrosis and bleedings when tumors grow over time. In contrast, the hypointense signal in the GCV-treated group, which did not develop tumors is mostly generated by remaining labeled mOct4⁻ BM-MAPCs. (green bar: mOct4⁻ BM-MAPC stereotactical injection; red bar: treatment phase)
 - B. Hypointense signal volume determination (3D T2* MRI) on 10% labeled mOct4⁻ BM-MAPCs showed statistically significant differences between stem cell injected animals (PBS/GCV) and sham operated animals one day after surgery (day 16). At the end of treatment (day 30), there was a statistically significant difference between sham operated and PBS-treated animals and between the PBS-treated and GCV-treated groups.
- * p<0.05, ** p<0.01, *** p<0.001, **** p<0.0001
- C. MR images of one representative animal stereotactically injected with 1% or 10% labeled mOct4⁻ BM-MAPCs showed that the hypointense contrast, delineated in red, generated by 10% labeled mOct4⁻ BM-MAPCs was more pronounced compared to 1% labeled cells.

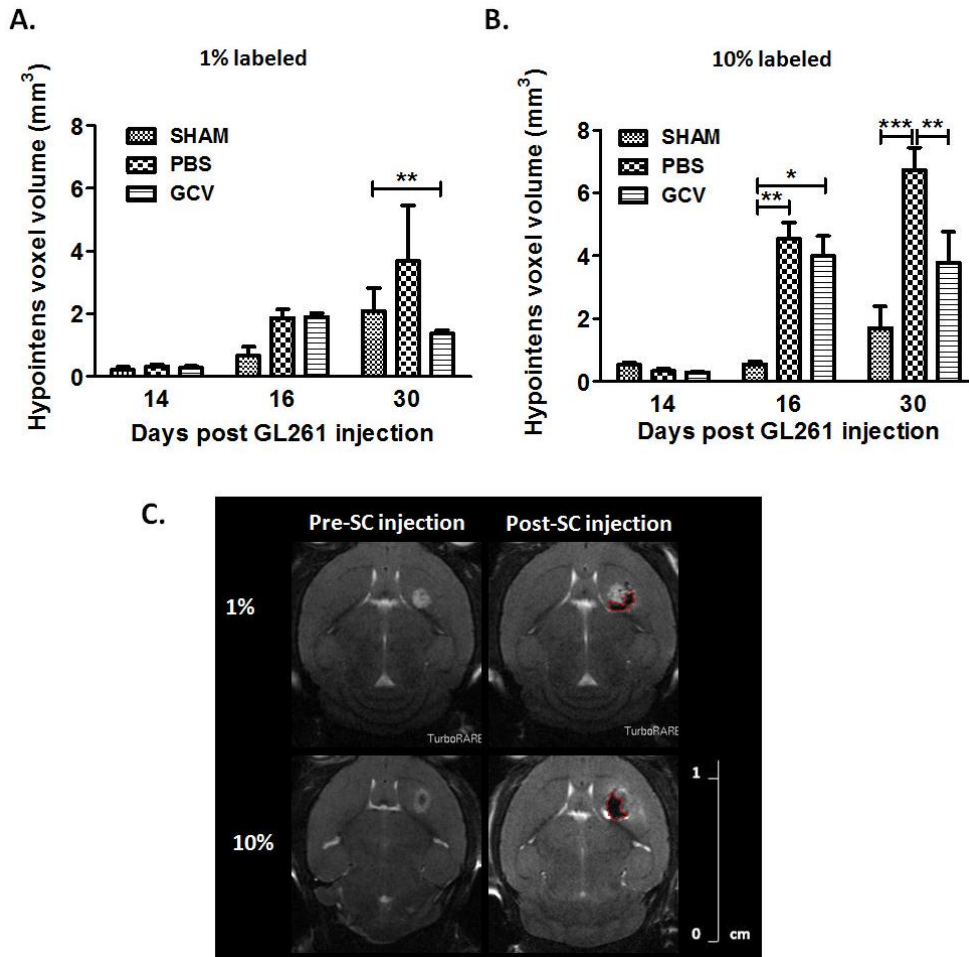
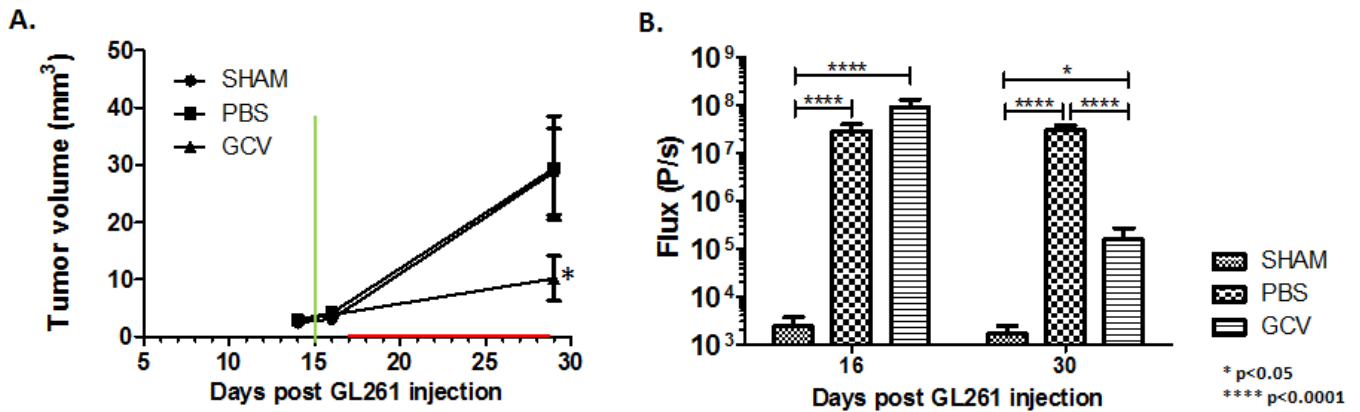


Figure 40: *In vivo* suicide gene therapy using eGFP-fLuc-HSVTK (+), SMG²-mPEGSi labeled mOct4⁻ BM-MAPCs in a mouse glioblastoma model (GL261).

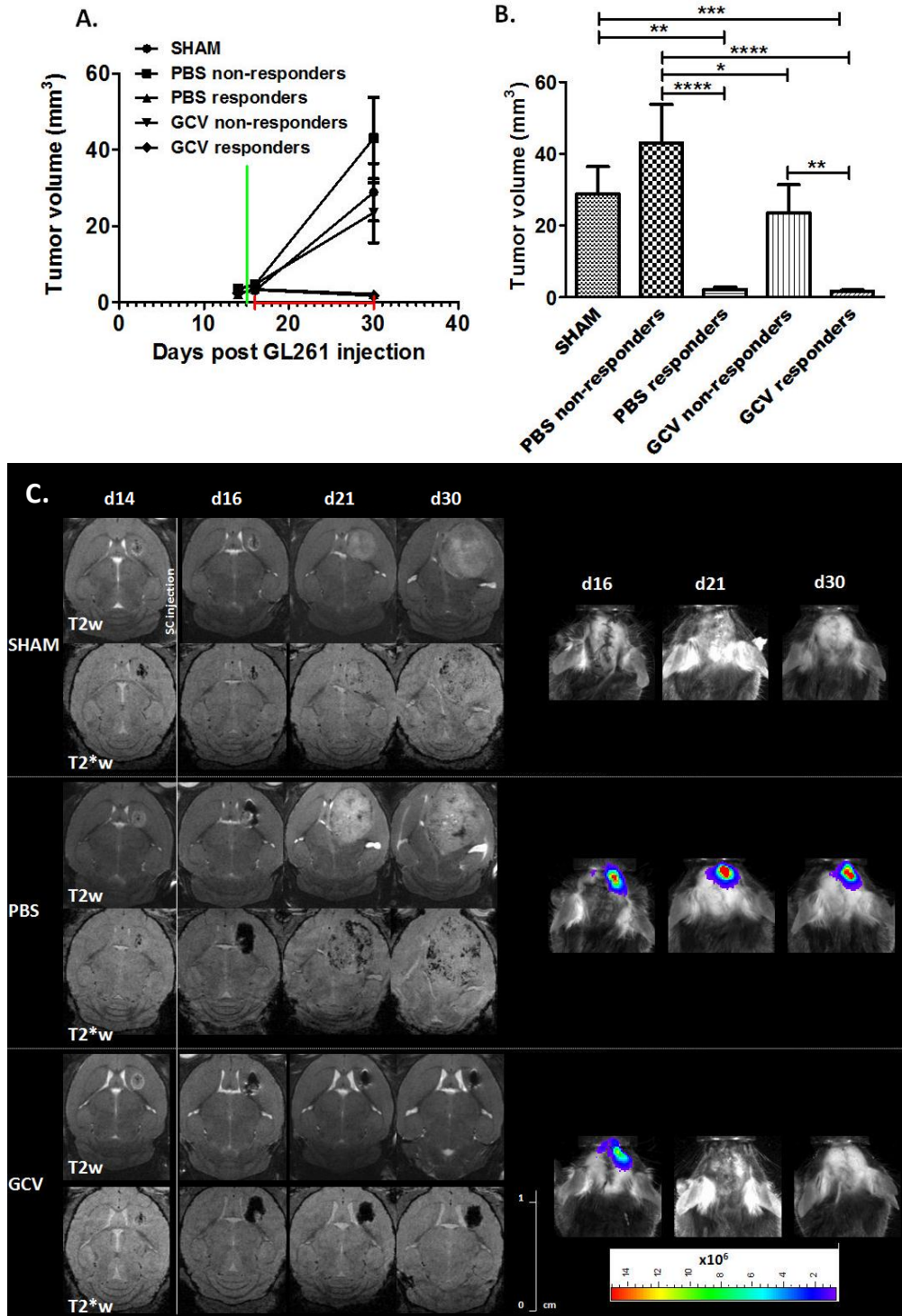
- Tumor volume determined for SHAM operated, PBS and GCV treated animals. No statistically significant differences could be found on day 14 and 16 between the different groups.
- Statistical analysis of the tumor volumes at the end of treatment (day 30) showed a statistically significant difference in tumor size between GCV-treated (N = 18) animals and SHAM operated (N = 5) / PBS treated animals (N = 12).
- mOct4⁻ BM-MAPC viability measurements showed a reduced cell viability for the GCV but not the PBS treated group.



During the previous analysis, it was observed that while all sham operated animals (N=5) showed substantial tumor masses at the end of the treatment period (day 30), some of the PBS-treated animals showed a substantially smaller tumor size compared to the rest (N=4 out of N=12 PBS-treated animals, see Figure 41A and B). Among the GCV-treated animals, 11 responded to treatment while 7 animals did not respond to treatment (Figure 41A and B). MRI analysis showed that sham operated (N = 5), non-responding PBS-treated animals (N = 8) and GCV-treated, non-responding animals (N=7) developed tumors on day 30 after transplantation of the glioblastoma cells that were not statistically different in size (see Figure 41A and B). GCV-treated animals, that responded to therapy (N = 11); showed a statistically significant reduction in tumor volume (after 14 days of GCV treatment). For all GCV-treated animals, BLI signal intensity decreased significantly (see Figure 40 B and 41C). No difference in BLI signal intensity was seen between responding and non-responding animals (data not shown). Furthermore, a few animals injected with mOct4⁻ BM-MAPCs and treated with PBS also displayed a reduced tumor size (N = 4) at the end of PBS administration (Figure 41A and B), although the BLI signal from the mOct4⁻ BM-MAPCs did not change over time (Figure 41C).

Figure 41: of *In vivo* suicide gene therapy using eGFP-fLuc-HSVTK (+), SMG²-mPEGSi labeled mOct4⁻ BM-MAPCs in a mouse glioblastoma model (GL261).

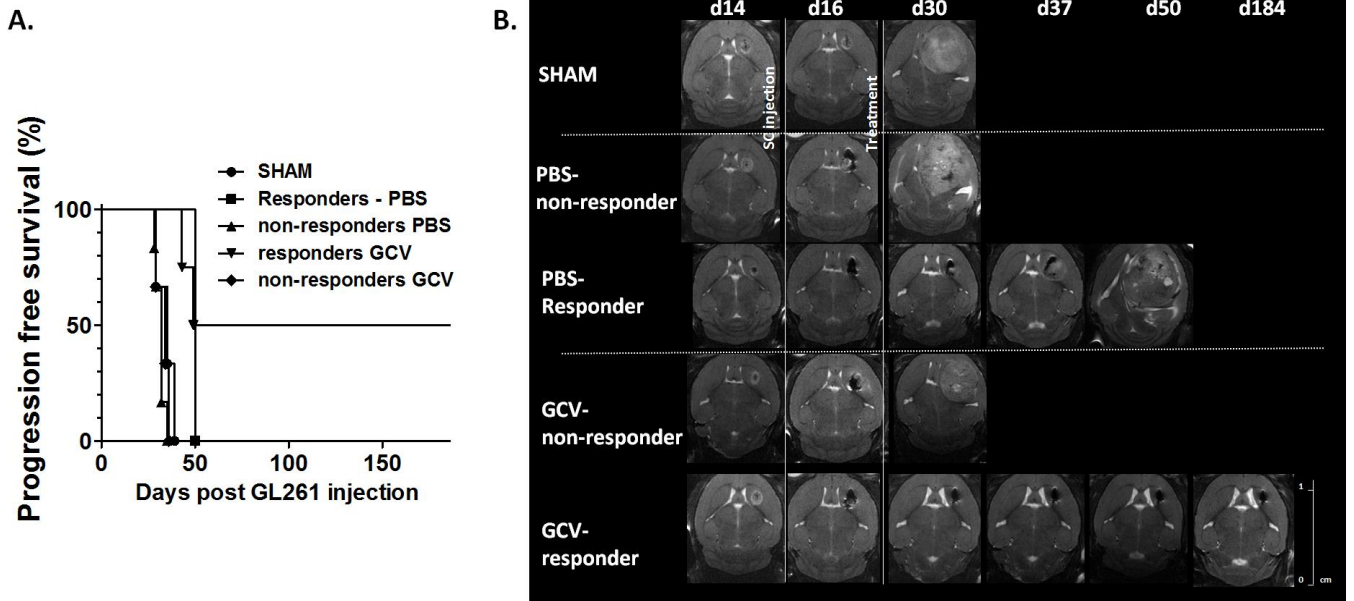
- Tumor volume determined for SHAM operated, PBS and GCV treated animals. No statistically significant differences could be found on day 14 and 16 between the different groups.
- Statistical analysis of the tumor volumes at the end of treatment (day 30) showed a statistically significant difference in tumor size between GCV responding (N = 11) animals and SHAM operated (N = 5) / PBS treated animals (N = 8). Furthermore, some GCV (N = 7) treated animals did not respond to therapy whereas some PBS treated (N = 4) animals also showed a reduced tumor size at the end of treatment.
- MR and BLI images of one representative animal for each group.



A number of animals were observed long-term to determine progression free survival (Figure 42). Progression free survival curves generated for sham operated animals (N = 3) and PBS-treated (N = 6) animals were comparable. From the GCV-treated animals, some (N=3) did not respond to treatment and showed a similar survival to the sham operated and PBS-treated animals. However, some GCV (N = 4) and one animal treated with PBS displayed a longer progression free survival with two animals of the GCV-treated group surviving long term (184 days) without any signs of tumor regrowth (Figure 42A). The median progression free survival of sham operated animals (35 days) was significantly lower compared to GCV responding animals (119.5 days) with $p = 0.0101$.

Figure 42: Progression free survival analysis.

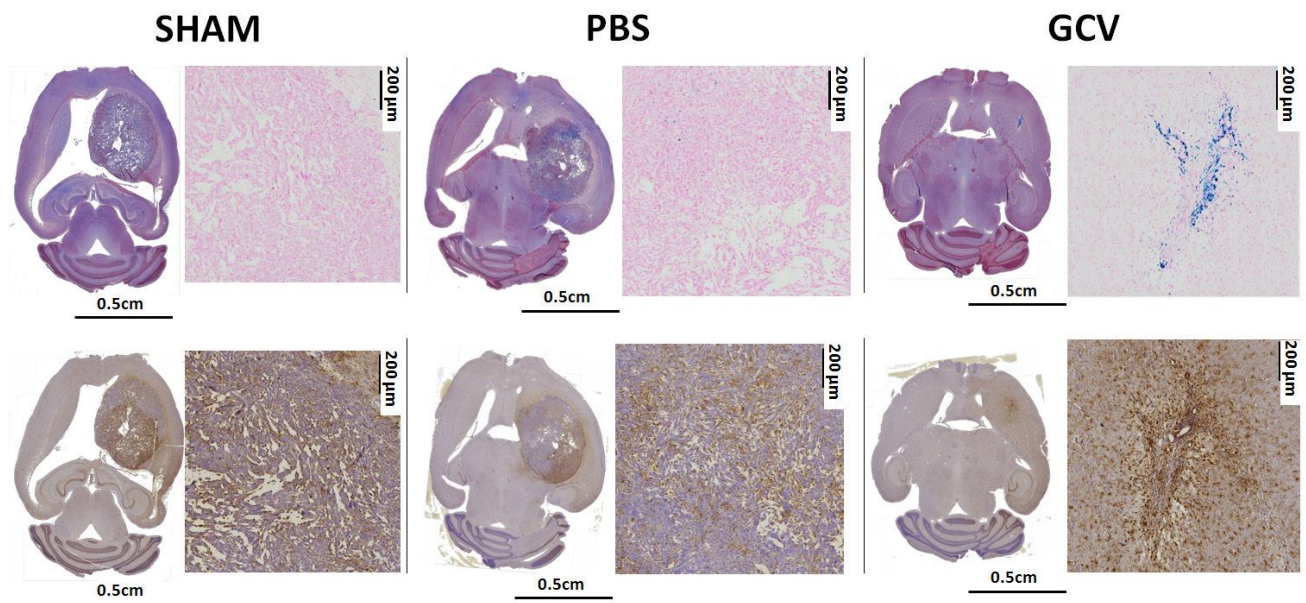
- A. A number of animals was observed for a progression free survival analysis. Sham operated animals (N = 3), PBS-treated (N = 6) and GCV (N = 3) unresponsive animals had comparable progression free survival curves whereas the animals that responded to GCV (N = 4) treatment and one animal treated with PBS but with a reduced tumor size after treatment displayed a prolonged progression free survival with two animals of the GCV-treated group surviving for 184 days without any sign of tumor regrowth.
- B. T2 weighted-MRI images showing tumor growth evolution in one representative animal for each of the three treatment groups.



Furthermore, histological analysis was performed to confirm the data obtained *in vivo*. Masson's trichrome staining showed the presence of large blood vessels explaining the hypointense signal in large tumors. Prussian blue staining confirmed the presence of SMG²-mPEGSi particles in and around the tumor. In small tumors, iron staining was more concentrated to the injection site in comparison to large tumors. Finally also an Iba I staining for the presence of activated microglia was performed which showed remarkably few activated microglial cells inside the tumor, although microglial activation was more pronounced surrounding the tumor (Figure 43).

Figure 43: Histological analysis of representative animals at the end of treatment.

Several animals were sacrificed at the end of treatment for histological analysis. Masson's Trichrome staining (upper left) of SHAM operated and PBS controlled animals showed very large tumors with a large amount of bleedings, corresponding to hypointense voxels on MRI. Prussian blue (upper right) staining was also performed which showed slight iron staining in PBS controlled animals. GCV treated responders showed high iron content as the cells remained more localized with smaller tumors. Finally, an Iba1 staining (bottem) was performed which showed microglial activation in the GCV treated responding group. Microglial activation was also very pronounced around the tumor in SHAM operated and PBS controlled animals.

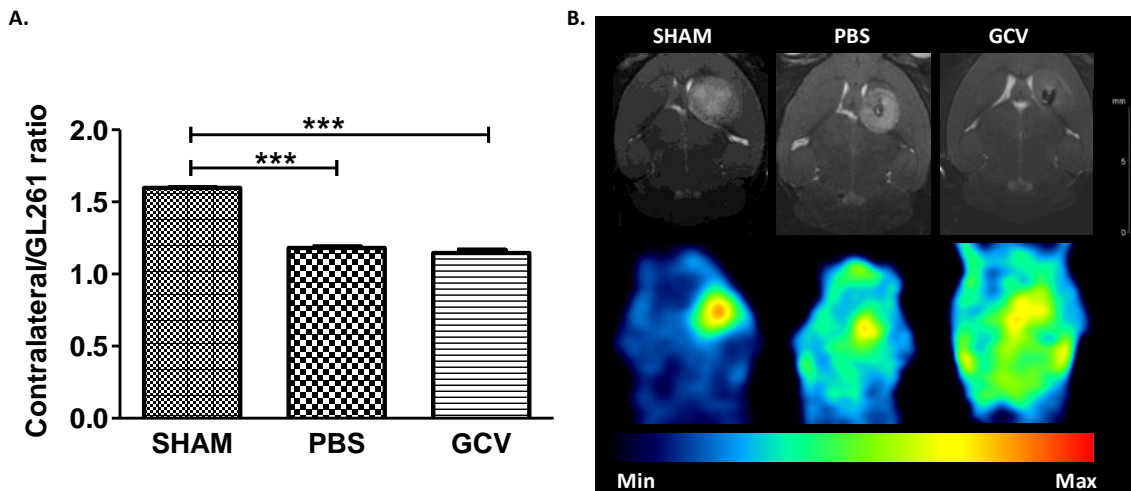


In order to gain further insights in tumor cell viability following suicide gene therapy, [¹⁸F] FET PET scan was acquired in addition to MR imaging. Statistical analysis (Figure 44A) showed that relatively large tumor sizes were required for detection by [¹⁸F] FET PET as displayed by the sham operated group (N = 2). No statistically significant distinction could be made between the PBS treated group (N = 2) and the GCV treated group (N = 3) based on [¹⁸F] FET PET, although it was very clear on MRI that tumor sizes in the PBS treated group were

larger than in the GCV treated group. MR and PET images of one representative animal from each treatment group are shown in Figure 44B. These show clearly that although tumors in PBS and GCV control animals could be detected by [^{18}F] FET PET, it was indeed very difficult to distinguish between both groups, which was much more clear on MR images.

Figure 44: [^{18}F] FET PET analyze on GL261 tumor bearing animals treated with mOct4⁻ BM-MAPCs.

- A. .Statistical analysis of sham operated (N = 2), PBS control (N = 2) and GCV treated (N = 3) groups showed that sham operated animals had significantly more tracer uptake in the tumor area compared to PBS and GCV treated animals.
- B. Overview of MR and corresponding [^{18}F] FET PET images of one animal from each treatment group.
 Top: T2W coronal MR images from one animal of each treatment group.
 Bottom: [^{18}F] FET PET images from one animal of each treatment group.
 Left: A relatively large tumor could be detected by [^{18}F] FET PET in the sham operated group
 Middle: The tumor of a PBS treated group could also be detected by [^{18}F] FET PET but tracer uptake was rather low.
 Right: The tumor of a GCV treated animal could barely be detected by [^{18}F] FET PET.



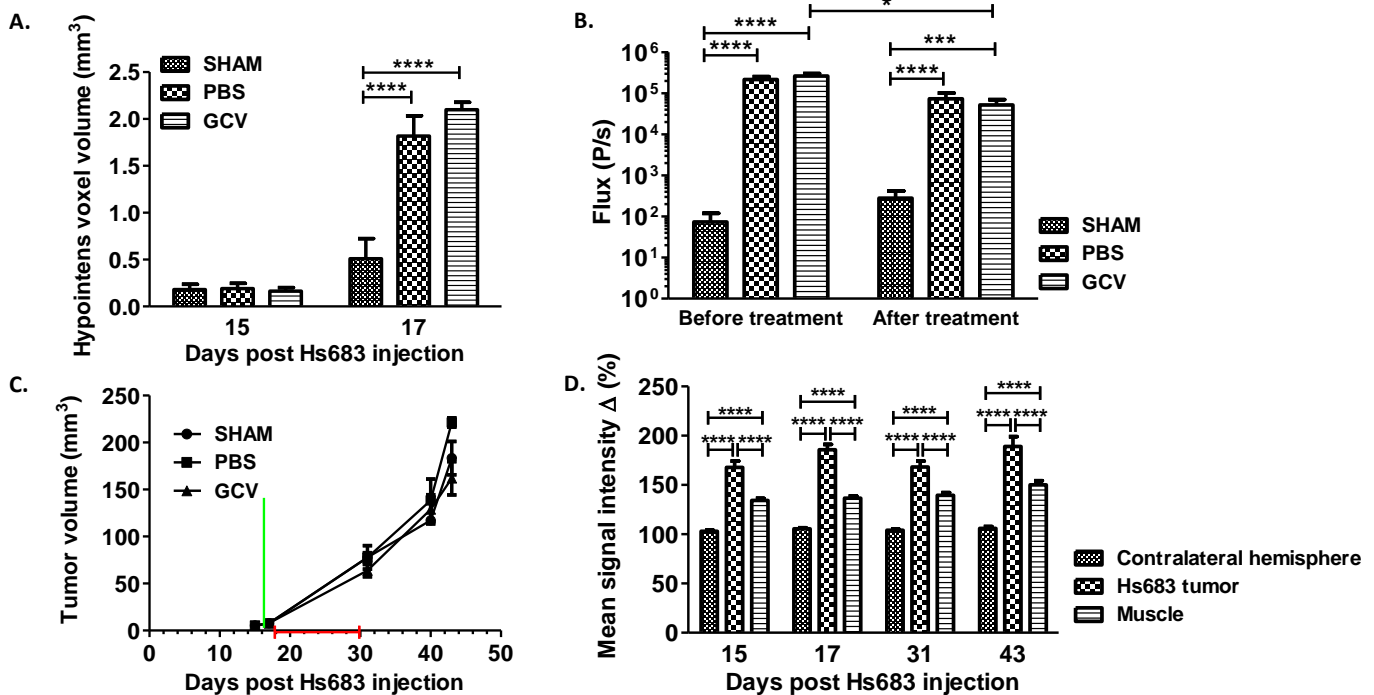
6.3.1 Bystander killing effect assessment in a human malignant glioma xenograft models (Hs683/U87-MG)

6.3.1.1 hMultistem mediated suicide gene therapy in a human glioma xenograft model (Hs683)

5×10^5 transduced and 1% SMG²-mPEGSi labeled hMultistem's were injected stereotactically in the striatum of Hs683 tumor bearing Hsd:athymic Nude-Foxn1^{nu} mice, after which PBS or GCV (50mg/kg) treatment was administered for 14 consecutive days. MRI data showed that hMultistem's could be detected *in vivo* following stereotactic injection (Figure 45A). BLI data showed that although expression of the fLuc gene was sufficiently high for detection of the hMultistem's following injection, no statistically significant difference in viability could be obtained between GCV treated and PBS treated animals after initiation of treatment. Only a slight decrease was observed in the GCV, but not the PBS treated group when comparing the BLI signal intensity before and after treatment (Figure 45B). Concurrent with these results, no statistically significant differences in tumor volume were found between the sham operated (N = 3), PBS treated (N = 6) and GCV treated (N = 6) groups at the end of the treatment (day 31), nor in their subsequent progression of tumor growth (Figure 45C). Irrespective of the treatment group, developing tumors showed statistically significant tumor enhancing regions on T1 weighted pre- and post contrast MR images (Figure 45D).

Figure 45: *In vivo* suicide gene therapy using hMultistem as cellular vehicles in a human glioma xenograft (Hs683) model.

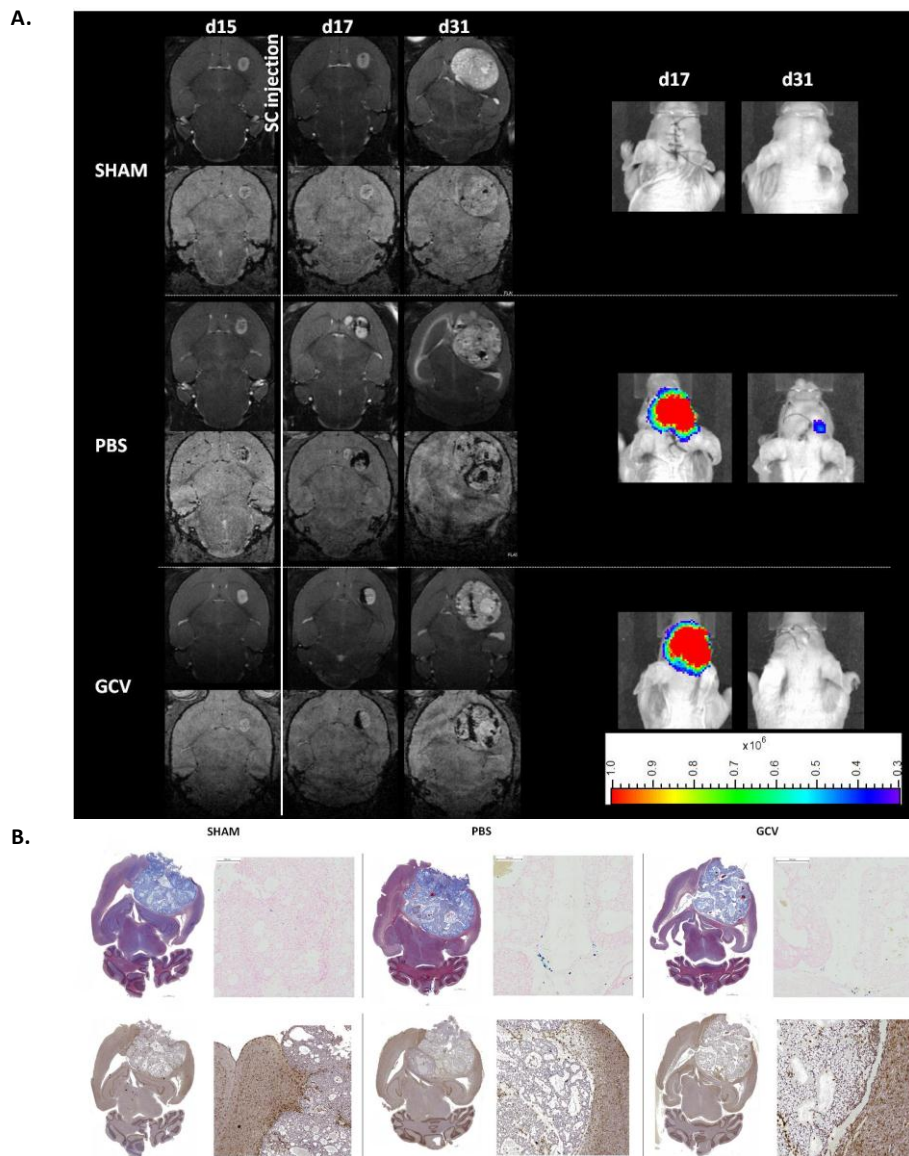
- Hypointense voxel volume quantification of SMG²-mPEGSi labeled eGFP-fLuc-HSVTK + hMultistem cells in the Hs683 model showed sufficient *in vitro* labeling for *in vivo* detection of 1% labeled cells in the tumor one day post hMultistem injection. (sham: N = 3, PBS treated: N = 6, GCV treated: N = 6).
- Bioluminescent imaging data showed that the stem cells were detectable through BLI but no statistically significant decrease in stem cell viability could be detected following treatment although there was a small decrease in the BLI signal from the GCV treated group compared to the beginning of treatment.
- Tumor volume measurements proved no statistical differences between sham operated, PBS treated or GCV treated animals. (green bar: hMultistem injection; red bar: duration of GCV/PBS treatment).
- T1 weighted MRI pre- and post contrast injection showed BBB integrity loss in the Hs683 tumor compared to the contralateral hemisphere and the extracranial muscle at all timepoints. (N = 15)



MRI and BLI images of one representative animal are shown for each group in Figure 46A. Histological analysis (Figure 46B) showed the presence of large bloodvessels, explaining some of the hypointense signal in large tumors. Furthermore, PB staining showed iron accumulation only in PBS and GCV treated animals, most likely arising from the SPIO labeled stem cells. Finally, Iba I staining for the presence of activated microglia was performed which showed remarkably few activated microglial cells inside the tumor in addition to more pronounced microglial cell activation surrounding the tumor.

Figure 46: *In vivo* suicide gene therapy using hMultistem as cellular vehicles in a human glioma xenograft (Hs683) model.

- A. MRI images (left) of one representative animal from sham, PBS and GCV treated groups show a comparable tumor growth prior to hMultistem injection on T2 weighted coronal MR images (upper row for each group) whereas there is little hypointense contrast visible on 3D T2* MR images (lower row for each group). 1% SMG²-mPEGSi labeled hMultistem's could be detected by 3D T2* MRI on day 1 after injection. When tumors grew larger, the hypointense voxels got more dispersed over time.
- B. One week after the end of therapy, animals developed symptoms after which histological analysis was performed. Masson's Trichrome staining (upper left) of all animals showed very large tumors with a large amount of bleedings, corresponding to hypointense voxels on MRI. Prussian blue (upper right) staining was also performed which showed iron staining in PBS and GCV treated animals. Finally, an Iba1 staining (bottom) was performed which showed a predominant absence of activated microglia in all treatment groups. Microglial activation was however more pronounced around the tumor.



6.3.1.2 hMultistem mediated suicide gene therapy in a human glioma xenograft model (U87-MG)

Subsequently, 2.5×10^5 eGFP-fLuc-HSVTK expressing and SMG²-mPEGSi labeled (1%) hMultistem's were stereotactically injected in the striatum of mCherry-rLuc expressing U87-MG tumor bearing Hsd:athymic Nude-Foxn1^{nu} mice, after which PBS or GCV (50mg/kg) treatment was administered for 14 consecutive days. MRI data showed that hMultistem's could be detected *in vivo* following stereotactic injection (Figure 47A) when labeling only 1% of the injected cells. BLI data showed that expression of the fLuc gene was sufficient for detection of the hMultistem's following injection and prior to treatment initiation. Both PBS treated and GCV treated groups displayed a decrease of the hMultistem viability by the end of treatment, indicating that the tumor environment induced cell death of the injected hMultistem's (Figure 47B). The BLI signal of the rLuc-expressing tumor cells, using Coelenterazine-h as a substrate, was used as an indicator for tumor cell viability. An increase of the BLI signal for the sham operated group and the PBS treated group but not for the GCV treated group was observed when compared with the signal intensity before initiation of the treatment (Figure 47C). This slightly reduced increase in tumor cell viability does however not correlate with the tumor size after treatment as there were no statistically significant differences between the sham operated, PBS treated and GCV treated groups observed. This decreased viability might however reflect a slight increase in necrotic area size, which is difficult to assess on MRI due to the existence of bleedings and the iron oxide label present in the hMultistem's. Developing tumors showed statistically significant tumor enhancing regions on T1 weighted pre- and post contrast MR images (Figure 47D). MRI and BLI images of one representative animal are shown for each group in Figure 48A. Two weeks after the end of treatment, all animals started to develop symptoms due to tumor growth, after which animals were sacrificed and histological analysis was performed (Figure 48B). Trichrome staining confirmed the MRI data, which showed large and dense tumors. Furthermore, Prussian blue staining was performed which showed iron staining preferentially in PBS treated animals in comparison to sham operated and GCV treated animals. Iba 1 staining was performed to assess the microglial activation status between groups, which showed no clear

differences between the different treatment groups. Although much less microglial activation surrounding the tumor was observed when compared to the Hs683 model.

Figure 47: *In vivo* suicide gene therapy using hMultistem as cellular vehicles in a human glioma xenograft (U87-MG) model.

- A. Hypointense voxel volume quantification of SMG²-mPEGSi labeled eGFP-fLuc-HSVTK + hMultistem cells in the U87-MG model showed sufficient *in vitro* labeling for *in vivo* detection of 1% labeled cells in the tumor one day post hMultistem injection. (sham: N = 3, PBS treated: N = 5, GCV treated: N = 6).
- B. Bioluminescent imaging (fLuc) data showed that hMultistem's displayed a decreased viability at the end of therapy irrespective of the treatment group.
- C. Bioluminescent imaging (rLuc) data showed an increase in tumor viability at the end of treatment for the sham operated and the PBS treated group but not the GCV treated group.
- D. Tumor volume measurements proved no statistical differences between sham operated, PBS treated or GCV treated animals. (green bar: hMultistem injection; red bar: duration of GCV/PBS treatment).
- E. T1 weighted MRI pre- and post contrast injection showed BBB integrity loss in the U87-MG tumor compared to the contralateral hemisphere and the extracranial muscle at all timepoints. (N = 11)

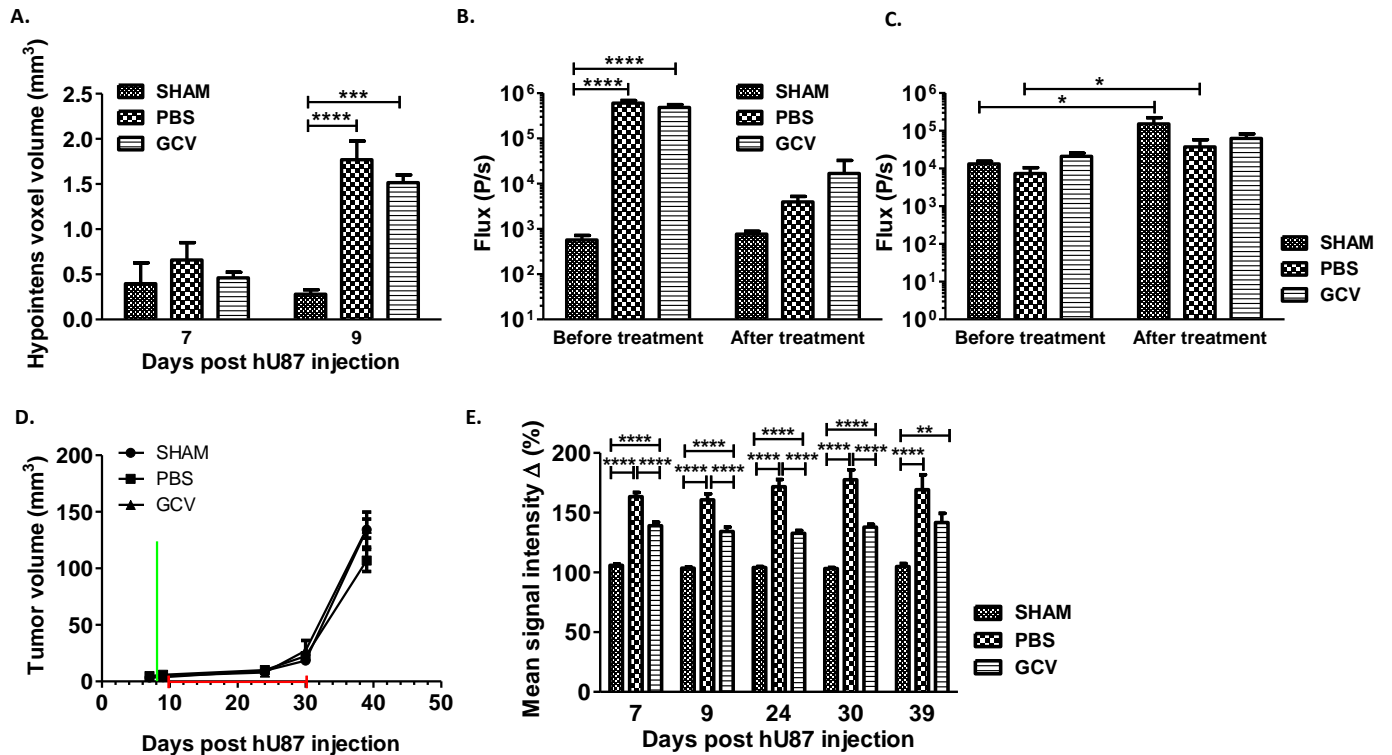
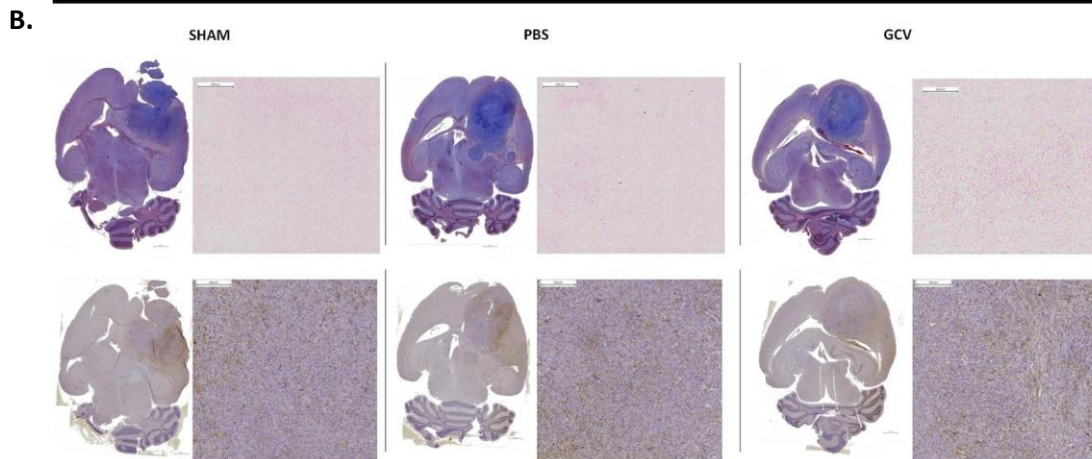
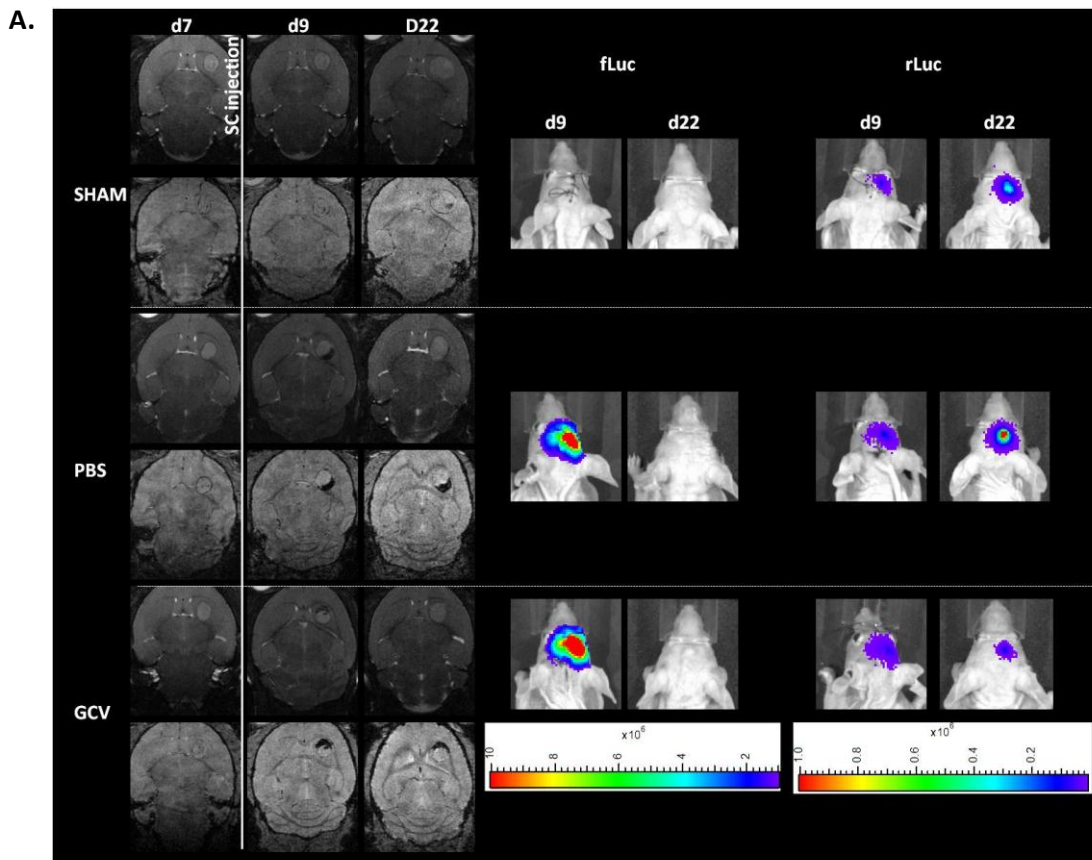


Figure 48: *In vivo* suicide gene therapy using hMultistem as cellular vehicles in a human glioma xenograft (u87-MG)

model.

- A. MRI images (left) of one representative animal from sham, PBS and GCV treated groups show a comparable tumor growth prior to hMultistem injection on T2 weighted coronal MR images (upper row for each group) whereas there is little hypointense contrast visible on 3D T2* MR images (lower row for each group). 1% SMG²-mPEGSi labeled hMultistem's could be detected by 3D T2* MRI on day 1 after injection, which was still detectable at the end of treatment (day 22 post U87-MG injection).
- B. Two weeks after the end of therapy, animals developed symptoms after which histological analysis was performed. Masson's Trichrome staining (upper left) of all animals showed large, dense tumors with very little bleedings. Prussian blue (upper right) staining was also performed which showed iron staining in PBS treated mice but much less in sham operated or GCV treated animals. Finally, an Iba1 staining (bottom) was performed which did not show much differences in activated microglial status between treatment groups.



6.4 Discussion

Unfortunately, results obtained in clinical trials have been limited, mainly due to insufficient expression and poor intratumoral distribution of the viral vectors encoding for the suicide gene [199]. Therefore, HSV-TK expressing stem cells that are able to track tumor cells [82, 84, 150-152] have been considered as vehicle for suicide gene delivery with increasing emphasis on non-invasive follow-up of the fate of stem cells while performing these experiments in the preclinical phase [198, 200]. aiming for better translatability from mouse to man. Tumor size, viability and location can be validated with MRI, PET or BLI prior to stem cell injection, thus identifying outliers earlier [198, 200]. Furthermore, the location and viability of the stem cells prior to initiation of treatment is crucial as this will greatly influence the bystander suicide treatment response. Moreover, animals can be followed longitudinally, thus reducing the number of animals needed while additional information can be obtained to gain a better understanding of the dynamics of this experimental glioblastoma treatment and to exclude outliers that are based on experimental errors like failure of correct cell implantation.

In this study, GL261 tumor bearing C57BL6/j mice received 5×10^5 syngeneic HSV-TK / fLuc expressing and SMG²-mPEGSi labeled mMSC's (1%), mOct4⁺ BM-HypoSCs (1%) or mOct4⁻ BM-MAPCs (1-10%) for longitudinal follow-up of suicide gene therapy in immunocompetent animals following *in vitro* and *in vivo* detection feasibility studies.

mMSC treated GL261 tumor bearing animals did not show significant differences in tumor growth when comparing most GCV treated to PBS control animals. Only one mouse out of 4 animals in the GCV treated group showed a reduction in tumor size, which was probably related to experimental variation.

In the mOct4⁺ BM-HypoSC treated GL261 tumor bearing animals, no statistical difference was found in terms of tumor size of GCV treated and PBS control animals, although a slight growth delay was observed for both groups. Although GCV treatment reduced the BLI signal originating from the stem cells treated with GCV, background signal intensity levels were never reached, indicating that in the tumor environment, optimal stem cell killing can not be achieved. As mOct4⁺ BM-HypoSCs form masses themselves when injected in the

brain, endpoint tumors might consist of a combination of masses formed by GL261 and mOct4⁺ BM-HypoSCs.

Hypointense signal volume determination (3D T2* MRI) on 1% labeled mOct4⁻ BM-MAPCs did not show statistically significant differences between stem cell injected animals (PBS/GCV) and sham operated animals one day after surgery (day 16). At the end of treatment (day 30), there was however a significant difference between sham operated animals and GCV-treated animals due to the smaller tumor sizes in the GCV-treated group. In the sham operated and PBS-treated group, tumor formation was present which is accompanied with necrosis and bleedings when tumors grow over time. In contrast, the hypointense signal in the GCV-treated group, which did not develop tumors is mostly generated by remaining labeled mOct4⁻ BM-MAPCs.

Results showed that labeled mOct4⁻ BM-MAPCs were located in and in close proximity to the tumor from one day post injection for all animals. Therefore, treatment was commenced on day one post injection following multi-modal imaging (MRI / BLI). In the majority of GCV, but not PBS-treated animals, a significant difference was found in mOct4⁻ BM-MAPCs viability and tumor size at the end of treatment (Figure 40). However, not only the majority of GCV-treated animals but also some PBS-treated animals showed a significant decrease in tumor size compared to sham operated animals. One hypothesis in the suicide gene therapy field is that the initial, limited intratumoral cell killing caused by injection of the stem cells and the inhospitable tumor micro-environment, of both stem cells and tumor cells generates the release of immunostimulatory molecules resulting in the generation of a Th1 response [161-163], which helps to overcome immune suppression by the tumor.

Our results show however that all PBS-treated animals displayed mOct4⁻ BM-MAPCs survival during PBS administration as determined by BLI, indicating that the observed effect on tumor growth in the PBS-treated group is probably not majorly influenced by mOct4⁻ BM-MAPC cell death. Another possible explanation for the reduction of tumor growth could be the immunomodulatory properties of MAPCs themselves and their capability to exert both immune suppression and immune stimulation [201], which might cause the immune

system to favor immune stimulation rather than immune suppression in the tumor setting and thus contribute to a therapeutic effect and a reduction in tumor size.

This would however still need to be confirmed by additional studies. In any case, our studies demonstrate clearly that adding GCV treatment augments killing of the glioblastoma, which is likely the result of the typical bystander killing effect, and might be enhanced by the additional effect of the proposed Th1 response system described earlier. Furthermore, histological analysis showed the presence of large blood vessels explaining the hypointense signal in large tumors (Masson's Trichrome) and the presence of SMG²-mPEGSi particles in and around the tumor (Prussian blue staining). In smaller tumors, iron staining was more concentrated to the injection site in comparison to large tumors. Activated microglial cells were identified mostly at the tumor border although areas of microglial activation within the tumor tissue were also found. No clear differences could be found however between sham operated, PBS controlled and GCV treated animals in microglial activation status.

Furthermore, [¹⁸F] FET PET was performed in addition to MR imaging in order to gain further insights in tumor viability following suicide gene therapy. Large tumors present in the sham operated groups could be detected quite easily by [¹⁸F] FET PET whereas no statistical differences could be detected between the PBS treated group and the GCV treated group based on [¹⁸F] FET PET, which indicates a mismatch between the difference in tumor sizes between the PBS treated group (larger) and the GCV treated group (smaller) seen in MRI and the metabolic rate seen in PET.

Subsequently, Hs683 or (mCherry rLuc expressing) U87-MG tumor bearing Hsd:athymic Nude-Foxn1^{nu} mice were divided in a sham operated group, a PBS treated group and a GCV treated group (50mg/kg) of which the PBS and GCV treated group received treatment for 14 consecutive days. Labeled hMultistem's were located in close proximity to the tumor (inside and around) already one day post injection. Therefore, treatment was commenced at day one post injection following multi-modal imaging (MRI / BLI). The hMultistem viability decreased in both the PBS and the GCV treated group in the U87-MG tumor bearing animals but not in the Hs683 tumor bearing animals as assessed by BLI using D-luciferin as a substrate for

fLuc, indicating stem cell killing probably due to the harsh U87-MG tumor microenvironment. No differences could be found in either tumor model concerning tumor size between animals that were sham operated or treated with PBS or GCV. However, there was a stagnation of the number of viable tumor U87-MG tumor cells of GCV treated animals after treatment. This was not the case in PBS treated or sham operated animals. All in all, stem cell mediated suicide gene therapy in human glioma xenograft models proved much less effective when comparing the results with the data generated in the GL261 glioblastoma mouse model.

There are several plausible explanations for this failure of therapeutic response. First, developing tumors were generally larger in the U87-MG and Hs683 models compared to the GL261 model at the time of stem cell injection, which may mean that the injection of more stem cells might be necessary reach all tumor cells and hereby elicit a therapeutic response. Secondly, it is apparent that administration of 50mg/kg GCV is insufficient to efficiently kill all stem cells *in vivo* as indicated by the BLI experiments. Increasing the concentration of administered GCV was not feasible as this resulted in the development of side effects such as diarrhoea and weight loss. Increasing the HSV-TK expression in the stem cells would be another alternative but this might need a different approach for transgene insertion as application of higher concentrations lentiviral vector during transduction resulted in detrimental effects on cell propagation.

Furthermore, the bystander killing effect is dependent on the existence of gap junctions between adjacent cells. It has been described in literature that high grade glioma display less cell-cell communication and thus fewer gap junctions which might result in decreased therapeutic response [202]. It has been reported that the bystander killing effect is also in part T cell mediated [161-163], which would explain why no effect can be seen in the human glioma xenograft mouse models, which uses immune-compromized animals that lack T cells. This theory is also supported by our observation that in some cases PBS treated GL261 tumor bearing animals, which received mOct4⁺ BM-MAPCs, also showed a delayed tumor growth even when tumor growth comparable to sham operated controls was present at the time of stem cell injection.

As no T cells are present in immunodeficient mice, brain sections were stained for activated microglia. In Hs683 tumor bearing animals, very few activated microglia could be seen inside the tumor area. In contrast,

activated microglial cells were abundantly present in the tissue surrounding the tumor. In the U87-MG tumor model, some activated microglial cells were present inside the tumor area although no differences in microglial activation could be seen between the different treatment groups.

Finally, as the tumor has a doubling time of days rather than months, we would not be able to pick up marginal effects on tumor growth with only imaging before and after treatment. Additional scanning sessions might be beneficial although care should be taken with increasing the sedation sessions as this may result in profound weight loss as animals are already weakened due to tumor growth.

Thus, we have shown that suicide gene therapy using mOct4⁻ BM-MAPCs as cellular carriers, is effective in reducing the GL261 tumor size in the majority of the GCV-treated animals, resulting in a longer progression free survival compared to sham operated animals. We were however unable to show significant reduction in tumor size using hMultistem as cellular carriers in the human glioma xenograft models.

These results indicate that although stem cell based suicide gene therapy is a promising approach; further investigations are required to understand possible mechanisms of action in different tumor environments and the role of different stem cell types.

In conclusion, we have shown that suicide gene therapy using several stem cells in different malignant glioma models can be followed *in vivo* by MRI and BLI, where MRI can be used to ascertain stem cell location prior to treatment initiation and follow-up of tumor size. BLI can be used to assess stem cell and/or tumor cell viability prior to and following treatment response. Thus, outliers can be detected earlier, GCV treatment can be initiated based on stem cell distribution rather than on empirical time points and a more thorough follow-up can be provided prior to and following treatment of these animals. Although, PET can provide valuable information on the tumor and/ or stem cell metabolic activity, it was less suitable for our mouse models due to its low spatial resolution. This will contribute to a rapid and efficient validation of stem cell based therapeutic approaches of glioma and hereby to a better understanding and optimization of a promising therapeutic approach for glioblastoma patients.

Chapter 7:

General conclusions & Future perspectives

Chapter 7: General conclusions & future perspectives

7.1 General conclusions

Non-invasive imaging modalities such as MRI and PET are considered an essential tool in both the clinical and preclinical setting. Patients diagnosed with glioblastoma multiforme still face a dismal prognosis despite advances in general treatment regimes [3] and promising preclinical research on new treatment approaches. This discrepancy between preclinical and clinical efficacy for most experimental therapies is in part related to the tumor models used in preclinical research. A multitude of animal models exist ranging from models of spontaneously developing tumors, to syngeneic xenograft models which are usually mouse or rat models that do not entirely reflect human glioblastoma's, or human glioma xenograft models which use human glioblastoma cells in immunodeficient mice. The latter use human tumor cells/cell lines but very limited information can be gained in regard to immune responses to the tumor, as they minimally lack T cells, which is a major contributor to treatment. None of the available xenograft models however truly recapitulate all aspects of glioblastoma in human patients. For instance, most cell-line based animal models have limited infiltrating tumor cells, which are the main cause for recurrence and subsequent mortality in human patients. All results deduced from these animal models should therefore be carefully considered prior to making assumptions for human applications. Promising therapeutic approaches should also be tested in human biopsy models in order to fully evaluate the therapeutic response on human GBM as these recapitulate the geno- and phenotype much better compared to cell-line based models [52, 53], although care should be taken with therapeutic approaches which require immune system involvement. In any case, glioblastoma multiforme is actually a very heterogenous population [203] of tumors which makes it difficult to postulate hypotheses for the entire population. Which type of tumor model is most suited therefore depends heavily on the specific experimental therapy under investigation. In this study, we have selected an orthotopic mouse glioblastoma model in which GL261 cells are stereotactically injected in the striatum of syngeneic C57BL6/J mice for reproducible tumor growth. Additionally, two human malignant glioma xenograft models in Hsd:athymic Nude-Foxn1^{nu} mice were selected, namely the Hs683 oligodendroglioma

model which is perceived as a grade III or grade IV model and the U87MG cell line which is classified as a glioblastoma.

One of the promising preclinical therapies with yet clinically rather disappointing results is suicide gene therapy. One of the major causes for this is believed to be the poor distribution of the suicide gene inside and around the tumor [70]. Therefore, attention turned to stem cells carrying the suicide gene to the tumor cells in order to achieve more efficient tumor cell killing [82, 84, 150, 151]. It is however necessary to follow-up animals longitudinally not only to assess initiation of therapy, therapeutic response, and possible side effects but also to track stem cell fate for safety purposes as stem cells are capable of longitudinal proliferation and differentiation into several cell types including such with unwanted side effects, such as mass formation. In both, clinical and preclinical settings, diagnosis and follow-up is usually mainly based on ^1H MRI although a number of difficulties remain including reliable grading [204] and pseudoprogession [205]. Additionally [^{18}F] FET PET, which is also routinely used in some hospitals or ^1H MR spectroscopy, can be performed to gain further information on metabolism in the tumor [196], thus further identifying regions to be biopsied and subsequently graded by a histopathologist. We opted to assess both approaches in the selected tumor models, complemented by stem cell viability information gained from BLI measurements.

The overall problems in regard to diagnosis, treatment and follow-up of patients diagnosed with glioblastoma multiforme, was discussed in Chapter 1. Subsequently, the aims of this work were specified in Chapter 2 and included: 1. Label and transduce stem cells and glioma cells to obtain cells with therapeutic potential and which are traceable with non-invasive, multi-modal imaging (MRI, BLI, PET); 2. Characterize and optimize different glioma models; 3. Conduct *in vivo* multi-modal imaging proof-of-principle experiments on stem cells and glioma cells in order to generate a model for screening of stem cell mediated suicide gene therapy in different preclinical glioblastoma models; 4. Assess stem cell mediated suicide gene therapy in different preclinical glioblastoma models using multi-modal small animal imaging, including MRI/BLI/PET for follow-up of stem cell distribution and treatment response.

Suicide gene therapy using stem cells as cellular vehicles to deliver the suicide gene to the tumor area requires alteration of the stem cells in order to stably express a therapeutic gene. Therefore, lentiviral vectors were designed and produced. In addition, reporter genes such as eGFP and fLuc were included to allow for multi-modal imaging follow-up. Initial experiments included optimization of the lentiviral vector promoter (CMV vs EF1 α) for applications in stem cells, as we showed that the CMV promoter was unable to induce stable eGFP expression in rOct4⁺ BM-HypoSCs. Subsequent assessment of an EF1 α promoter driven lentiviral vector encoding for eGFP however established stable eGFP expression in HEK 293T, mMSC, rOct4⁺ BM-HypoSCs and mOct4⁺ BM-HypoSCs after antibiotic selection. Next, the newly designed, multicistronic lentiviral vectors encoding for eGFP and fLuc or eGFP, fLuc and HSV-TK were produced and assessed in mMSC's, mOct4⁺ BM-HypoSCs, mOct4⁻ BM-MAPCs and hMultistem's for fLuc and HSV-TK expression. Both transgenes were considered to be expressed sufficiently for *in vivo* experimentation.

Furthermore, mMSC's, mOct4⁺ BM-HypoSCs, mOct4⁻ BM-MAPCs and hMultistem's were labeled with SMG²-mPEGSi particles for MRI-based *in vivo* tracking of the stem cells. ICP-OES and MRI on phantoms were performed to assess the amount of iron per cell and the hypointense contrast generation *in vitro*. Both confirmed efficient labeling in all cells, without significant differences in cell viability as assessed by BLI when compared to non-labeled eGFP-fLuc-HSVTK expressing controls. For mMSC's and mOct4⁺ BM-HypoSCs, labeling of the cells with SMG²-mPEGSi particles was compared to labeling with the previously commercially available contrast agent Endorem[®] which showed better uptake of the particles in the cells which also corresponded to quicker relaxation in the MRI phantom when using SMG²-mPEGSi particles.

Finally, when assessing therapeutic response, tumor size is not the most predictive and valuable parameter to be validated. Therefore, we attempted also to follow-up tumor growth by rLuc BLI. Therefore, rLuc expression was assessed in all tumor cell lines *in vitro*, namely the GL261, Hs683 and U87-MG cell line. BLI showed sufficiently high expression of rLuc *in vitro* for later *in vivo* assessment.

In conclusion, the *in vitro* detection and treatment characteristics of different stem cells and glioma cell lines were assessed successfully in Chapter 3.

In Chapter 4, the eGFP-fLuc-HSVTK + and SMG²-mPEGSi labeled mMSC's, mOct4⁺ BM-HypoSCs, mOct4⁻ BM-MAPCs and hMultistem's generated in Chapter 3 were assessed *in vivo* for multi-modal imaging detectability and response to GCV. All the mentioned cells types could be well localized and monitored by BLI measurements. Initial safety studies indicated that most stem cells, including mMSC's, mOct4⁻ BM-MAPCs and hMultistem's did not show any mass growth over time. MOct4⁺ BM-HypoSCs however did show mass formation and growth, which has already been described by Lo Nigro *et al* [145] for rOct4⁺ BM-HypoSCs. Most stem cell types responded very well to the GCV treatment with even no mass formation in mOct4⁺ BM-HypoSCs following GCV treatment. hMultistem's however did not respond well to GCV treatment. A plausible cause is that due to limited BBB integrity loss in the absence of mass formation in the brain, suboptimal levels of GCV reached the respective brain regions, as GCV does not efficiently cross the BBB [206]. These suboptimal GCV concentrations combined with a higher natural resistance to GCV killing, which was already apparent in the *in vitro* studies performed in Chapter 3. Higher concentrations of GCV were required to efficiently kill the hMultistem cells *in vitro* compared to the other stem cell types under investigation. Therefore, applying these stem cells in a malignant glioma model with BBB disruption might increase the attainable GCV levels in the brain and therefore result in more pronounced hMultistem killing. Furthermore, [¹⁸F] FHBG, which can be used as a tracer for HSV-tk detection [207], was evaluated *in vivo*. Hereby, eGFP-fLuc-HSVTK expressing HEK293T cells were injected as a xenograft, after which a 80 min dynamic PET scan was performed. Results showed that the cells could be observed *in vivo*. As [¹⁸F] FHBG does not easily pass the BBB [208], we chose to directly validate the PET contribution for *in vivo* assessment of the suicide gene therapy in a mouse glioblastoma (GL261) model. Hereby, mMSC's, mOct4⁺ BM-HypoSCs mOct4⁻ BM-MAPCs were injected in the GL261 tumor and [¹⁸F] FHBG PET was performed. Results showed that although there was some tracer uptake in the tumor area, this activity was rather low and mostly limited to the first half hour of scanning. This activity could be stem cell specific but due to the partial volume effect and the small tumor sizes in mice, no distinction could be made between stem cells, which are located on the tumor border and tumor cells, which should not have specific [¹⁸F] FHBG signal as

they do not express HSV-tk. In addition, this increased activity present in the first half hour of scanning might also be related to the multitude of blood vessels in the GL261 cells. Blood vessels in tumors are known for their contortuness and leakiness [209], which could be an alternative explanation for higher uptake in the tumor area. Based on our experiments we concluded that [^{18}F] FHBG PET is not the most suitable method to follow-up stem cell based glioma therapy in our mouse models. [^{18}F] FHBG PET imaging has been described both in a clinical [210] and preclinical [207] setting. Clinical reports have been limited so far and preclinical data usually reports very limited increases in signal intensity, which is concurrent with our findings. Follow-up of 5×10^5 stem cells during suicide gene therapy proved too much of a challenge in our model. As signals were perceived to be too low for actual suicide gene therapy follow-up and stem cells were also positive for fLuc, we decided to use BLI rather than PET imaging for follow-up of stem cell viability *in vivo*.

Subsequently, SPIO labeled stem cells were validated *in vivo* for their hypointense contrast generation potential. 3DT2*-weighted MR images showed that labeled mMSC's and mOct4⁻ BM-MAPCs could be detected easily for up to 8 days when injected into the mouse brain. One of the references for SPIO labeling of stem cells for *in vivo* cell tracking is Endorem[®], which is no longer commercially available. Therefore, Dr Jesse Trekker developed in house fabricated SMG²-mPEGSi particles [143] which emulate and even exceed the results obtained for Endorem[®] labeling in the stem cells used for these studies. Cell labeling efficiencies can however differ greatly, depending on the cell type. It is therefore very important to optimize labeling strategies for each individual cell line [211].

Finally, we also evaluated the detectability of the mCherry-rLuc transduced glioma cell lines *in vivo* by BLI using coelenterazin-h as a substrate. Results showed that only tumor growth in the human glioma xenograft U87-MG glioblastoma model could be followed over time, although *in vitro* and *ex vivo* BLI signals also showed rLuc expression in the GL261 and Hs683 models. A multitude of reasons for this failure of sensitive detectability for the GL261 and Hs683 cell lines exist. First, rLuc emits light at 480nm (blue light). At this wavelength, much more absorption occurs by the animal's skin, skull, brain tissue and blood (albumin) compared to eGFP which emits at 560nm (green light). Therefore, less light reaches the surface for *in vivo*

detection. Furthermore, in Hs683 tumors, BBB disruption is incomplete (see Chapter 5), which might cause insufficient levels of GCV as it does not pass the BBB easily [206]. GL261 tumors do however display a BBB integrity loss (Chapter 5), so it does not explain the discrepancy between the *in vitro* and *in vivo* data for this cell line. Another reason could be the presence of efflux pumps, which are present on tumor cells [164]. Furthermore, the human glioma xenograft tumor models that we used are generated in Hsd:athymic Nude-Foxn1^{nu} mice. These mice do not synthesize melanin, which also absorbs light. The GL261 model however has a syngeneic host, namely C57BL6/j mice, which do produce melanin that can therefore further absorb the light coming from the brain. We would like to stress that a combination of all these factors may have contributed to the failure to detect GL261 and Hs683 tumor cells *in vivo*.

In Chapter 5, the selected malignant glioma models were optimized and characterized *in vivo*. 2.5×10^5 GL261, 5×10^4 Hs683 or 3×10^5 U87-MG cells were stereotactically injected and followed by MRI measurements. These tumor models generated grade 3 symptoms due to volume effects caused by tumor growth at 4 (U87-MG), 5 (GL261) and 6-8 weeks post injection (Hs683), respectively. GL261 grew homogenous with central necrosis and large bleedings developing over time as apparent on both MRI and histological analysis. Blood vessels were also observed both inside the tumor and on the tumor periphery which has been reported to be derived either from the host or caused by neo-angiogenesis [165]. The U87-MG tumor model also grew quite homogeneously but with far fewer and smaller blood vessels inside and surrounding the tumor. The Hs683 tumors grew exceptionally large and developed large fluid filled cysts which were apparent on MRI and histology. Histological analysis showed some main characteristics of malignant gliomas including infiltration, mitosis, nuclear atypia, the presence of blood vessels/bleedings. Central necrosis was apparent in the GL261 model but no distinctive regions of necrosis could be identified using histological assessment for the U87-MG and Hs683 models. The formation of connective tissue in the U87-MG tumors was very striking on Masson's trichrome staining. GFAP staining proved negative for the Hs683 and GL261 model, which has been described previously for both models by Szatmari *et al* [155] and Belot *et al* [180], respectively.

Additionally, the BBB integrity was assessed by CE-T1W MRI and Evans blue injection in one mouse glioblastoma model (GL261) and two high-grade human glioma xenograft models (Hs683 and U87-MG). One of the hallmarks of high grade gliomas is neo-angiogenesis [178], which is correlated with tumor grade and malignancy [168]. It is therefore important to monitor the BBB status during therapy. Furthermore, some experimental brain tumor treatments, using for instance systemically injected stem cells or administration of large or hydrophilic therapeutic molecules, could be hampered by incomplete BBB disruption, which might result in less efficient treatment. It is therefore crucial to characterize tumors models very carefully before starting treatment regimes. BBB integrity loss was observed in all models using CE T1W MRI, although the Hs683 model proved to have a very heterogenous BBB integrity loss. The U87-MG and GL261 models displayed a more homogenous contrast enhancement, very soon in the tumor development (one week post injection for U87-MG tumors, two weeks post injection for GL261 tumors, respectively) with non-enhancing regions appearing over time when necrosis or bleedings occurred, which is concurrent with the data obtained by histology. Evans blue assessment was concurrent with these results for the GL261 tumors with enhancement starting from week 2 post injection. In contrast, this was not the case for Hs683 tumors where no positive Evans blue staining was observed at any time point. The BBB integrity loss demonstrated by both techniques for the GL261 model is concurrent with data obtained by Cha *et al* [35]. Although, loss of BBB integrity is a general characteristic of glioblastoma, little is known about the actual mechanisms involved in this BBB disruption [182]. The discrepancy between MRI data and Evans blue staining suggest incomplete BBB integrity loss in the Hs683 model as Evans blue binds to albumin and is therefore much larger compared to Dotarem.

In Chapter 6, therapeutic stem cells were injected in the selected tumor models and treated with GCV for 14 consecutive days. First, eGFP-fLuc-HSVTK expressing and SMG²-mPEGSi labeled mMSC's, mOct4+ BM-HypoSCs were evaluated in the GL261 model followed by hMultistem evaluation in the Hs683 and U87-MG models. All stem cells were detectable one day after injection by both MRI and BLI, indicating that SMG²-mPEGSi labeling and transgene expression are sufficiently high, even for stem cell detection in a tumor

model where stem cells are dispersed over the entire tumor volume and beyond. Furthermore, we observed that stem cells are already located at the border of the tumor one day post stem cell injection. No subsequent stem cell re-location/migration was observed, indicating that stem cell treatment could be commenced at that time. This early initiation of treatment is beneficial as it was shown by Amano et al that for treatment of rapidly growing tumors using HSV-TK gene therapy, early GCV administration is required for an effective tumoricidal effect [212].

mMSC treated GL261 tumor bearing animals did not show significant differences in tumor growth when comparing most GCV treated to PBS control animals. Only one mouse out of 4 animals in the GCV treated group showed a reduction in tumor size, which was probably related to experimental variation.

In the mOct4⁺ BM-HypoSC treated GL261 tumor bearing animals, no statistical difference could be found in tumor size of GCV treated and PBS control animals. Although a slight growth delay was observed for both groups. Unfortunately, although GCV treatment reduced the BLI signal originating from the stem cells treated with GCV, low background levels in BLI signal intensity were never reached, indicating that in the tumor environment, optimal stem cell killing can not be achieved using this cell line. As mOct4⁺ BM-HypoSCs form masses themselves when injected in the brain, endpoint tumors might consist of a combination of GL261 and mOct4⁺ BM-HypoSCs masses.

In the majority of GCV treated, but not PBS control, GL261 tumor bearing animals injected with mOct4⁻ BM-MAPCs, animals displayed a significant difference in mOct4⁻ BM-MAPCs viability and tumor size at the end of treatment as assessed by MRI. Furthermore, O-(2-[¹⁸F]fluoroethyl)-L-tyrosine positron emission tomography ([¹⁸F] FET PET) was acquired in addition to MR imaging in order to gain further insights in tumor viability following suicide gene therapy. Large tumors present in the sham operated groups could be detected quite easily by [¹⁸F] FET PET whereas no statistical differences could be detected between the PBS treated group and the GCV treated group based on [¹⁸F] FET PET, although it was very obvious on MRI that tumor sizes in the PBS treated group were larger than in the GCV treated group. [¹⁸F] FET PET is used clinically for tumor grading as it is a measure for tumor metabolism. It is however generally accepted that mouse tumor models

not always fully encompass the full range of malignancy as in human tumors. It might be therefore possible that the metabolism in our model is not quite as high as observed in human tumor patients. Furthermore, the resolution of the μ PET scanner is around 1.4 mm which makes it rather difficult to distinguish between different, relatively small tumors in the brain.

Some PBS treated animals showed also a significant decrease in tumor size compared to sham operated animals and the majority of the PBS treated animals. One hypothesis in the suicide gene therapy field is that the initial, limited intratumoral cell killing generates immunostimulatory molecules, resulting in the generation of a Th1 response [161-163], which helps to overcome the immune suppression by the tumor [213]. Our results show however that all PBS treated animals displayed mOct4⁻ BM-MAPCs survival during PBS administration as determined by BLI, indicating that the observed effect on tumor growth in the PBS treated group is not solely attributable to mOct4⁻ BM-MAPC cell death. It is also described in literature that MAPCs themselves possess immunomodulatory properties, and are thus capable of both immune suppression and immune stimulation [201], which might cause the immune system to favor immune stimulation rather than immune suppression in the tumor setting, thus further contributing to a reduced tumor size. This would also explain the delay in tumor growth in the mOct4⁺ BM-MAPCs that was seen initially, irrespective of the treatment groups. Adding GCV treatment seems to augment this effect even further which could be related to the additional effect of the proposed Th1 response system described earlier. As some BLI signal remained following GCV treatment in the mOct4⁺ BM-MAPCs treated animals, mass formation caused by mOct4⁺ BM-MAPCs explains the lack of difference in tumor size in these animals.

Subsequently, Hs683 or (mCherry rLuc expressing) U87-MG tumor bearing Hsd:athymic Nude-Foxn1^{nu} mice were stereotactically injected intratumorally with 5×10^5 or 2.5×10^5 eGFP-Fluc-HSVTK expressing and SPIO labeled (1%) hMultistem's, respectively for longitudinal follow-up of suicide gene therapy. Three groups were distinguished for both malignant glioma models, including a sham operated group, a PBS treated group and a GCV treated group (50mg/kg) of which the PBS and GCV treated groups received treatment for 14 consecutive days. Results showed that labeled hMultistem's were also situated in close proximity to the

tumor already one day post injection, therefore warranting initiation of treatment. hMultistem viability decreased in both the PBS and the GCV treated group in the U87-MG tumor bearing animals but not in the Hs683 tumor bearing animals as assessed by BLI using D-luciferin as a substrate for fLuc. This indicates stem cell killing probably due to the harsh U87-MG tumor microenvironment. No differences could be found in either tumor model concerning tumor size between animals that were sham operated or treated with PBS or GCV. A stagnation of the tumor viability in U87-MG tumors of GCV treated animals was observed after treatment. This was not the case in PBS treated or sham operated animals. All in all, stem cell mediated suicide gene therapy in human glioma xenograft models proved much less effective when comparing the results with the data generated in the GL261 glioblastoma mouse model.

There are several plausible explanations for this failure of therapeutic response. First, developing tumors were generally larger in the U87-MG and Hs683 models compared to the GL261 model at the time of stem cell injection, which may mean that the injection of more stem cells might be necessary to elicit a therapeutic response. Secondly, it is apparent that administration of 50mg/kg GCV is insufficient to elicit efficient stem cell killing *in vivo*. Increasing the concentration of administered GCV was not studied systematically as this resulted in the development of side effects such as diarrhoea and weight loss. Another method to increase the amount of GCV reaching the brain is to use a 1,4-dihydrotrigonelline modified GCV which crosses the BBB more easily and is subsequently trapped inside the brain [206]. Increasing the HSV-TK expression by the stem cells would be another alternative but this might need a different approach for transgene insertion as application of higher concentrations of lentiviral vectors during transduction resulted in detrimental effects on cell propagation. An alternative strategy to augment transgene expression is to use the CAG promoter in stead of the EF1 α promoter to drive gene expression.

Thirdly, it has been described in literature however that high grade glioma display less cell-cell communication and thus fewer gap junctions which might result in decreased therapeutic response [202, 214].

More importantly, we have to use immune-compromized mice for the human glioma xenograft model. It was reported that the bystander killing effect is also in part T cell mediated [161-163] which would explain also why no effect can be seen in the human glioma xenograft mouse models which do not have T cells. This theory is also supported by our observation that in some cases PBS treated GL261 tumor bearing animals which received mOct4⁻ BM-MAPCs also show a decreased tumor growth even when clear tumor growth was present at the time of stem cell injection.

Brain sections were stained for activated microglia, which are normally activated by Th1 cells. In Hs683 tumor bearing animals, very few activated microglia could be seen inside the tumor area, whereas activated microglial cells were abundantly present in the tissue surrounding the tumor. In the U87-MG tumor some activated microglial cells were present inside the tumor area although no differences in microglial activation could be seen between the different treatment groups. In GL261 tumor bearing animals however, microglial cells were also present in certain part of the tumor tissue in sham operated and PBS control animals. In GCV responding animals, many more microglial cells were present in and around the graft, indicating efficient microglial cell activation and clearing of the tumor.

Finally, as the tumor has a doubling time of days rather than months, we would not be able to pick up marginal effects on tumor growth with only imaging before and after treatment. Additional scanning sessions might be beneficial although care should be taken with increasing the sedation sessions as this may result in profound weight loss as animals are already weakened due to tumor growth. Furthermore, the bystander killing effect is dependent on the existence of gap junctions between adjacent cells.

These results indicate that although stem cell based suicide gene therapy is a promising approach; further investigations are required for possible mechanisms of action in different tumor environments, using a variety of stem cells to optimize therapeutic effects. With the development of the mentioned imaging techniques it is now possible to monitor these different stem cells, and other parameters longitudinally *in vivo*, which allows more rapid screening and optimization of malignant glioma models.

In conclusion, we have shown that suicide gene therapy using several stem cells in different malignant glioma models can be followed and guided *in vivo* by MRI and BLI. Hereby, MRI can be used to ascertain stem cell location prior to treatment initiation and tumor growth follow-up. BLI can be used to assess stem cell viability prior to and following treatment response. Thus, outliers can be detected earlier, GCV treatment can be initiated based on stem cell distribution rather than on empirical time points and a more thorough follow-up can be provided prior to and following treatment of these animals.

7.2 Future perspectives

This work has shown that *in vivo* follow-up of suicide gene therapy mediated by stem cells delivering the suicide gene to the tumor site is feasible with multi-modal imaging. In our hands, MRI and BLI were best suited for this purpose in our preclinical setting. However, a more thorough understanding of tumor cell viability is also required for assessment of treatment efficacy. This information could be generated by BLI. However, rLuc was not successful in our models. Due to its low resolution in the mouse model, [¹⁸F] FET PET imaging conveyed little additional information with regard to tumor viability. For clinical relevance and translationability, it is however preferable to use PET instead of BLI. Concurrent MRI and PET might result in more accurate quantification as co-registration becomes possible. Therefore, a transferable animal bed for MRI and PET purposes is required to obtain both images at the same time. Alternatively, multiple MRI/PET systems have become available which also aid this co-registration. Thus, the tumor area can be delineated on the MR images after which PET image analysis can be performed on the same region. In our study, PET data analysis was performed on the striatum derived from a mouse brain atlas. However, as described PET imaging was very challenging in a mouse model, ultimately, rat glioblastoma models could be more suitable for PET imaging as the rat brain is larger and a rat brain atlas is also available for striatal delineation.

In this study, the use of mOct4⁺ BM-MAPCs resulted in a delayed tumor growth in most of the GCV treated animals when compared to PBS control animals. However, 7 out of 18 animals did not show a response to GCV treatment, although stem cells were efficiently killed as shown by BLI. As we mentioned earlier, one underlying mechanism of action for the suicide gene therapy is possibly the generation of a Th1 response

which fortifies the tumor clearance. Treatments which enhance this Th1 response might further ameliorate the results obtained in this study. Therefore an approach combining suicide gene therapy with intralesional infusion, using for instance an ommaya reservoir adapted with an osmotic pump, of the Th1 promoting cytokine interleukin-12 (IL-12) [215] might ameliorate the evoked Th1 response and aid further clearance of residual tumor tissue. Further optimization is also required in HSV-TK expression levels as in our study, a dose of 50mg/kg GCV was used in order to reach sufficiently high levels for killing of the therapeutic stem cells *in vivo*. Further elevation of the GCV dose without exerting side effects proved to be challenging. Therefore, increasing the expression levels of HSV-TK might enable us to decrease the concentration of GCV required for generating an efficient therapeutic response and obtain higher response rates. This could, for example, be achieved by employing the CAG promoter to drive transgene expression. Furthermore, homogeneous GCV distribution might be hampered by the heterogenous nature of the studied malignant glioma models. A more optimized GCV distribution could be reached in the brain by using an adapted form of GCV, such as a liposomal formulation which crosses the BBB more easily and traps the GCV within the brain, resulting in higher homogenous GCV concentrations within the tumor and further increasing a therapeutic response [206].

The current advancements in molecular multi-modal imaging have created a multitude of options for follow-up of both stem cell fate and therapeutic efficacy when employing stem cell based suicide gene therapy. In this study, we have optimized protocols for stem cell tracking using MRI (distribution) and BLI (viability) during treatment of several malignant glioma models. The established imaging protocols to follow suicide gene therapy in different malignant glioma models using several different therapeutic stem cells enables researchers to screen a multitude of possible therapeutic stem cells in order to identify the most suitable stem cells and to gain further insights in the mechanisms involved in this therapeutic approach. This additional information might aid researchers in optimizing suicide gene therapy for clinical applications which might result in significant improvements regarding the poor prognosis faced by glioblastoma patients today.

References

1. Dolecek, T.A., et al., *CBTRUS Statistical Report: Primary Brain and Central Nervous System Tumors Diagnosed in the United States in 2005-2009*. Neuro Oncol, 2012. **14 Suppl 5**: p. v1-v49.
2. Kagadis, G.C., et al., *In vivo small animal imaging: current status and future prospects*. Med Phys, 2010. **37**(12): p. 6421-42.
3. Stupp, R., et al., *Effects of radiotherapy with concomitant and adjuvant temozolomide versus radiotherapy alone on survival in glioblastoma in a randomised phase III study: 5-year analysis of the EORTC-NCIC trial*. Lancet Oncol, 2009. **10**(5): p. 459-66.
4. Aranguren, X.L., et al., *Multipotent adult progenitor cells sustain function of ischemic limbs in mice*. J Clin Invest, 2008. **118**(2): p. 505-14.
5. Louis, D.N., et al., *The 2007 WHO classification of tumours of the central nervous system*. Acta Neuropathol, 2007. **114**(2): p. 97-109.
6. Walker, P.R., et al., *T-cell immune responses in the brain and their relevance for cerebral malignancies*. Brain Res Brain Res Rev, 2003. **42**(2): p. 97-122.
7. Cheng, L., et al., *Elevated invasive potential of glioblastoma stem cells*. Biochem Biophys Res Commun, 2011. **406**(4): p. 643-8.
8. Brustle, O., et al., *Primitive neuroectodermal tumors after prophylactic central nervous system irradiation in children. Association with an activated K-ras gene*. Cancer, 1992. **69**(9): p. 2385-92.
9. Bleeker, F.E., R.J. Molenaar, and S. Leenstra, *Recent advances in the molecular understanding of glioblastoma*. J Neurooncol, 2012. **108**(1): p. 11-27.
10. James, M.L. and S.S. Gambhir, *A molecular imaging primer: modalities, imaging agents, and applications*. Physiol Rev, 2011. **92**(2): p. 897-965.
11. Janowski, M., J.W. Bulte, and P. Walczak, *Personalized nanomedicine advancements for stem cell tracking*. Adv Drug Deliv Rev, 2012. **64**(13): p. 1488-507.
12. Contag, C.H., et al., *Visualizing gene expression in living mammals using a bioluminescent reporter*. Photochem Photobiol, 1997. **66**(4): p. 523-31.
13. Hilderbrand, S.A. and R. Weissleder, *Near-infrared fluorescence: application to in vivo molecular imaging*. Curr Opin Chem Biol, 2010. **14**(1): p. 71-9.
14. Dinca, E.B., R.V. Voicu, and A.V. Ciurea, *Bioluminescence imaging of invasive intracranial xenografts: implications for translational research and targeted therapeutics of brain tumors*. Neurosurg Rev, 2010. **33**(4): p. 385-94.
15. Ozawa, T. and C.D. James, *Establishing intracranial brain tumor xenografts with subsequent analysis of tumor growth and response to therapy using bioluminescence imaging*. J Vis Exp, 2010(41).
16. Jost, S.C., et al., *Measuring brain tumor growth: combined bioluminescence imaging-magnetic resonance imaging strategy*. Mol Imaging, 2009. **8**(5): p. 245-53.
17. Badr, C.E. and B.A. Tannous, *Bioluminescence imaging: progress and applications*. Trends Biotechnol, 2011. **29**(12): p. 624-33.
18. Zhao, S., et al., *Biologic correlates of intratumoral heterogeneity in 18F-FDG distribution with regional expression of glucose transporters and hexokinase-II in experimental tumor*. J Nucl Med, 2005. **46**(4): p. 675-82.
19. Di Chiro, G., et al., *Glucose utilization of cerebral gliomas measured by [18F] fluorodeoxyglucose and positron emission tomography*. Neurology, 1982. **32**(12): p. 1323-9.
20. Alavi, J.B., et al., *Positron emission tomography in patients with glioma. A predictor of prognosis*. Cancer, 1988. **62**(6): p. 1074-8.
21. Miyagawa, T., et al., *"Facilitated" amino acid transport is upregulated in brain tumors*. J Cereb Blood Flow Metab, 1998. **18**(5): p. 500-9.
22. Bergstrom, M., et al., *Comparison of the accumulation kinetics of L-(methyl-11C)-methionine and D-(methyl-11C)-methionine in brain tumors studied with positron emission tomography*. Acta Radiol, 1987. **28**(3): p. 225-9.

References

23. Kracht, L.W., et al., *Delineation of brain tumor extent with [11C]L-methionine positron emission tomography: local comparison with stereotactic histopathology*. Clin Cancer Res, 2004. **10**(21): p. 7163-70.
24. Grosu, A.L., et al., *An interindividual comparison of O-(2-[18F]fluoroethyl)-L-tyrosine (FET)- and L-[methyl-11C]methionine (MET)-PET in patients with brain gliomas and metastases*. Int J Radiat Oncol Biol Phys, 2011. **81**(4): p. 1049-58.
25. Grosu, A.L., et al., *An interindividual comparison of O-(2-[18F]fluoroethyl)-L-tyrosine (FET)- and L-[methyl-11C]methionine (MET)-PET in patients with brain gliomas and metastases*. Int J Radiat Oncol Biol Phys, 2010. **81**(4): p. 1049-58.
26. Ullrich, R.T., L.W. Kracht, and A.H. Jacobs, *Neuroimaging in patients with gliomas*. Semin Neurol, 2008. **28**(4): p. 484-94.
27. Chen, X., et al., *Longitudinal microPET imaging of brain tumor growth with F-18-labeled RGD peptide*. Mol Imaging Biol, 2006. **8**(1): p. 9-15.
28. Wehrl, H.F., et al., *Multimodal Elucidation of Choline Metabolism in a Murine Glioma Model Using Magnetic Resonance Spectroscopy and 11C-Choline Positron Emission Tomography*. Cancer Res, 2013. **73**(5): p. 1470-1480.
29. Collins, S.A., et al., *PET imaging for gene & cell therapy*. Curr Gene Ther, 2012. **12**(1): p. 20-32.
30. Penheiter, A.R., S.J. Russell, and S.K. Carlson, *The sodium iodide symporter (NIS) as an imaging reporter for gene, viral, and cell-based therapies*. Curr Gene Ther, 2012. **12**(1): p. 33-47.
31. Casteels, C., et al., *Construction and evaluation of multitracer small-animal PET probabilistic atlases for voxel-based functional mapping of the rat brain*. J Nucl Med, 2006. **47**(11): p. 1858-66.
32. Vande Velde, G., et al., *Magnetic resonance imaging and spectroscopy methods for molecular imaging*. Q J Nucl Med Mol Imaging, 2009. **53**(6): p. 565-85.
33. Choi, J.K., A. Dedeoglu, and B.G. Jenkins, *Application of MRS to mouse models of neurodegenerative illness*. NMR Biomed, 2007. **20**(3): p. 216-37.
34. Hoehn, M., et al., *Application of magnetic resonance to animal models of cerebral ischemia*. J Magn Reson Imaging, 2001. **14**(5): p. 491-509.
35. Cha, S., et al., *Dynamic, contrast-enhanced perfusion MRI in mouse gliomas: correlation with histopathology*. Magn Reson Med, 2003. **49**(5): p. 848-55.
36. Doblbas, S., et al., *Glioma morphology and tumor-induced vascular alterations revealed in seven rodent glioma models by in vivo magnetic resonance imaging and angiography*. J Magn Reson Imaging, 2010. **32**(2): p. 267-75.
37. Hoehn, M., et al., *Cell tracking using magnetic resonance imaging*. J Physiol, 2007. **584**(Pt 1): p. 25-30.
38. Srinivas, M., et al., *Customizable, multi-functional fluorocarbon nanoparticles for quantitative in vivo imaging using 19F MRI and optical imaging*. Biomaterials, 2010. **31**(27): p. 7070-7.
39. Schwarcz, A., et al., *Localized proton MRS of cerebral metabolite profiles in different mouse strains*. Magn Reson Med, 2003. **49**(5): p. 822-7.
40. He, Q., et al., *Magnetic resonance spectroscopic imaging of tumor metabolic markers for cancer diagnosis, metabolic phenotyping, and characterization of tumor microenvironment*. Dis Markers, 2003. **19**(2-3): p. 69-94.
41. Rosol, M., et al., *Metabolism of orthotopic mouse brain tumor models*. Mol Imaging, 2009. **8**(4): p. 199-208.
42. Simoes, R.V., et al., *Preliminary characterization of an experimental breast cancer cells brain metastasis mouse model by MRI/MRS*. MAGMA, 2008. **21**(4): p. 237-49.
43. Nelson, S.J., *Assessment of therapeutic response and treatment planning for brain tumors using metabolic and physiological MRI*. NMR Biomed, 2011. **24**(6): p. 734-49.
44. Gerstner, E.R., et al., *Advances in neuroimaging techniques for the evaluation of tumor growth, vascular permeability, and angiogenesis in gliomas*. Curr Opin Neurol, 2008. **21**(6): p. 728-35.

References

45. Peet, A.C., et al., *Functional imaging in adult and paediatric brain tumours*. Nat Rev Clin Oncol, 2012. **9**(12): p. 700-11.
46. Vrabc, M., et al., *MR perfusion and diffusion imaging in the follow-up of recurrent glioblastoma treated with dendritic cell immunotherapy: a pilot study*. Neuroradiology, 2011. **53**(10): p. 721-31.
47. Van Cauter, S., et al., *Gliomas: diffusion kurtosis MR imaging in grading*. Radiology, 2012. **263**(2): p. 492-501.
48. Van Cauter, S., et al., *Integrating diffusion kurtosis imaging, dynamic susceptibility-weighted contrast-enhanced MRI, and short echo time chemical shift imaging for grading gliomas*. Neuro Oncol, 2014.
49. Assi, H., et al., *Gene therapy for brain tumors: basic developments and clinical implementation*. Neurosci Lett, 2012. **527**(2): p. 71-7.
50. Ardon, H., et al., *Integration of autologous dendritic cell-based immunotherapy in the standard of care treatment for patients with newly diagnosed glioblastoma: results of the HGG-2006 phase I/II trial*. Cancer Immunol Immunother, 2012. **61**(11): p. 2033-44.
51. Dietrich, J., A.D. Norden, and P.Y. Wen, *Emerging antiangiogenic treatments for gliomas - efficacy and safety issues*. Curr Opin Neurol, 2008. **21**(6): p. 736-44.
52. Lee, J., et al., *Tumor stem cells derived from glioblastomas cultured in bFGF and EGF more closely mirror the phenotype and genotype of primary tumors than do serum-cultured cell lines*. Cancer Cell, 2006. **9**(5): p. 391-403.
53. Sakariassen, P.O., et al., *Angiogenesis-independent tumor growth mediated by stem-like cancer cells*. Proc Natl Acad Sci U S A, 2006. **103**(44): p. 16466-71.
54. Barth, R.F. and B. Kaur, *Rat brain tumor models in experimental neuro-oncology: the C6, 9L, T9, RG2, F98, BT4C, RT-2 and CNS-1 gliomas*. J Neurooncol, 2009. **94**(3): p. 299-312.
55. Kruse, C.A., et al., *A rat glioma model, CNS-1, with invasive characteristics similar to those of human gliomas: a comparison to 9L gliosarcoma*. J Neurooncol, 1994. **22**(3): p. 191-200.
56. Mathieu, D., et al., *Standardization and detailed characterization of the syngeneic Fischer/F98 glioma model*. Can J Neurol Sci, 2007. **34**(3): p. 296-306.
57. Sibenaller, Z.A., et al., *Genetic characterization of commonly used glioma cell lines in the rat animal model system*. Neurosurg Focus, 2005. **19**(4): p. E1.
58. Tzeng, J.J., et al., *Phenotype and functional activity of tumor-infiltrating lymphocytes isolated from immunogenic and nonimmunogenic rat brain tumors*. Cancer Res, 1991. **51**(9): p. 2373-8.
59. de Vries, N.A., J.H. Beijnen, and O. van Tellingen, *High-grade glioma mouse models and their applicability for preclinical testing*. Cancer Treat Rev, 2009. **35**(8): p. 714-23.
60. Ausman, J.I., W.R. Shapiro, and D.P. Rall, *Studies on the chemotherapy of experimental brain tumors: development of an experimental model*. Cancer Res, 1970. **30**(9): p. 2394-400.
61. Zimmerman, H.M., Hildegard A., *Experimental Brain Tumors I. Tumors Produced with Methylcholanthrene*. Cancer res, 1941. **1**(12): p. 20.
62. Maes, W. and S.W. Van Gool, *Experimental immunotherapy for malignant glioma: lessons from two decades of research in the GL261 model*. Cancer Immunol Immunother.
63. Candolfi, M., et al., *Intracranial glioblastoma models in preclinical neuro-oncology: neuropathological characterization and tumor progression*. J Neurooncol, 2007. **85**(2): p. 133-48.
64. Norden, A.D., J. Drappatz, and P.Y. Wen, *Novel anti-angiogenic therapies for malignant gliomas*. Lancet Neurol, 2008. **7**(12): p. 1152-60.
65. di Tomaso, E., et al., *Glioblastoma recurrence after cediranib therapy in patients: lack of "rebound" revascularization as mode of escape*. Cancer Res, 2011. **71**(1): p. 19-28.
66. Maes, W., et al., *DC vaccination with anti-CD25 treatment leads to long-term immunity against experimental glioma*. Neuro Oncol, 2009. **11**(5): p. 529-42.
67. Dey, M., I.V. Ulasov, and M.S. Lesniak, *Virotherapy against malignant glioma stem cells*. Cancer Lett, 2010. **289**(1): p. 1-10.

References

68. Holzmuller, R., et al., *YB-1 dependent virotherapy in combination with temozolomide as a multimodal therapy approach to eradicate malignant glioma*. *Int J Cancer*, 2011. **129**(5): p. 1265-76.
69. Kwiatkowska, A., et al., *Strategies in gene therapy for glioblastoma*. *Cancers (Basel)*, 2013. **5**(4): p. 1271-305.
70. Juratli, T.A., G. Schackert, and D. Krex, *Current status of local therapy in malignant gliomas--a clinical review of three selected approaches*. *Pharmacol Ther*, 2013. **139**(3): p. 341-58.
71. Bernardes, N., A.M. Chakrabarty, and A.M. Fialho, *Engineering of bacterial strains and their products for cancer therapy*. *Appl Microbiol Biotechnol*, 2013. **97**(12): p. 5189-99.
72. Germano, I.M., M. Uzzaman, and G. Keller, *Gene delivery by embryonic stem cells for malignant glioma therapy: hype or hope?* *Cancer Biol Ther*, 2008. **7**(9): p. 1341-7.
73. Duarte, S., et al., *Suicide gene therapy in cancer: where do we stand now?* *Cancer Lett*, 2012. **324**(2): p. 160-70.
74. Germano, I.M. and E. Binello, *Gene therapy as an adjuvant treatment for malignant gliomas: from bench to bedside*. *J Neurooncol*, 2009. **93**(1): p. 79-87.
75. Verfaillie, C.M., *Adult stem cells: assessing the case for pluripotency*. *Trends Cell Biol*, 2002. **12**(11): p. 502-8.
76. Eckfeldt, C.E., E.M. Mendenhall, and C.M. Verfaillie, *The molecular repertoire of the 'almighty' stem cell*. *Nat Rev Mol Cell Biol*, 2005. **6**(9): p. 726-37.
77. Burns, T.C. and G.K. Steinberg, *Stem cells and stroke: opportunities, challenges and strategies*. *Expert Opin Biol Ther*, 2011. **11**(4): p. 447-61.
78. Bang, O.Y., et al., *Autologous mesenchymal stem cell transplantation in stroke patients*. *Ann Neurol*, 2005. **57**(6): p. 874-82.
79. Vaes, B., et al., *Application of MultiStem((R)) Allogeneic Cells for Immunomodulatory Therapy: Clinical Progress and Pre-Clinical Challenges in Prophylaxis for Graft Versus Host Disease*. *Front Immunol*, 2012. **3**: p. 345.
80. Park, S.A., et al., *CXCR4-transfected human umbilical cord blood-derived mesenchymal stem cells exhibit enhanced migratory capacity toward gliomas*. *Int J Oncol*. **38**(1): p. 97-103.
81. Eskandary, H., et al., *The role of stem cells in tumor targeting and growth suppression of gliomas*. *Biologics*. **5**: p. 61-70.
82. Miletic, H., et al., *Bystander killing of malignant glioma by bone marrow-derived tumor-infiltrating progenitor cells expressing a suicide gene*. *Mol Ther*, 2007. **15**(7): p. 1373-81.
83. Alexander, D.B. and G.S. Goldberg, *Transfer of biologically important molecules between cells through gap junction channels*. *Curr Med Chem*, 2003. **10**(19): p. 2045-58.
84. Li, S., et al., *Bystander effect-mediated gene therapy of gliomas using genetically engineered neural stem cells*. *Cancer Gene Ther*, 2005. **12**(7): p. 600-7.
85. Matuskova, M., et al., *HSV-tk expressing mesenchymal stem cells exert bystander effect on human glioblastoma cells*. *Cancer Lett*. **290**(1): p. 58-67.
86. Egea, V., et al., *TNF-alpha respecifies human mesenchymal stem cells to a neural fate and promotes migration toward experimental glioma*. *Cell Death Differ*.
87. Paino, T., et al., *Inhibition of ATP-sensitive potassium channels increases HSV-tk/GCV bystander effect in U373 human glioma cells by enhancing gap junctional intercellular communication*. *Neuropharmacology*. **59**(6): p. 480-91.
88. Massoud, T.F. and S.S. Gambhir, *Molecular imaging in living subjects: seeing fundamental biological processes in a new light*. *Genes Dev*, 2003. **17**(5): p. 545-80.
89. Koul, D., et al., *Cellular and in vivo activity of a novel PI3K inhibitor, PX-866, against human glioblastoma*. *Neuro Oncol*, 2010. **12**(6): p. 559-69.
90. Asanuma, T., et al., *Diffusion tensor imaging and fiber tractography of C6 rat glioma*. *J Magn Reson Imaging*, 2008. **28**(3): p. 566-73.

References

91. Kharuzhyk, S.A., N.A. Petrovskaya, and M.A. Vosmitel, *Diffusion-weighted magnetic resonance imaging in non-invasive monitoring of antiangiogenic therapy in experimental tumor model*. *Exp Oncol*, 2010. **32**(2): p. 104-6.
92. Tofts, P.S., et al., *Estimating kinetic parameters from dynamic contrast-enhanced T(1)-weighted MRI of a diffusable tracer: standardized quantities and symbols*. *J Magn Reson Imaging*, 1999. **10**(3): p. 223-32.
93. Zhao, Y., et al., *Targeted suicide gene therapy for glioma using human embryonic stem cell-derived neural stem cells genetically modified by baculoviral vectors*. *Gene Ther*, 2012. **19**(2): p. 189-200.
94. Zhang, K., et al., *Comparison of cerebral blood flow acquired by simultaneous [(15)O]water positron emission tomography and arterial spin labeling magnetic resonance imaging*. *J Cereb Blood Flow Metab*, 2014. **34**(8): p. 1373-80.
95. Brubaker, L.M., et al., *Magnetic resonance angiography visualization of abnormal tumor vasculature in genetically engineered mice*. *Cancer Res*, 2005. **65**(18): p. 8218-23.
96. Keunen, O., et al., *Anti-VEGF treatment reduces blood supply and increases tumor cell invasion in glioblastoma*. *Proc Natl Acad Sci U S A*, 2011. **108**(9): p. 3749-54.
97. Spaeth, N., et al., *Uptake of 18F-fluorocholine, 18F-fluoro-ethyl-L: -tyrosine and 18F-fluoro-2-deoxyglucose in F98 gliomas in the rat*. *Eur J Nucl Med Mol Imaging*, 2006. **33**(6): p. 673-82.
98. Assadian, S., et al., *FDG-PET imaging for the evaluation of anti-glioma agents in a rat model*. *Neuro Oncol*, 2008. **10**(3): p. 292-9.
99. Hekmatyar, S.K., et al., *(1)H nuclear magnetic resonance spectroscopy characterisation of metabolic phenotypes in the medulloblastoma of the SMO transgenic mice*. *Br J Cancer*, 2010. **103**(8): p. 1297-304.
100. Park, I., et al., *Hyperpolarized 13C magnetic resonance metabolic imaging: application to brain tumors*. *Neuro Oncol*, 2010. **12**(2): p. 133-44.
101. Lagae; U. Himmelreich, A.D.H.C.V.G.V.V.H.J.S.M.N.D.J.J.T.S.S.M.L. *Gold nanostars as a theranostic agent for multimodal imaging and photothermal treatment of cancer*. in *9th European Molecular Imaging Meeting*. 2014. Antwerp (Belgium).
102. Van de Broek, B., et al., *Specific cell targeting with nanobody conjugated branched gold nanoparticles for photothermal therapy*. *ACS Nano*, 2011. **5**(6): p. 4319-28.
103. Day, E.S., et al., *Antibody-conjugated gold-gold sulfide nanoparticles as multifunctional agents for imaging and therapy of breast cancer*. *Int J Nanomedicine*, 2010. **5**: p. 445-54.
104. Qian, X., et al., *In vivo tumor targeting and spectroscopic detection with surface-enhanced Raman nanoparticle tags*. *Nat Biotechnol*, 2008. **26**(1): p. 83-90.
105. Yi, D.K., et al., *Matrix metalloproteinase sensitive gold nanorod for simultaneous bioimaging and photothermal therapy of cancer*. *Bioconjug Chem*, 2010. **21**(12): p. 2173-7.
106. Maes, W., et al., *In vivo bioluminescence imaging in an experimental mouse model for dendritic cell based immunotherapy against malignant glioma*. *J Neurooncol*, 2009. **91**(2): p. 127-39.
107. Jang, S.J., et al., *Application of bioluminescence imaging to therapeutic intervention of herpes simplex virus type I - Thymidine kinase/ganciclovir in glioma*. *Cancer Lett*, 2010. **297**(1): p. 84-90.
108. Winkler, F., et al., *Imaging glioma cell invasion in vivo reveals mechanisms of dissemination and peritumoral angiogenesis*. *Glia*, 2009. **57**(12): p. 1306-15.
109. Himmelreich, U. and T. Dresselaers, *Cell labeling and tracking for experimental models using magnetic resonance imaging*. *Methods*, 2009. **48**(2): p. 112-24.
110. Tavares, R., et al., *Monitoring of in vivo function of superparamagnetic iron oxide labelled murine dendritic cells during anti-tumour vaccination*. *PLoS One*, 2011. **6**(5): p. e19662.
111. Miyagawa, T., et al., *Imaging of HSV-tk Reporter gene expression: comparison between [18F]FEAU, [18F]FFEAU, and other imaging probes*. *J Nucl Med*, 2008. **49**(4): p. 637-48.
112. Johnson, M., et al., *Titration of variant HSV1-tk gene expression to determine the sensitivity of 18F-FHBG PET imaging in a prostate tumor*. *J Nucl Med*, 2009. **50**(5): p. 757-64.

References

113. Zhou, J., et al., *Differentiation between glioma and radiation necrosis using molecular magnetic resonance imaging of endogenous proteins and peptides*. Nat Med, 2011. **17**(1): p. 130-4.
114. Spaeth, N., et al., *Uptake of 18F-fluorocholine, 18F-fluoroethyl-L-tyrosine, and 18F-FDG in acute cerebral radiation injury in the rat: implications for separation of radiation necrosis from tumor recurrence*. J Nucl Med, 2004. **45**(11): p. 1931-8.
115. Jarzabek, M.A., et al., *In Vivo Bioluminescence Imaging Validation of a Human Biopsy-derived Orthotopic Mouse Model of Glioblastoma Multiforme*. Mol Imaging, 2012. **12**(3): p. 161-72.
116. Corroyer-Dulmont, A., et al., *Noninvasive assessment of hypoxia with 3-[18F]-fluoro-1-(2-nitro-1-imidazolyl)-2-propanol ([18F]-FMISO): a PET study in two experimental models of human glioma*. Biol Chem, 2013. **394**(4): p. 529-39.
117. Corroyer-Dulmont, A., et al., *Detection of glioblastoma response to temozolomide combined with bevacizumab based on muMRI and muPET imaging reveals [18F]-fluoro-L-thymidine as an early and robust predictive marker for treatment efficacy*. Neuro Oncol, 2013. **15**(1): p. 41-56.
118. Cronin, M., et al., *High resolution in vivo bioluminescent imaging for the study of bacterial tumour targeting*. PLoS One, 2012. **7**(1): p. e30940.
119. Chu, S.H., et al., *In vitro and in vivo radiosensitization induced by hydroxyapatite nanoparticles*. Neuro Oncol, 2013.
120. Bach, P., et al., *Specific elimination of CD133+ tumor cells with targeted oncolytic measles virus*. Cancer Res, 2013. **73**(2): p. 865-74.
121. Llaguno-Munive, M., et al., *Mifepristone improves chemo-radiation response in glioblastoma xenografts*. Cancer Cell Int, 2013. **13**(1): p. 29.
122. Cen, L., et al., *Efficacy of protracted temozolomide dosing is limited in MGMT unmethylated GBM xenograft models*. Neuro Oncol, 2013.
123. Viel, T., et al., *Analysis of the growth dynamics of angiogenesis-dependent and -independent experimental glioblastomas by multimodal small-animal PET and MRI*. J Nucl Med, 2012. **53**(7): p. 1135-45.
124. Schwartz, D.L., et al., *HIF-1-dependent stromal adaptation to ischemia mediates in vivo tumor radiation resistance*. Mol Cancer Res, 2011. **9**(3): p. 259-70.
125. Baumann, B.C., et al., *An integrated method for reproducible and accurate image-guided stereotactic cranial irradiation of brain tumors using the small animal radiation research platform*. Transl Oncol, 2012. **5**(4): p. 230-7.
126. Zhou, H., et al., *Dynamic near-infrared optical imaging of 2-deoxyglucose uptake by intracranial glioma of athymic mice*. PLoS One, 2009. **4**(11): p. e8051.
127. Dorsey, J.F., et al., *Tumor necrosis factor-related apoptosis-inducing ligand (TRAIL) and paclitaxel have cooperative in vivo effects against glioblastoma multiforme cells*. Mol Cancer Ther, 2009. **8**(12): p. 3285-95.
128. Wei, L.H., et al., *Changes in tumor metabolism as readout for Mammalian target of rapamycin kinase inhibition by rapamycin in glioblastoma*. Clin Cancer Res, 2008. **14**(11): p. 3416-26.
129. Vrabcic, M., et al., *MR perfusion and diffusion imaging in the follow-up of recurrent glioblastoma treated with dendritic cell immunotherapy: a pilot study*. Neuroradiology.
130. Law, M., et al., *Glioma grading: sensitivity, specificity, and predictive values of perfusion MR imaging and proton MR spectroscopic imaging compared with conventional MR imaging*. AJNR Am J Neuroradiol, 2003. **24**(10): p. 1989-98.
131. Gursel, D.B., N. Berry, and J.A. Boockvar, *Therapeutic stem cells encapsulated in a synthetic extracellular matrix selectively kill tumor cells, delay tumor growth, and increase survival in a mouse resection model of malignant glioma*. Neurosurgery, 2012. **70**(6): p. N17-9.
132. Ulloa-Montoya, F., et al., *Comparative transcriptome analysis of embryonic and adult stem cells with extended and limited differentiation capacity*. Genome Biol, 2007. **8**(8): p. R163.

References

133. Roobrouck, V.D., et al., *Differentiation potential of human postnatal mesenchymal stem cells, mesoangioblasts, and multipotent adult progenitor cells reflected in their transcriptome and partially influenced by the culture conditions*. Stem Cells, 2011. **29**(5): p. 871-82.
134. Verfaillie, C.M., *Multipotent adult progenitor cells: an update*. Novartis Found Symp, 2005. **265**: p. 55-61; discussion 61-5, 92-7.
135. Breyer, A., et al., *Multipotent adult progenitor cell isolation and culture procedures*. Exp Hematol, 2006. **34**(11): p. 1596-601.
136. Branle, F., et al., *Evaluation of the efficiency of chemotherapy in in vivo orthotopic models of human glioma cells with and without 1p19q deletions and in C6 rat orthotopic allografts serving for the evaluation of surgery combined with chemotherapy*. Cancer, 2002. **95**(3): p. 641-55.
137. Ibrahim, A., et al., *Highly efficient multicistronic lentiviral vectors with peptide 2A sequences*. Hum Gene Ther, 2009. **20**(8): p. 845-60.
138. Subramanian, K., et al., *Isolation procedure and characterization of multipotent adult progenitor cells from rat bone marrow*. Methods Mol Biol, 2010. **636**: p. 55-78.
139. Trekker, J., Jans K., Damm H., Mertens D., Nuytten T., Vanacken J., Moshchalkov V., D'Haen J., Stakenborg T., Van Roy W., Himmelreich U. , *Synthesis of PEGylated magnetic nanoparticles with different core sizes*. IEEE Trans Magn, 2013(49): p. 219-226.
140. Trekker, J., et al., *Sensitive in vivo cell detection using size-optimized superparamagnetic nanoparticles*. Biomaterials, 2013. **35**(5): p. 1627-35.
141. Struys, T., et al., *Magnetic resonance imaging of human dental pulp stem cells in vitro and in vivo*. Cell Transplant, 2013. **22**(10): p. 1813-29.
142. Rosland, G.V., et al., *Long-term cultures of bone marrow-derived human mesenchymal stem cells frequently undergo spontaneous malignant transformation*. Cancer Res, 2009. **69**(13): p. 5331-9.
143. Trekker, J., et al., *Sensitive in vivo cell detection using size-optimized superparamagnetic nanoparticles*. Biomaterials, 2013.
144. Cunningham, J.J., et al., *Lessons from human teratomas to guide development of safe stem cell therapies*. Nat Biotechnol, 2012. **30**(9): p. 849-57.
145. Lo Nigro, A., et al., *MAPC culture conditions support the derivation of cells with nascent hypoblast features from bone marrow and blastocysts*. J Mol Cell Biol, 2012. **4**(6): p. 423-6.
146. Chien, L.Y., et al., *In vivo magnetic resonance imaging of cell tropism, trafficking mechanism, and therapeutic impact of human mesenchymal stem cells in a murine glioma model*. Biomaterials, 2011. **32**(12): p. 3275-84.
147. Sun, N., A. Lee, and J.C. Wu, *Long term non-invasive imaging of embryonic stem cells using reporter genes*. Nat Protoc, 2009. **4**(8): p. 1192-201.
148. Wolfs, E., et al., *Optimization of multimodal imaging of mesenchymal stem cells using the human sodium iodide symporter for PET and Cerenkov luminescence imaging*. PLoS One, 2014. **9**(4): p. e94833.
149. Wang, N., et al., *Comparison of transduction efficiency among various lentiviruses containing GFP reporter in bone marrow hematopoietic stem cell transplantation*. Exp Hematol, 2013. **41**(11): p. 934-43.
150. Jacobs, A.H., et al., *Improved herpes simplex virus type 1 amplicon vectors for proportional coexpression of positron emission tomography marker and therapeutic genes*. Hum Gene Ther, 2003. **14**(3): p. 277-97.
151. Kucerova, L., et al., *Adipose tissue-derived human mesenchymal stem cells mediated prodrug cancer gene therapy*. Cancer Res, 2007. **67**(13): p. 6304-13.
152. Miletic, H., et al., *Normal brain cells contribute to the bystander effect in suicide gene therapy of malignant glioma*. Clin Cancer Res, 2007. **13**(22 Pt 1): p. 6761-8.
153. Barth, R.F., *Rat brain tumor models in experimental neuro-oncology: the 9L, C6, T9, F98, RG2 (D74), RT-2 and CNS-1 gliomas*. J Neurooncol, 1998. **36**(1): p. 91-102.

References

154. Kovacsovics-Bankowski, M., et al., *Pre-clinical safety testing supporting clinical use of allogeneic multipotent adult progenitor cells*. *Cytotherapy*, 2008. **10**(7): p. 730-42.
155. Szatmari, T., et al., *Detailed characterization of the mouse glioma 261 tumor model for experimental glioblastoma therapy*. *Cancer Sci*, 2006. **97**(6): p. 546-53.
156. Leten, C., et al., *In vivo and ex vivo assessment of the blood brain barrier integrity in different glioblastoma animal models*. *J Neurooncol*, 2014.
157. Jacobs, A.H., et al., *Imaging-guided gene therapy of experimental gliomas*. *Cancer Res*, 2007. **67**(4): p. 1706-15.
158. Le Mercier, M., et al., *Knocking down galectin 1 in human hs683 glioblastoma cells impairs both angiogenesis and endoplasmic reticulum stress responses*. *J Neuropathol Exp Neurol*, 2008. **67**(5): p. 456-69.
159. Nichols, J., et al., *Formation of pluripotent stem cells in the mammalian embryo depends on the POU transcription factor Oct4*. *Cell*, 1998. **95**(3): p. 379-91.
160. Fillat, C., et al., *Suicide gene therapy mediated by the Herpes Simplex virus thymidine kinase gene/Ganciclovir system: fifteen years of application*. *Curr Gene Ther*, 2003. **3**(1): p. 13-26.
161. Vile, R.G., et al., *Targeted gene therapy for cancer: herpes simplex virus thymidine kinase gene-mediated cell killing leads to anti-tumour immunity that can be augmented by co-expression of cytokines in the tumour cells*. *Biochem Soc Trans*, 1997. **25**(2): p. 717-22.
162. Vile, R.G., et al., *Generation of an anti-tumour immune response in a non-immunogenic tumour: HSVtk killing in vivo stimulates a mononuclear cell infiltrate and a Th1-like profile of intratumoural cytokine expression*. *Int J Cancer*, 1997. **71**(2): p. 267-74.
163. Braumuller, H., et al., *T-helper-1-cell cytokines drive cancer into senescence*. *Nature*, 2013. **494**(7437): p. 361-5.
164. Perek, N. and D. Denoyer, *The multidrug resistance mechanisms and their interactions with the radiopharmaceutical probes used for an in vivo detection*. *Curr Drug Metab*, 2002. **3**(1): p. 97-113.
165. Zagzag, D., et al., *Vascular apoptosis and involution in gliomas precede neovascularization: a novel concept for glioma growth and angiogenesis*. *Lab Invest*, 2000. **80**(6): p. 837-49.
166. Wesseling, P., D.J. Ruiters, and P.C. Burger, *Angiogenesis in brain tumors; pathobiological and clinical aspects*. *J Neurooncol*, 1997. **32**(3): p. 253-65.
167. Kaya, M. and B. Ahishali, *Assessment of permeability in barrier type of endothelium in brain using tracers: Evans blue, sodium fluorescein, and horseradish peroxidase*. *Methods Mol Biol*, 2011. **763**: p. 369-82.
168. Roberts, H.C., et al., *Quantitative estimation of microvascular permeability in human brain tumors: correlation of dynamic Gd-DTPA-enhanced MR imaging with histopathologic grading*. *Acad Radiol*, 2002. **9 Suppl 1**: p. S151-5.
169. Just, M., et al., *MRI-assisted radiation therapy planning of brain tumors--clinical experiences in 17 patients*. *Magn Reson Imaging*, 1991. **9**(2): p. 173-7.
170. Roberts, H.C., et al., *Dynamic, contrast-enhanced CT of human brain tumors: quantitative assessment of blood volume, blood flow, and microvascular permeability: report of two cases*. *AJNR Am J Neuroradiol*, 2002. **23**(5): p. 828-32.
171. Nomura, T., T. Inamura, and K.L. Black, *Intracarotid infusion of bradykinin selectively increases blood-tumor permeability in 9L and C6 brain tumors*. *Brain Res*, 1994. **659**(1-2): p. 62-6.
172. Preston, E. and J. Webster, *Differential passage of [¹⁴C]sucrose and [³H]inulin across rat blood-brain barrier after cerebral ischemia*. *Acta Neuropathol*, 2002. **103**(3): p. 237-42.
173. Loveless, M.E., et al., *A quantitative comparison of the influence of individual versus population-derived vascular input functions on dynamic contrast enhanced-MRI in small animals*. *Magn Reson Med*, 2011. **67**(1): p. 226-36.
174. Matuskova, M., et al., *HSV-tk expressing mesenchymal stem cells exert bystander effect on human glioblastoma cells*. *Cancer Lett*, 2009. **290**(1): p. 58-67.

References

175. Hata, N., et al., *Platelet-derived growth factor BB mediates the tropism of human mesenchymal stem cells for malignant gliomas*. *Neurosurgery*, 2010. **66**(1): p. 144-56; discussion 156-7.
176. Pardridge, W.M., *Drug targeting to the brain*. *Pharm Res*, 2007. **24**(9): p. 1733-44.
177. Vandeputte, C., et al., *Characterization of the inflammatory response in a photothrombotic stroke model by MRI: implications for stem cell transplantation*. *Mol Imaging Biol*. **13**(4): p. 663-71.
178. Jain, R.K., et al., *Angiogenesis in brain tumours*. *Nat Rev Neurosci*, 2007. **8**(8): p. 610-22.
179. Lee, S.W., et al., *Blood-brain barrier interfaces and brain tumors*. *Arch Pharm Res*, 2006. **29**(4): p. 265-75.
180. Belot, N., et al., *Molecular characterization of cell substratum attachments in human glial tumors relates to prognostic features*. *Glia*, 2001. **36**(3): p. 375-90.
181. Lamoral-Theys, D., et al., *Long-term temozolomide treatment induces marked amino metabolism modifications and an increase in TMZ sensitivity in Hs683 oligodendroglioma cells*. *Neoplasia*, 2010. **12**(1): p. 69-79.
182. Wolburg, H., et al., *The disturbed blood-brain barrier in human glioblastoma*. *Mol Aspects Med*, 2012. **33**(5-6): p. 579-89.
183. Mathieu, V., et al., *Combining bevacizumab with temozolomide increases the antitumor efficacy of temozolomide in a human glioblastoma orthotopic xenograft model*. *Neoplasia*, 2008. **10**(12): p. 1383-92.
184. Sturm, D., et al., *Hotspot mutations in H3F3A and IDH1 define distinct epigenetic and biological subgroups of glioblastoma*. *Cancer Cell*, 2012. **22**(4): p. 425-37.
185. Szerlip, N.J., et al., *Intratumoral heterogeneity of receptor tyrosine kinases EGFR and PDGFRA amplification in glioblastoma defines subpopulations with distinct growth factor response*. *Proc Natl Acad Sci U S A*, 2011. **109**(8): p. 3041-6.
186. Barajas, R.F., Jr., et al., *Regional variation in histopathologic features of tumor specimens from treatment-naïve glioblastoma correlates with anatomic and physiologic MR Imaging*. *Neuro Oncol*, 2012. **14**(7): p. 942-54.
187. Kremer, S., et al., *Evaluation of an albumin-binding gadolinium contrast agent in multiple sclerosis*. *Neurology*, 2013. **81**(3): p. 206-10.
188. Stupp, R., et al., *Radiotherapy plus concomitant and adjuvant temozolomide for glioblastoma*. *N Engl J Med*, 2005. **352**(10): p. 987-96.
189. Chiocca, E.A., et al., *Neurosurgical delivery of chemotherapeutics, targeted toxins, genetic and viral therapies in neuro-oncology*. *J Neurooncol*, 2004. **69**(1-3): p. 101-17.
190. Zu, C. and J. Wang, *Tumor-colonizing bacteria: a potential tumor targeting therapy*. *Crit Rev Microbiol*, 2014. **40**(3): p. 225-35.
191. Binello, E. and I.M. Germano, *Stem cells as therapeutic vehicles for the treatment of high-grade gliomas*. *Neuro Oncol*, 2012. **14**(3): p. 256-65.
192. Namba, H., et al., *Efficacy of the bystander effect in the herpes simplex virus thymidine kinase-mediated gene therapy is influenced by the expression of connexin43 in the target cells*. *Cancer Gene Ther*, 2001. **8**(6): p. 414-20.
193. Mesnil, M., et al., *Bystander killing of cancer cells by herpes simplex virus thymidine kinase gene is mediated by connexins*. *Proc Natl Acad Sci U S A*, 1996. **93**(5): p. 1831-5.
194. Mori, K., et al., *Bystander killing effect of thymidine kinase gene-transduced adult bone marrow stromal cells with ganciclovir on malignant glioma cells*. *Neurol Med Chir (Tokyo)*, 2010. **50**(7): p. 545-53.
195. Cha, S., *Update on brain tumor imaging: from anatomy to physiology*. *AJNR Am J Neuroradiol*, 2006. **27**(3): p. 475-87.
196. Heiss, W.D., P. Raab, and H. Lanfermann, *Multimodality assessment of brain tumors and tumor recurrence*. *J Nucl Med*, 2011. **52**(10): p. 1585-600.
197. Deroose, C.M., et al., *Noninvasive monitoring of long-term lentiviral vector-mediated gene expression in rodent brain with bioluminescence imaging*. *Mol Ther*, 2006. **14**(3): p. 423-31.

References

198. Waerzeggers, Y., et al., *Multimodal imaging of neural progenitor cell fate in rodents*. Mol Imaging, 2008. **7**(2): p. 77-91.
199. Chiocca, E.A., et al., *A phase I open-label, dose-escalation, multi-institutional trial of injection with an E1B-Attenuated adenovirus, ONYX-015, into the peritumoral region of recurrent malignant gliomas, in the adjuvant setting*. Mol Ther, 2004. **10**(5): p. 958-66.
200. Winkeler, A., et al., *Switching on the lights for gene therapy*. PLoS One, 2007. **2**(6): p. e528.
201. Luyckx, A., et al., *Mouse MAPC-mediated immunomodulation: Cell-line dependent variation*. Exp Hematol, 2010. **38**(1): p. 1-2.
202. Huang, R.P., et al., *Reduced connexin43 expression in high-grade human brain glioma cells*. J Surg Oncol, 1999. **70**(1): p. 21-4.
203. Mischel, P.S., S.F. Nelson, and T.F. Cloughesy, *Molecular analysis of glioblastoma: pathway profiling and its implications for patient therapy*. Cancer Biol Ther, 2003. **2**(3): p. 242-7.
204. Scott, J.N., et al., *How often are nonenhancing supratentorial gliomas malignant? A population study*. Neurology, 2002. **59**(6): p. 947-9.
205. Fink, J., D. Born, and M.C. Chamberlain, *Pseudoprogression: relevance with respect to treatment of high-grade gliomas*. Curr Treat Options Oncol, 2011. **12**(3): p. 240-52.
206. Bodor, N. and P. Buchwald, *Recent advances in the brain targeting of neuropharmaceuticals by chemical delivery systems*. Adv Drug Deliv Rev, 1999. **36**(2-3): p. 229-254.
207. Min, J.J., M. Iyer, and S.S. Gambhir, *Comparison of [18F]FHBG and [14C]FIAU for imaging of HSV1-tk reporter gene expression: adenoviral infection vs stable transfection*. Eur J Nucl Med Mol Imaging, 2003. **30**(11): p. 1547-60.
208. Slutsky, E.D., *Modeling of [18F]-FHBG in tumor and normal tissue*, in *Department of Nuclear Science and Engineering*. 2007, Massachusetts institute of technology: Massachusetts. p. 40.
209. Goldman, C.K., et al., *Epidermal growth factor stimulates vascular endothelial growth factor production by human malignant glioma cells: a model of glioblastoma multiforme pathophysiology*. Mol Biol Cell, 1993. **4**(1): p. 121-33.
210. Yaghoubi, S.S., et al., *Noninvasive detection of therapeutic cytolytic T cells with 18F-FHBG PET in a patient with glioma*. Nat Clin Pract Oncol, 2009. **6**(1): p. 53-8.
211. Ketkar-Atre, A.S., T. Soenen, S. Lambrichts, I. Verfaillie, C. De Cuyper, M. Himmelreich, U., *Viability in contrast agent uptake by different but similar stem cell types*. International Journal of Nanomedicine, 2013(8): p. 4577-4591.
212. Amano, S., et al., *Timing of ganciclovir administration in glioma gene therapy using HSVtk gene-transduced mesenchymal stem cells*. Cancer Genomics Proteomics, 2011. **8**(5): p. 245-50.
213. Gomez, G.G. and C.A. Kruse, *Mechanisms of malignant glioma immune resistance and sources of immunosuppression*. Gene Ther Mol Biol, 2006. **10**(A): p. 133-146.
214. Bertram, J.S., *The molecular biology of cancer*. Mol Aspects Med, 2000. **21**(6): p. 167-223.
215. Athie-Morales, V., et al., *Sustained IL-12 signaling is required for Th1 development*. J Immunol, 2004. **172**(1): p. 61-9.

Curriculum Vitae

Personalialia:

Name: Cindy Leten

Address: Haspengouwstraat 3, 3560 Lummen

email: cindy.leten@med.kuleuven.be

Mobile no: 0032 497205837

Date of Birth: 18/03/1986

Nationality: Belgian

Education

2007-2009: Master in Biomedical Sciences (KU Leuven)

2004-2007: Bachelor in Biomedical Sciences (KU Leuven)

Work experience:

2009-2014: Doctoral research on Multi-modal small animal imaging for brain tumor therapy assessment in the lab of Biomedical MRI of Prof. U Himmelreic at KU Leuven, Belgium and BIL of Prof. Annemie Van Der Linden at University of Antwerp, Belgium.

2014-present: Global data manager for Valesta at Janssen Pharmaceutica, Belgium.

List of publications

1. **Leten C.**, Roobrouck VD., Struys T., Dresselaers T., Vande Velde G., Santermans J., Lo Nigro A., Ibrahimi A., Gijbsers R., Eggermont K., Lambrichts I., Verfaillie CM., Himmelreich U. , Controlling and monitoring stem cell safety in vivo in an experimental rodent model. *Stem cell*, 2014.
2. **Leten C.**, Struys T., Dresselaers T., Himmelreich U., *In vivo and ex vivo assessment of the blood brain barrier integrity in different glioblastoma animal models.* *J Neurooncol*, 2014. **119**(2): p. 297-306.
3. **Leten C.**, Trekker J., Struys T., Dresselaers T., Gijbsers R., Vande Velde G., Lambrichts I., Van der Linden A., Verfaillie C., Himmelreich U. Assessment of bystander killing mediated therapy of malignant brain tumors using a multi-modal imaging approach. (Submitted to *Stem cell research & therapy*)
5. Trekker J., **Leten C.**, Struys T., Lazenka VV., Argibay B., Micholt, L., Lambrichts I., Van Roy W., Lagae L., Himmelreich U., *Sensitive in vivo cell detection using size-optimized superparamagnetic nanoparticles.* *Biomaterials*, 2013.
6. Nemethova, A., **Leten, C.**, Gomez Pinilla PJ., van Bree SH., van Heijningen, C., Cailotto, C., Himmelreich, U., Depoortere, I., Matteoli, G., Boeckxstaens G., Effect of ghrelin administered before or after surgery in a mouse model of postoperative ileus. (Submitted to *PLOS ONE*)

4. Struys T., Ketkar-Atre A., Gervois P., **Leten C.**, Hilkens P., Martens W., Bronckaers A., Dresselaers T., Politis C., Lambrichts I., Himmelreich U., *Magnetic resonance imaging of human dental pulp stem cells in vitro and in vivo*. Cell Transplant, 2012. **22**(10): p. 1813-29.

Conference abstracts

1. **Leten C.**, Trekker J., Struys T., Gijssbers R., Debyser Z., Lambrichts I., Verfaillie C., Himmelreich U. (2013) Proof of principle: imaging of suicide gene therapy for glioblastoma. *World Molecular Imaging Congress (WMIC), Savannah, Georgia, USA* (oral presentation).
2. **Leten C.**, Struys T., Verfaillie C., Himmelreich U. (2013) Monitoring safety of sem cells in vivo. *Belgian Molecular Imaging Congress (BMIC), Leuven, Belgium* (oral presentation).
3. **Leten C.**, Struys T., Verfaillie C., Himmelreich U. (2013) Monitoring safety of sem cells in vivo. *European Molecular Imaging Meeting (EMIM), Torino, Italy* (poster presentation).
4. **Leten C.**, Trekker J., Struys T., Maris M., Gijssbers R., Debyser Z., Himmelreich U. (2012) Multi-modal imaging of therapeutic HSV-tk expressing stem cells for glioma treatment. *World Molecular Imaging Congress (WMIC), Dublin, Ireland* (poster presentation).
5. **Leten C.**, Maris M., Debyser Z., Himmelreich U. (2010) Multi-modal validation of stem cell based tumor therapy. *Young Belgian Magnetic Resonance Scientists (YBMRS), Blankenbergen, Belgium* (poster presentation).